Development and Implementation of an Extended-Gate Ion-Sensitive Field-Effect Transistor (EGFET) Biosensor for the Detection of β-lactamase Activity

Callum David Silver

Doctor of Philosophy

University of York

Electronic Engineering

June 2021

Abstract

Antimicrobial resistance (AMR) is a major threat to global public health. A leading cause behind the acceleration of AMR is the inappropriate and unnecessary use of antibiotics. To enable informed prescribing behaviours and to preserve the efficacy of existing antibiotics, better diagnostic technology is required that enables analysis of bacterial susceptibility, at the time of prescription. One of the most common forms of resistance is to β-lactam antibiotics such as penicillins. This resistance is primarily caused by β-lactamase enzymes, which catalytically hydrolyse β-lactam drugs, rendering them ineffective. Current methods for point-of-care detection of these enzymes often use pH-sensitive dyes to detect solution acidification caused by β-lactam hydrolysis. However, these assays are typically qualitative and have been shown to be ambiguous for cases of low-level enzyme expression. This work describes the development and testing of an extended-gate ion-sensitive field-effect transistor (EGFET) as the transduction element of an acidimetric β-lactamase assay. The EGFET uses a discrete, commercial metal-oxide-semiconductor field-effect transistor (MOSFET) coupled to a IrO_x electrode which is capable of producing high pH sensitivities above 60 mV/pH with a less than two second time-response. This device was used to perform quantitative measurements of β-lactamase activity. Measurements were demonstrated for a β-lactamase blend containing as low as 0.4-0.7 IU β-lactamase I and 0.06-0.1 IU β-lactamase II. Additionally, this work demonstrates the use of a surface-bindable β-lactam antibiotic which reacts in the presence of β-lactamase enzymes in both buffer and physiological media (undiluted urine). By localising the hydrolysis reaction to the sensor surface, it is anticipated that the combination of the surface-tethered antibiotic and EGFET will increase the sensitivity of the assay. Such high-sensitivity, quantitative measurements of β-lactamase activity in a miniaturised device, could ultimately provide an unambiguous assay for point-of-care detection of β-lactam resistance.

Contents

List of Figures

Acknowledgements

I would like to thank all of those who I have had the pleasure of working with and those that have encouraged me throughout this project. This work would not be possible without the continuing support of a number of people.

First, I would like to thank my supervisor Dr. Steve Johnson. His enthusiasm for interdisciplinary research has been inspirational and has motivated me to explore areas of science I wouldn't have even considered as an undergraduate electronic engineer. I am very grateful for the support, opportunities, and humour he has provided over the years. It has been a real privilege and pleasure to work with him. Thank you for challenging my ideas and dealing with me for this long.

My thanks also extend to Prof. Thomas Krauss for his support, inspiration, and for always asking the tough but interesting questions. I would also like to thank Prof. Anne-Kathrin Duhme-Klair and Prof. Gavin Thomas for their advice and guidance throughout this project. Thank you also to Prof. Christoph Wälti for allowing me to explore research beyond my own project.

I would also like to thank all the past and present members of the Bio-Inspired Technologies and Photonics research groups. My appreciation goes out to Alexander Drayton, thank you for your friendship and support throughout; Dr. Lisa Miller, Dr. Matt Simmons, Dr. Casper Kunstmann-Olsen, Dr. Steve Thorpe, Dr. Jose Juan-Colás, George Duffett, Isabel Barth, Manuel Deckart, Josh Male, Rhys Ashton, Kalum Thurgood-Parkes, Elena Mancinelli, Shrishty Bakshi, Dr. Ben Coulson, Dr. Giampaolo Pitruzzello, Dr. Kezheng Li, Dr. Donato Conteduca, Dr. Christopher Reardon, Dr. Yue Wang, Dr. Lewis Reeves, Dr. Elena Koutsoumpeli, Adam Stroughair, Reyme Herman, and Dr. Augusto Martins. The breadth of knowledge possessed by these people has been invaluable. Thank you all for the interesting discussions, kindness, and laughter. It has been an absolute pleasure working alongside you all for nearly four years and I hope we can all meet again for a coffee soon.

Thank you also to Arnold, Janet, Edgar, Pepe, Vish, Aeri, Kafi, Sumu, Jack, James, and Nils. It has been wonderful to get to know you all over the past three years. Thank you for everything. You have made me try so many new things.

A special thank you to Nick Banks, Wendy Robinson, Lydia Sharpe, Oli Withams, and Ben Rowlinson. Even though we no longer live together, you have all been there for me. I can't wait to see you all again soon.

An enormous gratitude goes to my parents and my family. You have always been supportive in everything I do and I am extremely lucky. I would not be the person I am today without you.

My deepest thanks goes to Beth Jenkins, who has endlessly supported me through the highs and lows of this project. Your encouragement, kindness, and love has meant more than you will ever know. This work would not have been possible without you.

Author's Declaration

I, Callum Silver, declare that this thesis is a presentation of original work and I am the sole author. I can confirm that:

- This work has not previously been presented for an award at this, or any other, University.
- The work presented in chapter 6 of this thesis is published as a joint lead-authorship publication in *ACS: Applied Materials and Interfaces* under the title 'A Surface-bound Antibiotic for the Detection of β-lactamases'. For clarity, work done by the other authors, primarily Dr. Lisa M. Miller and Mr. Reyme Herman, is included in this chapter, but is be explicitly specified. Synthesis of the surface-bindable molecules used in this chapter was carried out solely by L. Miller. Purification of the penicillin binding proteins used in this chapter was jointly carried out by L. Miller and R. Herman.
- The X-ray photoelectron spectroscopy discussed in chapter 4, was carried out by Dr. Benjamin Coulson.
- All sources are acknowledged as References.

Publications

The following lists provide detail of publications and conferences that have contributed to this thesis as well as side projects have been involved in.

1. L. M. Miller, C. D. Silver, R. Herman, A. K. Duhme-Klair, G. H. Thomas, T. F. Krauss, and S. D. Johnson, "Surface-Bound Antibiotic for the Detection of β-Lactamases," *ACS Applied Materials and Interfaces*, vol. 11, no. 36, pp. 32 599–32 604, Sep. 2019.
2. L. Jasaitis, C. D. Silver, A. E. Rawlings, D. T. Peters, F. Whelan, L. Regan, L. Pasquina- Lemonche, J. R. Potts, S. D. Johnson, and S. S. Staniland, "Rational Design and Self- Assembly of Coiled-Coil Linked SasG Protein Fibrils," *ACS Synthetic Biology*, vol. 9, no. 7, pp. 1599–1607, Jul. 2020.

Conferences

1. C. D. Silver, L. M. Miller, A-K. Duhme-Klair, G. Thomas, T.F. Krauss, S. Johnson, Functionalised antibiotic surfaces for the detection of β-lactamases, **Rapid Communication Presentation** at the 6th International Conference on Bio-Sensing Technology, Kuala-Lumpur, Malaysia
2. C. D. Silver, L. M. Miller, A-K. Duhme-Klair, G. Thomas, T.F. Krauss, S. Johnson, A Surface-Bound Antibiotic for the Detection of β-Lactamases, **Poster Presentation** at Sensors in Medicine 2019, London, England

Awards

1. Finalist at the York Talks, PhD Spotlight Competition, 2019
2. Departmental Prize for the Best 2nd Year PhD Poster at the Electronic Engineering Departmental PhD Conference, 2019

To Beth Jenkins

"The most beautiful thing we can experience is the mysterious. It is the source of all true art and science."

Albert Einstein

"Who would've guessed reading and writing would pay off?"

Homer Simpson

Chapter 1

Introduction

This chapter introduces the motivation for this work, namely the need for better technologies for rapidly determining the presence of antimicrobial resistance in clinical infections. The chapter concludes with a discussion of the aims of this work and an outline of the thesis structure.

1.1 Antimicrobial Resistance: What needs to be done?

Antimicrobial Resistance (AMR) is the ability for microbes to grow in the presence of antimicrobial compounds, such as antibiotics [1]. Although the term AMR relates to all microbial species such as viruses, fungi and parasites, one of the largest areas of concern is the rising rate of antibiotic resistant bacterial infections. While the evolution of resistance is a natural, evolutionary process, the overuse of antibiotics has been shown to directly correlate to the number of resistant infections [2–4]. In the past, these infections were limited to hospitals, where antibiotics are commonly used. However, bacterial infections are increasingly requiring treatment with second- and third-line antibiotics, not only in hospitals, but in the wider community [5]. Antibiotic-resistant infections are now a global issue. It is estimated that these resistant infections claim 700,000 lives per year worldwide, with nearly 50,000 in the EU and US alone [6, 7]. At the current rate of increase, the total deaths per year are set to rise to 10 million by the year 2050 [5], while the increase in healthcare needs caused by these infections may end up costing a global $100 trillion, equating to an extra $10,000 per person [5]. Although these numbers remain a source of debate [8], there is no doubt of the increasing burden associated with AMR.

With increased resistance, everyday infections become more dangerous and difficult to treat. However, this issue does not just include death caused by the inability to treat standard infections. Antibiotics are used routinely throughout medicine to prevent infections during many medical procedures, such as surgery and chemotherapy. In these cases, it is possible for the immune system to be suppressed and, without the ability to prevent infection with antibiotics, these procedures become impractical and risky.

The O'Neil report was a two-year study of the economic and societal impact AMR will have in the near future [5]. It discussed several points for improvement that must be put into place to prevent the further development of AMR, such as the societal changes and research needs. One key aspect discussed for preventing the further development and acceleration of AMR is public awareness. A number of campaigns have been set up with the aim to discourage over-prescription and reduce the overall use of antibiotics [9–11]. These campaigns have been shown to be effective as a low-cost method for increasing public commitment to reducing AMR [12]. However, in cases where antibiotics are thought

to be required, there is still an issue with the prescription of ineffective and unnecessary antibiotics. A study investigating prescribing behaviours for respiratory problems in the US found that, of 40 million prescribed antibiotics, 27 million were thought to be given questionably [13]. Incorrect and unnecessary prescriptions are one of the principal areas which needs to be addressed to slow the progression of AMR. The O'Neil report stated that by 2020 it should be mandatory that antibiotic prescriptions are informed by data [5], however, this is still not the case in 2021 [14]. Conventional methods used to identify antibiotic susceptibility, such as growth assays, can take days to complete and often require isolation of the pathogenic bacteria [15, 16], thus, for patient safety and satisfaction, antibiotics are often prescribed without prior knowledge of the infections susceptibility to the drug or even whether the infection is bacterial.

To enable informed prescribing behaviours, better diagnostic technology must exist which allows the analysis of a patient's infection, at the time of prescription. For this to be feasible, the technology has to be usable in a point-of-care setting and produce fast results. Furthermore, the current technology available for detecting resistance is low-cost and simple to use, therefore, for a new technology to be readily adopted, it must also meet these criteria.

1.2 Goals of this Thesis

Given the need for new diagnostic technology which is applicable at the point-of-care, this thesis describes the development towards a diagnostic assay for the detection of the most common form of resistance, β-lactam resistance. By determining the presence of resistance denoting enzymes, known as β-lactamases, the assay should be able to determine the suitability of prescribing this class of antibiotics. The assay utilises a discrete, extended-gate ion-sensitive field-effect transistor (EGFET) to detect the acidification of a solution due to the β-lactam-β-lactamase reaction. The EGFET device was developed such that it could be fabricated using low-cost methods and could be easily incorporated into an automated diagnostic system. Additionally, this thesis demonstrates the use of a surface-bindable β-lactam probe which responds to the presence of β-lactamase enzymes which could be incorporated into the discrete EGFET device as well as a number of alternative surface-sensitive biosensor technologies.

Investigate a low-cost, high-sensitivity, and fast pH sensing device to quantifiably detect β-lactam acidification due to β-lactamase hydrolysis

It is well established that hydrolysis of β-lactam antibiotics by β-lactamase enzymes leads to acidification of the bulk solvent. Thus, by developing a low-cost pH sensing device which was sensitive and fast enough to detect this acidification reaction, it could be used as the transducing element for a quantifiable point-of-care assay. Previous qualitative acidimetric assays have demonstrated pH changes of more than 1 pH unit from β-lactam-β-lactamase hydrolysis in as little as 1 min [17, 18], thus the device should exhibit a limit of detection of less than 1 pH level and have a time-response of less than 0.01 pH per

second to quantifiably detect this change over time.

Determine a quantifiable metric which can be used to determine β-lactamase activity in an acidimetric assay

The purpose of this work is to develop a point-of-care device which allows for the quantifiable measurements of β-lactamase activity. Therefore, it is necessary to find a quantity which could easily be measured using electronic hardware and is directly related to the concentration, and thus the activity, of β-lactamase.

Investigate the use of a surface-bound β-lactam antibiotic which is capable of enabling β-lactamase catalysed hydrolysis at a sensor surface

Previous work has demonstrated that a higher signal-to-noise ratio can be achieved by bringing the target reaction of the acidimetric assay to the sensor surface [19]. Therefore, the investigation of a surface-bindable β-lactam which is still capable of being hydrolysed by β-lactamase enzymes once bound may allow for an improvement in device sensitivity.

1.3 Outline of this thesis

This thesis is comprised of seven chapters. The contents of each chapter are as follows:

Chapter 1: Introduction

This chapter introduces the motivation of this work and describes the thesis goals and content.

Chapter 2: Background and Theory

This chapter discusses the issue of antimicrobial resistance and gives an introduction to β-lactam antibiotics and associated resistance mechanisms. It also covers the theory needed to understand the proposed β-lactamase assay and the EGFET device. Finally, it discusses some of the current and emerging techniques for β-lactamase detection as well as giving an overview of developments in Ion-Sensitive Field Effect Transistor (ISFET) technology.

Chapter 3: Fabrication, Equipment and Experimental Techniques

This chapter describes the fabrication methods used to build the discrete component Extended-Gate Ion-Sensitive FET (EGFET) devices. It also discusses the equipment utilised for both measurements and fabrication, as well as the fundamental theory behind the techniques used to characterise EGFET devices.

Chapter 4: Development of an Iridium Oxide Extended-Gate ISFET

This chapter presents the iridium oxide EGFET device used throughout this project. It discusses the characterisation of the device's pH sensing properties and limit of detection.

Following this, it presents an investigation into the effect of electrode parameters on the pH sensing properties of the device. Finally, the chapter concludes with an investigation into the physical properties of the iridium oxide film.

Chapter 5: EGFET-based detection of β-lactamase Activity

This chapter demonstrates the use of the developed EGFET device for detection of β-lactamase activity. The chapter begins with a discussion on the theory surrounding β-lactam acidification, investigating the mechanism through which this effect occurs. Following this, the chapter discusses the development of the analyte used for the assay, discussing the effect that the various parameters have on the buffer capacity and the observed pH change. Finally, the chapter explores the use of the developed EGFET device in conjunction with an optimised acidimetric β-lactamase assay, demonstrating its ability to quantify β-lactamase activity.

Chapter 6: Immobilisation of a tethered β-lactam for β-lactamase Detection

This chapter discusses the development of a surface-bindable antibiotic probe which is able to react to the presence of β-lactamases. The chapter begins by discussing the methods used to ensure the antibiotic did not degrade once bound to a surface. Following this, the antibiotic functionalised surface was analysed to determine its suitability for β-lactamase detection. Finally, the chapter concludes with a demonstration of the surface-bindable antibiotic use in undiluted urine.

Chapter 7: Conclusions and Outlook

This chapter summarises the work presented in this thesis and discusses potential areas for further development, both in terms of short-term optimisation of the EGFET technology and long-term translation of the technology into a clinical application.

Chapter 2

Background and Theory

This chapter will discuss the challenge of antimicrobial resistance with a particular focus on β-lactam antibiotics and the associated resistance mechanisms. It also covers the theory that underpins the proposed β-lactamase assay and the EGFET device. Finally, it discusses some of the current and promising techniques that have been demonstrated for β-lactamase detection as well as giving an overview of ISFET technology developments.

2.1 Antimicrobials and Antimicrobial Resistance

Antimicrobials are any substances that inhibit the growth of, or kill, microorganisms such as bacteria, fungi, and viruses [20]. These range from disinfectants, to specific forms of antiviral treatments [21]. Antimicrobials are essential for modern medicine. Without them, many common surgical procedures and treatments would carry an increased risk of infection, leading to severe mortality rates. Many antimicrobials are non-selectively harmful to all macro- and microorganisms, thus, to control infectious disease within a patient, non-toxic antimicrobials, which are effective only against the infecting microbe, must be used. The most commonly used non-toxic antimicrobials for treating bacterial infections are antibiotics; chemical compounds which specifically inhibit bacterial processes. Kick-started by the discovery of penicillin in 1928 [22], over one hundred different antibiotics have been developed over the years [23]. Despite this large number of antibiotics, most fall into specific categories, depending on the mechanism of action with which they inhibit bacterial reproduction. Table 2.1 shows the various antibiotic categories and their mode of action.

Many antibiotics are not as effective at treating infections as they once were, due to increasing levels of antibiotic resistance. Antibiotic resistance is the ability for bacteria to survive in the presence of antibiotics that would otherwise kill or inhibit them [1]. The development of resistance is a natural, evolutionary process. When bacteria are subject to antibiotics, in order for them to survive and thrive, they can occasionally develop mutations which allow them to grow in the presence of the, originally harmful, antibiotic. In cases where antibiotics are at sub-lethal levels for most bacteria in a community, resistance has been shown to spread rapidly [26][27]. Although we are only beginning to see the major impact that antibiotic resistance will have on society, the development of resistance itself is not a new phenomenon. In his 1945 Nobel lecture, Alexander Fleming described, "*It is not difficult to make microbes resistant to penicillin by exposing them to concentrations not sufficient to kill them*" [22]. The "sufficient concentration" that Fleming was referring to is defined as either the Minimum Inhibitory Concentration (MIC), the concentration of antimicrobial at which no growth is seen after incubation, or the Minimum Bacterici-

Target	Examples	Mechanism of Action
Cell Wall Synthesis	Penicillins Cephalasporins Carbapenems	Binds to transpeptidase, the protein responsible for cross-linking peptides in cell wall.
	Vancomycin	Binds to the two D-ala molecules on the end of the peptide chains, preventing cross-linking.
Protein synthesis (30S)	Tetracyclines	Prevents binding of aminoacyl-tRNA to the 30s subunit of the ribosome.
	Kanamycin	Binds to the 30s subunit, causing mistranslation of mRNA
Protein synthesis (50S)	Macrolides Chloramphenicol	Binds to the 50S subunit of the ribosome, preventing peptidyl transferase activity.
RNA Synthesis	Rifampin Actinomycin	Prevents RNA transcription by binding to RNA polymerase.
DNA Synthesis	Fluoroquinolones	Interfere with DNA gyrase, preventing super-coiling of DNA.
	Metronidazole	Disrupts nuclead acid production through the use of its biproduct.
Folic Acid Metabolism	Trimethoprim Sulfanomides	Replaces para-aminobenzoic acid, which the cell needs to produce folic acid.
Mycolic Acid Metabolism	Isoniazid	Interferes with mycolic acid formation in mycobacteria, preventing cell wall synthesis.

Table 2.1: Table showing the various classes of antibiotics that are currently available with examples of each, and a description of their mechanism of action. Adapted from:[20, 24, 25]

dal Concentration (MBC), the concentration at which the antimicrobial will prevent any further growth when the bacteria are introduced into fresh, antimicrobial free, media [28].

Bacteria are capable of passing on resistance genes through a number of mechanisms, using one of two pathways. The primary pathway is vertical gene transfer, through reproduction, where cells divide and pass the genome to their offspring. The other pathway is known as horizontal gene transfer. This occurs when cells pass their genetic code to unrelated members of the community. For bacteria, this can occur through one of three methods, transformation, transduction, or conjugation [20]. Transformation occurs when bacteria release fragments of DNA into the environment, allowing other cells to uptake and incorporate them into their own genome. Transduction happens when genes are passed through bacteriophage. Bacteriophage reproduce by replicating inside bacterial cells; how-

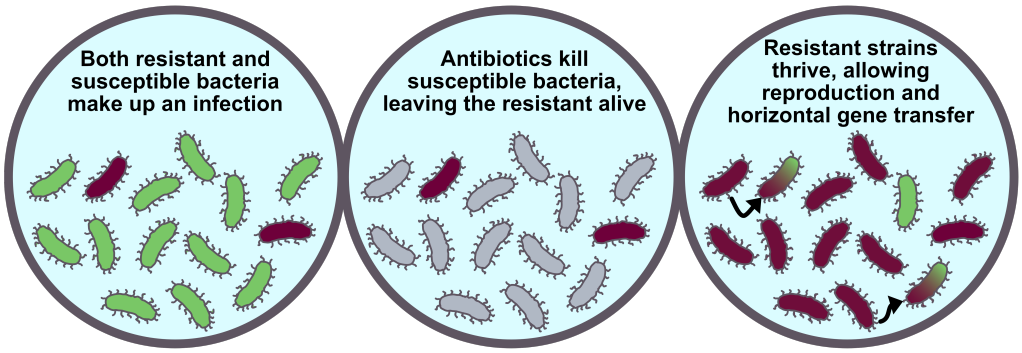

Figure 2.1: Diagram demonstrating the mechanism through which polyclonal infections can develop larger populations of antimicrobial-resistant bacteria. Adapted from [29] under the Open Government License.

ever, it is possible for the replicating bacteriophage to gain bacterial DNA instead. If this happens, the DNA can be transferred to an unrelated bacteria as the bacteriophage attempts to replicate. Both transformation and transduction do not require the cells to be in close proximity. In contrast, conjugation is a horizontal mechanism in which bacteria can produce an extruding structure from their membrane, known as a pilus, to transfer DNA to other cells. All three mechanisms allow transfer of DNA to other members of a community, enabling them to alter their phenotype and develop resistance.

The numerate ways in which bacteria can pass on their resistance leads to increasingly high populations of resistant bacteria when resistant strains are not treated with an effective antibiotic. As mentioned previously, sub-MIC or -MBC concentrations can cause resistance to develop rapidly; however, another issue arises when treating patients with polyclonal infections, meaning there are multiple strains or species of microbes. In these cases, susceptible strains can be killed easily, leaving behind only the resistant strains, as shown in figure 2.1. These strains now have little competition for nutrients and are able to reproduce until the majority of the population is resistant. The accelerated development of resistance following exposure to ineffective antimicrobials further demonstrates the need for better susceptibility testing. By rapidly determining an effective antimicrobial against an infection, the risk of resistance development and spread is reduced.

Given there are multiple ways in which antibiotics can kill bacteria, it is perhaps not surprising that there are also many ways in which bacteria can convey resistance. Bacteria have evolved resistance to antibiotics in three main ways [30]. The first, is by chemically modifying and inhibiting the antibiotic, usually carried out through the use of an enzyme. For example, β-lactam antibiotic resistance is often developed through the production of β-lactamase enzymes [31–33]. These enzymes hydrolyse sections of the antibiotic, rendering them unable to bind to their targets. The second form of resistance is achieved by preventing the antibiotic from reaching the target site in the first place. This form of resistance occurs when a bacterium has either a decreased permeability or developed a membrane modification known as an efflux pump, capable of actively removing the antibiotic from the cell [20]. The final form of resistance is caused by the bacterium modifying the binding site of the antibiotic target. This is the case for vancomycin resistance, where the amino-acid structure of the bacterium's cell wall is modified [34]. Many of the afore-

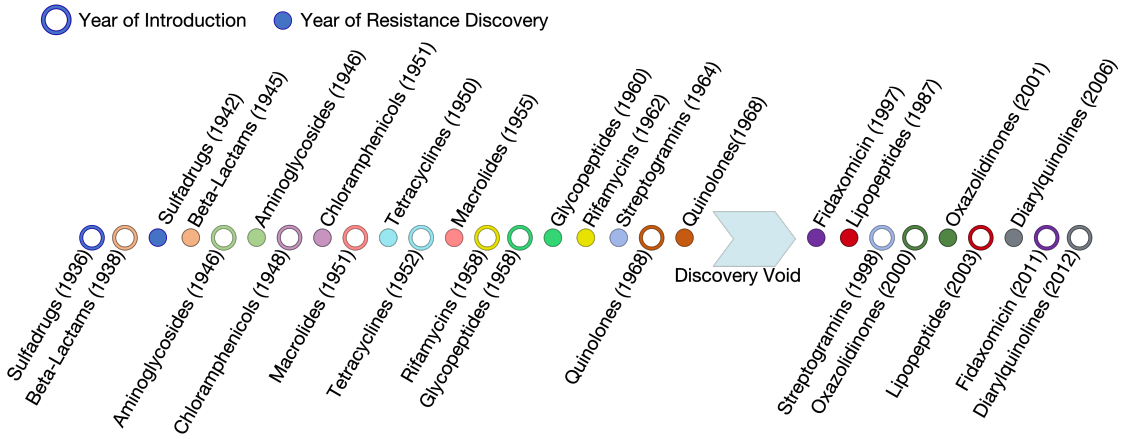

Figure 2.2: Timeline showing the year in which antibiotics were introduced into the market in comparison to the discovery of their related resistances. Image adapted from [25] based on data from [36] and [39].

mentioned resistances to antibiotics are formed through selective pressure; however, some antibiotics inherently won't work on certain species of bacteria, as the target mechanisms which the drug inhibits are not easily accessible, or simply not present [35]. Knowing which antibiotics will be effective at treating an infection is imperative to prevent further development of resistance. Furthermore, knowing the variety of resistance mechanisms can be useful when designing and testing susceptibility tests, as this can change the way results are perceived and inform the development of new methods for detecting resistance.

For every currently available antibiotic, there is an opposing form of resistance that has been identified [36]. Figure 2.2 shows the timeline of antibiotic development relative to the observation of associated resistance [25]. This illustrates how rapidly resistance can develop and highlights the struggle we face with treating bacterial infections. For example, urinary tract infections (UTIs) were previously a simple infection to treat using ampicillin, however, they often now require second- and third-line antibiotics such as trimethoprim and nitrofurantoin [37]. Prescribing the wrong antibiotic can lead to recurring infections and further medical complications. Primarily, antimicrobial resistance cases originate from hospitals, where antibiotics are used frequently; however, there have been increasing reports of resistance occurring outside the clinic [5]. With the development of new classes of drugs slowing [38, 39], antimicrobial stewardship and smarter prescriptions have never been more crucial. In order for greater stewardship to be possible however, diagnostic tests which determine antimicrobial susceptibility to specific drugs must be used.

2.1.1 Current Techniques for Antimicrobial Resistance Detection

Antimicrobial Susceptibility Tests (ASTs) are used routinely to properly diagnose bacterial infections and to identify the most appropriate treatment. ASTs are typically phenotypic assays which measure the efficacy of antibiotics on the growth of bacteria [40]. Given the innumerate mechanisms through which bacteria can convey resistance to drugs, the best indicator of the efficacy of an antibiotic is bacterial growth; however, tests which rely on this metric typically require several overnight steps. Nevertheless, these tests are crucial

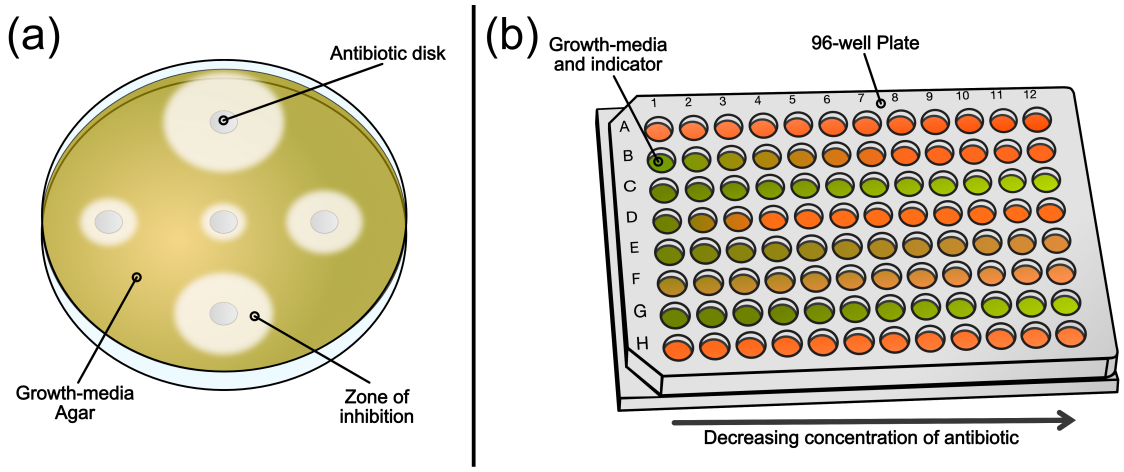

Figure 2.3: **(a)** - Diagram demonstrating the results of a disk diffusion assay to various antibiotics. The larger the zone of bacterial inhibition, the more effective the antibiotic is. **(b)** - Diagram showing a 96-well plate used for broth dilution assays. A change in the colour of the indicator indicates the presence of growing bacterial cultures. The well-plate contains decreasing concentrations of antibiotic across its rows, allowing the MIC to be determined.

as they allow the correct antibiotic to be given.

Disk diffusion assays are the predominant susceptibility tests and have been used for over 50 years [16]. In these tests, bacterial isolates are mixed with agar and left to incubate in Petri dishes containing antimicrobial-soaked disks, as shown in figure 2.3a. After a 24 hour period of incubation, the bacteria will have grown throughout the agar. Where the bacterial isolate is sensitive to the antibiotics contained in the pads, there will be a zone of inhibited growth around the disk. This particular method does have certain drawbacks however, such as its susceptibility to human error, as is the case with all manual tests. Secondly, the MIC or MBC cannot be quantified reliably; although, similar diffusion assays, such as the e-test, allow for more quantitative information to be acquired [41]. In spite of their shortcomings, the low cost and ease-of-operation of these methods are what has made them so widely used.

In broth dilution susceptibility tests, varying concentrations of antimicrobials are added to separate samples of bacterial growth media, often containing a reporter molecule, such as resazurin which changes colour depending on the amount of growth [15, 42] (Figure 2.3b). Similar to the disk diffusion method, these samples are incubated overnight to determine whether the bacteria will grow. By measuring the turbidity of the various samples, the efficacy of the measured antimicrobial-bacteria combination can be determined. While broth dilution assays are more time consuming and laborious than disk diffusion methods, the MIC and MBC can be accurately quantified. Many companies are beginning to manufacture systems to automate the dilution assay [43–47], however these are currently expensive to run.

Despite their limitations, susceptibility tests based on bacterial growth are a necessity and should be utilised as much as possible, as they allow for increased antimicrobial stewardship. It should be noted that for certain infections such as septicaemia, there is not usually time for isolation, growth, and susceptibility testing using the previously

described techniques. Therefore, antibiotics are often given precautionarily to prevent further damage [48]. In such cases, Gram stain testing is carried out as an initial test, allowing the clinician to identify whether bacteria are present, but this does not determine susceptibility. Cases like this further demonstrate the need for new tests that provide the speed and simplicity required to prescribe the right antibiotic at the right time.

Currently, there is no known 'universal indicator', such as a single protein or small molecule to rapidly determine which antimicrobials will work. One approach to determine resistance quickly and without the need for overnight growth, is to detect specific resistance mechanisms. Currently, resistance mechanisms are typically detected through genotypic or proteomic methods, such as Polymerase Chain Reaction (PCR) or Matrix Assisted Laser Desorption/Ionization - Time of flight - Mass Spectroscopy (MALDI-TOF-MS) [49, 50]. These techniques look for DNA sequences or specific proteins that confer resistance. There is also some promise that these techniques can be used directly on clinical samples without the need for bacterial isolation [51]. Genotyping techniques excel when there is a known resistance gene, as is the case for outbreaks of Methicillin-resistant *Staphylococcus aureus* (MRSA) and Vancomycin-resistant Enterococci (VRE), where these techniques are often used [52–54]. Topically, PCR techniques are essential for detecting infections where growth techniques are not suitable, such as those caused by viruses. If the viral strain is known, PCR can be used to diagnose and realise the best form of treatment.

Although there are many benefits of molecular genotyping techniques, there are also reasons why it has not been as widely adopted as bacterial growth techniques. In comparison with their phenotypic alternatives, genotypic tests typically require expensive machines, increased labour costs, and costly reagents. It is also possible for genotypic techniques to miss certain forms of mutation if their structure or sequence is significantly different, or in the case where the resistance gene is not known [55]. Finally, it has been shown that the genotype of a bacterium does not necessarily equate to the phenotype [56]. In certain cases, a bacterium could contain the presence of resistance genes, but never express them. In these instances, higher line antibiotics may be being given when not required. This is not to say that these techniques do not have their place in clinics, as they can rapidly determine resistant infections in much shorter periods of time; however, when possible, they should be used in conjunction with phenotypic techniques.

In conclusion, with the wide variety in the ways that antimicrobials act, the numerous forms antimicrobial resistance can take, and the lack of a single rapid 'resistance indicator', a rapid, all-encompassing test for antimicrobial resistance is far from a reality. Many antibiotics are no longer used to treat certain infections, due to high recorded levels of resistance. For example, ampicillin and trimethoprim were once commonly used antibiotics for treating urinary tract infections [57, 58]. However, the percentage of infections which are resistant towards these antibiotics has increased beyond the point where they can be considered effective [59]. This means these drugs are often not prescribed and are often not tested against. By targeting specific, common forms of resistance for rapid testing, we can continue to use first- and second-line drugs on those cases where they remain effective, minimising the use of higher line drugs and slowing the progression of resistance.

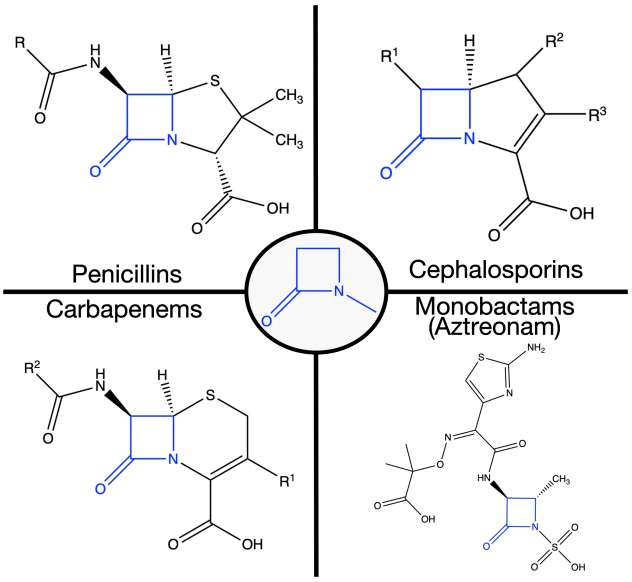

Figure 2.4: Diagram showing the various types of β-lactam antibiotics. The β-lactam ring is highlighted in blue on each of the four classes.

2.2 β-lactam Antibiotics

β-lactam antibiotics are the most commonly prescribed class of antibiotics [60, 61]. Perhaps the most well-known β-lactam antibiotic, is penicillin. In 1928, Alexander Fleming discovered a mould growing in one of his cultures of *Staphylococcus aureus*. Surrounding this mould, there were no signs of bacterial growth, as cells appeared to lyse when close to it. This mould was extracted and named *Penicillium notatum* (later found to be *Penicillium rubens* [62, 63]). This extract was found to inhibit the growth of many species of bacteria and was later used as an experimental treatment on animal tissues and human wounds. However, it was a number of years after the Nobel prize was awarded for Sulfa drugs [64], that interest in discovering new antibiotic compounds became of great interest. Nearly twelve years after the initial discovery of penicillin, Howard Florey began to investigate antibacterial substances found in moulds, focussing on *Penicillium notatum*. By 1941, the group had reported successful purification of penicillin and demonstrated its clinical use in both animals and patients [65]. The next step was a large clinical trial, however this required much more penicillin than could be made in the lab. With this in mind, Florey successfully produced larger quantities using fermentation processes. Following successful clinical trials, companies began to show interest allowing the drug to be one of the first antibiotics to be produced on a wide scale. Finally, in 1946, Fleming, along with Florey and Chain, were presented with the Nobel prize for medicine [66].

Since the development and commercialisation of penicillin in the 1940s, there have been over 30 different β-lactam antibiotics developed from the penicillin structure [67]. These iterations of the penicillin structure are all designed to help increase stability and combat resistance to the drug. The β-lactam family of antibiotics are typically grouped into four main categories: penicillins, monobactams, cephalosporins, and carbapenems (Figure 2.4). Although their surrounding structures vary significantly, they all feature one

similar chemical component, the β-lactam ring; a highly reactive 3 carbon and 1 nitrogen ring structure, as shown in figure 2.4. This β-lactam ring is the active chemical centre of the drug and is responsible for the antibiotic property of the drugs.

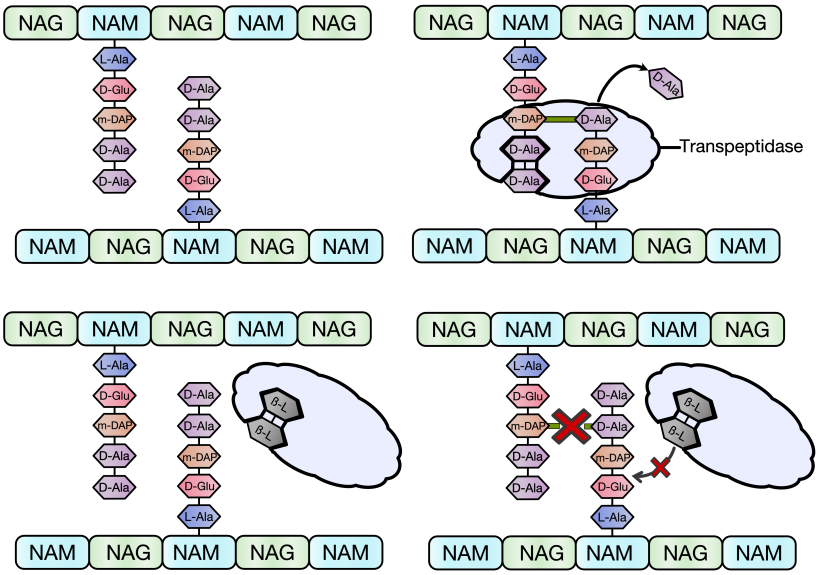

Figure 2.5: Diagram illustrating the process through which transpeptidase cross-links the peptidoglycan layers in a gram-negative bacteria, as well as the effect of β-lactam inhibition. The transpeptidase reacts a D-ala with an m-DAP moiety, forming a covalent bond between them and removing an adjoined D-ala group. If the transpeptidase is inhibited by a β-lactam, this process is not possible. Image adapted from [68] under the Creative Commons License.

When bacterial cells undergo reproduction through binary fission, weak sections of cell wall could cause both cells to lyse. In order to overcome these issues, bacteria have evolved a rigid layer within their cell wall known as peptidoglycan. This rigid layer is a product of polysaccharide layers, comprised of N-acetylglucosamine (NAG) and acetylmuramic acid (NAM) with additional amino acids, shown in figure 2.5 [20]. To increase the strength of these polysaccharide layers, bacteria produce enzymes with the ability to cross-link the additional peptide and glycan groups between the layers. These proteins are often characteristically referred to as penicillin binding proteins (PBPs), as this class of proteins is the pharmaceutical target of β-lactam drugs. Most penicillin binding proteins contain domains known as transpeptidase domains [69]. These enzymatic sections are responsible for transpeptidation, a reaction in which a D-alanine (D-ala) amino acid is cross-linked with either a Diaminopimelic acid (DAP) molecule (gram negative bacteria) or a L-lysine (gram positive)[69][20] (Figure 2.5). In both cases, the original residue before reacting is a D-ala, D-ala moiety. Structurally, this is very similar to the beta lactam molecules. Originally discovered by Tipper and Strominger [70], this similarity, shown in figure 2.6, leads to the transpeptidase domain binding favourably to the β-lactamase molecule, instead of performing the transpeptidase reaction. The binding of β-lactam antibiotics in comparison to the D-ala-D-ala structure is also much more stable, causing the transpeptidase domain to become inactive and unable to cross-link the peptidoglycan layer (Figure 2.5). After inactivation of the enzyme, the cell continues to produce peptidoglycan. However,

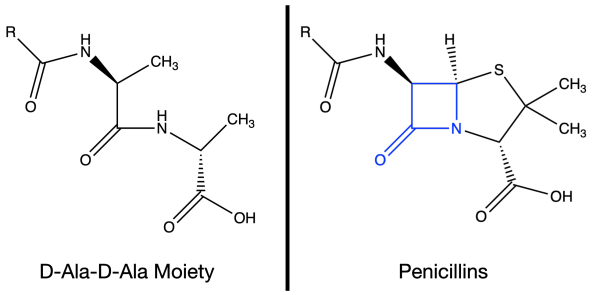

Figure 2.6: Diagram demonstrating the similarity of D-ala moiety to the β-lactam ring. The β-lactam ring is highlighted in blue on the penicillin.

it is much weaker, given the lack of cross-linking, thus causing the cell to lyse under its own osmotic pressure.

2.2.1 β-lactam Resistance

Given that β-lactam antibiotics are the most used class of antibiotic, it is no surprise that one of the most prevalent forms of antibiotic resistance is to these drugs. There are multiple mechanisms through which bacteria have evolved resistance to these drugs such as: having a lower permeability in their outer membrane or having efflux pumps capable of removing the drug from the cell, both resulting in fewer molecules being present in the periplasm [71, 72]; having modified penicillin-binding proteins, which show lower affinity to the β-lactam antibiotics [73]; through the production of enzymes, capable of changing the structure of the β-lactam molecule [33]. The most common form, and the target of this thesis, is through production of enzymes, known as β-lactamase. β-lactamase enzymes are a class of enzymes which bacteria produce in order to hydrolyse β-lactam antibiotics, before they are able to bind to PBPs.

β-lactamases existed long before β lactam antibiotics were widely available on the market [33] and provided a defence against naturally occurring penicillins. There are over 7000 different β lactamase enzymes currently known, compiled in a database known as the β-lactamase database (BLDB) [74]. β-lactamases have been categorised using many different methods over the years [75]; however, they are most commonly categorised into four main types, based on their amino acid sequence, known as the Ambler classification [76]. These categories are A B C and D. Classes A (e.g. TEM, SHV, CTX-M and KPC), C (e.g. CMY and ADC), and D (e.g. OXA) all operate through a similar mechanism, relying on a serine residue present in their structure to hydrolyse β-lactams. Class B enzymes (e.g. NDM and VIM) are metallo-enzymes that use metal ions, often zinc ions, to hydrolyse the drug. There is also a push towards a different method of classification proposed by Bush and Jacoby which looks to classify these enzymes based on efficacy against particular antibiotics, a more clinically relevant metric than the amino sequence [77]. Here, β-lactamases will be referred to under the Ambler classification, as this is currently the most commonly used classification.

The mechanism of action of category A, C and D β-lactamases is shown in figure 2.7 [78]. A base amino acid group donates an electron to the serine group present within the

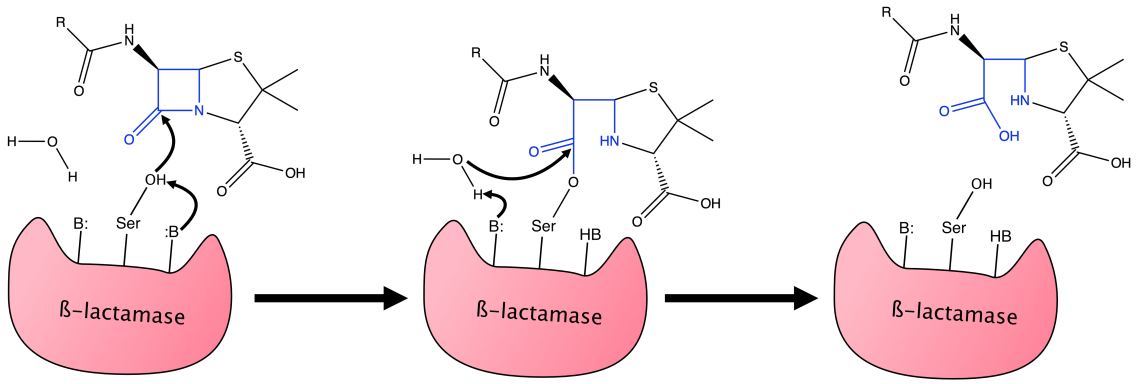

Figure 2.7: Schematic showing the serine reaction for β-lactamase. Adapted from [79] under the Creative Commons License.

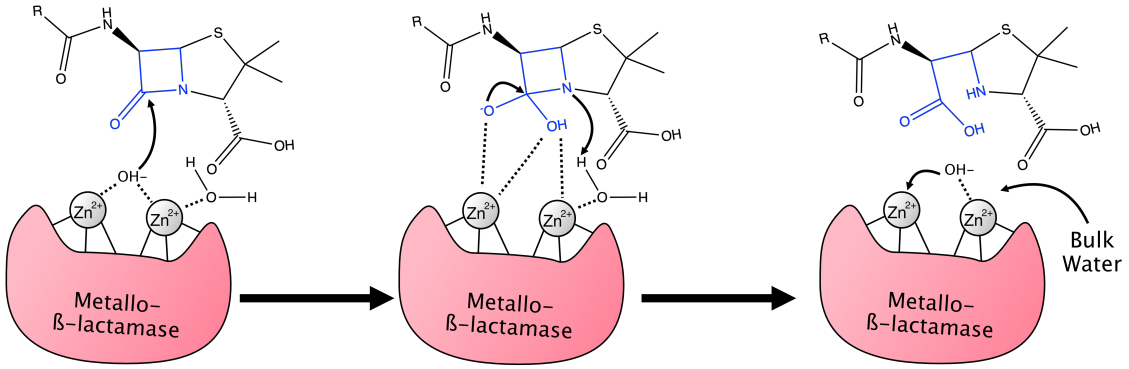

Figure 2.8: Schematic showing the hydrolysis reaction for metallo-β-lactamase. Adapted from [79] and [80] under the Creative Commons License.

enzyme, allowing the serine group to perform a nucleophilic attack on the β-lactam ring. This process is known as acylation, due to the formation of the covalent acyl-enzyme bond, and can be seen in step two in figure 2.7. The covalent bond is broken after another base amino acid within the enzyme is able to activate a water molecule for another nucleophilic attack. The activated water molecule replaces the serine group, detaching the enzyme and freeing it for further reactions (Figure 2.7 step three). The product that is left behind no longer includes the reactive β-lactam ring and is thus no longer able to bind to PBP.

Class B β-lactamases rely on a different hydrolysis mechanism, based on associated zinc ions. The mechanisms of these enzymes are less understood, due to the complexity and variety of metallo-β-lactamases [80]. It is thought that these metallo-enzymes are much more efficient at hydrolysing β-lactams as they directly activate nearby water, as shown in figure 2.8, although the mechanism through which this happens is debated [81, 82]. Something that should be noted is the wide variety of β-lactam antibiotics that these enzymes can hydrolyse [83]. Their unique mechanism also means that there are no currently available inhibitors for these enzymes, making them one of the most concerning classes of β-lactamases.

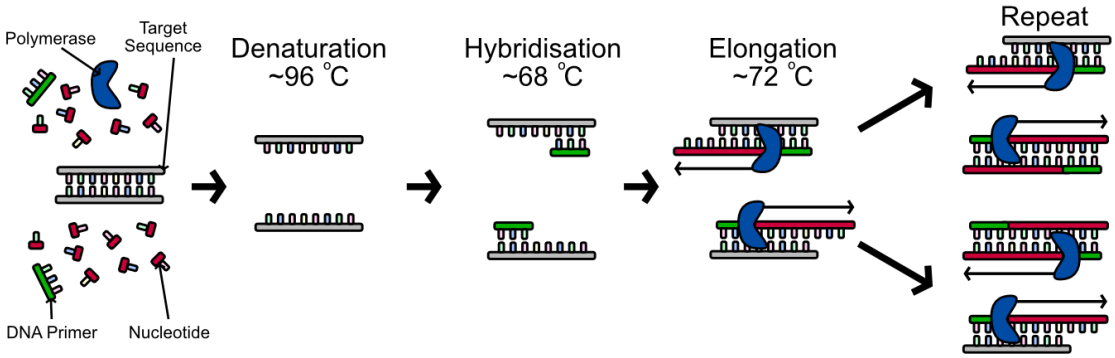

Figure 2.9: Diagram showing a typical PCR process. A solution containing a target sequence of DNA along with polymerase enzymes, specific DNA primers designed for the target sequence, and free nucleotides is heated to $\approx 96\ ^{\circ}C$ to denature and split the target sequence. The solution is then cooled to $\approx 68\ ^{\circ}C$ to allow the DNA primers to bind to the target sequence. The solution is then re-heated to $\approx 72\ ^{\circ}C$ to allow the polymerase to bind the free nucleotides to the primed sequences, creating copies of the original target sequence. This thermal cycle is then repeated multiple times to allow further amplification of the target sequence. Adapted from [88] under the Creative Commons License.

2.2.2 Detection of β-lactam Resistance

Given the widespread use of β-lactam antibiotics [60, 61], detection of resistance towards them is key to ensuring good prescribing practice. The focus of this project was to develop a low-cost, miniaturised test for detecting β-lactamase activity, indicating resistance to β-lactam antibiotics, at the point-of-care. Although resistance to β-lactam antibiotics is not limited to enzyme-mediated resistance[71–73], the most prominent form of resistance is through the production of β-lactamase enzymes [84]. This section will explore the techniques which are used to detect this form of resistance, with a focus on technologies which allow rapid and potentially point-of-care applications. Adaptations of growth-based assays exist for detection of specific β-lactamases [85], however, these tests take several days to produce results and are not suitable for point-of-care susceptibility testing, thus they will not be discussed further in this work.

Genomic Detection

Genomic techniques are becoming increasingly common for detecting β-lactam resistance in clinical settings [86]. As they do not rely on several overnight stages of bacterial growth, they are able to improve the time-to-result of β-lactam resistance detection significantly when compared to phenotypic growth assays. The most common method for genomic detection utilises the Polymerase Chain Reaction (PCR), a commonly used method for DNA amplification [87]. Figure 2.9 describes the thermal cycling method used for typical DNA amplification by PCR. Quantification of the amplified DNA is possible using a variety of techniques such as UV spectroscopy or gel electrophoresis, with the time-to-result being typically only a few hours. However, although efforts have been made to perform this process directly on clinical samples [51], it is typically performed on clinical isolates, requiring overnight growth.

In its simplest forms, PCR is only capable of amplifying single sequences of resistance-denoting DNA. This is useful for cases of outbreaks, where the target resistances are often known and a simple binary answer will suffice [52–54, 89]. However, the specific resistance gene is not always known *a priori* and could be one of a number of genes relating to different β-lactamase enzymes. A technique which looks to resolve this issue is multiplex PCR, a variant of PCR which allows the amplification of multiple target DNA strands at the same time [90]. This technique requires careful calibration of amplification conditions, as well as precise design of DNA primers, in order to prevent poor sensitivity, poor specificity, or preferential amplification of specific targets [91, 92]. There is a lot of work being done to develop protocols that utilise multiplex PCR for detection of β-lactamase enzymes [93–97], with some techniques reporting 100% in both specificity and sensitivity [98]. With the vast number of different β-lactamase enzymes that exist [74], each causing varying levels of β-lactam resistance, multiplex PCR look to allow for a drastic decrease in the time taken to determine a suitable treatment.

Quantification of the amplified strands is often achieved using UV absorption or gel electrophoresis techniques. However, this process can be laborious and time-consuming. Advancements in PCR have allowed for simultaneous amplification of DNA strands alongside quantification of the amplified strands. Known as Real-Time PCR or quantitative PCR (qPCR) [99–101], this technique utilises fluorescence resonance energy transfer (FRET) pairs which are cleaved apart as the DNA is amplified, giving a measurable fluorescence signal which increases with respect to the number of DNA copies [102]. Several reports have demonstrated this process for the detection and quantification of both specific β-lactamase enzyme genes [103], as well as multiplexed approaches, allowing detection of several classes of β-lactamase enzyme genes at once [104–111]. These techniques remove the need for post-amplification processing in order to quantify the DNA sequences present, thus, reducing the time-to-result significantly.

Although PCR methods offer a rapid time-to-result, they often still require samples to be sent to central laboratories with specialist equipment to perform the thermal cycling required for amplification. A promising technique which does not require thermal cycling is Loop-mediated Isothermal Amplification (LAMP) [112]. LAMP uses specifically designed primers and DNA polymerases which remove the need for denaturation and hybridisation, allowing the DNA to be elongated at a constant temperature. Without the need for thermal cycling, the systems which perform this technique can be miniaturised simply, making it a promising method for point-of-care diagnosis of antibiotic resistance [100]. Several works have shown LAMP-based amplification of β-lactamase genes [113–116] and commercial LAMP systems have been reported with a time-to-result of < 1 hr and excellent sensitivity [117, 118]. However, their use in clinical settings appears to be limited as of yet, potentially due to expensive reagents and more complex design of the DNA primers compared to traditional PCR.

Arguably the biggest limitation of genomic techniques is the requirement that the DNA sequence of the resistance gene is already known, restricting their use to known sequences for β-lactamase variants. Furthermore, it has been shown that the genotype

of certain microbes does not always equate to its phenotype [119]. Therefore, performing these measurements as the only method for detecting β-lactam resistance could lead to incorrect prescription. Finally, their operation often requires expensive and specialist equipment. For these reasons, phenotypic assays are still recommended as the primary method for β-lactamase detection in clinical settings [85].

Colorimetric Assays

Both phenotypic growth assays and genotypic assays are suitable for diagnosing almost all forms of antibiotic resistance. However, this universality means they are often not suitable for point-of-care analysis, as the techniques require either bacterial growth, taking manycarb days to complete, or expensive, bulky, systems to analyse the samples making them unsuitable for a point-of-care setting. Given the prevalence of β-lactam resistance, there have been many tests developed which utilise direct detection of β-lactamase activity alongside a colorimetric readout, making them miniaturisable and simple to interpret. This section will focus on the recent advancements and clinically used colorimetric tests which are used to directly detect β-lactamase activity in a sample.

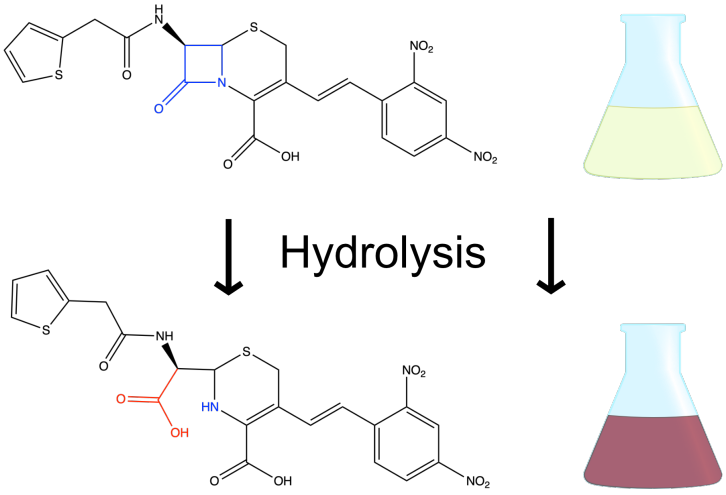

Figure 2.10: Schematic of nitrocefin before and after hydrolysis. After hydrolysis nitrocefin turns from a clear yellow-ish colour to red.

One of the oldest and widely used colorimetric compounds for β-lactamase detection is nitrocefin (Figure 2.10). Nitrocefin is a chromogenic cephalosporin-based compound which, once hydrolysed, moves from an ultraviolet absorption ($\approx$ 380 nm), giving a yellowy colour, to a visible light absorption of $\approx$ 500 nm, giving a red colour [120]. Many commercially available colorimetric β-lactamase assays utilise nitrocefin as the colorimetric compound [121–125]. These assays offer a fast time-to-result, claiming results in $<$ 1 hr from complex samples such as saliva, urine or serum. They are capable of producing quantifiable information on β-lactamase activity, however, this requires a spectrophotometer to measure the change in optical density at 490 nm over time. A drawback of β-lactam based colorimetric compounds is due to the difference in affinity between different β-lactamases [126]. As the compound is based on a cephalosporin β-lactam, certain β-lactamase en-

zymes will not hydrolyse nitrocefin as readily, leading to a minimal change in colour. These differences can result in false-negatives, thus, it is important to understand the differences in substrate affinity when performing these tests [121]. In certain cases, this selectivity can be beneficial. A test which utilises this difference in enzyme affinity is the β-Lacta test (Bio-Rad) that uses a different chromogenic cephalosporin which has been designed to not respond to penicillinases and only respond to extended-spectrum, AmpC, and carbapenemase β-lactamases [127]. By using a compound which is selectively hydrolysed, the test can quickly determine the level of β-lactam resistance within an infection with a high sensitivity and specificity [128, 129].

A colourimetric test which does not utilise chromogenic β-lactam molecules is the Extended-Spectrum β-Lactamase (ESBL) NDP test named after its creators (P. Nordmann, L. Dortet, and L. Poirel) [17]. In this work, a colorimetric β-lactamase test was developed based on the acidification of cefotaxime molecules after they are hydrolysed. To detect this pH change, a pH indicator, phenol red, was used. The initial report of this test showed its efficacy on 255 different bacterial strains, showing a sensitivity and specificity of 92.6% and 100%, respectively, which was later confirmed in other reports [130]. The test was also shown to work on both spiked blood cultures and centrifuged urine samples [131–133], which could allow for shorter time-to-result. Results from this test took $\approx$ 2 hr, however, this did not include the initial 24 h growth of samples. Compared to the β-Lacta test, a reported benefit of the ESBL NDP test comes from its specificity to ESBLs and carbapenemases, and not AmpC β-lactamases. By specifically detecting the enzyme's response to a particular antibiotic, there is less ambiguity in the treatment that should be applied. Further work by Nordmann et al. also looked to develop a test that was specific to carbapenemases using the same phenol red acidification technique [18]. This assay specifically detects the presence of carbapenemases through the use of imipenem, a carbapenem β-lactam antibiotic. However, although this test shows a 100 % specificity to negative cultures, it has been reported to show a low sensitivity of 72.5 % due to the low carbapenemase activity of certain strains [134].

The use of pH indicators, particularly phenol red, for the detection of β-lactamase activity is not unique to this work. Reports have shown its use in penicillinase detection as early as 1976 [135]. Although these assays use specific β-lactams as their β-lactamase substrates, this assay could easily be adapted to determine resistance to different levels of β-lactam antibiotics. Most β-lactam antibiotics hydrolyse in a similar way, producing an extra carboxylic acid group within their structure, leading to a pH change. Thus, by multiplexing different β-lactam antibiotics as the substrate in the reaction, specific resistances could easily be discerned. Furthermore, many of the reported losses in sensitivity are thought to be due to low levels of enzyme expression, leading to ambiguous results. This is a common issue with colorimetric assays that are analysed by eye, as the associated colour change can be subjective. Thus, by using methods which produce a quantifiable readout of the solution, such as a pH measurement, these false-negative results could potentially be avoided.

Another method for detecting low levels of β-lactamase expression is proposed by T.

R. deBoer et al. [136]. Termed DETECT, this assay uses a modified β-lactam structure tagged with a thiophenol structure and a secondary caged enzyme. After the hydrolysis of the β-lactam molecule, the thiophenol moiety is released, uncaging the secondary enzyme which then hydrolyses Nα-benzoyl-l-arginine-p-nitroaniline (BAPA) molecules, producing a colorimetric output. By using this secondary enzyme, the signal from the hydrolysis of the β-lactam is greatly amplified. In their work, they claim detection limits of 100 fM TEM-1 within a spiked buffer sample, several orders of magnitude lower than the equivalent test performed using nitrocefin. Furthermore, the assay claims to work directly on clinical samples of urine within 30 min, detecting β-lactamase resistance in samples as low as 10^4 CFU/mL. However, tests performed directly on urine samples showed only 73% sensitivity across 11 samples, which was claimed to be due to the samples containing concentrations of bacteria lower than the detection limit of the system. Furthermore, the system appears to show no selectivity for different β-lactamase classes due to the bespoke β-lactam used. Due to the high-prevalence of β-lactam resistance, this test may be more suited to determining samples which are β-lactamase negative, allowing prescription of lower-line β-lactam antibiotics. However, the proposed system shows detection limits far below other colorimetric assays and appears to work directly on clinical samples, furthering its suitability for a binary answer at the point-of-care.

Conclusions

This section has discussed a number of currently-used and emerging techniques for determining β-lactam resistance and the presence of β-lactamase enzymes. Currently, phenotypic assays such as disk-based growth methods are the recommended techniques for β-lactamase detection [85] due to their ease of operation, low-cost, and accuracy. However, these techniques can take days for results to be obtained. Therefore, as techniques such as PCR and LAMP become more affordable and widely available, it is possible to see that they will become more prominent for detection of resistance. Finally, colorimetric tests for β-lactamase detection look to play a larger role in the future of diagnostics, especially with the increasing number of carbapenemase producing infections [137]. Although these tests often only target a single form of resistance, the nature of these tests allows for results in under and hour, potentially direct from minimally processed patient samples. For cases such as carbapenem resistance, results need to be obtained quickly, making these tests ideal. However, the ambiguity of their readout can lead to false-negative results. By developing a method which could quantifiably measure the solution in a point-of-care situation, this ambiguity could be removed.

2.3 pH and pH Measurements

Many of the aforementioned β-lactamase detection methods rely on the innate acidification of β-lactam molecules after they are hydrolysed by β-lactamase enzymes. In order to explain this phenomenon, the nature of pH must first be explored. This section will discuss the origin of pH in a solution and how β-lactam hydrolysis can lead to shifts in

bulk pH. Finally, it will discuss some of the methods used to detect and quantify the resulting change in solution pH.

2.3.1 pH

The pH of an aqueous solution is related directly to the activity of positively charged hydrogen ions (protons). This relationship is described as [138]:

$$pH = -\log_{10}\left([\mathrm{H}^+]\right) \tag{2.1}$$

where $[\mathrm{H}^+]$ is the activity of hydrogen ions in an aqueous solution. However, for low concentrations (approximately below 0.1 M), the activity is simply equivalent to the concentration of hydrogen ions. Hydrogen ions exist in aqueous solutions due to the natural ionic dissociation of water and are present as hydronium ions ($\mathrm{H_3O^+}$):

$$2\,\mathrm{H_2O} \rightleftharpoons \mathrm{H_3O^+} + \mathrm{OH^-} \tag{2.2}$$

Or more commonly written as:

$$\mathrm{H_2O} \rightleftharpoons \mathrm{H^+} + \mathrm{OH^-} \tag{2.3}$$

These ions are usually at a low concentration (below 0.1 M), but both are always present in aqueous solutions. Assuming a constant temperature, the product of $\mathrm{H^+}$ and $\mathrm{OH^-}$ concentration is always constant, making the pH and pOH (the equivalent of pH for hydroxide ions) inversely proportional to one another. In pure water, at $25°C$, their concentrations are equal and approximately 10^{-7} M, hence the familiar value of water's pH being 7 and 'neutral' due to the balance of both ions. The lower the pH value, the more acidic the solution. Inversely, the higher the pH the more basic a solution is, meaning there are higher concentrations of hydroxide ($\mathrm{OH^-}$) ions, shown in figure 2.11.

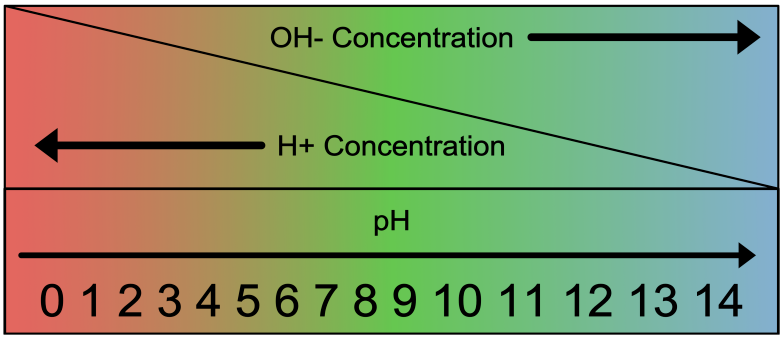

Figure 2.11: Diagram showing the pH scale as decreasing and increasing concentrations of $\mathrm{H^+}$ and $\mathrm{OH^-}$, respectively.

Many molecules can become a source of $\mathrm{H^+}$ ions when introduced into an aqueous solution. As shown for water in equations 2.2 and 2.3, $\mathrm{H^+}$ ions will often dissociate from

a molecule. This dissociation can be expressed as:

$$\mathrm{HA} \rightleftharpoons \mathrm{H^+} + \mathrm{A^-} \tag{2.4}$$

where HA is the chemical species and $\mathrm{A^-}$ is the conjugate base for that species. Depending on the molecule, dissociation of $\mathrm{H^+}$ will happen to varying degrees, determined by the acid dissociation constant K_a, defined as:

$$K_a = \left(\frac{[H^+][A^-]}{[HA]} \right) \tag{2.5}$$

However, given the magnitude of this number and its relation to pH, the dissociation constant is often referred to in the inverse logarithmic form pK_a:

$$pK_a = -\log_{10} \left(\frac{[H^+][A^-]}{[HA]} \right) = -\log_{10} (K_a) \tag{2.6}$$

The lower the pK_a value, the stronger the acid and the more $\mathrm{H^+}$ ions the molecule will donate. For strong acids such as HCl (Hydrochloric acid), with a pK_a of -6.3, approximately all of the $\mathrm{H^+}$ ions will be dissociated. For most concentrations of HCl, the concentration of $\mathrm{H^+}$ is thus equivalent to the concentration of HCl and thus the pH of solutions where strong acids are added can be calculated easily.

From equation 2.6, it can be shown that the pK_a of a molecule is the pH at which half of the $\mathrm{H^+}$ ions have dissociated. This means that for weaker acids and bases, it is more common for some $\mathrm{H^+}$ ions to still be associated with the molecule and therefore not contribute to the pH. Calculating the pH for weaker acids and bases requires calculating the ratio of dissociation from the pKa. By manipulating equation 2.6, it can be shown:

$$pH = pK_a + \log_{10} \left(\frac{[A^-]}{[HA]} \right) \tag{2.7}$$

This equation is more commonly known as the Henderson-Hasselbach [138] and is used routinely when calculating pH changes.

2.3.2 Acidification Through β-lactam Hydrolysis

It is well established that hydrolysis of β-lactam antibiotics leads to acidification of the surrounding solution [17, 18, 135]. This is often simply reported as [139–141]:

$$\beta\text{-lactam} + \mathrm{H_2O} \xrightarrow{\beta-lactamase} \beta\text{-lactam acid} + \mathrm{H^+} \tag{2.8}$$

However, this reaction is not strictly correct. As shown in section 2.2.1, when β-lactam antibiotics are hydrolysed, the pharmaceutical core of the antibiotic, the β-lactam ring, is opened. This results in the molecule having an extra carboxylic acid group present, as shown in figure 5.2. However, there is also formation of an additional secondary amine group (NH), meaning that, for equation 2.8 to be true, an additional $\mathrm{H^+}$ ion should be formed, which is not the case (Figure 2.12).

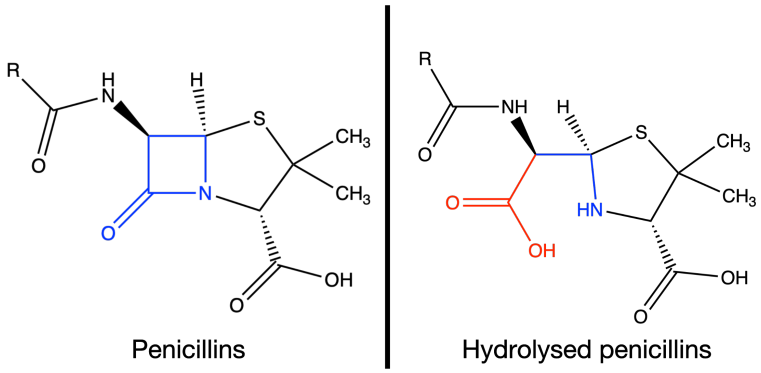

Figure 2.12: Schematic diagram showing both an intact penicillin β-lactam antibiotic (left) and its hydrolysed form (right). The β-lactam ring is highlighted in blue on the intact penicillin. Following hydrolysis, an additional carboxylic acid (highlighted in red) and amine group (highlighted in blue) are present within the drug's structure.

Instead, by introducing these additional groups into the structure, the overall pK_a of the molecule is reduced, meaning it is more likely to donate H^+ ions from its acidic groups [17]. Assuming the surrounding solution is not able to buffer the additional protons, the solution will also become more acidic, which can be detected through a number of methods. However, this will not be a 1:1 relationship of H^+ ions to hydrolysed β-lactams, as indicated by equation 2.8. The expected ratio of this reaction will be explored in more detail in chapter 5, where the detection of this β-lactam acidification is discussed.

2.3.3 Measuring pH

There are several ways in which the pH of a solution can be measured, each with varying levels of accuracy, precision, and use-cases. Perhaps the most commonly known are those that use pH-sensitive indicator dyes. Many substances have varying absorption spectra depending on their pH (e.g. litmus, which turns red in acidic conditions and blue in basic.). This change in spectra is a result of protonation and deprotonation of amphoteric groups, moieties which are able to both accept and donate H^+ ions depending on the surrounding H^+ concentration, as shown in figure 2.13. However, this change of structure occurs over a finite pH range, depending on the pK_a of the molecule, making their use-cases limited. These dyes are often used to measure specific pH changes of acid-base titrations when calculating the strength of an unknown acid or base, as their colour change is usually easily detectable by eye and their use is relatively simple.

Although these dyes only work within a specific pH range, a 'universal indicator' can be made by combining dyes which have overlapping limits throughout the pH scale, resulting in a pH sensitive solution that can be used for a much wider pH range. These universal indicators can be used to give a quick indication of a solution's pH, but they are not useful for accurately determining a pH level. It is possible to more accurately determine pH with these dyes with a spectrophotometer, but this requires precise concentrations of dye and assumes the solution has little or no background absorption. For these reasons, these dyes are rarely used for diagnostic purposes where quantifiable answers are required. However, as described in section 2.2.2, there are a number of qualitative β-lactamase detection

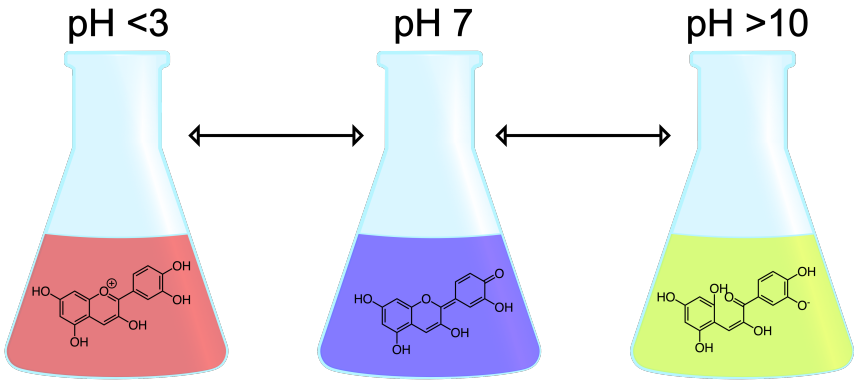

Figure 2.13: Diagram exampling an anthocyanin pH sensitive dye's response to changes in pH. As the pH changes, the oxide groups within the molecule protonate or deprotonate accordingly, changing the molecule's absorption properties [142].

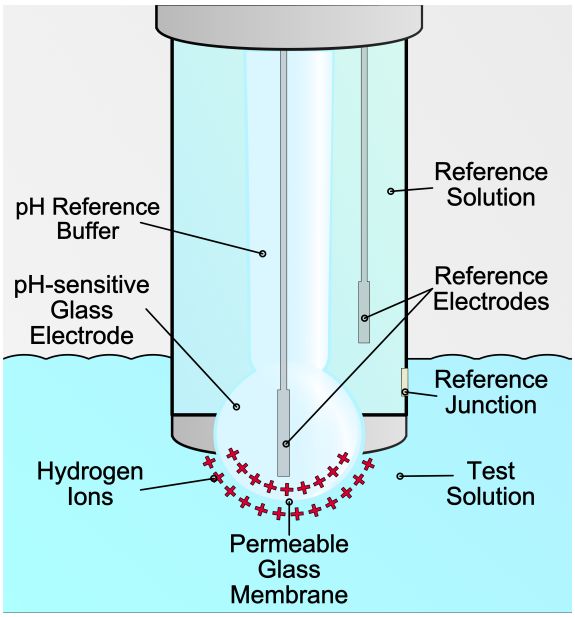

Figure 2.14: Diagram showing the component parts of a glass electrode pH meter. By measuring the potential difference between the two electrodes, the solution pH can be determined.

techniques which utilise these dyes because of their ease of use and the lack of specialist equipment required, making them suitable for quick, disposable tests which do not require quantification.

For cases where a more accurate measurement is needed, electrochemical pH meters are more commonly used. One of the most common electrochemical pH meters is the glass electrode. This device often consists of two electrodes, a pH-sensitive measurement electrode and a reference electrode, usually enclosed in a single body, as shown in figure 2.14. The reference electrode is an electrochemical electrode which remains at a fixed and known potential, regardless of the surrounding solution; these electrodes are discussed in further detail in section 3.2.1 of chapter 3.

The pH sensitive probe is a thin, bulb-like glass structure, filled with a solution of known pH. Once submerged into a solution, the outer layer of this bulb hydrates, allowing

the diffusion of H^+ ions, leading to a build-up of charge. This charge build-up is highly dependent on the concentration of H^+ ions, and thus the pH. As the inside of the bulb is also hydrated with a solution of known pH, and there is no current flow between the inner and outer membranes, a separation of charge occurs across the glass membrane, resulting in an electric potential. By measuring the potential across this glass membrane with respect to the reference electrode, the pH of a solution can be determined. The potential caused by the electrode submerged in a solution is determined by the Nernst equation [143]:

$$E = E_0 + \frac{RT}{F} \ln Q \tag{2.9}$$

which describes the electrochemical potential of any cell. Where E is the measured potential; E_0 is the standard electrode potential, the potential that would exist for the reaction under standard conditions (1 M concentration, 1 atmosphere pressure, 25 $^\circ C$ temperature); R is the gas constant, T is the temperature in Kelvin; F is the Faraday constant; and Q is the reaction quotient, the concentration ratio of the potential-forming reactants. For pH electrodes, the reactants are the H^+ ions inside the electrode, and the H^+ ions from the measured solution. At room temperature this can be simplified to:

$$E = E_0 + 0.0592 \log \left(\frac{[H^+_{Inside}]}{[H^+_{Outside}]} \right) \tag{2.10}$$

$$E = E_0 + 0.0592 \left(\log [H^+_{Inside}] - \log [H^+_{Outside}] \right) \tag{2.11}$$

Since the potential inside the electrode, due to $[H^+_{inside}]$ should remain constant due to the known pH of the solution, this can be included as part of the standard potential, leaving:

$$E = E'_0 - 0.0592(pH_{Outside}) \tag{2.12}$$

This leaves a simple potential which is determined by the pH of the measured solution.

Glass electrodes are a staple for many chemistry laboratories for a number of reasons. Their ability to easily quantify pH values to an accurate and precise level is something that is often required for many biochemical applications. Glass electrodes have a wide response range across the pH scale, making them suitable for almost all static pH measurements. Finally, these electrodes can be reused for thousands of measurements, making them suitable for routine laboratory work.

There are however some disadvantages to glass electrodes. The need for a large glass bulb make glass electrodes bulky and fragile and thus unsuitable for many biomedical applications. Although their sensitivity is suitable for most applications, it is limited by physical laws. It can be shown from equation 2.12 that the sensitivity of these electrodes has a maximum value of approximately 59.2 mV/pH. This value is often referred to as the Nernstian limit and is considered to be a limiting factor to the detection limit of electrochemical pH electrodes. The response time of these electrodes is also a limiting factor as it is heavily dependent on the diffusion of ions in and out of the glass membrane and can sometimes take tens of seconds to equilibrate.

There have been many efforts to try and create electrochemical pH electrodes which

overcome these disadvantages [144]. One of the most popular alternatives is the Ion-Sensitive Field-Effect Transistor (ISFET), which promises miniaturisation, durability, and a fast response time. For rapid, quantifiable, detection of β-lactamase activity in a small hand-held device, all of these factors are important. Therefore, ISFETs were chosen as the tool to use for development of this test.

2.4 ISFETs in Theory

Ion-Sensitive Field-Effect Transistors (ISFETs) are pH sensitive semiconductor devices based on Metal-Oxide-Semiconductor Field-Effect Transistors (MOSFETs). Therefore, in order to fully describe the nature of ISFETs, MOSFETs will first be explained.

2.4.1 MOSFETs

MOSFETs are three-electrode devices, where the voltage on one electrode (called the gate) determines the conductivity between the remaining two electrodes (the source and drain). MOSFETs often have a fourth electrode known as the body or base, which is usually connected to the source electrode. These devices are essential for the modern world as they make up the backbone of almost all digital electronic devices.

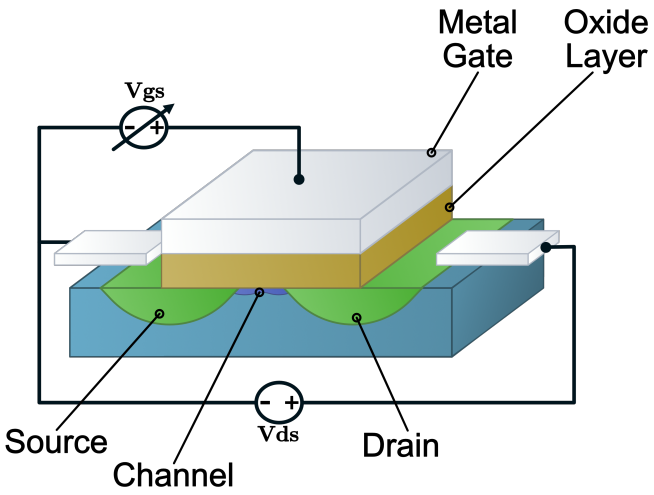

Figure 2.15: Diagram showing a typical MOSFET structure.

A MOSFET is shown in figure 2.15. The MOSFET contains two heavily doped regions (either P or N, depending on the device type) implanted into a semiconductor substrate of the opposing doping type. An oxide layer is deposited on the surface between these two regions, on top of which a further layer of metal is added (Hence the name Metal-Oxide-Semiconductor). Other MOSFET structures do exist, such as those that utilise electrodes of larger doping densities, rather than opposing doping types; However, as their operation remains nominally the same, for the ease of explanation, the traditional MOSFET structures will be described.

The operation of a MOSFET relies on the Metal-Oxide-Semiconductor (MOS) layer, which behaves like a capacitor. By applying a voltage to the metal layer of the MOS

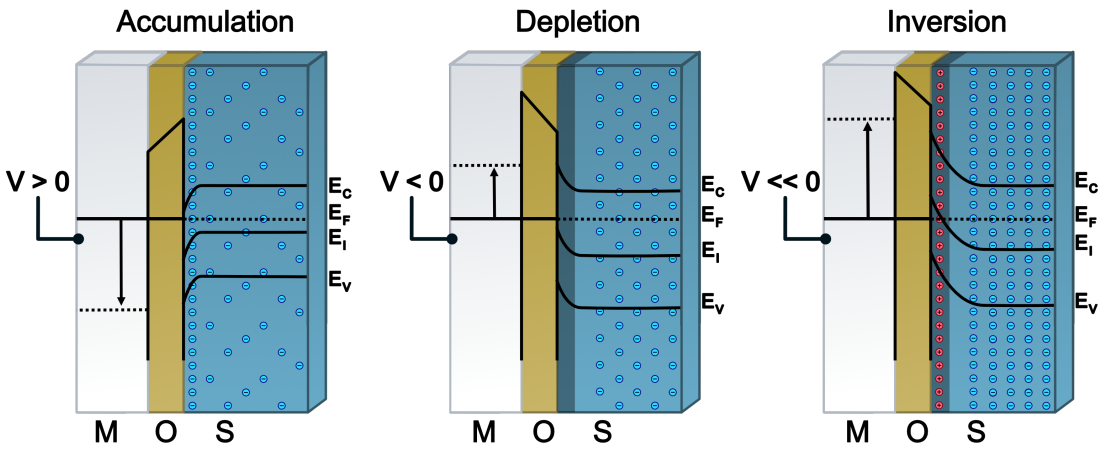

Figure 2.16: Diagram showing the charges and band structure within three metal-oxide-semiconductor structure for the three main operating conditions: accumulation, depletion, and inversion [145].

section, the semiconductor's electrical properties can be modified in one of three ways: Accumulation of charge, depletion of charge, or inversion of charge, as shown in figure 2.16. Accumulation occurs when the voltage applied to the metal is of the opposing sign of the charge carriers in the semiconductor, causing them to accumulate at the semiconductor-oxide interface. Conversely, depletion occurs when the voltage applied is of the same sign as the charge carriers, causing them to deplete from the semiconductor-oxide interface. Inversion occurs when the voltage applied to deplete the region of the dominant charge carrier in the semiconductor, is large enough to attract charge carriers of the opposing type. This is termed 'inversion' due to the semiconducting material at the interface behaving as if it were inverted to the opposing doping type.

These three modes can be applied to create, or deplete charge carriers in the semiconductor layer, leading to a change in conductivity between source and drain contacts. As shown in figure 2.15, the MOS section of the MOSFET sits between two heavily doped regions, meaning that when a voltage is applied to the MOS section, it is possible to change the conductivity between the heavily doped regions. There are four main types of MOSFET: N-channel enhancement, N-channel depletion, P-channel enhancement, and P-channel depletion (shown in figure 2.17). Enhancement-mode MOSFETs rely on inversion of the channel between the two doped regions, allowing current to flow between them, this makes them 'always off' switches as they require a voltage to turn them on. Depletion-mode MOSFETs already have a channel which allows current to flow with zero gate voltage; however, by applying a voltage which depletes the carriers from this channel, the resistance can be increased. Depletion mode devices are known as 'always on', as they require a voltage to prevent current flow. The difference between N- and P-channel MOSFETs is simply the channel doping type, and thus the voltage that is required to manipulate the conductivity. In N-type, the carriers are negatively charged electrons and in P-type, the carriers are positively charged holes.

The current that is drawn through an N-channel enhancement-mode MOSFET with a

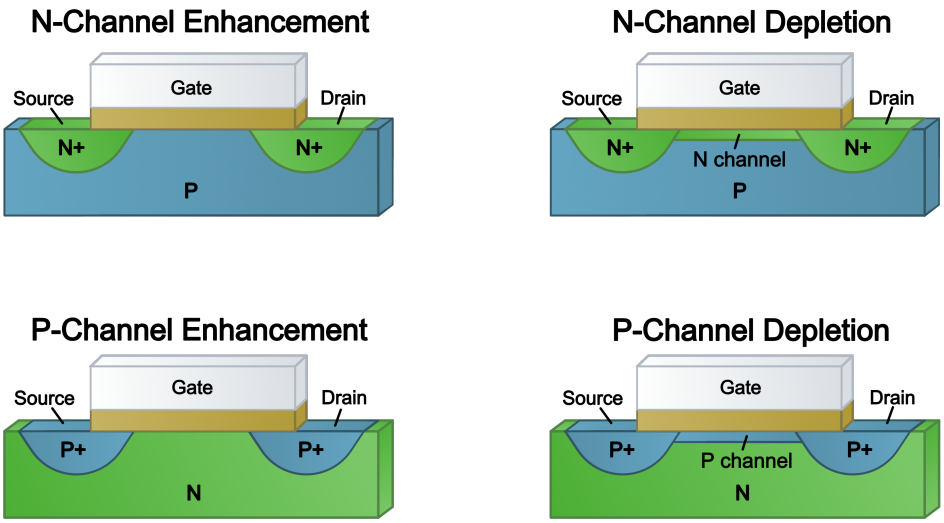

Figure 2.17: Diagram showing the four main operation modes for MOSFET devices: N-Channel enhancement, N-Channel Depletion, P-Channel enhancement, and P-Channel Depletion [146].

potential difference between drain and source is described by the following:

$$I_{DS} = \begin{cases} 0, & \text{for } [V_{GS} \leq V_{Th}] \\ \mu_n C_{ox} \frac{W}{L} \left[(V_{GS} - V_{Th}) V_{DS} - \frac{{V_{DS}}^2}{2} \right], & \text{for } [V_{GS} > V_{Th}, V_{DS} \leq V_{GS} - V_{Th}] \\ \frac{\mu_n C_{ox}}{2} \frac{W}{L} \left[V_{GS} - V_{Th} \right]^2, & \text{for } [V_{GS} > V_{Th}, V_{DS} > V_{GS} - V_{Th}] \end{cases} \tag{2.13}$$

Where: I_{DS} is the current between the drain and source; V_{GS} is the voltage at the gate compared to the source; V_{Th} is the threshold voltage, i.e. the voltage at which inversion is observed in the channel; V_{DS} is the voltage between the drain and source; μ_n is the carrier mobility in the channel; C_{ox} is the capacitance per unit area of the oxide in the MOS structure; W is the width of the channel; and L is the channel length. $\mu_n C_{ox} \frac{W}{L}$ is a constant dependent on the device parameters and is often referred to as K for many applications [147]. This equation describes the I-V characteristics of an N-channel device, however P-channel devices have very similar I-V characteristics, but with their voltages inverted. Depletion-mode MOSFETs are also similar, although their V_{Th} is replaced with a cut-off voltage, V_{CUTOFF}. The three equations above describe the three modes of a MOSFET operation: sub-threshold or weak inversion, where the gate voltage is below the threshold and the device does not allow current to flow (although, in this mode, small numbers of charge carriers may pass through the channel due to thermal energy, leading to a leakage current); Triode or linear region, where the device current increases linearly with increasing drain-source voltage; and the saturation region, where the device current is no longer dependent on the drain-source voltage, due to the saturation of current density within the channel region. An example of the current in these triode and linear regions is shown in figure 2.18. The key point for building electrochemical sensors using these devices is that, for all MOSFET types and operation modes, the current flow through the drain-source channel is always dependent on the voltage at the gate.

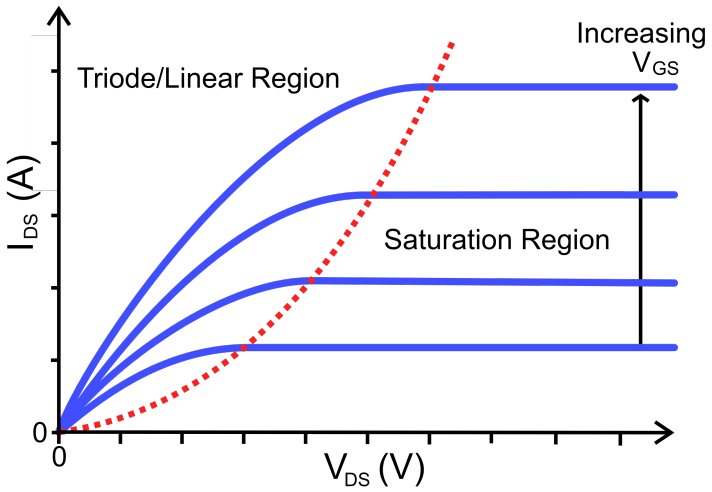

Figure 2.18: Typical source-drain current output for a MOSFET device in relation to its source-drain voltage [146]. Below the threshold, where $V_{GS} > V_{Th}, V_{DS} \leq V_{GS} - V_{Th}$, the current through the transistor is linearly related to the voltage across it. After the threshold, where $V_{GS} > V_{Th}, V_{DS} > V_{GS} - V_{Th}$, the current no longer increases with increasing V_{DS}. The saturation current increases with increasing V_{GS}.

2.4.2 ISFETs: The Electrochemical Double Layer and The Site-Binding Model

The Ion-Sensitive Field-Effect-Transistor (ISFET) was chosen as the pH sensing device for this project for a number of reasons; the design allows for ease of integration with both electronics and fluidics in a small package, essential for devices which are intended to be hand-held; the fast response time associated with ISFETs allows changes in pH to be measured almost instantaneously; and finally, simple modifications to the traditional ISFET design allows for low-cost sensors to be manufactured, essential for widespread and frequent use of any diagnostic technology.

Traditional ISFETs are very similar in design to MOSFETs, however, the metal gate is removed and replaced with an ion-sensitive layer, an electrolyte, and a reference electrode, as shown in figure 2.19 [148]. The operation of the ISFET is also similar in nature to that of the MOSFET, however, rather than the source-drain current being modified by a voltage applied to the gate electrode, the source-drain current is altered by changes in pH at the ion-sensitive layer interface. This section will discuss the mechanism through which this is possible and summarise the work that has previously been performed to develop and utilise these devices.

The Electrochemical Double Layer Model

To fully describe the response of an ISFET sensor to changes in pH, we must first investigate the nature of the interface which occurs whenever a surface comes into contact with a solution. Due to the excess of charge carriers within conducting or semiconducting materials, such as those used for ISFET gates, an innate electrical charge exists at their surface. When this surface comes into contact with a solution containing charged ions, the ions

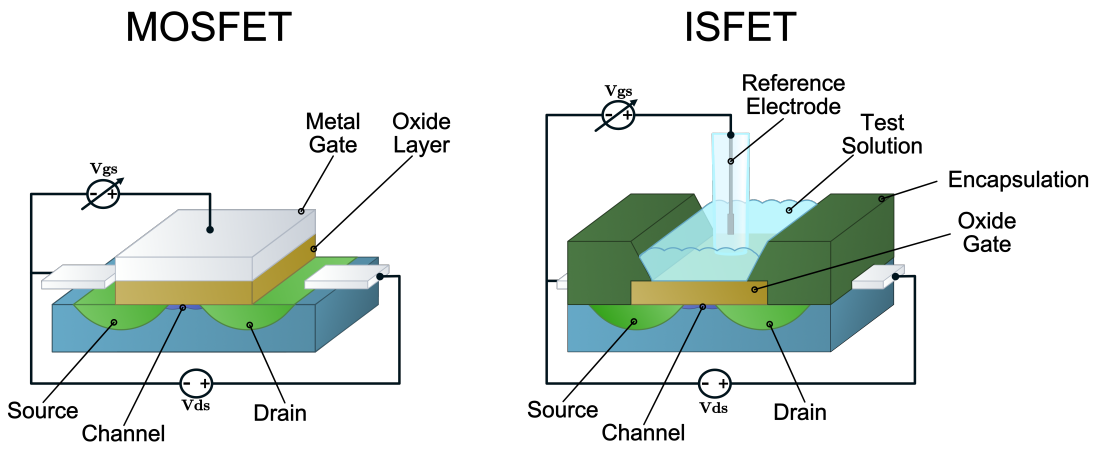

Figure 2.19: Diagram of typical MOSFET and ISFET structures. The ISFET structure is similar to the MOSFET, however the metal gate is removed, and the gate oxide is often encapsulated to allow a solution connection to an external reference electrode.

begin to migrate towards to surface, in order to neutralise this surface charge. This aggregation of charges at the electrode-solution interface is described as the electrochemical double-layer.

The electrochemical double layer was first described by H. Helmholtz in 1853 [149]. This model, termed the Helmholtz layer model, describes the interface as a charged layer within the surface of the material completely coated in a second layer of solvated counter-ions. The solvation of these counter-ions leads to two oppositely charged layers separated by a distance, causing this interface to behave as a charged capacitor. The Helmholtz model is however incomplete, as it assumes that ions at the interface are all of opposite charge to the electrode, completely solvated, and immobile [143]. As a result of thermal energy, we see that the ions are not immobile and restricted to the electrode surface, but instead populate a diffuse cloud surrounding the electrode, with higher concentrations of opposingly charged counter-ions nearer to the surface. This was the model proposed by both L. Guoy and L. Chapman in the early 1910's [150, 151]. A more accurate model is a combination of the two theories, as described by O. Stern in 1924 [152]. Stern's theory of the electrochemical double layer took into account both the Helmoholtz and Guoy-Chapman models and also considered the effect of parameters such as the finite size of ions and ability to lose their solvation shell. If an ion of any charge loses its solvation shell, it is possible for it to adsorb onto the electrode surface, either through van der Waals or Coulombic interactions [143]. This charged layer of unsolvated, adsorbed ions is known as the Inner-Helmholtz plane. However, ions which maintain their solvation shell are unable to adsorb as closely, leading to a second charged layer known as the outer-Helmholtz plane. The region between these two layers is referred to as the Stern layer. Extending away from these two charged planes is a layer of diffuse ions, similar to that described by Guoy and Chapman. The distribution of charge throughout these layers leads to a potential difference between the electrode and the bulk solution. Figure 2.20 shows a schematic representation of this electrochemical double layer model.

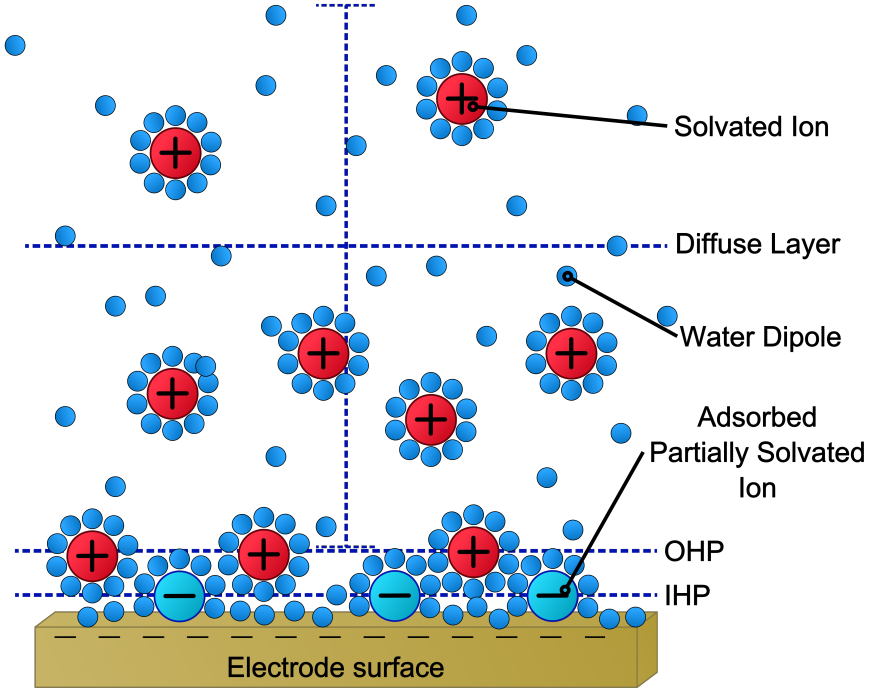

Figure 2.20: Schematic showing the Guoy-Chapman-Stern model of the electrochemical double layer. The model consists of three main layers: The inner Helmholtz plane (IHP), the central distribution of adsorbed charges without their solvation shell; the outer Helmholtz plane (OHP), the central plane of the adsorbed counter-ions with solvation shells; and the diffuse layer, the outer layer of diffuse ions containing the majority of the opposing charge to neutralise the charge at the electrode surface. Adapted from [153] under the Creative Commons License.

The electrochemical double layer has a large impact on the efficacy of electrochemical biosensors, such as ISFETs. The distribution of charge throughout this layer acts with a charge screening effect, preventing any detection of charge within the bulk solution. The length of this screening effect typically ranges between 0.1-10 nm and is characterised by the Debye length, the length of a charge carrier's electrostatic effect within a solution. The Debye length is defined by the equation [154]:

$$\lambda_D = \sqrt{\frac{\epsilon_0 \epsilon_r K_B T}{2 N_A e^2 I}} \tag{2.14}$$

where: ϵ_0 is the permittivity of free space; ϵ_r is the dielectric constant of the electrode; K_B is the Boltzmann constant; T is temperature; N_A is the Avagradro constant; e is the elementary charge constant; and I is the ionic strength of the electrolyte. For ISFET devices detecting changes in pH, this screening effect is minimal, as the surface charge with respect to the pH is determined by short amphoteric groups at the electrode surface which sit far below the Debye length. However, for cases where the electrode is functionalised to detect other biomolecules, such as proteins, this screening effect has to be considered.

The Electrochemical Double Layer Capacitance

As described previously, the build-up of separated charges at the electrode-solution interface behaves as a capacitor with a capacitance of C_{DL}. Since the capacitance of this double-layer is a function of the potential at the electrode surface, it can be described by [148]:

$$C_{DL,i} = \frac{\sigma_0}{\psi_0} = -\frac{\sigma_{dl}}{\psi_0} \tag{2.15}$$

where: $C_{DL,i}$ is the average double-layer capacitance; σ_0 is the charge density of the electrode surface; σ_{dl} is the charge density at the edge of the neutralising diffuse layer; and ψ_0 is the potential across the double-layer. The capacitance across this layer affects how the ISFET will respond to pH and ion concentration, as the more charge that is able to be stored within this layer, the larger the electric field at the gate.

As shown in figure 2.20, the electrochemical double layer has two major components, the Stern layer, and the diffuse layer (sometimes referred to as the Guoy-Chapman layer). Both of these layers contain some capacitance per area, which will contribute to the overall capacitance and potential across the double-layer. As these capacitances behave as if they were in series [155][148], the total average capacitance per area can be determined by:

$$\frac{1}{C_{DL,i}} = \frac{1}{C_{Stern,i}} + \frac{1}{C_{Diff,i}} \tag{2.16}$$

Where C_{Stern} is the Stern layer capacitance and C_{Diff} is the diffuse layer capacitance. The Stern layer capacitance is the capacitance between the surface and point x_H, the charge plane of the OHP, and can therefore be described as:

$$C_{Stern,i} = \frac{\sigma_0}{\psi_0 - \psi_H} = \frac{\epsilon_{r,s}\epsilon_0}{x_H} \tag{2.17}$$

where ψ_H is the potential at the point x_H; $\epsilon_{r,s}$ is the relative permittivity of the Stern layer; and ϵ_0 is the vacuum permittivity. For most cases, the Stern capacitance is assumed to be $20\mu F/cm^2$ as $\epsilon_{r,s} \approx 11$ and $x_H \approx 5$ Å[148].

By manipulating equations 2.15, 2.16 and 2.17, the diffuse layer capacitance can be described as:

$$C_{Diff,i} = -\frac{\sigma_{dl}}{\psi_H} \tag{2.18}$$

The charge stored within the diffuse layer is more complex, as the charges are mobile, and the capacitance is not constant throughout the layer. In order to calculate the charge density at the Stern-diffuse-layer interface, some assumptions have to be made. First, it is assumed that the ions in this diffuse layer only exist outside of the Stern layer and cannot approach any further than a minimum distance x_H, defined by the OHP. Secondly, the diffuse layer should contain an equal and opposite amount of charge as the electrode surface, as the layer between the IHP and OHP should, by its nature, contains zero charge density. Assuming these conditions, the σ_{dl} can be given by [156]:

$$\sigma_{dl} = -\left(8kT\epsilon_{r,d}\epsilon_0 n^0\right)^{\frac{1}{2}} \sinh\left(\frac{zq\psi_H}{2kT}\right) \tag{2.19}$$

where: k is the Boltzmann constant; T is temperature; $\epsilon_{r,d}$ is the relative permittivity of the diffuse layer; n^0 is the number of ions per unit volume; z is the valence of the ions (i.e. the ionic charge); and q is the elementary charge of the proton or electron. This equation is derived from the Poisson-Boltzmann equation [157], which describes the distribution of ionic charge in relation to the electrostatic potential. From this, an average capacitance of the double layer can be given as a rather complex function of ion concentration and potential [156]:

$$\frac{1}{C_{DL,i}} = \frac{x_H}{\epsilon_{r,s}\epsilon_0} + \frac{\left(\psi_0 - \frac{\sigma_0 x_H}{\epsilon_{r,s}\epsilon_0}\right)}{(8kT\epsilon_{r,d}\epsilon_0 n^0)^{\frac{1}{2}} \sinh\left(\frac{zq\psi_H}{2kT}\right)} \tag{2.20}$$

Equation 2.20 describes an average capacitance of the layer between the zero-potential of the surface (the point at which there is an average-zero surface charge) and the potential ψ_0 [143]. This factor is known as the integral capacitance, $C_{DL,i}$. Due to the variable nature of the diffuse layer capacitance to surface charge and ion concentration, a more useful quantity, when discussing electrochemical sensors, is the differential capacitance, $C_{DL,d}$, which describes the ability of the double-layer to store charge with small perturbations in surface potential [157], given by:

$$C_{DL,d} = \frac{\partial \sigma_0}{\partial \psi_0} = -\frac{\partial \sigma_{dl}}{\partial \psi_0} \tag{2.21}$$

By combining equations 2.20 and 2.21, the differential capacitance of the double-layer can be described [156]:

$$\frac{1}{C_{DL,d}} = \frac{x_H}{\epsilon_{r,s}\epsilon_0} + \frac{1}{\left(\frac{2\epsilon_{r,d}\epsilon_0 z^2 q^2 n^0}{kT}\right)^{\frac{1}{2}} \cosh\left(\frac{zq\psi_H}{2kT}\right)} \tag{2.22}$$

This shows that the differential capacitance, and thus the electric field generated at the ISFET gate, is dependent on changes in the surface potential, as well as ion concentration.

The Site-binding Model

To explain the pH sensing operation of the ISFET, the pH sensitive layer must be considered. Due to compatibility with traditional CMOS manufacturing, this layer has traditionally been either silicon dioxide or silicon nitride. The pH sensitivity of these layers comes from their amphoteric nature, meaning they are able to both donate and accept protons (H^+ ions) from solution. This property arises from exposed oxide or nitride groups at the surface and can bind to free H^+ ions in the solution. Depending on the concentration of H^+ ions and thus pH of a solution, these oxide and nitride groups exist in one of three forms [158] neutral, acceptor (negatively charged), donor (positively charged), as shown in figure 2.21. For an oxide surface, the higher the concentration of H^+ ions in solution (lower pH), the more likely that the oxide will exist as an acceptor due to the diffusion of H^+ ions towards the surface. The opposite is true of solutions of high pH containing low concentrations of H^+ ions, in this case, the sites have a higher probability of being in their donor state. This binding and donation of H^+ ions from the surface is often termed the

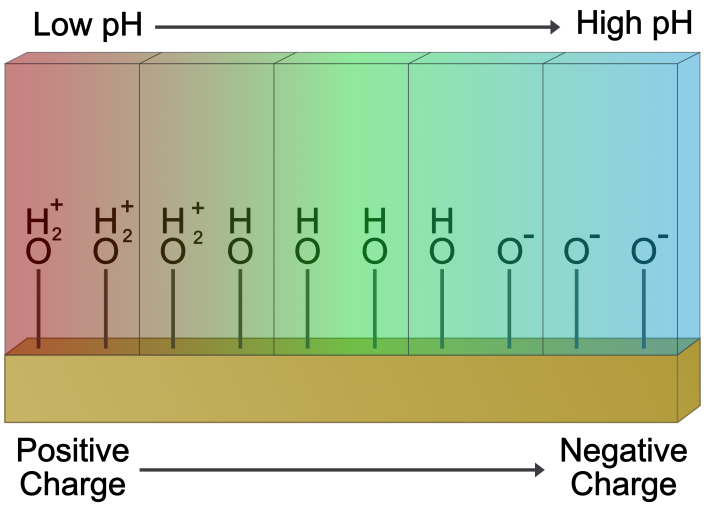

Figure 2.21: Diagram demonstrating an oxide surface's response to changes in solution pH according to the site-binding theory model. As the solution pH becomes more acidic, the surface groups begin to protonate. As the solution pH becomes more basic, these groups deprotonate.

site-binding model, and is used when describing the electrochemical potential that exists at the ISFET sensor surface.

For example, considering the oxide groups on the surface of SiOH, two reactions can occur [148, 158]. Protonation:

$$\mathrm{SiOH_2^+} \rightleftharpoons \mathrm{SiOH} + \mathrm{H_S}^+ \tag{2.23}$$

or deprotonation:

$$\mathrm{SiOH} \rightleftharpoons \mathrm{SiO^-} + \mathrm{H_S}^+ \tag{2.24}$$

where $\mathrm{H_S}^+$ is a hydrogen ion at the surface. As described in section 2.3.1, the likelihood that the $\mathrm{SiOH_2^+}$ will act as an acid and donate its $\mathrm{H^+}$ ion is determined by its acid dissociation constant K_a, given by:

$$K_a = \left(\frac{[H^+][SiOH]}{[SiOH_2^+]} \right) \tag{2.25}$$

and the likelihood that $\mathrm{SiO^-}$ will act as a base and accept an $\mathrm{H^+}$ ion is determined by the base constant K_b

$$K_b = \left(\frac{[H^+][SiO^-]}{[SiOH]} \right) \tag{2.26}$$

Each of these protonated/deprotonated sites contributes to the overall charge at the sensor surface. In order to calculate the total expected charge at the surface, and thus the potential, for a given pH, a relationship between surface charge and $\mathrm{H^+}$ ion must be determined.

The total charge residing at the surface is a combination of the $\mathrm{SiO^-}$ and $\mathrm{SiOH_2^+}$ groups, as the SiOH groups are of neutral charge. Therefore, the total surface charge can

be considered to be:

$$\sigma_0 = q\left([\mathrm{SiOH_2^+}] - [\mathrm{SiO^-}]\right) \tag{2.27}$$

the difference in the number of the two oppositely charged groups. The surface of a material will have a discrete number of amphoteric sites available, N_s, meaning that the total of the three forms of $SiOH$ must be constant and equal to N_s. With this, the surface charge due to H^+ ions can be given in the form[148]:

$$\sigma_0 = qN_s\left(\frac{[\mathrm{H_S^+}]^2 - K_aK_b}{K_aK_b + K_a[\mathrm{H_S^+}] + [\mathrm{H_S^+}]^2}\right) \tag{2.28}$$

As H^+ ions are small enough to penetrate through the double layer, the surface concentration is directly related to the bulk concentration, and thus the pH of the solution. Due to the electric field generated at the surface and the double layer, this relationship is defined by the Boltzmann equation [148]:

$$[\mathrm{H_S^+}] = [\mathrm{H_B^+}]\exp\left(\frac{-q\psi_0}{kT}\right) \tag{2.29}$$

or more usefully:

$$pH_S = pH_B + \left(\frac{-q\psi_0}{kT}\right) \tag{2.30}$$

which can be substituted into equation 2.28 to give the surface charge in relation to the bulk pH of the solution. Finally, the surface potential ψ_0 can be given as a self-referencing function of ψ_0 and bulk solution pH_B, which can be used to simulate the response of ISFET surfaces to pH [159]:

$$\psi_0 = \frac{\sigma_0}{C_{DL,i}} = \frac{qN_sf(\psi_0, pH_B)}{C_{DL,i}} \tag{2.31}$$

where $f(\psi_0, pH_B)$ is:

$$\left(\frac{\left([\mathrm{H_B^+}]\exp\left(\frac{-q\psi_0}{kT}\right)\right)^2 - K_aK_b}{K_aK_b + K_a\left([\mathrm{H_B^+}]\exp\left(\frac{-q\psi_0}{kT}\right)\right) + \left([\mathrm{H_B^+}]\exp\left(\frac{-q\psi_0}{kT}\right)\right)^2}\right) \tag{2.32}$$

Sensitivity of ISFETs

The pH sensitivity of an ISFET is important as it determines the magnitude of the response to changes in solution pH. Inherently, the sensitivity is determined by the ability of the surface to buffer the solution pH by protonating or deprotonating. This ability is referred to as the intrinsic buffer capacity, β_{int}, which represents the change in the number of H^+ accepting groups at the surface with respect to small changes in surface pH [148]:

$$\frac{\partial B}{\partial pH_S} = \beta_{int} \tag{2.33}$$

and is thus related to the surface charge by:

$$\frac{\partial \sigma_0}{\partial pH_S} = -q\frac{\partial B}{\partial pH_S} = -q\beta_{int} \tag{2.34}$$

From this definition of surface charge change with respect to surface pH, it can be shown that small change in surface pH has an effect on the surface potential defined by:

$$\frac{\partial \psi_0}{\partial pH_S} = \frac{\partial \psi_0}{\partial \sigma_0}\frac{\partial \sigma_0}{\partial pH_s} = \frac{-q\beta_{int}}{C_{DL,d}} \tag{2.35}$$

by evaluating this, we can get an expression for the general sensitivity of ISFET devices.

$$\frac{\partial \psi_0}{\partial pH_B} = -2.3\frac{kT}{q}\alpha \tag{2.36}$$

where α is a sensitivity constant between 0-1 defined by:

$$\alpha = \frac{1}{\frac{2.3kTC_{DL,d}}{q^2\beta_{int}} + 1} \tag{2.37}$$

Assuming a perfect system where $\alpha = 1$, the maximum sensitivity of a traditional ISFET sensor is 59.2 mV/pH at room temperature, recognisable as the Nernstian limit for pH sensitivity. The example used here was for SiO_2, which has a rather low intrinsic buffer capacity; however, different amphoteric oxides have different values for K_a, K_b, and β_{int}; which can make them more suitable for ISFET devices. The material choice not only affects the sensitivity of the ISFET, but also its operating range. Materials such as SiO_2 have a low operating range, losing sensitivity at higher concentrations of H^+, whereas SiN has a much larger β_{int} meaning it is able to maintain sensitivity across a wider pH range [159].

2.5 ISFETs in Literature

Following the discussion of the theory surrounding ISFET devices, this section will review the historic development of ISFETs. Given the vast number of publications appearing every year using ISFET-based devices, it is not possible to cover all aspects of ISFET research. Instead, this section will discuss the key works in the area, with a focus on the use of ISFETs for biological measurements.

2.5.1 Origin of the ISFET pH Sensor

Originally described in a short communication paper by Piet Bergveld in 1970, ISFETs were initially designed to replace the two electrode system used for the measurement of neurophysiological activity [160]. Traditionally, biophysical measurements of neurophysiology would use a two-electrode system which was able to measure spikes in ionic activity due to the altering double layer potentials between the electrodes, however, this set-up meant that any spikes between the electrodes would affect the measurement and activity

close to the electrodes would dominate. Bergveld described a system based on a MOSFET device which would rectify this issue by measuring the surface-charge density, rather than the potential across the double layer. By doing this, local ion activity could be measured without being affected by the surrounding solution effects. The initial design was based on the combination of a glass pH electrode and a MOSFET in which the metal layer on the gate electrode was removed to expose the SiO gate dielectric. In this work, Bergveld demonstrated the application of this device for the measurement of NaCl concentration, showing a correlation between the source-drain current and the concentration of ions in the solution in contact with the exposed gate dielectric. Two years later, in 1972, Bergveld published a follow-up article describing the principles of ISFET device operation and demonstrating their use for measuring a variety of ionic solutions such as KCl, $MgCl_2$, and $CaCl_2$ [161]. This work also described the pH dependent behaviour of ISFET devices. Although not the initial intention for these devices, the comparison between these SiO ISFETs and the glass pH electrode led the discussion towards using ISFET devices for pH measurements where glass electrodes would not be suited such as measuring small volumes and measuring fast changes in pH [162].

2.5.2 CMOS ISFETs

The miniaturisation of ISFET devices allows for devices to be built within the same order of magnitude as biological cells, allowing for measurements of single cell activity which were not possible with standard glass pH electrodes [163]. As well as being able to measure small volumes, the miniaturisation of ISFET devices allows for sensor arrays to be fabricated, allowing two-dimensional mapping of pH gradients [164–166]. The first example of a large-scale ISFET array was produced by T.C.W. Yeow et al. in 1997 [167]. This work demonstrated an addressable SiN-based 15×16 sensor array chip, with each device showing a sensitivity of ≈ 40 mV/pH. Although the work used primarily CMOS processes for fabrication of the underlying FET structure, the gate oxidation and formation of the ion-sensitive layer were performed using non-CMOS-standard growth methods, meaning additional steps were required alongside the typical CMOS fabrication methods. To allow large-scale and commercial fabrication of ISFET devices, they should ideally be fabricated entirely using CMOS processes, as this allows existing facilities to fabricate devices. The first example of an entirely CMOS processed ISFET was performed by J. Bausells et al. [168]. By retaining the metal gate layer of the MOSFET structure, typically not included in traditional ISFET structures, no additional etching was needed. Furthermore, a CMOS-compatible, silicon oxynitride layer was used as the pH-sensitive gate material. By making these changes, J. Bausells et al. were able to fabricate ISFET devices with sensitivities of ≈ 47 mV/pH, using only CMOS processes. Recently, CMOS-based ISFETs have typically employed a silicon nitride layer, rather than oxynitride, as this is a standard material in microelectronics fabrication and allows for a better pH response [155, 169].

CMOS fabrication allows for the simple production of ISFET sensor arrays, however, the interface between the SiN and metal gate layer can lead to parasitic capacitances [170, 171] as well as trapped charges within the ion-sensitive layer itself [172]. These parasitic

effects can lead to large variations of the threshold voltages across ISFET devices on a single sensor array. However, in work by Hu et al., it was shown that these parasitic effects can compensated for using additional control circuitry which allowed for both an automatic variable gain compensation and removal of trapped charge, for each ISFET within a 32×32 array [173].

Although CMOS-based devices suffer from parasitic affects within the structure, the development of CMOS-compatible processes for fabricating ISFET devices was a significant step for the fabrication of large-scale ISFET array devices [155]. This development has also led to devices which are able to contain on-chip control circuitry, allowing for integration of elements such as low-power readout circuitry [174], temperature compensation [175], and automatic device variation compensation [173]. Furthermore, by using arrays of micron-scale ISFET devices, spatial information can be gained about a number of biological processes which would normally be lost when using more traditional pH electrodes [163, 176]. For more information on CMOS-based ISFET technology, the reader is referred to a recent, in-depth review article [177].

2.5.3 Extended-Gate ISFETs

Traditionally, ISFETs are similar in structure to that of MOSFET devices, although, the metal gate is removed, and the gate oxide is encapsulated to allow for solution to be in contact with the exposed surface without interfering with the source-drain electrodes. Despite significant research effort, encapsulation of these devices remains challenging [162, 178, 179]. One method which allows for simple isolation of the ion-sensitive electrode and the adjoining FET device is the Extended-Gate ISFET. First demonstrated by J. Van der Spiegel et al. in 1983 [180], EGFET devices consist of a traditional MOSFET structure with a signal line connecting the metal gate to an ion-sensitive electrode, separate from the FET structure, as shown in figure 2.22. In their work, J. Van der Spiegel et al. demonstrated the development of a multi-species EGFET-based sensor which was capable of sensing three different ionic species (H^+, Cl^-, and F^-). As the sensing electrode is separate from the MOSFET electrodes, their design allows for the simple deposition and patterning of a wide range of ion-sensing materials, as well as the simple encapsulation of both the MOSFET structure and sensing electrode. However, due to the high-input impedance of the MOSFET gate, the signal line can act as an antenna, introducing additional noise into the system if not properly shielded, for example, via a coaxial grounding layer fabricated over the signal line to minimise external noise.

Due to the lack of encapsulation and surface modification of the MOSFET gate in EGFET devices, EGFETs also allow for sensors to be built with varying MOSFET channel dimensions, which have varying effects on the device sensitivity and noise. As shown in equation 2.38, the current through a MOSFET channel is related to the aspect ratio of the device channel W/L [179].

$$I_{DS} = \mu_n C_{ox} \frac{W}{L} \left[(V_{GS} - V_{Th})\, V_{DS} - \frac{{V_{DS}}^2}{2} \right] \tag{2.38}$$

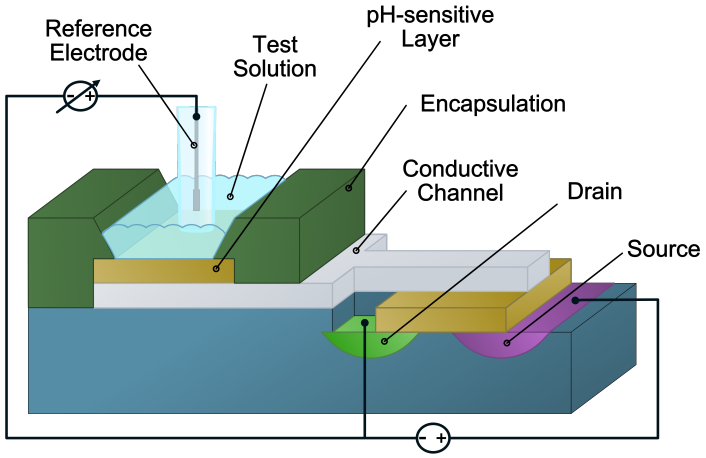

Figure 2.22: Diagram of a typical EGFET structure.

Thus, it is expected that a larger current signal will be observed for high aspect ratio devices. However, as noted in the work by N. Rajan et al., the noise of a MOSFET device is also related to its channel dimensions and linearly correlated to the $\sqrt{WL}$ [181]. Thus, careful design has to be taken to ensure the sensitivity of the device is not affected by the device dimensions. However, the flexibility of the MOSFET device structure in EGFETs allows for simpler implementation of low-power, low-noise, and fast time-response devices [182]. More recently, EGFET devices have also been implemented with novel FET structures which allow for amplification of the pH sensitivity, within the FET structures themselves [183, 184]

As well as allowing for flexibility in terms of the MOSFET structure, the design of EGFETS allow for the use of commercial, pre-packaged, MOSFETs (Figure 2.23). Sometimes referred to as Separative EGFETs (SEGFETs) or ExFETs [179], these discrete-component EGFETs allow for low-fabrication and low-cost implementation of pH sensing. The first example of this type of sensor is often attributed to L.L. Chi et al., who described a system which used a commercial MOSFET connected to an SnO ion-sensitive electrode [185, 186]. The device was able to achieve a pH sensitivity of ≈ 58 mV/pH and was shown to have minimal response to changes in light exposure, something which has been shown to be an issue for many traditional exposed-gate ISFET structures [175, 187, 188]. Furthermore, the nature of the discrete sensing electrode is well suited for biosensing applications where contamination may be an issue, as the sensing electrode can be disposed of without the need to dispose of the controlling MOSFET circuitry. Since the work done by L.L. Chi et al., commercial MOSFETs have been used in a number of pH sensing, EGFET systems some of which allow low-cost and multiplexed sensing in a single platform [189–192]

Recent research into EGFET devices has focussed on two main areas, incorporation of novel ion-sensitive materials, which will be discussed in a subsequent section, and the use of EGFET devices for specific biosensing applications. Although the structure of EGFET sensors does not allow for wide arrays of devices to be placed on the same chip, as seen with some CMOS-based devices, they have seen a lot of application in areas where only

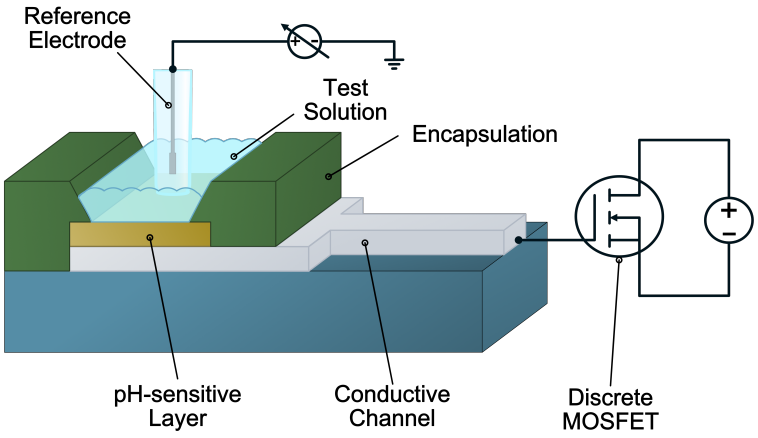

Figure 2.23: Diagram of a typical discrete EGFET structure.

single pH, ion, or biomarker measurement is required, often due to their simple fabrication, versatility in terms of electrode composition, or disposable sensing electrode [193–195].

Typically, EGFETs are used for the purpose of determining ion concentration in solution, however, the versatility of the extended gate material has allowed for applications requiring specific surface functionalisation for the detection of biomolecules. Sometimes referred to as BioFETs [196], these modified FET sensors primarily utilise surface-bound receptors, such as antibodies, enzymes, or DNA to detect the presence of specific biomolecules such as proteins, small molecules, or DNA sequences. Instead of measuring the potential shift due to protonation and deprotonation, these sensors rely on changes in surface charge due to the binding of biomolecules to the surface-bound receptors. For example, A. Tarasov et al. demonstrated an EGFET for detection of protein biomarkers in which a gold sensing electrode functionalised with the glycoprotein E (gE) of Bovine Herpes Virus 1 (BHV-1) was used for the detection of anti-BHV-1 antibodies [197]. In this work, they were able to demonstrate similar detection limits of anti-BHV-1 in diluted serum to the laboratory standard assay (based on the widely used enzyme-linked immunosorbent assay) but in a much shorter time of < 10 min. By enabling fast detection from diluted serum, point-of-care immunoassays which allow for quantitative readouts could become a reality. Although the assay was used for the specific detection of anti-BHV-1, the surface of the extended electrode could easily be modified to allow the detection of other protein biomarkers, as has been demonstrated in a number of reports [195, 198–200].

An area where EGFETs have seen a number of uses is in the field of urea sensing for diagnostics [200–203]. The choice of ion-sensitive devices for the detection of a small molecule such as urea is primarily due to the reaction which occurs between urease enzymes and urea; when urea is catalysed by urease enzymes, a number of by-products are formed, such as bicarbonate and ammonia, which alter the pH of the surrounding solution [204]. By immobilising urease enzymes onto the surface of an EGFET gate, urea is catalysed directly at the sensor surface, leading to changes in local pH at the pH-sensitive gate. An example of this type of sensor was demonstrated by J-C Chen et al. [205], who used a

disposable, SnO, EGFET structure to detect urea diluted into buffer between the ranges of 0.31 to 120 mg/dl in approximately 2 minutes, well within the limit for increased urea concentration seen for renal disease [206].

It should be noted that surface-functionalised BioFET devices are not limited to EGFETs [207], however, the versatility of the extended gate material and topology make it an attractive option for this class of biosensor. Please refer to the large number of recent review articles on the applications of BioFETs for further information on this topic [179, 198, 208].

EGFET sensors offer significantly simpler fabrication of the ion-sensitive structure due to their separation of the sensing and FET structures. These devices also enable better flexibility in terms of device structure and choice of ion-sensitive material, allowing the fabrication of high-sensitivity and low noise devices. By using pre-packaged MOSFETs, EGFETs can also be fabricated simply and at low-cost. Furthermore, the discrete nature of this structure allows for sensors which have disposable sensing electrodes and reusable MOSFET circuits [209]. For this reason, a discrete component EGFET which utilised a commercial MOSFET was used as the pH sensing device for this project.

2.5.4 Ion-Sensitive Layers in ISFETs

Perhaps the most important aspect of pH-sensitive FET devices is the ion-sensitive layer. This layer determines the pH-sensing properties of the device such as its pH-sensitivity, response time, and stability over time. Initially, the ion-sensitive layer for ISFET devices was limited to the few materials compatible with CMOS manufacturing processes, hence the use of SiO in the original ISFET device [160, 162]. For the same reason, many early ISFET devices used materials such as SiN and AlO for the ion-sensitive layer deposited using chemical vapour deposition (CVD) [210]. While these traditional ion-sensitive materials are still widely used, particularly in CMOS-based ISFET devices [170, 211–214], they are not necessarily the best materials for high-sensitivity, low-drift applications [215]. Given that ISFET-based devices have been developed for over 50 years [160], a vast number of different pH-sensitive materials have been investigated. Many of these materials show similar pH sensing properties and have been covered in several review articles [179, 216, 217]. Therefore, this section will only discuss a few materials which have novel properties such as exceptional sensitivity, stability, or simple deposition procedure.

An issue with many of the materials used for ISFET fabrication is the need for expensive deposition equipment within a cleanroom environment. One method which removes the need for these instruments is sol-gel based deposition. This method uses colloidal suspensions of metal oxides within a gel-like solution, referred to as sol-gels, which can be used to deposit thin films by simply drying the sol-gel on surface, causing the colloidal suspension to form a dense network. Sol-gel deposition methods have been demonstrated for a number of pH-sensitive materials, all of which appear to show good sensitivity [218–221]. For example E.M. Guerra et al., used a vanadium oxide (VO) sol-gel to form a pH sensitive layer on an extended-gate electrode [222]. The sol-gel was formulated using well-reported methods and formation of the VO film was achieved simply by drop-casting onto

a glassy carbon electrode and leaving at room temperature to dry. The fabricated EGFET showed an almost linear response to pH of 58.1 mV/pH across a wide pH range (2-12). Another method for ion-sensitive material deposition which does not require cleanroom instrumentation is to use a pH sensitive polymer such as polyaniline (PANI) which will self-assemble on a surface. N. Vieira et al. describe a method for forming multi-layer, nanostructured, poly(vinyl sulfonic acid) (PVS)-PANI films by repeatedly immersing gold electrodes in alternating solutions of PANI followed by PVS [223]. The discrete extended gate PVS/PANI electrode showed a high sensitivity to pH of $\approx$ 58 mV/pH.

Drift due to external factors such as temperature is a significant issue for ISFET-based devices as it makes quantification of results difficult. One method for reducing the effect of drift is the reference FET (REFET). This is similar in structure to an ISFET, however, instead of an ion-sensitive membrane, a membrane is used which insensitive to changes in pH [224]. By using a matched device with an insensitive membrane alongside an ISFET, the effect of any stimuli external to the changes in pH can be removed. A material which has been shown to work as this insensitive membrane is Parylene-C [225]. However, as well as being able to be used as an insensitive membrane, T. Trantidou et al. demonstrated that by activation through UV exposure, the Parylene-C membrane can also be used as a pH-sensitive membrane [226]. Although the pH-sensitivity of these devices was only 23 mV/pH [227], the versatility of this material to be able to be used as a flexible substrate, encapsulation, pH-sensitive, and pH-insensitive layer would allow for devices to be fabricated using minimal deposition and etching techniques.

A material which has been shown to have an atypical response to pH is palladium oxide (PdO). A. Das et al. demonstrated an EGFET-based pH sensor which used PdO as the extended gate material [228]. In this work, they demonstrated their EGEFT device to exhibit a seemingly 'super-nernstian' response of $\approx$ 63 mV/pH, above the expected limit of 59.2 mV/pH. The device showed good linearity across a large pH range (2-12) and thus the sensitivity was thought to be due to high oxygen content, leading to higher oxidation states within the PdO layer, which can lead to in imbalance in the proton exchange at the surface. This phenomenon is not unique to PdO, thus this could well be the cause behind the enhanced sensitivity. A material in which this phenomenon is well-reported is iridium oxide, the material of choice for the EGFET used in this project.

Iridium Oxide

Iridium oxide (IrO) is an ion-sensitive material which has been used for a number of different pH-sensing applications [216]. When deposited using evaporation or sputtering techniques, IrO_x films exhibit similar properties to that of other metal oxides, showing a peak pH sensitivity of 59.2 mV/pH [229]. However, an interesting characteristic of IrO_x layers comes when they are deposited using electrodeposition techniques. These Electrodeposited Iridium Oxide Films (EIROFs), sometimes referred to as Anodic Iridium Oxide Films (AIROFs), exhibit a seemingly 'super-nernstian' sensitivity to pH, with a limit of $\approx$ 88 mV/pH [230]. This high sensitivity is not in fact a demonstration of pH sensitivity above the Nernstian limit but is due to a combination of electrochemical effects [229–231].

As discussed previously, the site-binding model describes the effect of changing pH on the state of free hydroxide groups on the surface. This reaction still occurs in IrO_x films [229]:

$$IrO(OH) + H^+ \rightleftharpoons IrO(OH_2)^+ \quad (Protonation) \tag{2.39}$$

$$IrO(OH) \rightleftharpoons IrOO^- + H^+ \quad (Deprotonation) \tag{2.40}$$

When IrO_x is deposited using electrodeposition, the film is typically a porous, hydrated, mixture of Ir(III) and Ir(IV) complexes, which can exist in a number of forms. In metal oxides, changes in pH can lead to shifts in the balance of oxidation states, which is thought to be part of the cause behind the deviation from the typical Nernstian sensitivity [230]. An example of this balance for Ir(III) and Ir(IV) is described by Olthuis et al. [229]:

$$2\,Ir(OH)_3 + H_2O \rightleftharpoons Ir_2O(OH)_6 + 2\,H^+ + 2\,e \tag{2.41}$$

If the site binding model is considered for each of these Ir oxidation states, then each complex can protonate and deprotonate to different extents as such [229]:

$$Ir(OH)_3 \longrightarrow Ir(OH)_2O^- + H^+ \tag{2.42}$$

$$Ir_2O(OH)_6 \longrightarrow Ir_2O(OH)_3O_3{}^{3-} + 3\,H^+ \tag{2.43}$$

By combining the two effects of the site-binding model and the equilibrium between oxidation states, equations 2.41, 2.42, and 2.43 can be combined to give:

$$2\,Ir(OH)_2O^- + H_2O \rightleftharpoons Ir_2O(OH)_3O_3{}^{3-} + 3\,H^+ + 2\,e \tag{2.44}$$

where it can be shown that an imbalance of H^+ to electrons is possible. By applying this reaction to the Nernst equation it is possible to show that:

$$E = \frac{1}{2}0.0592 \log_{10}[H^+]^3 \tag{2.45}$$

Which can be simplified to:

$$E = \frac{3}{2}0.0592 \times pH = 88.8\ mV/pH \tag{2.46}$$

Therefore, this imbalance of the movement of protons and electrons within the reaction leads to a seemingly higher level of pH sensitivity than that observed in traditional ion-sensitive materials. This high pH sensitivity, alongside the ease with which it can be deposited on conductive electrodes, is the reason EIROFs were chosen as the ion-sensitive electrode material for this project. It should be noted that this atypical pH sensitivity phenomenon is not unique to IrO_x and has been demonstrated in other materials such as RuO and PdO [228, 232], however, techniques for their deposition are less well documented, when compared to IrO_x.

Most ion-sensitive electrode EIROFs are prepared using an alkaline iridium oxalate solution, first described by K. Yamanaka [233]. Although efforts have been made to

improve upon this deposition solution [234–236] they still contain some form of Ir(IV)-oxalate complex. It is thought that deposition from this solution is performed by anodic oxidation of the oxalato ligand surrounding the Ir(IV) complex. By oxidising the oxalato ligand, CO_2 is formed and the ligand is removed, leaving a free IrO_x complex to form a solid film at the electrode surface. This process was described by K. Yamanaka using the following reaction [233]:

$$[Ir(COO)_2(OH)_4]^{2-} \longrightarrow IrO_2 + 2\,CO_2 + 2\,H_2O + 2\,e^- \tag{2.47}$$

Typically, the electrodeposition is carried out by applying a fixed current or potential to an electrode submerged in the iridium oxalate solution [233, 234, 236]. However, it has been found that these films can exhibit poor mechanical qualities such as being soft, easily damaged, and delaminating from the underlying substrate. H. Elsen et al. found that by potentially cycling the electrode in the deposition solution, more durable and well adhered films could be formed, showing similar levels of pH sensitivity to those films prepared using fixed current methods [237]. For this reason, potential cycling was chosen for this project and is described in detail in chapters 3 and 4.

EIROFs have been used extensively for a variety of pH sensing applications, such as: extracellular pH changes due to myocardial acidosis [238]; flexible pH sensors [239]; and detection of in vivo concentrations of penicillin [240, 241]. However, there are relatively few reports on combining ISFET-based devices and these high-sensitivity films. An IrO_x-based CMOS ISFET was first described by J. Hendrikse et al. in 1997 [242]. The device showed a fast, almost drift free, response to changes in pH. However, the IrO_x film was prepared using sputtering techniques, limiting the pH sensitivity of the device to $\approx 59\ mV/pH$. IrO_x was also used in the original EGFET paper by J. Van der Spiegel et al., however, the layer was deposited using sputtering techniques with limited characterisation with regards to its pH response [180]. More recently, an EGFET based device using EIROF films in combination with a discrete MOSFET has been described. [243]. The device consisted of a pH-insensitive film coated onto the gate electrode of the EGFET. Connected to this, instead of a typical reference electrode, was an EIROF-coated ITO electrode serving as a pH-sensitive biasing electrode for the EGFET. By biasing the EGFET through the EIROF electrode, the voltage that appeared at the gate would be a summation of the applied voltage and the pH-sensitive chemical potential at the EIROF surface. With this device, they showed a pH sensitivity of $\approx 62.5\ mV/pH$, demonstrating the atypical pH response of EIROF electrodes. However, the key achievement with this device is the lack of requirement for a reference electrode, allowing the device to be easily miniaturised.

2.5.5 Future of ISFET-based Devices

ISFET-based devices have seen a lot of application in the area of biosensing due to their low-cost, miniaturisation, and response time [244]. This section will discuss some of the key applications for which ISFET-based devices have been developed, with a look to determine the future direction of this technology.

One of the most promising uses for ISFET-based devices is in the area of genomic sequencing. Originally demonstrated by T. Sakurai and Y. Husimi [245], the polymerase chain-elongation reaction used in many DNA sequencing techniques has been shown to affect the pH of a solution through the release H^+ ions, which can be easily measured using an ISFET device. The scalability of ISFET arrays allows for massive levels of multiplexed measurements, difficult to achieve using optical methods. An example of a commercial system which is able to perform these methods is the Ion Torrent system, originally described by J. Rothberg et al. [19]. In their work, they describe the development of a system which uses chips containing up to 13 M TaO-based ISFET devices within a single array. The system operates by splitting DNA into fragments and functionalising these unique sequences onto polymer beads. Individual beads are subsequently located locally to one of the millions of ISFET devices, allowing for parallel measurements of DNA polymerase reactions. As well as applications for whole-genome-sequencing, integrated ISFET chips have been demonstrated for use in quantitative PCR and LAMP based assays. C. Toumazou et al. demonstrated a chip for quantifying DNA amplification that consisted of 40 ISFET devices alongside control circuitry, resistive heaters, and temperature sensors all using an unmodified CMOS process [246]. In this work they demonstrate the use of their bespoke chip for use in both PCR and LAMP assays, showing comparative sensitivities to commercial, fluorescence-based, PCR and LAMP techniques. DNA sequencing has had a massive impact on medicine and research both with the prospect of whole-genome sequencing and gene-based detection methods. As CMOS fabrication techniques become more sophisticated, ISFET devices could easily play a large role in rapid and low-cost sequencing.

ISFET devices within the field of genomic detection appear to be limited to CMOS-based ISFET geometries, due to their allowance for arrays of ISFET devices to be placed alongside control circuitry on a single chip. An area in which EGFETs could play a larger role is in the field of low-cost biosensing. T. Prodromakis et al. [191] describe a methodology of using a separate transducer and sensing elements using commercial mass-manufactured MOSFETs as the transducer element, similar to the discrete EGFET demonstrated by L.L. Chi et al. [186]. Although the sensing apparatus they describe in their work was not entirely novel, they also demonstrate the use of PCB as a substrate for these devices, a well-established material for producing low-cost and mass manufactured devices PCB technology [247]. The sensitivity demonstrated on this PCB-based device was much lower than the Nernstian limit (22 mV/pH) however, this technique for PCB-based EGFETs was later used by M. Kaisti et al. in conjunction with a PANI ion-sensitive membrane and showing a near-Nernstian response to K^+ ions [192], demonstrating a technology which can be easily fabricated with high-sensitivity at a low-cost. It should be noted however, the bulky and expensive reference electrode required for ISFET operation remains a potential barrier to integrated low-cost technologies. For this class of low-cost biosensor to become feasible, the technology must be adapted to accommodate for on-board reference electrodes, a technique which has been demonstrated by D. Moschou et al. [248]. This work describes the fabrication of a PCB-based Ag/AgCl reference electrode

with good stability, which has also been demonstrated in conjunction with a similar FET-based biosensor [249]. By combining a low-cost, mass-manufacturable technology such as PCB with discrete EGFET devices, a low-cost and point-of-care technology could easily be realised.

Finally, an application where ISFET-based devices have seen a number of uses is in the detection of β-lactam antibiotics, mainly penicillin, often for the purpose of monitoring concentrations in patients, waste-water, or penicillin fermentation broths [139, 250–255]. These sensors are often based on immobilised penicillinase (a form of β-lactamase) and use the change in local pH to determine antibiotic concentration. To date, there appears to be no application which uses the acidification of β-lactam molecules to determine the presence and activity of β-lactamase enzymes. One work, by C. Hu et al., describes the use of a pH sensitive FET-type device for the measurement of an induced pH change due to the LAMP-based amplification of two β-lactamase genes [173]. However, no other work appears to have been carried out combining β-lactamase detection and ion-sensitive FET devices. The aim of this project was to utilise an IrO-based discrete EGFET device with a high-sensitivity to determine the activity of β-lactamase through the acidification of β-lactam molecules. The development of this device would allow for quantitative, low-cost detection of β-lactam resistance at the time of prescription, something which is not possible with the current technology.

Chapter 3

Fabrication, Equipment and Experimental Techniques

This chapter describes the experimental procedures and protocols that underpin the research presented in this thesis. Specifically, this chapter details the fabrication methods used to construct the discrete component Extended-Gate Ion-Sensitive FET (EGFET) devices including functionalisation of the electrode surface with a pH sensitive layer and reviews the characterisation techniques employed to characterise the fabricated EGFETs.

3.1 Electrode Fabrication Techniques

This section describes the techniques used to fabricate the extended gate electrodes and for electrodeposition of the pH sensitive iridium-oxide layers.

3.1.1 Cleaning

Standard, 50 × 75 mm glass microscope slides cut to 25 × 25 mm were used as the substrate for all devices. Contamination of the substrate surface can lead to inconsistency in device characteristics, issues with layer adhesion, and defects in device structure. Therefore, substrate cleaning is an essential aspect of micro- and nano-fabrication [256]. Contamination can come from a number of sources [257]: particulates from the air such as dust and hair; Organic contamination from skin; and contamination from processing, such as dried solvents. As well as ensuring that substrates are clean before fabrication, it is also essential that fabricated devices are cleaned before use to ensure no contamination interferes with the device characteristics. This section describes the two main procedures used to clean substrates prior to fabrication and fabricated devices.

Piranha Cleaning

Where more aggressive cleaning was needed, such as substrate cleaning prior to device fabrication, cleaved glass substrates were cleaned using a mix of sulfuric acid and hydrogen peroxide, commonly referred to as a piranha cleaning solution (H_2SO_5). The solution is highly oxidising and is able to rapidly remove and break down organic contaminants on the substrate surface, hence the name 'piranha'. Because of its nature, protective goggles and gloves should be worn at all times.

Hydrogen peroxide was slowly added to sulfuric acid at a ratio of 1:3, respectively, in a glass beaker. Samples were subsequently immersed in the solution and left for a period of

time, depending on the application. After cleaning, the samples were rinsed twice in deionised water to remove any remaining solution and then subjected to a 5 min sonication in acetone, followed by a 5 min sonication in Isoproyl Achohol (IPA), to remove any water contamination, and then finally dried using pressurised nitrogen.

UV O-zone Cleaning

For experiments where piranha solution was not suitable for cleaning, substrates were cleaned using a UV-ozone procedure. A UV-Ozone cleaner uses high-energy UV light to remove organic compounds from substrates. Cleaning occurs through two main procedures. The first is the decomposition of carbohydrates through UV-light. Long chain carbohydrates on the substrate surface are broken down into more volatile substances which are easily removed. Secondly, the high-energy UV light typically has peak wavelengths around 185 nm and 254 nm. These wavelengths are important as they allow the formation and decomposition of ozone, O_3 [258]. When O_2 is excited by 185 nm UV-light, it will form O_3, conversely, when O_3 is excited by the 254 nm UV-light, it decomposes back to O_2. When this process happens close to the surface, it is strongly oxidising, breaking down organic contamination on the surface.

The procedure for cleaning with UV-ozone was as follows. UV-ozone treatment (10 min); followed by a sonication in a 2% Hellmanex III solution (Hellma Analytics) (10 min) and then a sonication in Milli-Q ultrapure water (2×10 min), followed by a second UV-ozone treatment (30 min) and finally immersion in EtOH (30 min). The devices were dried using nitrogen following each wet cleaning stage.

3.1.2 Metal Evaporation Techniques

After the substrate had been sufficiently cleaned, conductive contacts had to be added to the substrate allow for iridium oxide electro-deposition. Two methods were used throughout this project: thermal evaporation and electron-beam evaporation. The reason for using both in this project was due to inaccessibility of the electron-beam evaporator for portions of this project. This section will describe the operation of both techniques.

Vapour Deposition Techniques for Metal Evaporation

Towards the beginning of this project, thermal evaporation was used to produce the thin, metal film electrodes. Thermal evaporation is one of the most common thin-film deposition techniques [259]. In this technique, a target substrate sample is placed above a pure metal source, sat in a conductive tungsten boat, or sometimes wrapped around a conductive tungsten wire. In order to evaporate the metal source, a high current (several hundred amps) is passed through the conductive crucible. Energy lost through resistive heating causes the material to reach temperatures comparable to the melting temperature of the metal source, causing it to liquefy and begin to produce metal vapour. In order to allow the metal vapour to rise and reach the sample substrate above, without interacting with other molecules, the chamber must be kept at a vacuum pressure (10^{-6} mBar in this instance).

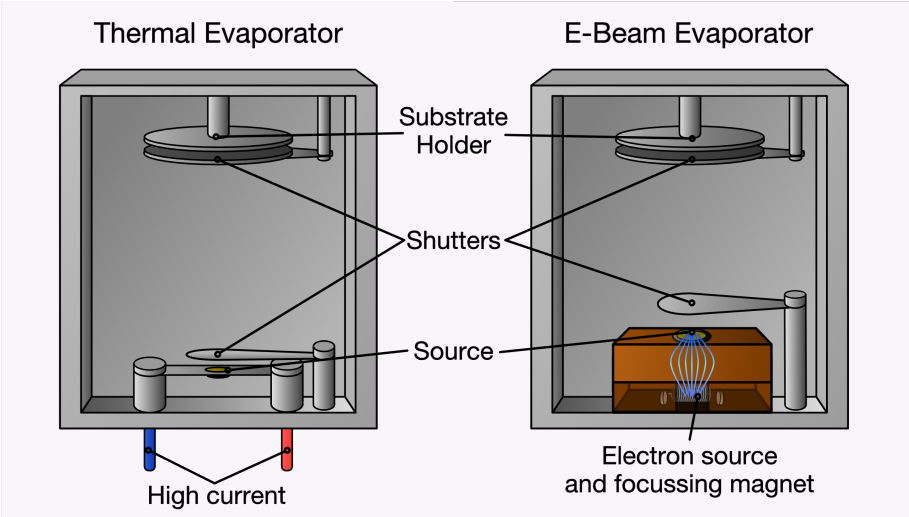

Figure 3.1: Diagram of thermal and e-beam evaporators. The key components are labelled alongside of each instrument.

As the sample substrate above the source metal is cooler than the vaporised metal, the metal begins to condense onto the substrate, leaving a thin film of solid metal. The rate of this evaporation, and thus the thickness of the film, is monitored using a resonating quartz-crystal micro-balance (QCM) placed within the chamber, near the sample. As the metal deposits on the QCM, the natural frequency with which it resonates begins to reduce. This lowering of frequency can be used to calculate a rate of deposition on the sample in real time and thus a thickness of the thin-film. A diagram of a thermal evaporator can be seen in figure 3.1. Thermal evaporation was carried out using a Mantis HEX resistive thermal evaporator.

The second metal evaporation technique that was used was electron-beam evaporation. This technique is similar in operation to that of thermal evaporation; however, the metal is not heated through resistive heating, but through a focussed beam of electrons. The layout of electron beam evaporators is almost identical to that of thermal evaporators. A sample is placed in a vacuum chamber above a pure source of the desired deposition material, contained within a crucible. Below the material crucible, is an electron gun, comprised of a filament electron source and a series of magnets. When a current is passed through the filament, it begins to emit electrons via thermionic emission. These electrons are then accelerated and guided by magnets within the gun, towards the source material. Once they hit the surface, their energy is transferred to the source material, causing it to heat, which in turn causes it to evaporate or sublime. Electron-beam evaporation is suitable for a wider range of materials compared to thermal evaporation, due to the higher energies and temperatures that can be achieved. Given the ability to control the focussing and energy of the electron beam, it also allows for more controlled deposition rates. Beyond these points, electron-beam and thermal evaporation are very similar in their operation. Both operate at a low vacuum pressure, and both measure the film thickness through a QCM. A diagram of an electron-beam evaporator can be seen in figure 3.1. The electron-beam evaporator used for this project was a custom-built M-Braun instrument.

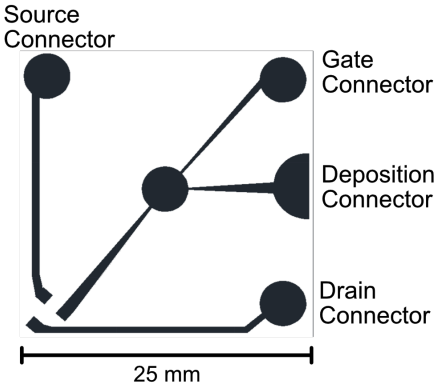

Figure 3.2: CAD design for the ion-sensitive electrode structure. The design allowed for the connection of the transistor directly on chip, as well as a separate connector for allowing IrO deposition.

In order to achieve the desired thin-film, a series of shutters are present in both machines. The first shutter, mounted above the substrate, is used to control of the film thickness; once a desirable thickness is reached, this shutter is closed, preventing any more metal vapour from reaching the substrate. As source metals are susceptible to surface contamination, both machines also contain a shutter which is able to cover the metal source. By covering the metal for a short time after the initial vaporisation, surface contamination is prevented from reaching the substrate, allowing only the pure metal vapour to be deposited on the sample.

These evaporation techniques were primarily used for depositing 100 nm thick gold contacts onto the glass substrates. A 10 nm layer of chromium was deposited to increase adhesion of the gold layer to the glass substrate. However, for thermal evaporation, a 10 nm aluminium layer was deposited instead due to the inability to reach a stable deposition rate with chromium. In both cases, the adhesion layer was deposited without breaking vacuum.

3.1.3 Patterning the Metal Contacts

Initially, both the discrete EGFET sensing electrode and transistor were attached directly onto a glass substrate. This required patterning of the metal electrodes. This section will discuss the techniques used to produce this patterned metal layer. Lithographic masks were designed using AutoCAD (Autodesk) and EAGLE PCB designer (Autodesk). The initial design for the chip is shown in figure 3.2.

Photolithography

One of the primary techniques used for metal patterning in this project was photolithography. Photolithography, sometimes referred to as optical lithography, is a technique which uses photosensitive polymers, known as photoresists, to produce patterned layers on a substrate [256]. For this technique, a liquid photoresist polymer is pooled on the substrate surface and then spun at a controlled speed to create a uniform, thin layer. Following this, the layer is cured at elevated temperatures to remove solvent and solidify the photoresist.

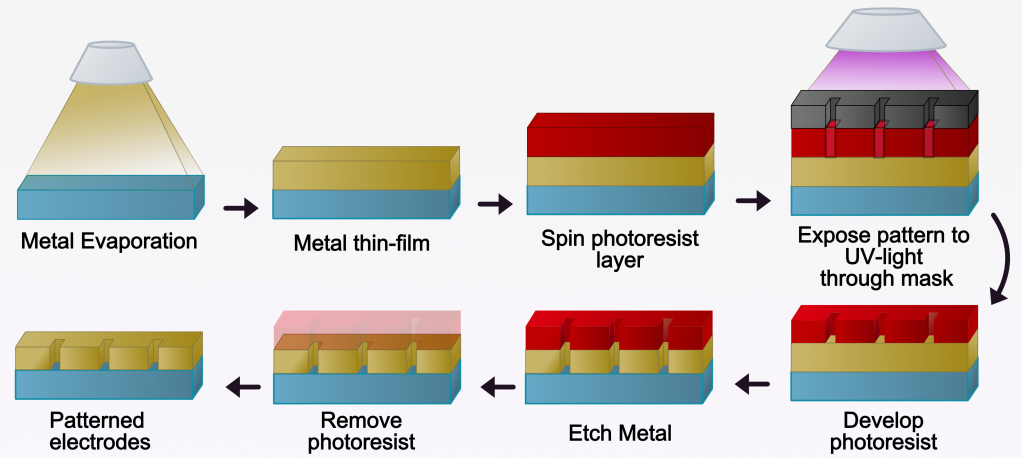

Figure 3.3: Schematic of the photolithography process used for this project.

Once cured, the pattern is written into the photoresist using UV light. Two types of photoresist exist, positive and negative, which determine how they react to UV light. When exposed, the organic bonds within positive photoresists begin to break, making it easier to remove when developed. For negative resists, the opposite is true; these bonds become stronger, making it harder to wash away when developed. UV exposure is often done using one of two methods, exposure through a photomask or direct-write with a laser. A photomask is an opaque template of the desired pattern. When UV-light is shone through the photomask, only the desired pattern is projected onto the photoresist. Direct-write, or mask-less lithography, uses a manoeuvrable, focussed, UV laser to draw the pattern on the photoresist surface. One of the benefits of direct-write techniques is that it can be used to prototype designs, as a photomask has to be designed and produced for each pattern. However, the time required for direct-write techniques is much higher than the equivalent photomask exposure. Following UV-light exposure, the photoresist layer on top of the substrate is patterned with the desired structure. Developing this exposed photoresist layer in an organic developer solution, removes the unwanted photoresist, leaving the desired pattern.

After the pattern has been produced in photoresist, the substrate can be used to produce patterned electrode structures using one of two methods. The first is through etching with chemicals or plasmas. Patterning the photoresist on top of a metal thin-film before etching results in the etchant only removing the film where it is not protected by the photoresist, leaving behind a patterned electrode. The second method is through deposition on top of the patterned resist and then dissolving the photoresist. As the photoresist is removed it also removes the unwanted thin-film, leaving behind the thin film only where it directly adheres to the substrate. The spatial resolution of photolithography is ultimately limited by the diffraction of the UV-light used, meaning structures at the nanometer scale are difficult to produce and require specialised systems [260]; however, for this project, structures of this size were not needed.

The photolithography protocol used for this project was as follows. MICROPOSIT S1818 positive photoresist (Shipley) was pooled onto a, piranha cleaned, 25×25 mm glass

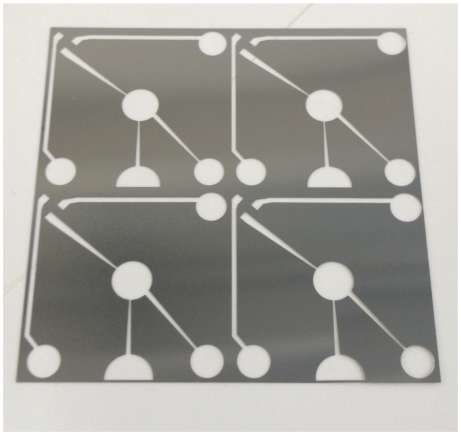

Figure 3.4: Example of the metal shadowmasks used in this project for shadowmask evaporation.

substrate with a 100 nm gold layer and a 10 nm chromium adhesion layer. This sample was loaded into a spin coater and spun at 4500 rpm for 60 seconds. The sample was then placed on a hotplate at 115 °C for 60 seconds. The sample was exposed for 10 seconds through a positive photomask, using a custom UV-lamp (NB: S1818 is a positive photoresist, therefore, areas exposed to UV-light will be washed away when developed). The sample was then rinsed in MICROPOSIT MF319 developer (Shipley) for 120 seconds, rinsed with de-ionised water, and dried with nitrogen. After the desired pattern had been produced in the S1818 layer, the sample was exposed to gold etchant (Sigma-Aldrich: 651842) for 30 seconds to remove the unwanted gold, and then rinsed in de-ionised water. To remove the unwanted adhesion layer, the sample was exposed to chromium etchant (Sigma-Aldrich: 651826) for 30 seconds, leaving behind the desired electrode pattern. Finally, the sample was cleaned in piranha solution for 30 seconds to ensure all of the S1818 was removed. A diagram of this process is shown in figure 3.3.

Shadow-mask Evaporation

Photolithography is capable of producing very fine patterned electrodes [260], however, for this project, the size of the electrodes was well above the resolution of photolithography. In order to accelerate the fabrication time, shadow-mask evaporation was later adopted to replace the photolithography stage. Shadow-mask evaporation is the process of placing a patterned stencil (shown in figure 3.4) between the substrate and the source when evaporating thin-films. The stencil masks any regions of the sample where the thin-film is undesired, leaving behind only the electrode pattern. The primary advantage of this technique, compared with other lithography techniques, is simplicity and speed. However, the technique does not allow for high-resolution structures, and can lead to smearing of thin-film layers if the mask is not aligned properly or not flat against the substrate. These downsides were compromises in this project, as we did not require high resolution, and great care was taken when attaching the stencil to the substrate.

The shadow-mask evaporation protocol was as follows. Piranha cleaned 25×25 mm glass substrates were loaded onto the E-beam evaporator sample holder. The shadow-mask was then attached to the samples using temperature-resistant kapton tape. The holder

was then loaded into the evaporator and the evaporation process was performed as usual. These steps are shown in figure 3.5.

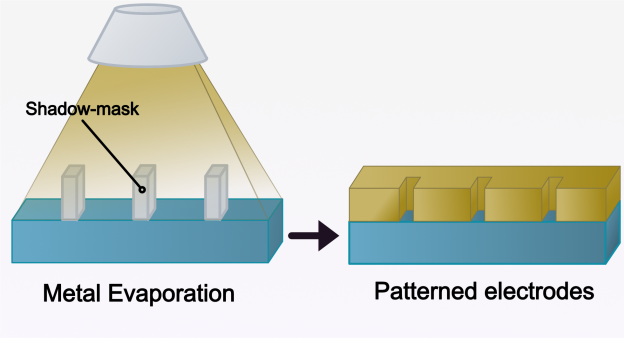

Figure 3.5: Schematic of the shadowmask evaporation process used for this project.

3.2 Electrochemical Techniques and Iridium Oxide Deposition

Electrochemistry is the field of chemistry which investigates the movement of charge in relation to chemical reactions [143]. From the mechanism of voltage production in batteries, to the purification of waste-water through electrolysis, electrochemistry is present in many aspects of science. The discrete EGFET used throughout this project is an example of an electrochemical device, as charge is being stored at the electrode surface, due to reactions with the free H^+ ions in solution. Electrochemical devices and techniques were used throughout this project for both the development of the EGFET sensor electrode and subsequent characterisation. This section will discuss the electrochemical devices and techniques used in this project.

3.2.1 The Electrochemical Cell

As described in chapter 2, when an electrode is placed into a solution, an electrochemical double-layer forms at the surface. This double-layer is particularly problematic when attempting to measure the voltage built up at a surface, as any other electrode placed into the solution will have its own double-layer and potential. This means that the typical set-up for measuring potential difference between conductors is not suitable as it would include the potential at both electrodes. To remedy this, an electrode with a fixed and known potential has to be used, referred to as a reference electrode.

Initially, reference electrodes were based on the redox reaction of gaseous hydrogen into its aqueous form [143]

$$2\,H^+(Aq) + 2\,e^- \rightleftharpoons H_2 \tag{3.1}$$

Hydrogen reference electrodes are constructed by bubbling H_2 gas over a platinum electrode in an acidic solution. At equilibrium, a stable potential forms at the platinum electrode surface. This electrode is known as a standard hydrogen electrode (SHE) and it forms the basis of all electrochemical measurements. The equilibrium potential of this

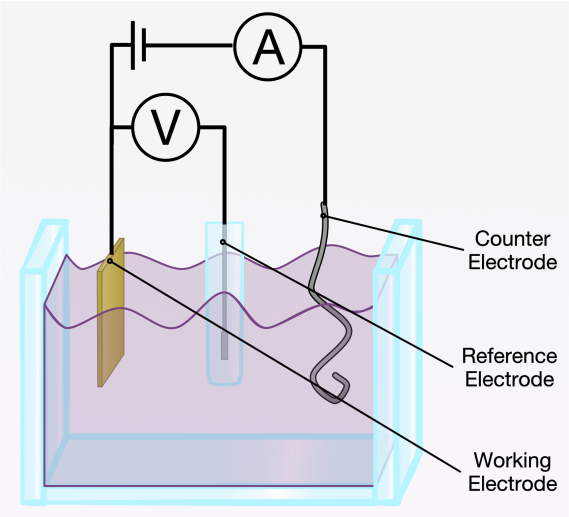

Figure 3.6: Diagram showing a typical three-electrode setup. The voltage of the working electrode is measured with respect to the reference electrode and the current is measured between the working and counter electrodes.

reaction is deemed to be 0 V at 25 °C. However, due to the impracticality of these electrodes, most electrochemical cells today use secondary reference electrodes whose stable potential can be referenced to the SHE.

The reference electrodes used for this project were silver-silver chloride ($Ag-AgCl$) electrodes. These are common reference electrodes for electrochemical applications as they are stable and relatively unintrusive. This electrode is comprised of a silver (Ag) wire encased in the sparingly soluble salt, AgCl, surrounded by a saturated solution of Cl ions, often in the form of a potassium chloride solution. The combination of these components leads to an equilibrium [143]:

$$AgCl \rightleftharpoons Ag^{+} + Cl^{-} \tag{3.2}$$

As the surrounding solution is saturated with chloride ions, an equilibrium is reached at the electrode interface. The potential of the Ag-AgCl electrode is considered to be $\approx 0.23V$ vs the SHE. By using these reference electrodes with known potentials, the potential of reactions and electrode surfaces can be determined.

In cases where current will flow between the electrodes after a potential is applied, a third electrode is required. This is because if large currents are drawn through the reference electrode, its potential will change, thus altering the measurement. In these cases, a three electrode electrochemical cell is used, shown in figure 3.6. These three electrodes are: the working electrode, which is the electrode at which the reaction occurs and the potential is measured; the reference electrode, which is used to produce a stable and measurable reference potential; and the counter electrode, which is often a platinum wire and is solely used as the current source for the reaction. Typical measurement equipment for measuring current and voltage does not allow for a three-electrode system therefore, a device known as a potentiostat must be used.

A potentiostat allows the control and measurement of a three-electrode electrochemical

cell. These devices work through an amplifier circuit which allows the counter electrode to be driven with respect to a reference electrode without any current flow between them, while allowing current to flow between the counter and working electrodes. For both the deposition and electrochemical analysis of the IrO_x layer, a three-electrode system and a potentiostat were required. The potentiostat used for this project was a Biologic SP300.

3.2.2 Cyclic Voltammetry

Cyclic voltammetry (CV) is a common technique for analysing electrochemically active systems [157]. In this technique, the potential voltage of an electrochemical cell is swept between two values at constant rate, while simultaneously measuring the current between the working and counter electrodes. Reversible electrochemical reactions, known as reduction-oxidation (redox) reactions occur at specific potentials defined by the species involved. As shown in figure 3.7a, when the electrode potential equals these redox potentials, electrons are added and removed from the redox-active molecules by the electrode, causing a peak in the measured current.

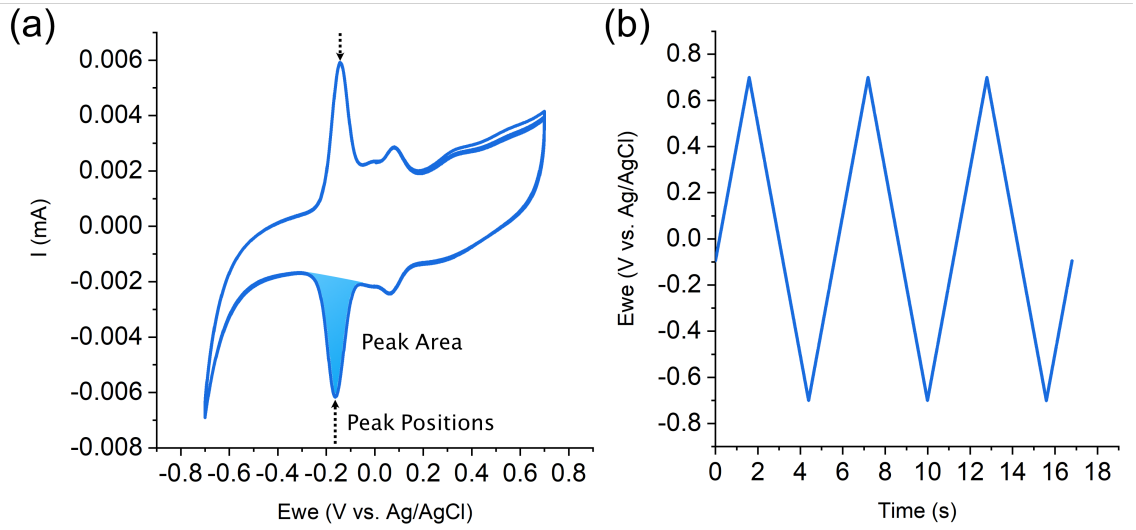

Figure 3.7: **(a)** - Example graph of a CV sweep with the peak positions and the peak area marked. **(b)** - Typical applied potential over time used to perform a CV sweep.

By measuring the voltage of the current peaks, the electroactive species present within a system can be discerned [143]. The area of these peaks indicates the total charge present for each molecule, allowing for calculation of the total number of species present [261]. This technique was used here to determine the number of active iridium oxide species within the electrodeposited layer, thus allowing calculation of the film density.

Cyclic voltammetry is an important and powerful tool for analysing electrochemical systems. For this project, cyclic voltammetry was used primarily for the deposition and analysis of the iridium oxide. It allowed for estimations of the oxidation states as well as the number of iridium oxide molecules, as discussed in chapter 4.

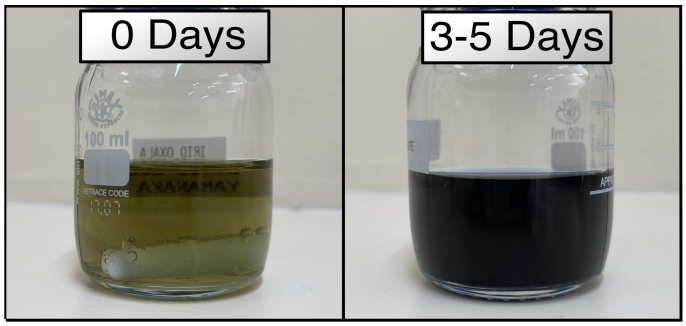

Figure 3.8: Example iridium oxalate solution at the time of production (0 days) and after stabilisation (3-5 days).

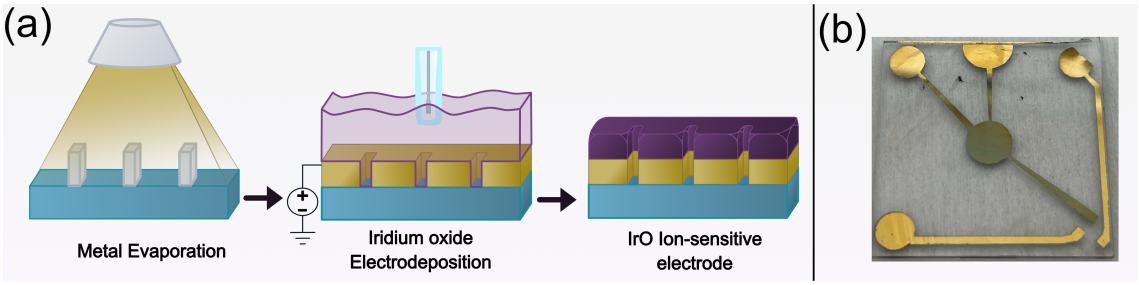

Figure 3.9: **(a)** - Schematic of the iridium oxide depostion process used in this project. **(b)** - Example of an IrO_x coated Au sensor made using a a potential cycling method.

3.2.3 Electrodeposition of Iridium Oxide

Electrodeposition was used to fabricate the iridium-oxide EGFET ion-sensitive electrode. Here, electrodeposition involves electrically reducing IrO_x complexes from solution, causing them to deposit onto an electrode surface. The chemical mechanism through which iridium oxide can be electrodeposited from solution is described in chapter 2.

The oxidised Iridium oxide was prepared in solution in the form of iridium oxalate, using the well reported method described by K. Yamanaka [233, 262]. Preparation of the iridium oxalate solution was as such: A 4.5 mM solution of Iridium(IV) Chloride hydrate (Alfa Aesar) was prepared in Milli-Q deionised water (75 mg in 50 mL) and stirred for 10 min; 0.5 mL of hydrogen peroxide (30 % w/w) (Sigma-Aldrich) was added to the solution and stirred for a further 10 min; 500 g oxalic acid dihydrate (Sigma-Aldrich) was added and stirred for another 10 min; finally, potassium carbonate (Sigma-Aldrich) was slowly added whilst stirring until the solution reached a pH of 10.5. This resulted in a yellowy-green solution which turned purple after two to three days, as shown in figure 3.8. Once this colour change had occurred, the solution was used to fabricate electrodes.

Electrodeposition was carried out using a potential cycling method described by P. Steegstra et al. [263], adapted from work by H. Elsen et al. [237]. This method was chosen as it was shown to improve both the reproducibility of the iridium oxide electrodes and increase their durability. Samples were submerged in the iridium oxalate solution and potentially cycled between $-500\ mV$ and $650\ mV$ at a rate of $1\ V/s$, for 600 cycles. The electrodes produced were lustrous and green/blue in colour (Figure 3.9). A schematic diagram of the iridium oxide electrode fabrication process is shown in figure 3.9a.

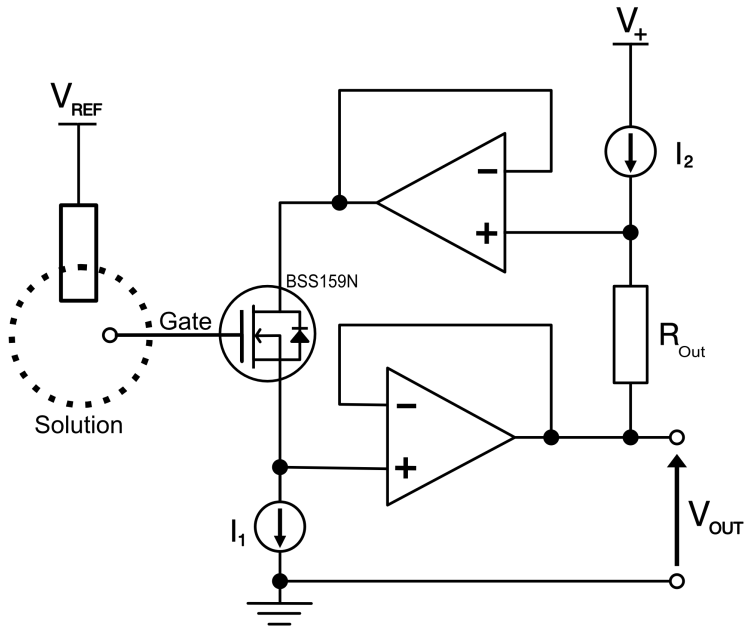

Figure 3.10: Schematic diagram of the source-drain follower readout circuit used to measure potential changes in the ion-sensitive electrode. Key components have been labelled.

Following deposition of the iridium oxide, the electrodes were stored in pH 7 potassium phosphate buffer, as this has been shown to prolong the lifespan of iridium oxide based pH sensors [264].

3.3 Characterisation of the pH Sensitive Properties of the Developed EGFET

As mentioned in chapter 2, the pH sensing device chosen for this project was the discrete Extended-Gate ISFET (EGFET). This section will discuss the circuitry and set-up used to read the output of the fabricated devices and determine their response to changes in pH.

3.3.1 Discrete EGFET Readout Circuit

The circuit chosen for the readout of the discrete EGFET device was based on a source-drain follower design, used for many ISFET and EGFET devices [172, 192, 265–267]. With the reference electrode held at a constant potential, any change in the gate voltage due to changes in chemical potential, can be seen at the output of the circuit (shown in figure 3.10). The voltage-matching of the gate voltage to the output primarily occurs because of the fixed current flowing through the transistor, controlled by I_2. By fixing the current through the triode-region-biased transistor, any change in gate voltage linearly relates to a change in the resistance between the source and drain. To accommodate for this change in resistance, the voltage at the point between the source terminal and current sink also changes, giving the circuit its gate-voltage dependant output. With these components, the

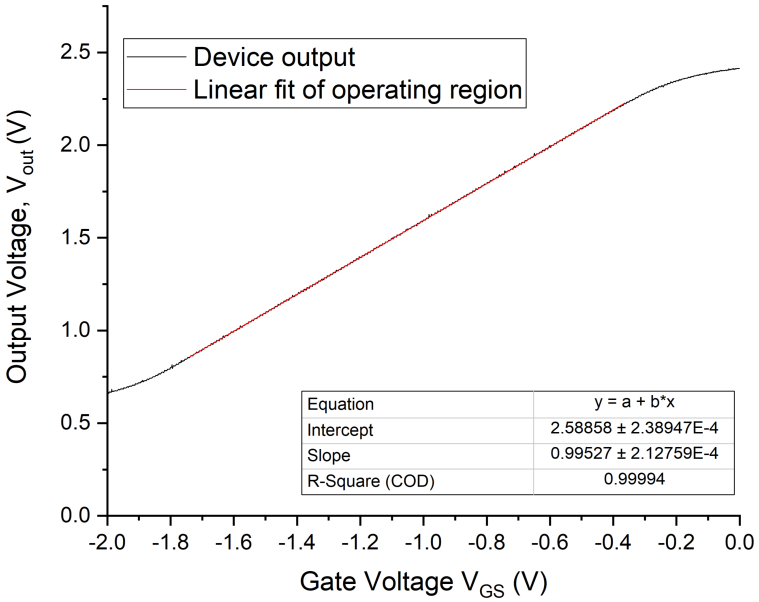

Figure 3.11: Example output of the source-drain follower circuit used for the EGFET readout. As the gate electrode voltage is swept, the output voltage of the circuit responds linearly with a slope of 0.995 ± 2.14E-4 ($R^2 = 0.99$). The fitted line (Red trace) was calculated by fitting a linear function using a Linear regression algorithm (Origin Pro 2018)

gate-voltage to output can be read, but do not allow for biasing the source-drain voltage, necessary for ensuring the transistor stays in the triode region. The source-drain biasing is achieved through the two op-amps, both in a voltage follower configuration, the second current source (I_1), and the resistor (R_{Out}). By fixing the current through the resistor, a fixed potential is developed. The two op-amps ensure that the voltage across this resistor is matched to the transistor, which will still shift its source terminal voltage with the gate voltage, but the drain voltage now accommodates this change by increasing or decreasing by the same amount. An example output of this circuit is shown in figure 3.11. This circuit allows for complete isolation of the input and output due to the high-impedance of the op-amps. This allows the output to be connected directly to an external ADC without altering the transistor biasing. The readout and control circuitry were constructed on a custom PCB designed using EAGLE (AutoDesk). As the transistor is susceptible to damage from external voltages (e.g., a misconnection with the reference electrode), this was placed on a separate, removable, PCB which connected to the primary control PCB. By doing this, any damaged transistors could be replaced easily without the need for new control and readout components.

For this project, a depletion-mode, N-type, BSS195N transistor was chosen as the MOSFET component for the EGFET, due to its low cost, low leakage current, and previous usage in EGFET devices [190][268]. Biasing of the MOSFET by the gate electrode was performed by applying a fixed potential to a reference electrode in solution with the extended ion-sensitive sensing electrode, which, in turn, was connected to the BSS159N gate terminal.

The circuitry was powered using a GW Instek GPS-4303 power supply, which allowed

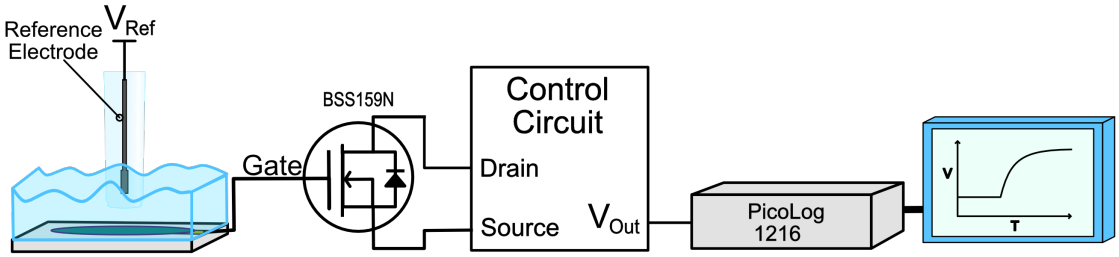

Figure 3.12: Diagram of the complete system used to measure changes in pH. Changes in solution pH result in changes in the ouput voltage of the control circuit. These changes are then read using a PicoLog 1216.

multiple channels for both positive and negative voltages. When testing the bias point of the MOSFET, the reference-electrode voltage was swept between 0 to -3 V. This allowed the bias to be set in the middle of the triode region, maximising the pH range that could be measured. Reference electrode sweeps were performed using a Keithley 2400 Sourcemeter. The output of the device was recorded using a PicoLog 1216 12-bit DAQ (Pico Technology). The complete system is shown in figure 3.12.

3.3.2 Fluidic Manifold Design

A fluidic device was designed and constructed to deliver samples to the sensor surface while maintaining electrical connection between sensing and reference electrodes. This device was designed so that liquid could be injected into a chamber using a standard, male-luer, syringe. The fluidic device was a pressure-sealed, completely 3D printed design. Initially, the device was designed to contain a PDMS gasket as the channel (Figure 3.13). However, the gasket used in this design only allowed for large volumes to be passed through the device, leading to issues with sample mixing and fluid flow out of the device.

In order to mitigate these issued, a device was designed with a microchannel instead of a gasket. The channel dimensions were $1 \times 7 \times 0.1$ mm, equivalent to a total channel volume $\approx 0.7\mu L$. To allow a high-pressure seal around the channel without breaking the sensing electrode, several rubber O-rings were included underneath the sensor. To ensure pressure was being applied uniformly and in the correct areas, the central O-ring was raised slightly, increasing the pressure around the microchannel. Connection between the sensing pad and the MOSFET gate was achieved using a spring-loaded contact pin. The fluidic manifold is shown in figure 3.14.

The initial design incorporated the reference electrode into the fluidic chamber; however, this proved to be problematic, as the point around the reference electrode trapped air bubbles, leading to an unreliable connection. To solve this, the reference electrode was placed in the waste reservoir, connected by microfluidic tubing. To ensure there was a good connection between the reference electrode and the device, the solution being measured had to be suitably conductive; therefore, 100 mM potassium sulfate (K_2SO_4) was added to the measured solution.

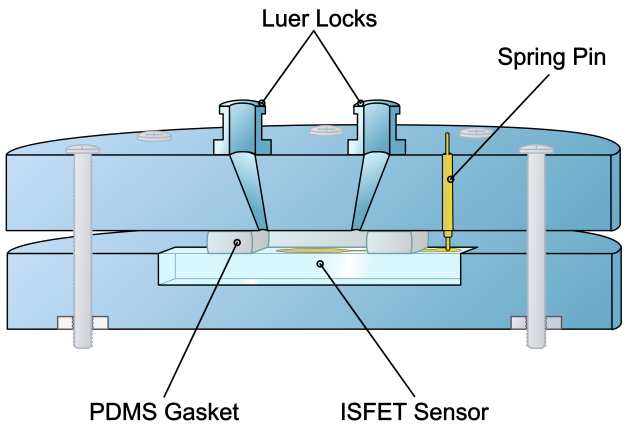

Figure 3.13: Schematic diagram of the PDMS-gasket fluidic manifold used at the beginning of this project. Key components have been labelled.

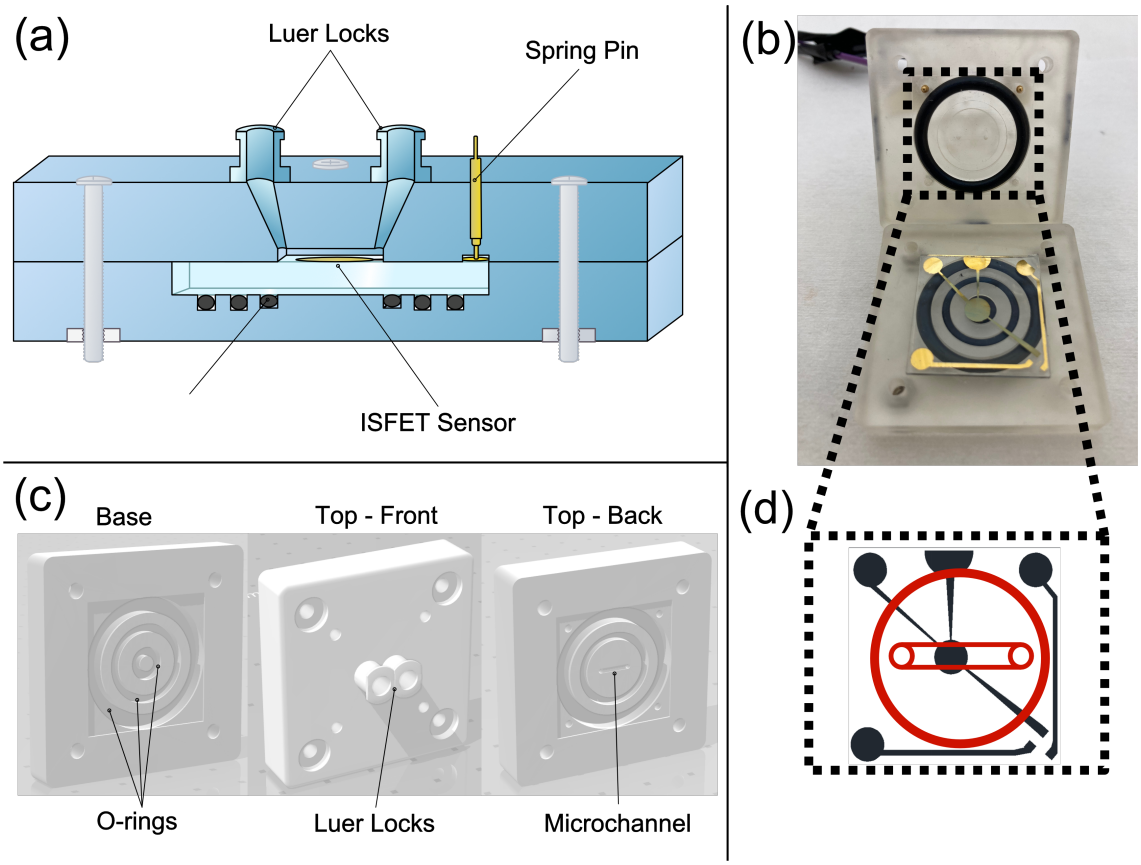

Figure 3.14: **(a)** - Schematic diagram of the fluidic manifold used for this project. Key components have been labelled. **(b)** - Image of the 3D-printed fluidic manifold used for this project. **(c)** - 3D CAD diagram of the fluidic manifold used for this project. Key components have been labelled. **(d)** - Schematic map of the microchannel above the sensing electrode.

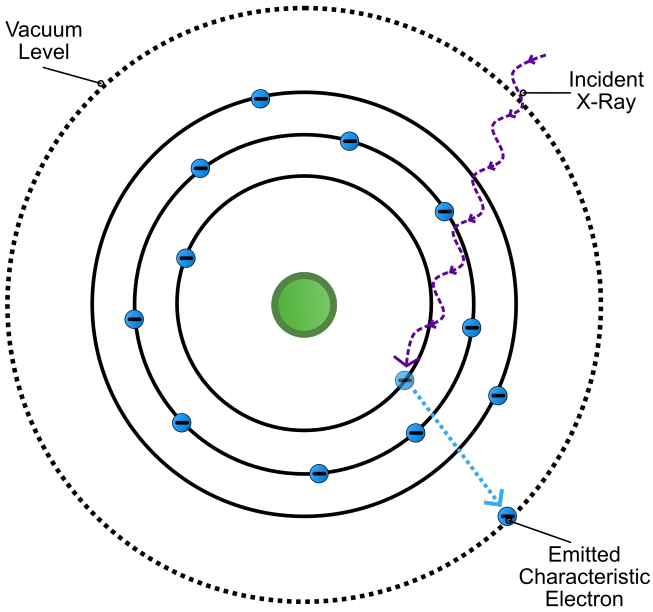

Figure 3.15: Diagram of the photoelectric process used for XPS analysis. Incident X-rays are absorbed by the core electrons causing them to be emitted with an energy characteristic of their position within the atom.

3.4 Characterisation of the Iridium Oxide Surface

Various analytical techniques were used throughout this project to analyse the iridium oxide surface. This section will discuss the operation and theory of these techniques, as well as their application within this project.

3.4.1 X-Ray Photoelectron Spectroscopy

X-Ray Photoelectron Spectroscopy (XPS) was used to analyse the surface composition of iridium oxide oxidation states, as well as the level of hydration in the layer. Based on the photoelectric effect, XPS uses X-rays to eject core electrons from a sample [269] (Figure 3.15). The energy of these ejected electrons is heavily dependent on the material from which they were ejected due to the quantised states in which electrons sit. The kinetic energy of the ejected electrons is measured using an electron energy analyser [269]. By counting the number of electrons of particular energies, the elemental composition of the material can be determined. Emitted electrons are typically notated by the orbital from which they were emitted (3f, 1s, 4p etc.). For orbitals other than s orbitals, the spin angular momentum of the electrons leads to a splitting of the observed electron energy. The notation of these energies is described by a subscript noting the j value of the electron, where j is the summation of the angular momentum quantum number and the spin angular momentum number [270]. The energy resolution of this technique is system dependant, however, high-resolution XPS systems allow for the determination of oxidation states within materials [271].

Although XPS allows for high resolution analysis of material composition, some considerations have to be taken. As this technique requires high energy x-rays, and the removal

of electrons from the sample, it is a destructive method, meaning analysis of thin films and surface chemistries can only be carried out once per sample. Also, due to the scattering of the emitted electrons, this technique only probes a short distance into a sample (1-10 nm), making it perfect for surface analysis, but less suitable for analysing the entire composition of films. For analysis of bulk composition, techniques such as Energy-Dispersive X-Ray Spectroscopy (EDX) must be used, which will be discussed in the following section.

All XPS measurements and fitting of spectra was carried out by Dr. Ben Coulson using a bespoke XPS system maintained by the Andy Pratt group at the University of York.

3.4.2 Energy-Dispersive X-Ray Spectroscopy

Energy-Dispersive X-ray Spectroscopy (EDX) was used in this project to analyse the composition of iridium oxide. Similar to XPS, EDX uses X-rays to determine the composition of materials; however, in the case of EDX, electrons are focussed onto a sample and the emitted X-rays are measured. Often performed on an electron microscope, EDX uses the electrons from the primary electron beam to excite electrons within the sample material. A collision between an electron within the electron beam and an inner shell electron of the atoms within the sample, can result in excitation of the substrate electrons to a higher energy state, leaving behind a low-energy vacancy. Electrons from the higher-energy states are then able to lose energy to fill these vacated states. As energy must be conserved, the energy lost through this process is emitted as an X-ray photon whose wavelength is characteristic of the material it was emitted from. The emitted X-rays are then detected using an X-ray spectrophotometer, allowing for quantification of the emitted wavelengths, and thus characterisation of the material. This process is demonstrated in figure 3.16.

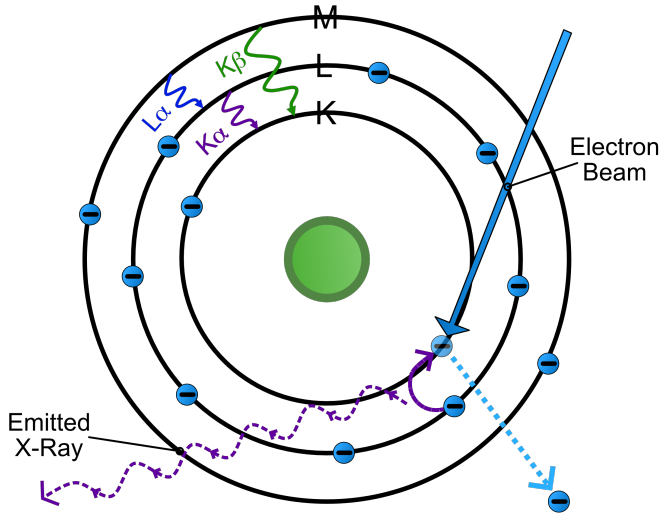

Figure 3.16: Diagram of the X-ray emission process used for EDX analysis. Incident electrons excite core electrons to a higher energy state. The relaxation of this process causes energy to be emitted in the form of a characteristic X-ray. Adapted from [272] under the Creative Commons License

Due to the number of electrons within a material's electron shells, X-rays of multiple energies that can be emitted. These X-rays are often referred to using the Siegbahn notation, a nomenclature which describes both the energy level from which the electron was excited and the level from which the X-ray was emitted [273]. If a single atom is considered, electrons around the atom exist in quantised shells, where the number of electrons that can occupy those shells follow a $2N^2$ rule (i.e., the first shell contains 2 electrons, the second 8, the third 18, etc.). The inner-most shell is referred to as the K shell, and the subsequent shells are known as the L, M, N, O, P, and Q shells. All shells, apart from the K shell, are split into sub-shells, where the energies between these sub-shells differ slightly. EDX focusses mainly on the K, L, and M shells, as the majority of X-rays are emitted following transitions between these shells. Siegbahn notation is used in this project and names the emitted X-ray as such: the element, followed by the shell from which the electron was excited, followed by either α, β or γ, denoting the strength of the emitted X-ray (shown in figure 3.16). For example, the strongest emission from an electron excited from the K shell in a silicon substrate is written as: $Si\ K_\alpha$.

As the emitted X-rays are able to penetrate back through the material, the measurement depth of EDX is much larger than XPS. The measurement depth of EDX is approximately equal to the penetration depth of the incident electrons, which is given by [274–276]:

$$R = 0.0276 \frac{A E_0^n}{\rho Z^{0.89}} \tag{3.3}$$

where: R is the penetration depth in μm; A is the atomic weight of the measured material; n is a beam-energy constant, often chosen to be 1.35 for low-energy beams ($< 5KeV$) or 1.67 for high-energy beams ($> 5KeV$); E_0 is the beam energy in KeV; Z is the atomic number of the measured material; and ρ is the material density. This usually equates to between 1-10 μm, significantly larger than the depth measured by XPS.

EDX does have limitations, however. As the technique relies on the de-excitation of electrons from outer electron shells, lighter elements with fewer shells are not able to be detected. Furthermore, many elements have similar energy gaps between their core electron shells, leading to similarities in the emitted X-rays. This similarity in energies often means that characteristic peaks overlap and are sometimes masked. EDX was performed using a JEOL 7800F Prime SEM microscope and analysis was carried out using AZtec EDS analysis software (Oxford Instruments).

3.4.3 X-ray Diffraction

X-ray diffraction (XRD) was used in this project to analyse the crystallinity of the electrodeposited iridium oxide film. Many solid materials exist as an ordered, three-dimensional, repeating structure of atoms, where the smallest unit of this repeating structure is referred to as a unit cell (Figure 3.17). These unit cells define the atomic positions within a crystal structure of a solid material and can exist as a variety of complex structures [277].

X-ray diffraction allows the observation of these crystal structures through the use of

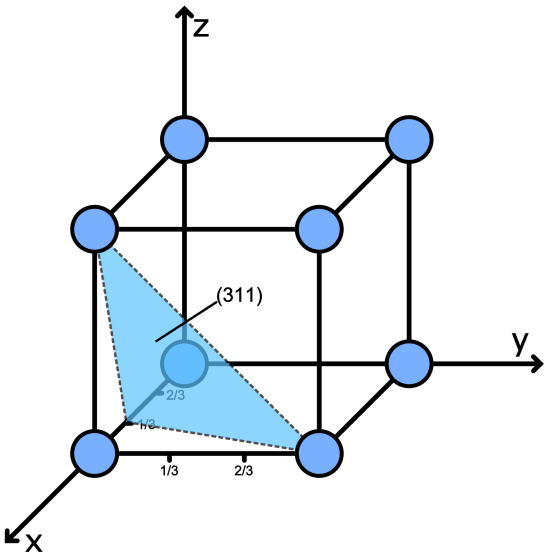

Figure 3.17: Diagram of a simple cubic crystal structure. The highlighted plane indicates a possible diffraction plane with a miller indices of (311).

constructive and destructive interference patterns produced by X-rays as a result of the inter-atomic distance. In this technique, X-rays are shone at a sample at an angle θ and reflected back towards a detector. As shown in figure 3.18, the wavelength of an X-ray is within the order of the inter-atomic distance, d. At particular angles, the incident X-rays reflected off the individual atoms constructively interfere, producing a peak in signal intensity. For this to occur, the inter-atomic distance must agree with Bragg's law, which states that constructive interference only occurs when [277]:

$$n\lambda = 2d\sin\theta \tag{3.4}$$

where λ is the wavelength of the incident X-ray; d is the inter-atomic distance; θ is the incident angle of the X-ray. Thus, constructive interference is heavily dependent on the incident angle. By moving the X-ray source and detector with respect to the substrate, an interference pattern for the substrate can be constructed. If the analysed sample is amorphous in nature, meaning it has no real periodicity in its atomic structure, then no constructive interference will occur.

Given the periodicity in multiple directions through the unit cell, many constructive reflections can exist for a single material dependant on the direction with which they are observed. Typically, these directional reflections are notated by the Miller indices from which they were observed. This notation system uses the reciprocal of the fractional intercepts of the unit cell axes to determine a lattice plane within the cell. For example, the plane demonstrated in 3.17 would be notated as a (311) plane as the plane intersects the X axis at 1/3 of the unit length, and extends the unit length of both the Y and Z axes, thus ($\frac{1}{3}$,1,1) would give a miller indices plane of (311). This notation is used in this work to describe the observed XRD reflections.

Due to the differences in the inter-atomic distances between different materials, the

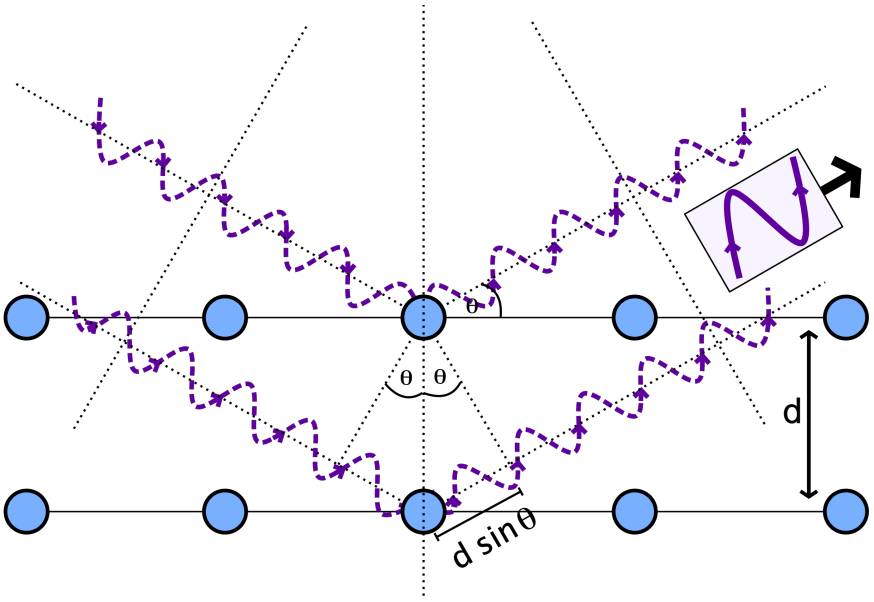

Figure 3.18: Diagram of the X-ray diffraction process used for XRD analysis. Incident X-rays are scattered off the atoms within the material. At particular incident angles, dependant on the inter-atomic distance, the incident X-rays constructively interfere. Adapted from [278] and [279] under the Creative Commons License

observed diffraction patterns from this technique are specific to a particular material, making it possible to characterise which crystal structures are present as well as the material from which they originate. Often these material diffraction patterns are described within databases containing patterns for a number of materials. The database used for this work was the Crystallography Open Database [280–286]. The XRD used for this project was a Rigaku SmartLab and XRD analysis was performed using 'Match!' (Crystal Impact) XRD analysis software.

3.5 Characterisation of the Surface-bindable β-lactam

Following the development and testing of the EGFET device for detecting β-lactamase activity, research focussed on a surface-bindable β-lactam with the hope that it would improve the detection limit and sensitivity of the developed assay. This section discusses the techniques used to analyse and test this surface-bindable β-lactam.

3.5.1 Infrared Spectroscopy

Infrared-spectroscopy (IR-spectroscopy) is an analytical technique which uses infrared light to measure the presence of particular molecules and molecular bonds within a substance.

Infrared spectroscopy relies on the fact that molecules have various degrees of freedom. A molecule containing N atoms has $3N$ degrees of freedom due to the multiple ways in which the atoms can move. These degrees of freedom can be split into three categories, translational, rotational, and vibrational [287]. For all molecules, three of the $3N$ degrees are translational, in which the molecule moves through the X, Y or Z plane. The number

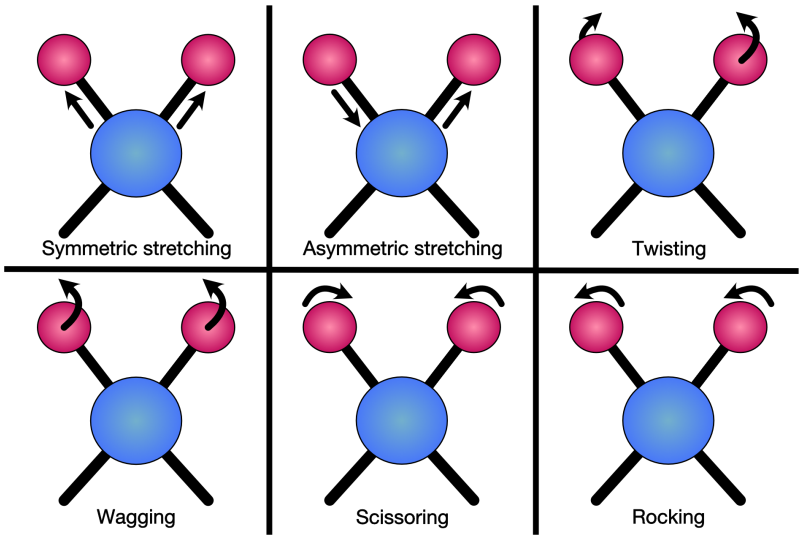

Figure 3.19: Diagram of the eight potential vibrational modes experienced by molecules. Adapted from [288] under the Creative Commons License.

of rotational degrees depends on the structure of the molecule. For linear molecules, where the atoms align in a straight line, there are only two rotational degrees of freedom, as rotation in the plane along the molecule does not move the atoms in any way. For non-linear molecules, there are three rotational degrees of freedom (X, Y, and Z). The remaining degrees of freedom ($3N - 5$ for linear, $3N - 6$ for non-linear) are known as vibrational modes and are due to the molecular bonds. These bonds behave as springs between the atoms and are able to stretch and bend to varying degrees determined by the atoms involved.

There are six ways in which bonds can vibrate: symmetric stretch, asymmetric stretch, twisting, wagging, scissoring, and rocking. All of these vibrational modes are demonstrated in figure 3.19. These bonds oscillate with a fixed energy and frequency depending on the type of bond and the atoms present. These vibrational modes can be excited by absorbing infrared light energy. Just as the energy of associated electrons is quantised, the energy with which these bonds vibrate is also quantised [287]. If broad-spectrum infrared-light is shone at a molecule, the waves with frequencies corresponding to the vibrational modes excite the molecule's bonds to a higher vibrational energy state, absorbing the infrared wave. The molecule's excited state does not remain for a long time, however, and is released as heat, returning it to its vibrational ground state. It should be noted that not all vibrational modes are able to absorb infrared light. For this to occur, the vibrational mode must result in a periodic change in the dipole moment of the molecule, as the process through which infrared light is absorbed is by inducing a change in this moment [289].

IR-spectroscopy works by shining IR light at a sample and detecting which wavelengths are transmitted and which are absorbed. Often this is plotted as transmittance (or absorbance) against wavenumber (the reciprocal of the wavelength in cm). The wavenumber is used here instead of frequency to reduce the magnitude of the numbers. By measuring the peak position of the absorbed wavelengths, specific molecular bonds and, thus, specific functional groups can be discerned.

Fourier Transform IR-Spectroscopy

When IR-spectrometers were originally designed, they were primarily dispersive spectrometers [290]. This class of spectrometer relies on a dispersive grating after the sample to split the broad-spectrum IR-light, spatially [291]. This spatially-dispersed light is then shone through a slit, leaving behind only a narrow band of IR-light. The grating was then moved, so that a different band is detected, repeating the process until the entire spectrum has been detected. Dispersive spectrometers have two main disadvantages: they are relatively slow, as they have to scan through the spectrum and their resolution is heavily dependent on the equipment. Interferometric spectrometers remove the need for the dispersive grating and have a much higher resolution.

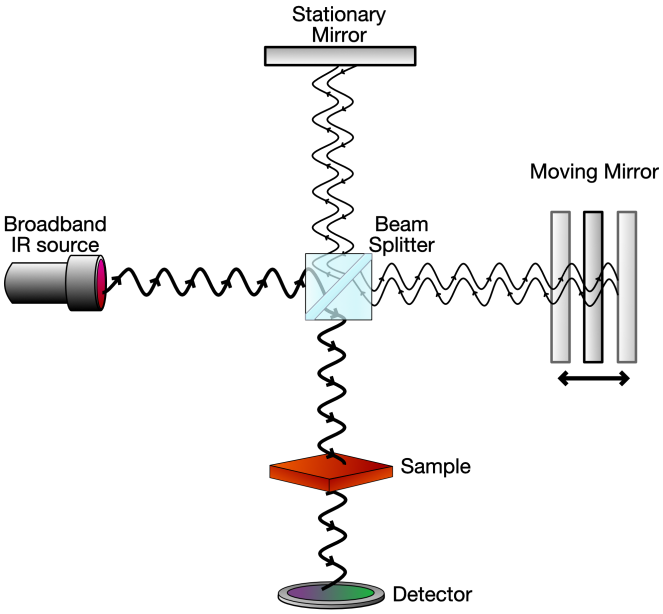

Figure 3.20: Schematic of an FTIR interferometer with the key components labelled. Adapted from [292] under the Creative Commons License.

Fourier-Transform IR-spectroscopy (FT-IR) spectrometers are an example of interferometric spectrometers. These devices use a Michelson interferometer, which operate as follows [269][293](shown in figure 3.20). Broad-band IR light is shone at a beam-splitter, which divides the light into two parts of equal intensity. One part is reflected from a moving mirror, the other is reflected off a fixed mirror. By moving the first mirror, the phase of the two reflected signals is changed, thus creating interference of the two beams, where some wavelengths will interfere constructively, others destructively. This interference signal is then passed through the sample, where the IR-active modes of the molecules absorb some wavelengths, and subsequently onto a detector. By moving the first mirror at a constant rate, and at such a maximum displacement that the entire spectrum of IR light is covered, an interference pattern containing a sum of all IR wavelengths is created. If the Fourier transform of this detector-voltage against mirror-position graph is taken, this will describe the frequency response of the sample to IR light. This technique is much faster than dispersive IR techniques, as the movement of the mirror is negligible compared to that of dispersive gratings. FT-IR also allows for much higher resolution of IR-spectra,

as dispersive IR is dependant on the size of the slit used to filter light.

FT-IR was used as the primary method for IR-spectroscopy in this project. The device used was a Bruker Vertex 70, which allows modular additions to the beam path, enabling different FT-IR techniques to be used. Traditional FT-IR does not easily allow for measurements of surface-bound molecules. For this, an additional technique was used known as Polarisation Modulation Infrared Reflection Adsorption Spectroscopy (PM-IRRAS).

Polarisation Modulation IR Reflection Absorption Spectroscopy

Polarisation Modulation Infrared Reflection Adsorption Spectroscopy (PM-IRRAS) is an IR-spectroscopy technique which allows the detection of IR-spectra from molecules on the surface of substrates. For a molecule adsorbed or bound to a surface to give an IR-signal, its induced dipole moment must have some component which is perpendicular to the surface. This is because any component that is parallel will induce an opposing dipole within the material [294]. By shining p-polarised (perpendicular to the sample) IR light at a grazing angle to a surface, dipoles associated with molecules adsorbed in the surface can align with this light, thus giving an IR signal. Typically, the signal of the IR spectra would be very weak, due to the strongly absorbing bands caused by water molecules present in the air [295–297]. Due to the aforementioned relationship between the IR-absorption and the dipole orientation, S-polarised light (parallel to the surface) is not absorbed by the IR-active surface-bound molecules, but still interacts with the absorbing water vapour. PM-IRRAS uses this S-polarised signal to remove the background absorption. This technique allows for highly sensitive measurements of surface-bound layers.

The device used to carry out PM-IRRAS of the sample surfaces was a Bruker PMA 50, an additional module for the Vertex 70. All PM-IRRAS measurements were carried out on $20 \times 30\ mm$ Au samples on Si substrate.

3.5.2 Quartz Crystal Microbalance with Dissipation

Quartz-Crystal Microbalance with Dissipation monitoring (QCM-D) was used throughout this project to characterise the surface-chemistries. QCM-D utilises the piezoelectric nature of quartz crystals to enable highly sensitive measurements of surface-bound molecules. When a voltage is applied to a quartz crystal, it oscillates at a specific frequency. Any change in mass at the surface of this crystal will result in a change in resonant frequency. The concept has various uses and has been used in measuring film thickness for thin-film deposition techniques for many years. QCM-D combines this standard quartz crystal sensor with fluidics, allowing measurements in liquid media, which is necessary for biological, and many surface-chemistry, measurements. The high sensitivity of the change in frequency allows for accurate and precise measurements of mass changes in the order of ng/cm^2. A diagram of this operation is shown in figure 3.21.

By periodically disabling the driving voltage to the crystal sensor, and measuring the rate of decay of the oscillation, the instrument is also able to measure the energy dissipated by the oscillating crystal. The dissipation, D, is a variable which is inversely proportional

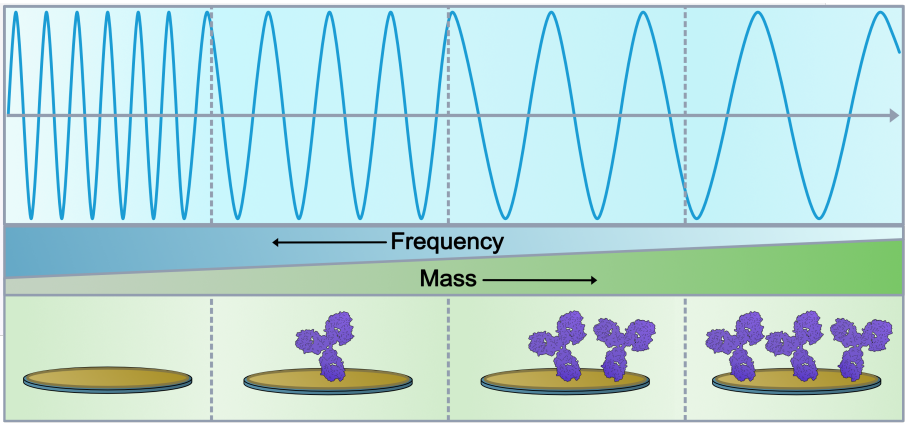

Figure 3.21: Diagram demonstrating the frequency response of a QCM-D to increasing surface-bound mass. As the mass increases, the resonant frequency decreases.

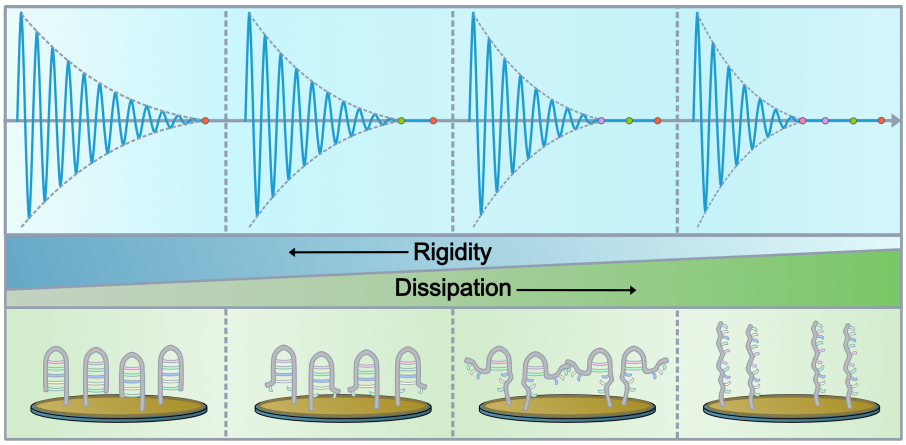

Figure 3.22: Diagram demonstrating the dissipation response of a QCM-D to decreasing rigidity of surface-bound molecules. As the rigidity decreases, the measured dissipation increases.

to the decay time of the crystal, τ, given by [298]:

$$D = \frac{1}{\pi f \tau} \tag{3.5}$$

where f is the resonant frequency of the crystal. This measurement describes the flexibility and interaction of the sensor surface and surface-bound molecules with the surrounding solution. The faster the decay of the oscillation, the higher the dissipation. A good example of this is conformational changes of DNA. Although no mass change occurs, the opening of DNA loops causes them to become more flexible, leading to higher interaction with the surrounding solution and causing a higher dissipation, as shown in figure 3.22.

As well as measuring the fundamental frequency of the quartz disk, the instrument also allows for simultaneous measurements of the various harmonic overtones. Each one of these overtones responds differently to a layer of soft material, due to the penetration depth into the media [299]. Lower frequencies probe further into the surface-bound layer and are thus dampened to a greater extent. By measuring these overtones, more information about the structure of the molecular layer can be inferred.

By measuring changes in both the frequency and dissipation, quantification of the

surface concentration of proteins and other molecules can be carried out, allowing insight into the binding kinetics and structural changes at the surface. Quantification of mass gain in relation to frequency measurements is often done using a number of models, each with varying complexity. The most commonly used model is the Sauerbrey model [300]:

$$\Delta f = -\frac{2f_0^2}{A\sqrt{\mu_q \rho_q}} \Delta m n \tag{3.6}$$

where Δf is the change in frequency due to added mass; f_0 is the fundamental frequency of the quartz sensor; A is the active crystal area between electrodes; ρ_q is the density of the quartz; μ_q is the shear modulus for quartz; Δm is the change in mass; and n is the overtone number of the measured frequency with respect to the fundamental frequency. Given that most of these are constant, equation 3.6 is often simplified to:

$$\Delta m = \frac{\Delta f}{n} \times 17.7 \; ng/cm^2 \tag{3.7}$$

allowing for simple calculations of mass in terms of frequency change. This model works well for thin, rigid layers, such as those gained from thin-film deposition techniques. However, due to additional frequency dampening caused by the innate viscoelasticity of liquid media and biological samples, it only gives an estimation for layers which are not thin and rigid.

As a rule-of-thumb, if a divergence of the overtones, and large changes in the measured dissipation are seen, the Sauerbrey model will underestimate the calculated mass. For these cases, viscoelastic models are often used instead. Many viscoelastic models exist [301]; however, the most commonly used is the Kevin-Voigt model [298, 302], which allows calculation of the density and thickness of an adsorbed layer. For this project, however, quantitative analysis was not necessary. Therefore, the Sauerbrey model was used purely as an estimation, with the caveat that this could be lower than the true value.

The instrument used for this project was a Q-Sense E4 system from Biolin Scientific. All QCM-D experiments were prepared by following the same cleaning and installation protocol. QCM-D sensors were cleaned using the UV O-zone protocol described in section 3.1.1. Cleaned sensors were then functionalised according to the type of surface employed, as discussed in chapter 6.

Following formation of the functionalised surfaces, each sensor was then installed into the flow modules of the Q-sense E4 system. Each chamber was filled with Milli-Q ultrapure water at a flow rate of 100 μL/min, controlled by a 4-channel peristaltic pump. To achieve a stable baseline, the running buffer was left to flow through the modules at 20 μL/min for 60-80 min, or until the drift in frequency was ± 1 Hz over 10 min. For all experiments, the temperature of the modules was kept at 37 °C (standard deviation 5×10^{-3} °C) and the flow rate was kept constant at 20 μL/min. Buffer was allowed to flow over the sensor surface between sample injections until a stable level was as achieved, corresponding to a drift in frequency ± 1 Hz over 10 min.

Chapter 4

Development of an Iridium Oxide Extended-Gate ISFET

4.1 Introduction

As discussed in chapter 2, one of the most common forms of antibiotic resistance is to β-lactam-based antibiotics mediated through the production of β-lactamase enzymes which hydrolyse the β-lactam structure. This reaction results in a change of the β-lactams pK_a, causing the molecule to become more acidic. Many of the methods used to determine β-lactam resistance do not utilise this phenomenon, relying on growth-based assays, which can take several days to produce results. Methods that quantify acidification of the β-lactam as a proxy for resistance, however, are much faster but often utilise colorimetric compounds to determine a pH change, requiring specialist equipment to gain quantitative information. By directly measuring the pH change over time, it would be possible not only to determine the presence of β-lactam resistance, but potentially also the level of resistance, allowing a more tailored approach to prescribing behaviour.

As the enzymatic activity of the β-lactamase is related to the rate of change in pH over time, the device used for pH change detection would require both a high sensitivity to pH and a fast time response to changes in pH. Because of these reasons, an ion-sensitive field-effect-transistor (ISFET) was chosen as the pH meter for this project. These devices have been shown to have high sensitivity as well as a quick response time compared to traditional glass electrode pH meters [268, 303].

As discussed in chapter 2, the discrete component extended-gate ISFET (EGFET) is a low-cost and simple pH sensor based on ISFET technology. EGFETs also have the benefit of allowing simple integration with fluidics, allowing simple transfer of solutions. As the MOSFET is separated from the sensing part of the device, the ion-sensitive electrode can be incorporated into fluidics without the need for specific encapsulation of the connected electronics. For these reasons, an electrodeposited Iridium oxide EGFET was chosen as the device to measure the pH changes in this project.

This chapter will discuss the development and testing of a low-cost, simple to fabricate, EGFET device. It will discuss preparation of the ion-sensitive electrodes, as well as characterisation of the pH sensitivity with respect to the various electrode parameters. Finally, an investigation into the physical and chemical composition of the deposited IrO_x layer is reported.

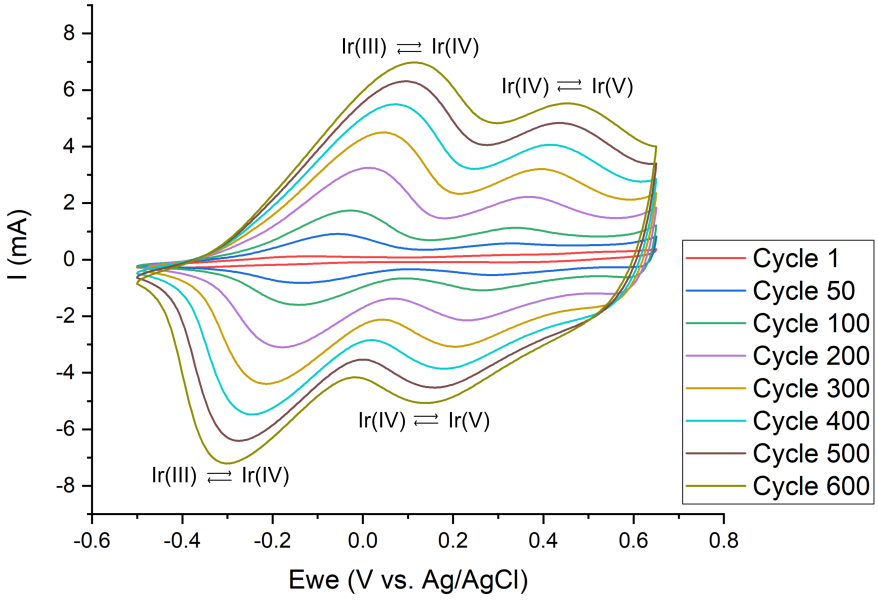

Figure 4.1: Example cyclic voltammetry sweep of IrO_x deposition on Au electrodes from an iridium oxalate solution. The deposition was performed for 600 cycles at 1 V/s using an Ag/AgCl reference electrode. Intermediate cycles are shown to demonstrate the growth of iridium after each potential cycle.

4.2 Ion-sensitive Electrode Preparation

Discrete Extended-Gate ISFETs (EGFETs) are composed of two main parts, a discrete, off-the-shelf, transistor and an ion-sensitive electrode. For this work, a depletion-mode, N-type, BSS195N transistor was chosen as the transistor component, due to its low cost, low leakage current, and previous usage in discrete EGFET devices [190, 191, 268]. The ion-sensitive electrode was a gold (Au) electrode, coated in iridium oxide (IrO_x). IrO_x was chosen as the ion-sensitive layer for the electrode for several reasons. The first is due to its seemingly 'super-Nernstian' response to changes in pH as a result of the oxidation states present in electrodeposited IrO_x [229, 230] (Discussed in more detail in chapter 2). The second is due to the ease with which an IrO_x surface can be produced; IrO_x films can be prepared on conductive electrodes through simple electrodeposition techniques [233]. Electrodeposited Iridium Oxide Films (EIROFs) were prepared using the method described in chapter 3. For this, the fabricated Au electrodes were submerged in an iridium oxalate deposition solution and subject to potential cycling (Figure 4.1).

Initially, EIROFs were produced using a potentiostatic method. However, the films were found to delaminate readily from the gold electrode, making them unsuitable for clamped fluidics (Figure 4.2 (a)). To remedy this, a potential cycling method was used, as described by P. Steegstra et al. [263], adapted from work done by H. Elsen et al. [237], which was shown to improve both reproducibility of EIROFs and increase their durability. Samples were potentially cycled between -500 mV and 650 mV at a rate of 1 V/s, for 600 potential cycles. This produced samples with a much higher stability and was thus used for the majority of this work. Another benefit in using cyclic voltammetry to produce

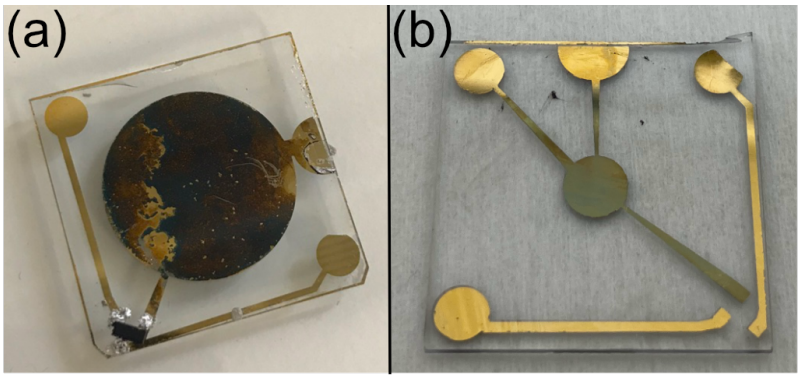

Figure 4.2: **(a)** - Example of delamination occurring on a IrO_x coated Au sensor made using a potentiostatic method. **(b)** - Example of an IrO_x coated Au sensor made using a a potential cycling method.

the EIROF electrodes, is that the IrO_x deposition is able to be tracked over time. As shown in figure 4.1 the total area under the cyclic voltammogram, and thus the amount of redox-active iridium, increases with each cycle. The redox peak pairs, present at ≈ -0.3, 0.1 V and ≈ 0.15, 0.45 V are reported to be transitional peaks between Ir(III), Ir(IV), and Ir(V) [304]. However, it is reported, and was later investigated, that the IrO film primarily exists in both III and IV states, rather than the higher V oxidation state. A deeper investigation into the oxidation states present in the EIROF is described later in this chapter. Samples produced using this method were green/blue in colour and did not appear to delaminate (Figure 4.2 (b)), indicating the successful deposition of a robust IrO_x layer.

4.3 Characterisation of Iridium Oxide EGFET

To determine the suitability of the IrO_x EGFET for measurements of pH and thus, measurements of the β-lactam turnover, the output of the devices were tested in order to determine their sensitivity to pH, time-response to changes in pH, and drift over time.

4.3.1 Device Readout

Devices were measured using the circuitry described in chapter 3 (Figure 4.3a)[172, 192, 265–267]. As shown in figure 4.3b, when the transistor is biased to operate within its triode region, the output of the device correlates linearly to that of the gate electrode, thus:

$$V_{Out} \propto V_{Ref} + V_{Chem} \tag{4.1}$$

where V_{Out} is the output voltage, V_{Ref} is the voltage at the reference electrode, and V_{Chem} is the potential at the ion-sensitive electrode surface due to chemical reactions arising from the pH of the analyte. Assuming a fixed reference voltage, V_{Ref}, then the output voltage, V_{Out}, should only respond to changes in the chemical potential of the iridium-coated ion-sensitive surface, thus:

$$V_{Out} \propto V_{Chem} \tag{4.2}$$

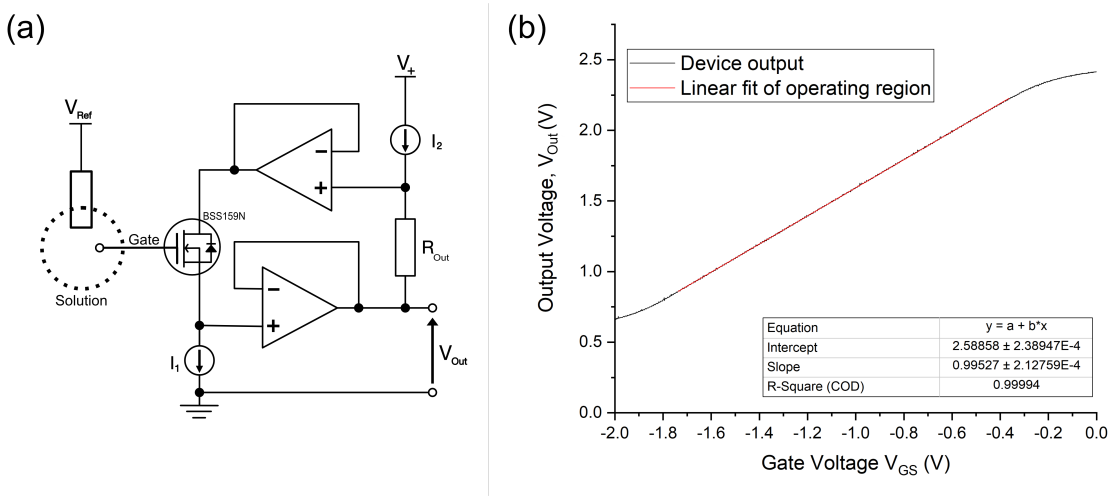

Figure 4.3: (a) - Schematic diagram of the source-drain follower readout circuit used to measure potential changes in the ion-sensitive electrode. The output voltage for the device is measured at V_{Out}.**(b)** - Example output of the control circuitry used for the EGFET readout. As the gate electrode voltage is swept, the output voltage of the circuit responds linearly with a slope of 0.995 ± 2.14E-4 ($R^2 = 0.99$). The fitted line (Red trace) was calculated by fitting a linear function using a linear regression algorithm (Origin Pro 2018)

To allow for the exchange of solutions, without the ion-sensitive IrO_x electrode disconnecting from the reference electrode, devices were tested using the fluidic manifold described in chapter 3.

4.3.2 pH Sensitivity

In order to measure the response of the iridium-oxide based EGFET devices to changes in pH, the output of the device was monitored whilst the sensing electrode was exposed to solutions of different pH that were injected over the sensor surface through the fluidic manifold. 50 mM potassium phosphate buffers (KPi) between pH 6 and pH 8, at 0.5 increments, as well as pH 4 and pH 10 calibration buffers (Thermo Scientific) were used. The pH of all buffers was measured using a glass electrode pH meter and were within ±0.02 of the reported value. A typical response of the EGFET device can be seen in figure 4.4.

These measurements enable a calculation of the pH sensitivity of the device. Figure 4.5 demonstrates the typical relationship of the mean value of the device output to the corresponding pH value. As the potential V_{Chem} is linearly correlated to the pH of the solution, the output of the device should also show a linear relationship to pH. A linear fit of this data showed the expected relationship between pH and device output ($R^2 = 0.994$). From the slope of this fit, the sensitivity of each device can be determined. Approximately 50% of the measured IrO_x EGFET devices showed a pH sensitivity of > 59.2 mV/pH, agreeing with the reported 'super-Nernstian' behaviour of EIROFs.

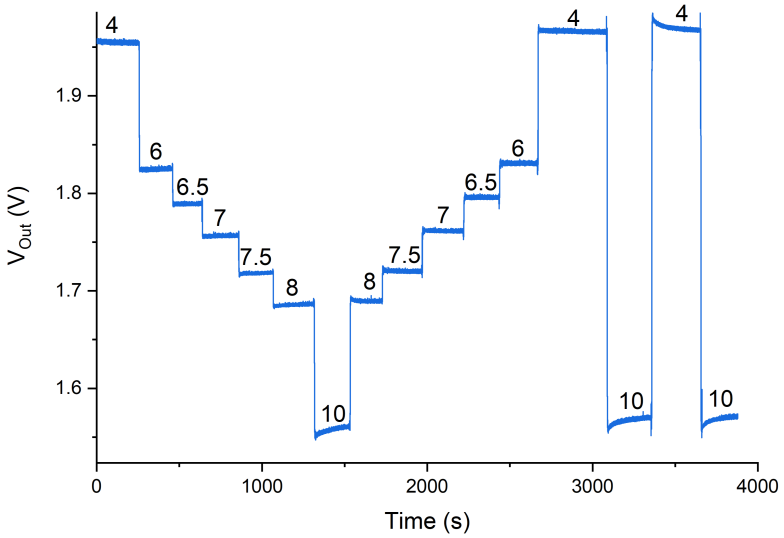

Figure 4.4: Typical output of the developed EGFET device to changes in solution pH. The solution pH was changed every 3 min and is marked above each point.

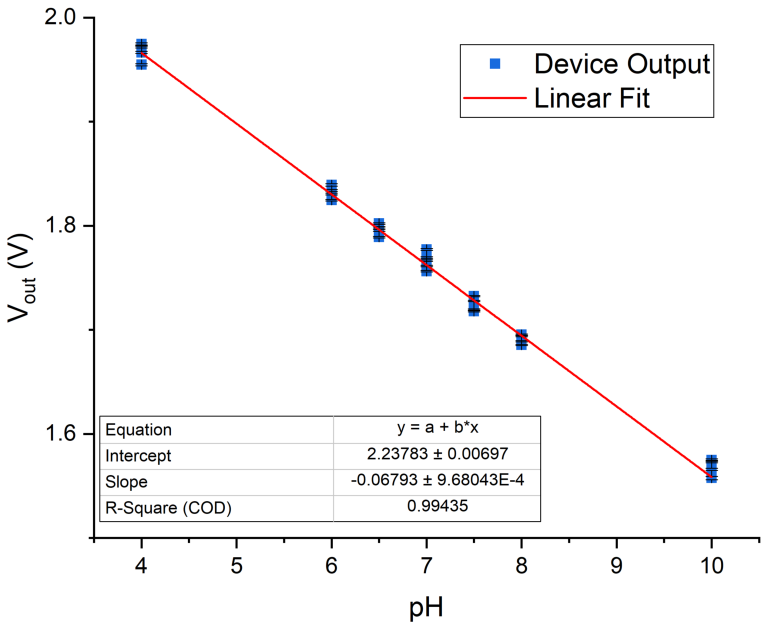

Figure 4.5: Example relationship between the EGFET device output and solution pH. Error is reported as the SD of the calculated mean for the device output at each pH level. The fitted line (Red trace) was calculated by fitting a linear function using a linear regression algorithm (Origin Pro 2018) and the error reported is the SE.

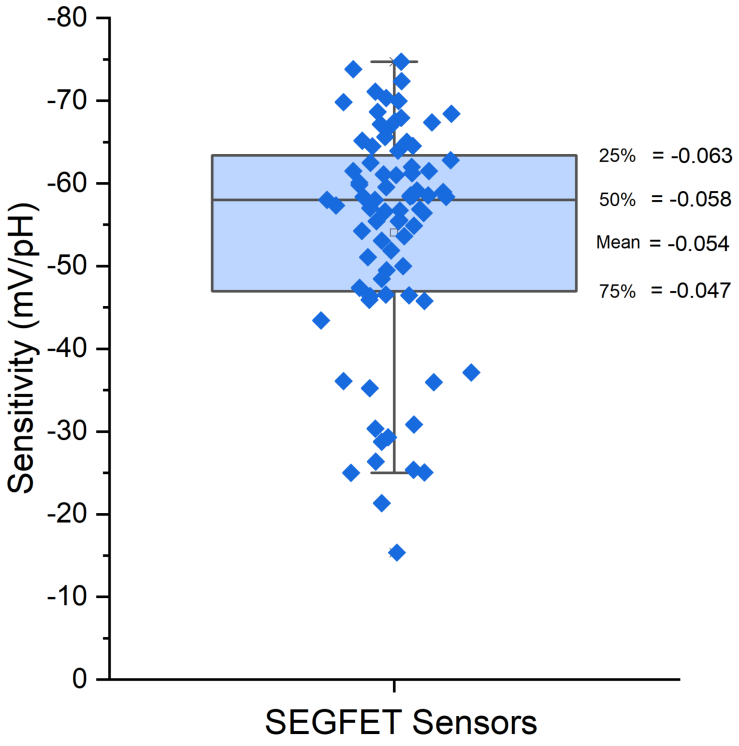

Figure 4.6: Plot demonstrating the variability in pH sensitivity across 80 EGFET sensors. The upper quartile, median, mean, and lower quartile are marked.

Device Variability

It should be noted that, IrO_x pH sensors have been previously reported to show large variability in their pH sensitivity [229]. In this work, a significant variability was seen across the developed EIROF electrodes. Figure 4.6 describes the pH sensitivity across a population of 80, nominally identical devices. As shown, the variability extends from -15 to -74 mV/pH, with a mean value of -54 mV/pH. The majority of sensors showed sensitivity values above -47 mV/pH. Devices which showed a sensitivity within the lower quartile of $<$ -47 mV/pH were not used for biological measurements.

4.3.3 Time Response

Another significant parameter required for detection of β-lactamase activity was the time-response of the EGFET devices. In order to determine kinetic information from the reaction, the device should have a low response time to changes in pH. A lag in its response would mean that the reaction would appear slower than its true value, making quantification difficult. However, as shown in figure 4.7, the time taken for the device to reach the target output voltage after the introduction of a new solution was approximately 2 s. Furthermore, the response time of the EGFET devices was independent of the magnitude of the pH change (Figure 4.7 (b). It was thought that the time response in these cases was due to either the response of the electronic readout to changes in chemical potential, or the rate of solution changeover, rather than the chemical response of the ion-sensitive

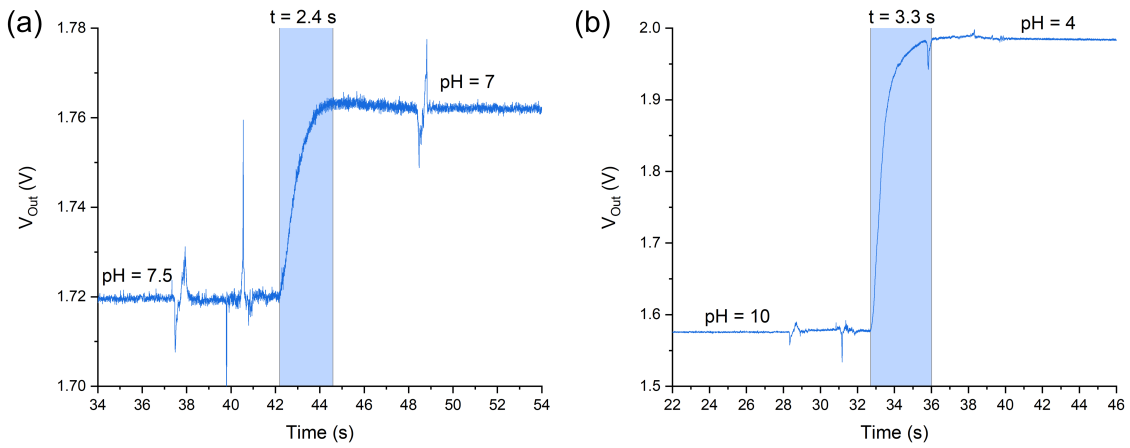

Figure 4.7: Time response of the EGFET device to changes in pH from **(a)** 7.5− > 7 and **(b)** 10− > 4. The highlighted region on each plot shows the transition period between the two pHs. Spikes on the plot are due to small disconnections between the ion-sensitive electrode and the reference electrode.

electrode itself. For this reason, the response rate of the developed EGFET device was not explored any further. With a response time in the order of seconds, the rate was sufficient to measure the kinetics of β-lactam hydrolysis, which was expected to take minutes as the purchased β-lactamase blend was used at a concentration of < 0.5 IU (where 1 IU refers to the hydrolysis of 1 μmol of β-lactam per min) and the number β-lactam moles used was between 1-10 μmol.

4.3.4 Limit of Detection

Although sensitivity plays a major role in the minimum change that can be measured by an ISFET-based device, this is not the only limiting factor. Noise within a system can have a significant effect on the detection limit of a device. The limit of detection (LOD) for a device is often described as [305]:

$$LOD = \frac{3\sigma}{Sensitivity} \tag{4.3}$$

where, σ is the standard deviation of the noise present in the device. By multiplying σ by three, this accounts for 99.7% of the potential noise in the signal. If the change is above this level, then it can be considered a change due to a change in stimuli. Assuming the sensitivity of the device is fixed, the only way to increase the LOD of a device is to decrease the noise present within the system.

Analysis of the noise spectrum present in the developed device showed a pink noise spectrum, with the majority of the noise existing in the lower frequencies (Figure 4.8). In electronic devices, noise can arise through a number of different sources, both internal and external to the device [146]. External noise sources arise due to interfering signals manifesting themselves in the device, either through crosstalk or through external sources. Crosstalk from external sources was minimised in this work through shielding. However, it was noted that a 50 Hz frequency can be seen in the noise spectra, which was thought to be

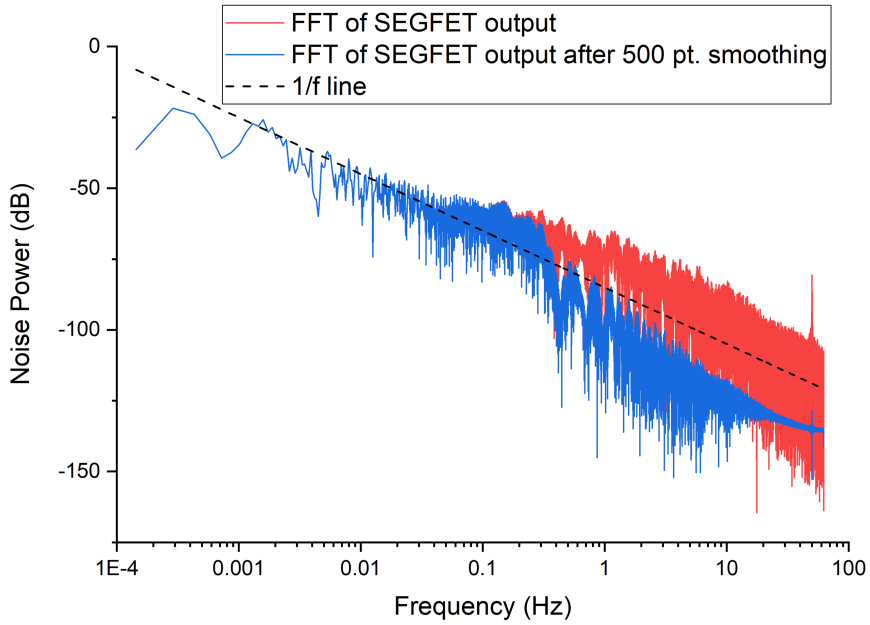

Figure 4.8: Noise spectrum of the EGFET device. Red - Fast Fourier Transform (FFT) of the EGFET device output with a peak at 50 Hz. Blue - FFT of the device output after a 500 pt. digital smoothing filter showing the reduction in the high frequency noise. 1/f is shown as a black dashed line demonstrating the large flicker noise component.

due to the external power supply. The remaining spectra shows a similar response to that of thermal noise, resulting from the thermal motion of charge; shot noise, resulting from the discrete nature of electrical charge; and flicker noise, a more complex noise source that dominated at low frequencies [306]. Both thermal and shot noise are white noise sources, meaning the amplitude does not change with frequency. Flicker noise, however, decreases with increasing frequency at a rate of $\frac{1}{f}$. As shown in figure 4.8, the noise in the lower frequencies is clearly dominated by this flicker noise. This low frequency noise was not explored any further, however this could be the subject of future work, as reduction of this interference would improve the limit of detection significantly.

To reduce the higher frequency noise, a digital averaging smoothing filter was utilised. This filter works by taking a rolling average of a data-point window, behaving in a similar way to a low pass filter. It should be noted that a smoothing low pass filter comes at a cost in terms of the time response of the device, as the higher-frequency components are filtered out, making the change appear slower. The larger the averaging window, the slower the time response of the system. In order to determine the correct averaging window, the LOD of the device for different sizes of window was calculated. From this, a 500-point smoothing filter was chosen as, above this window size, no significant decrease in the limit of detection was seen (Figure 4.9 (a)). The 500-point averaging filter also did not adversely impact the response time of the device, as the time-delay introduced by the filter was <1 s for a change of 2 pH levels (Figure 4.9(b)). As shown in figure 4.8, performing this smoothing operation reduced the higher frequency components of the noise signal, almost removing the unwanted 50 Hz component.

Considering the variability of the devices, this gave a minimum LOD for the selected

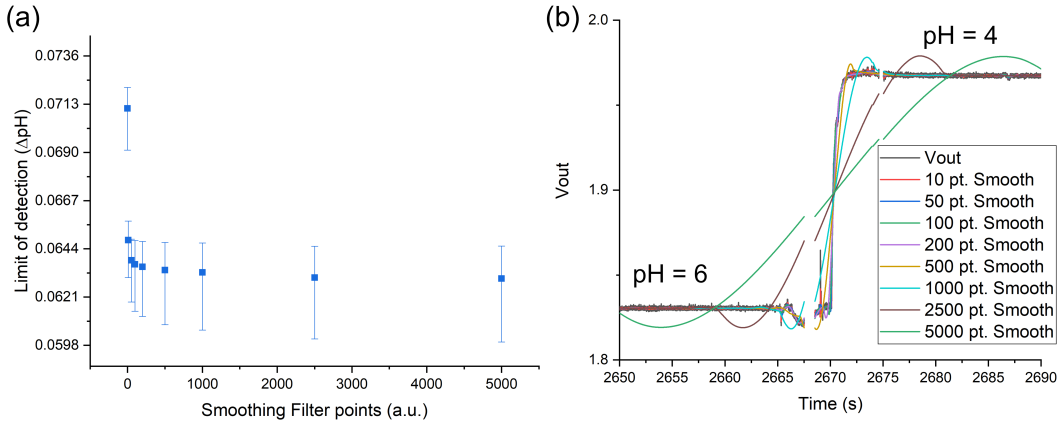

Figure 4.9: **(a)** Comparison of the limit of detection with the smoothing filter window size. Error was calculated from the SE of the calculated sensitivity. **(b)** Example of the effect of the smoothing filter window size on the time response of the EGFET. Missing points were removed due to disconnection of the reference and ion-sensitive electrodes. The pH step measured was from $6- > 4$.

devices of 0.09 pH units, far lower than the expected pH change for the β-lactamase turnover, which will be discussed in chapter 5. Another significant quantity with regards to biosensing devices is termed the limit of quantification (LOQ). This is the lowest limit at which a signal change can be reliably used to quantitatively determine changes in an analyte. Similarly to the LOD, this is described as [307]:

$$LOQ = \frac{10\sigma}{Sensitivity} \tag{4.4}$$

As the EGFET devices were to be used to quantify β-lactamase activity, this quantity is a more accurate representation of the device's capabilities. For the devices used in this project the minimum LOQ was deemed to be 0.3 pH units, which, again, was lower than the expected change for the β-lactamase assay.

4.3.5 Sensor Drift

It is often reported that metal-oxide-based ISFET devices demonstrate high levels of drift. This drift is thought to be due to a number of factors, such as temperature variation [308, 309], buried active sites within the ion-sensing layer [215, 310], and the slow oxidation of the surface due to dissolved oxygen in the solution [229, 242]. This drift often presents itself as a slow, logarithmically shaped, change in the output voltage over time, which can make measurement and quantification of pH change difficult.

Varying levels of drift were observed in the IrO_x EGFETs. Although the cause of the drift was not explored, devices were measured for their stability prior to use. Figure 4.10 gives an example of the three types of drift that were observed across the devices: low-linear drift (Fig. 4.10 Red), high-linear drift (Fig. 4.10 Blue), and non-linear drift(Fig. 4.10 Green). Although the drift often followed a logarithmic shape, the voltage appeared to settle towards a linear trend after approximately 10 min. The linearity referred to in these noise classifications regards the drift measured after the devices had been exposed

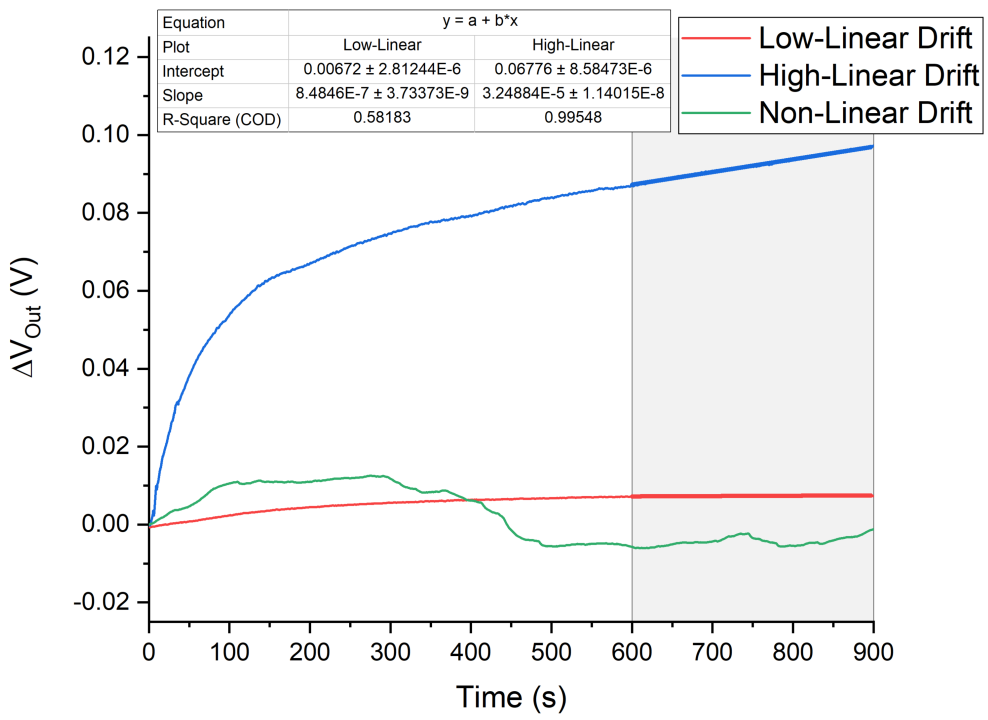

Figure 4.10: Example drift outputs of the EGFET devices, measured over 15 min. Red - A usable low-linearly drifting sensor. Blue - An unusable high-linearly drifting sensor. Green - An unusable non-linearly drifting sensor. The fitted line (Red trace) was calculated by fitting a linear function using a linear regression algorithm (Origin Pro 2018) and the error reported is the SE.

to a solution for 10 min. Some devices did not appear to settle after 10 min and were classified as non-linear (Fig. 4.10 Green); these devices were not used for measurements as this could not be easily accounted for. Devices with a seemingly linear drift after 10 min were used, with a maximum threshold of 1 mV/min, deeming them low-linear or high-linear below and above this threshold, respectively. To account for low-linear drift when performing β-lactamase activity measurements, a linear correction was performed using a line-fitting method and subtracting the slope from the measurement.

It should be noted that the drift does not just arise in EGFET sensors due to the ion-sensitive electrode. MOSFET devices have a temperature-dependant threshold voltage [311] meaning that, when the device is biased in the triode-region, variations in temperature will present themselves as changes in the output voltage. Thus, it was expected that the observed drift was due to a combination of temperature and chemical effects. The effect of temperature on the developed EGFET device was not explored experimentally. However, SPICE simulations, developed using OrCAD tools (Cadence Design Systems inc.), indicate that the device should have an ideal temperature response of $\approx 3\ mV/°C$ (Figure 4.11). No temperature control was carried out in this work, other than removing sources of temperature fluctuation. For the device to be used in a point-of-care setting, where environmental temperature may not be controllable, ideally, temperature should either be fixed within the device enclosure or monitored so that its affects can be accounted for.

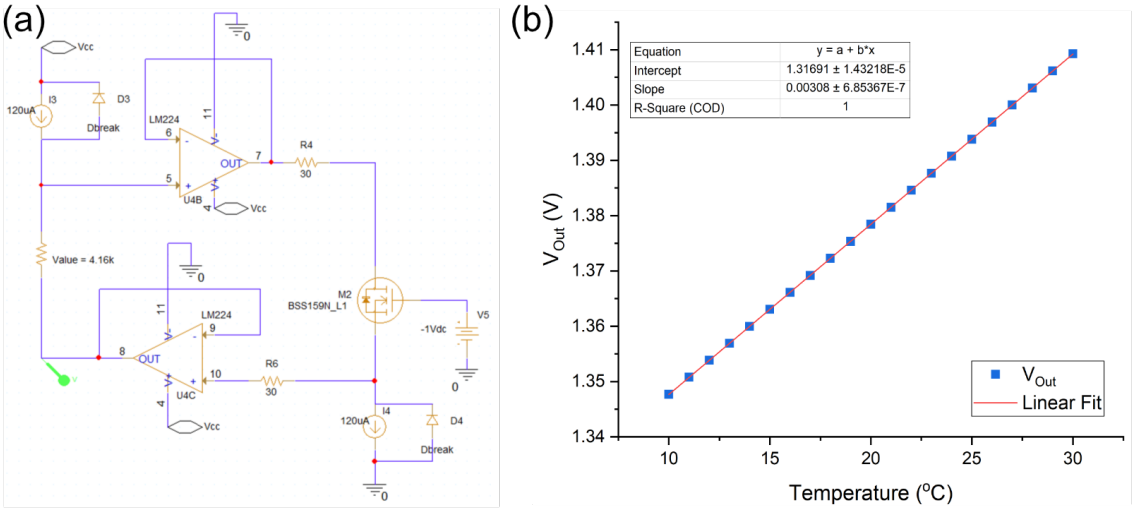

Figure 4.11: **(a)** - SPICE circuit diagram used to simulate effects of temperature on the EGFET control circuitry. **(b)** - SPICE simulated temperature response of the EGFET control circuitry. The fitted line (Red trace) was calculated by fitting a linear function using a linear regression algorithm (Origin Pro 2018) and the error reported is the SE.

4.4 Effect of Ion-sensitive Electrode Parameters on Sensitivity

To ensure that the optimum conditions were used for the iridium electrodeposition, a study was carried out to determine the effect of deposition conditions on the resulting device sensitivity.

4.4.1 EIROF Thickness

The first parameter that was explored was the thickness of the EIROF. In work done by Elsen et al. [237], they describe a relationship between the thickness of the EIROF substrate and the observed sensitivity. They postulate that, if a full coating of iridium oxide is not present at the surface, then the pH sensitivity of the IrO_x layer begins to drop. With complete coverage, the sensitivity did not appear to change with film thickness. Their work used a galvanostatic method for these measurements, however, as discussed, the films produced using this method were not sturdy. To ensure that the number of cycles used for this work (600) was sufficient for complete coverage of the electrode surface, and thus would not affect the sensitivity, samples were produced using 100-1600 potential cycles and their sensitivities were compared. As shown in figure 4.12a, there appeared to be no significant correlation between cycle number and device sensitivity. Similarly, there appeared to be no significant correlation between film thickness, measured using a profilometer (Bruker, DektakXT), and pH sensitivity (Figure 4.12b).

However, as expected, the number of potential cycles performed on the electrode seemed to correlate with the thickness measured, showing an exponentially decaying trend ($R^2 = 0.873$) (Figure 4.13). From this, it was deemed that 600 cycles was sufficient to produce a sturdy, pH sensitive EIROF. Although cycle numbers below 600 did not seem to

affect the device sensitivity, they did not appear to show the same green/blue film typical of IrO_x sensors, making it difficult to determine their mechanical stability. For this reason, devices were made using 600 potential cycles.

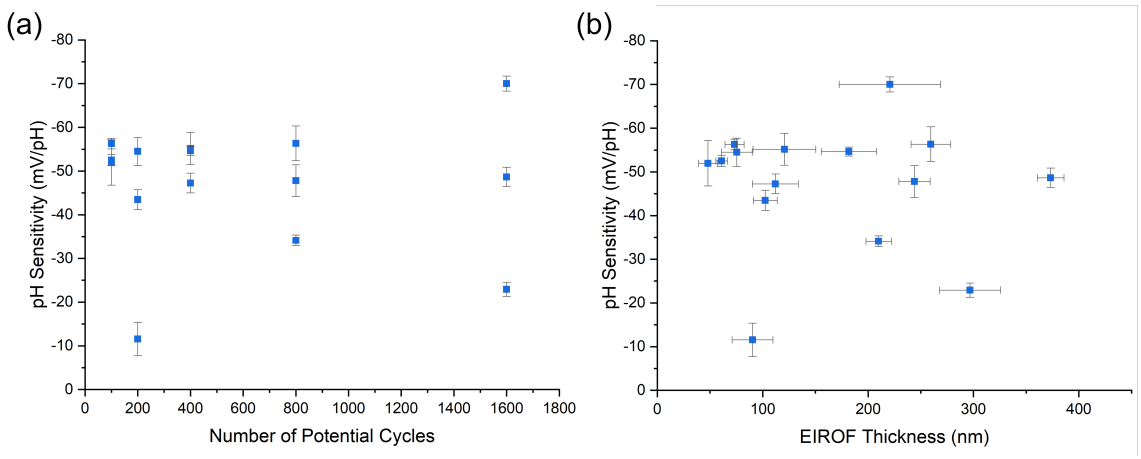

Figure 4.12: **(a)** - Effect of the number of potential cycles on the device pH sensitivity. Error reported is the SE of the calculated sensitivity across three devices. **(b)** - Effect of the EIROF thickness on the device pH sensitivity. X error reported is the SD of the measured thickness across 5 measurements. Y error reported is the SE of the calculated sensitivity across three devices.

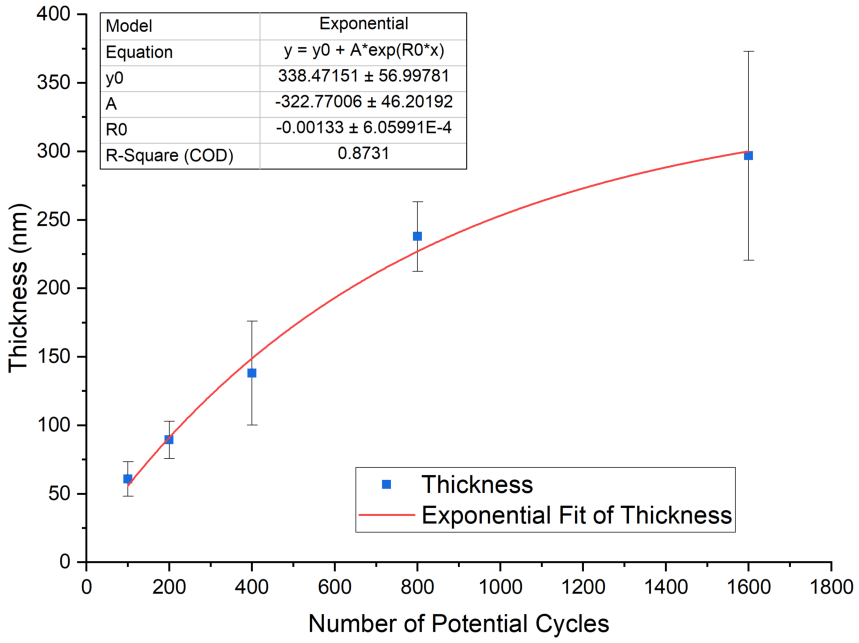

Figure 4.13: Relationship between the number of potential cycles and the measured EIROF thickness. Error reported is the SD of the mean measured thickness. The fitted line (Red trace) was calculated by fitting an exponential function using a Levenberg-Marquardt algorithm (LMA) (Origin Pro 2018)

4.4.2 Sensor Contact Area

A parameter which is not often discussed is the contact area of the ion-sensitive gate. Theoretically, this parameter should not affect the device sensitivity, as the charge density of the IrO_x layer, and thus the electric field produced, should not change with respect to the area of the ion-sensitive electrode. Yin et al. [312] briefly discussed a decrease in pH sensitivity when their Indium Tin Oxide (ITO) based sensing electrode was below 6 mm^2; however, this was not explained in any detail or explored further.

Although theoretically the electrode area does not influence device sensitivity, it was unknown how this parameter would affect the quality of the EIROF produced. Sensors of varying electrode diameter between 1 mm and 15 mm were fabricated using the previously discussed method. As shown in figure 4.14, there appears to be no significant correlation between the sensor area and the resulting device sensitivity. All measured devices were within the variability range for usable sensors.

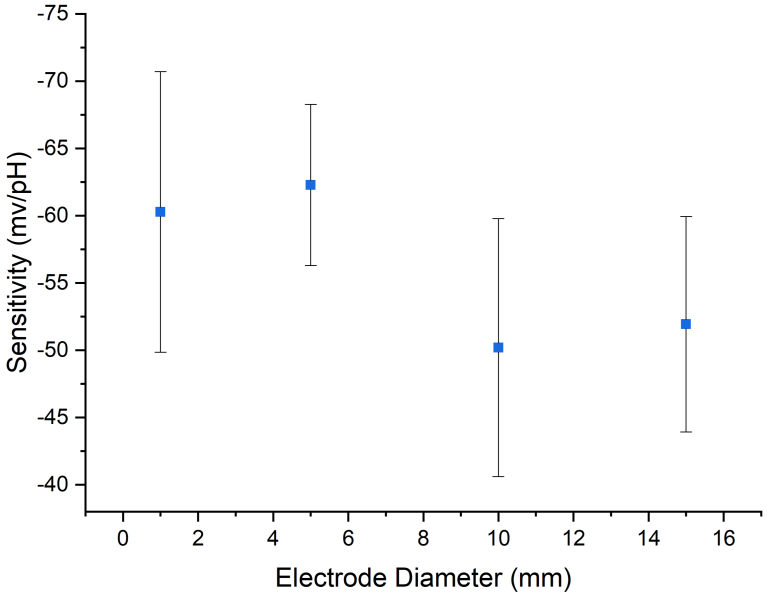

Figure 4.14: Comparison of the electrode diameter to the measured pH sensitivity. Five devices of each diameter were fabricated and tested. Error reported is the SD of the calculated pH sensitivity across at least three devices.

Given the lack of correlation between the sensor area and sensitivity, a diameter of 1 mm was chosen for future measurements, as this allowed for the smallest volume within the fluidic manifold, whilst also being large enough to fabricate reliably using shadow-mask evaporation.

4.4.3 Iridium Oxalate Solution Age

As described in chapter 3, the iridium oxalate solution used for electrodeposition requires a 2-3 day period of stabilisation after preparation. It is believed that this time is required for the formation of both IrO_x nanoparticles and Ir(IV) complexes, resulting in the blue/black solution colour [263].

The iridium oxalate solutions used to produce the ion-sensitive electrodes were used over a period of three months, as it has been reported that the solutions were stable across this time frame [264]. To ensure that no degradation of the solution occurred within this time, five devices were compared which had been fabricated at both 1 week after the solution preparation, and three months after. As shown in figure 4.15, within this time period, the age of the iridium oxalate solution did not appear to influence the pH sensitivity of the device. It should be noted that the standard deviation for the three-month old solution appeared to be lower, which could potentially be due to solution stability; however, given that only five devices were tested for this experiment, it is not possible to draw this conclusion, as all of the produced devices showed sensitivities within the expected range.

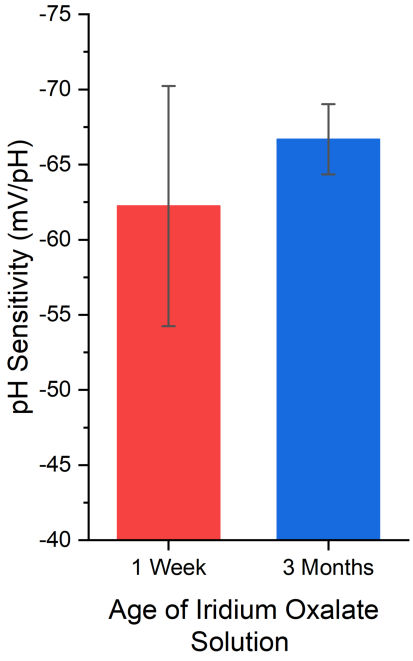

Figure 4.15: Measured sensitivity of five EIROF devices fabricated using a one week old iridium oxalate solution (Red) and a three month old iridium oxalate solution (Blue). Error reported is the SD of the calculated sensitivities.

4.5 Investigation of the EIROF Physical Properties

Following the characterisation of the IrO_x EGFETs pH sensing properties, an investigation was carried out to characterise the physical composition of the EIROF.

4.5.1 EIROF Density

Producing EIROFs using cyclic voltammetry (CV) enabled analysis of the electrodeposition voltammograms, providing insight into the formation of the layer. A parameter which is often measured for IrO_x electrodes is the Cathodic Charge-Storage Capacity (CSC_C). The CSC_C is a measure of the charge density within an electrode, measured as coulombs

per volume. This parameter is often reported for IrO_x-based neural electrodes, as it gives an indication of how much charge the electrode can inject during neural stimulation and recording [313]. Although this aspect of the parameter is not significant for this work, it is reported that the CSC_C gives an indication of the amount of redox-active iridium at the surface [313], as, assuming each IrO_x complex is redox active, the total charge in the film should be directly related to the number of IrO_x complexes. By integrating the negative cathodic portion of the CV sweep for each cycle [314], as shown in figure 4.16a, the CSC_C can be calculated as the EIROF is formed. Figure 4.16b shows the evolution of the CSC_C across 1600 potential cycles.

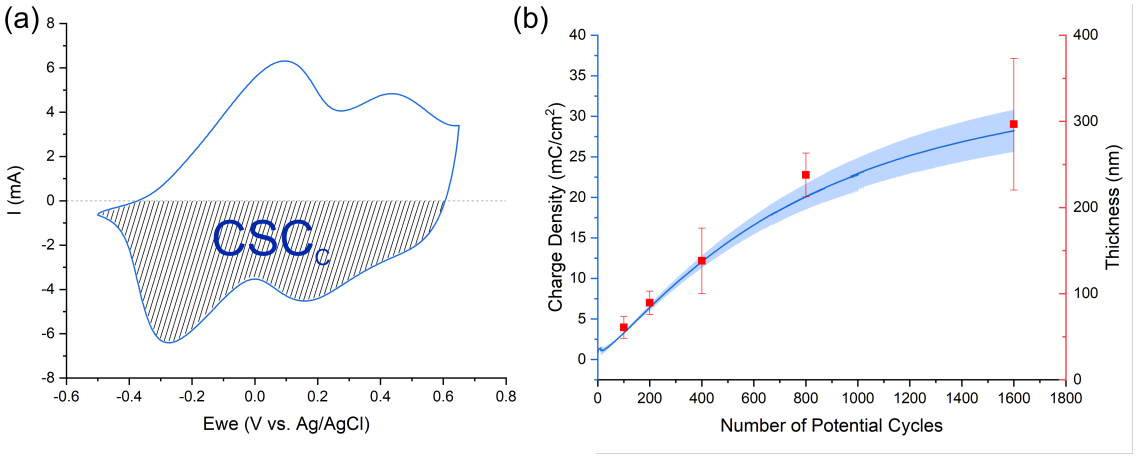

Figure 4.16: **(a)** - Cycle 600 of a 1600 cycle EIROF film deposition. The hatched region indicated the integrated area used to calculate the CSC_c of the electrode. **(b)** - Comparison of the number of potential cycles to the calculated CSC_C (Blue axis) and the thickness of the EIROF (Red axis). Error reported for the CSC_C is SD the of the integrated area mean across three devices. Error reported for the thickness is the SD of the measured thickness mean across three devices.

As shown in figure 4.16b, both the measured thickness and the calculated CSC_C of the EIROFs show an approximated exponential trend. By comparing the values of these parameters it can be confirmed that there appears to be a linear correlation between the thickness of the EIROF and the CSC_C (Figure 4.17a) ($R^2 = 0.936$), suggesting that the density of the EIROF should be constant throughout the layer. However, after further investigation, this was found not to be the case.

If it is assumed that all of the IrO_x complexes are redox active (as indicated by the linear correlation between thickness and CSC_C), and that there are only two single-electron redox processes occurring (Ir(III) $\leftrightarrow$ Ir(IV) and Ir(IV) $\leftrightarrow$ Ir(V)) [304], then the number of complexes present, and thus their density, can be estimated from the CSC_C and measured thickness using the equation:

$$\rho = \frac{m}{V} = \frac{na_W}{N_a V} \tag{4.5}$$

where: ρ is the density in g/cm^3; m is the mass in g; V is the calculated volume of the EIROF from the measured thickness and electrode size, measured in cm^3; n is the number of atoms, which in this case is IrO_x complexes; a_W is the atomic weight in g/mol; and N_a is Avagadro's constant. Given the previous assumptions, n can be calculated using the

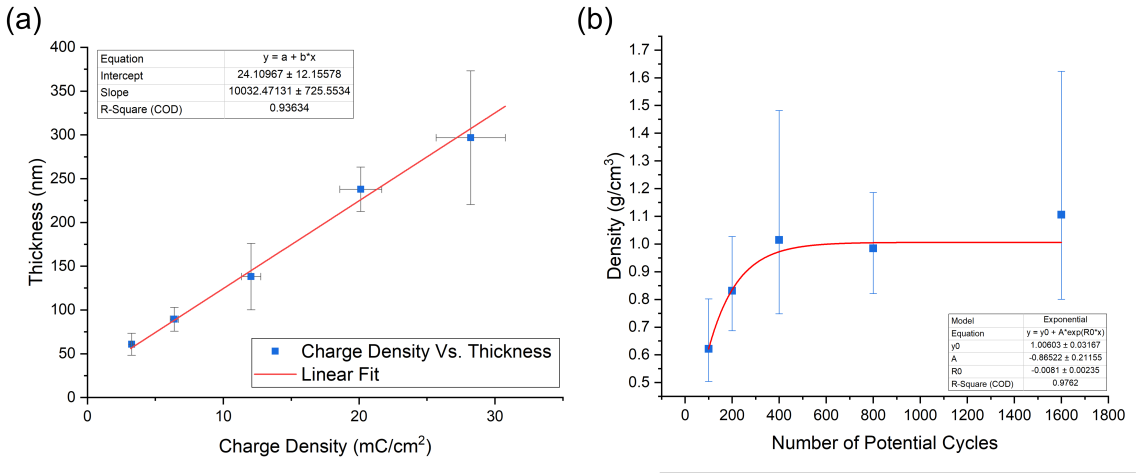

Figure 4.17: (a) - Comparison of the measured thickness to the calculated charge density. **(b)** - Comparison of the calculated density over the number of potential cycles applied. The fitted lines (Red traces) were calculated by fitting a linear or exponential function using a linear regression or Levenberg-Marquardt algorithm (LMA) (Origin Pro 2018).

following:

$$n = \frac{CSC_C\ A}{2e} \tag{4.6}$$

where: A is the electrode area, and e is the charge of an electron. Meaning equation 4.5 can be simplified to:

$$\rho = \frac{CSC_C}{t} \times \frac{a_w}{2N_a e} \tag{4.7}$$

where t is the EIROF thickness. Using this, the density of the growing EIROF was calculated. As shown in figure 4.17b, the density of the film was not found to be constant, with lower cycle numbers producing seemingly less dense layers. The density of the film appears to follow an exponential trend, plateauing at approximately $1 \pm 0.5\ g/cm^3$. Although these calculations are fairly simplistic, the measured density is comparable to those described in other work [315] and is $\approx 10\%$ of the bulk density of an iridium oxide crystal ($11.68\ g/cm^3$), indicating that the structure is porous in nature.

4.5.2 Scanning Electron Microscope (SEM) Images and Energy Dispersive X-Ray (EDX) Analysis

To investigate the morphology of the EIROF, SEM images were taken of an electrode surface. Figure 4.18 shows the EIROF surface (Figure 4.18b, when compared to the bare gold surface (Figure 4.18a). The EIROF appears to be mainly composed of a rough, nanostructured, material. Within this nanoscale roughness, larger particles can be observed, thought to either be large clusters caused by nucleation during the formation of the EIROF, or deposited nanoparticles. Investigation into the size of these larger clusters showed that the majority had diameters ranging between approximately 100-200 nm. It has been previously reported that iridium oxalate solutions can contain particles within this size range [263], however, the cause behind these clusters was not explored any further in this work.

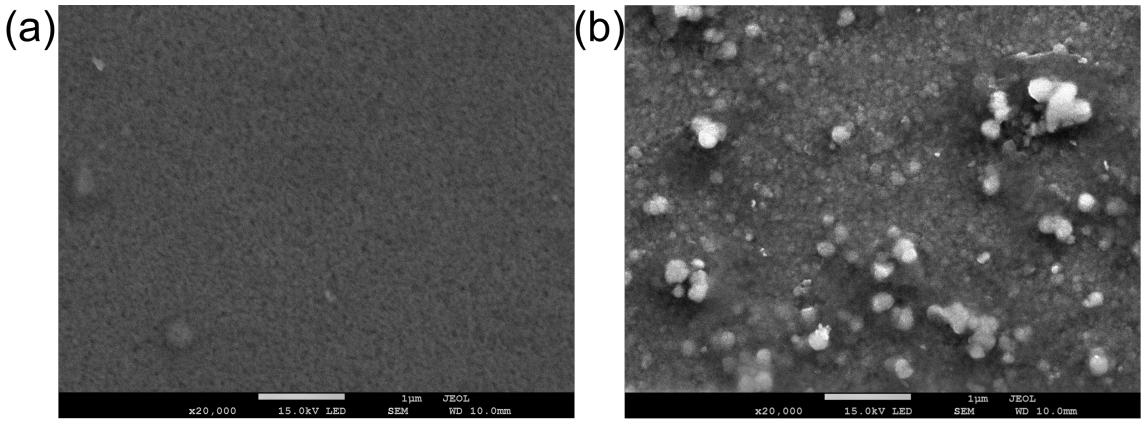

Figure 4.18: **(a)** - SEM image of a planar gold surface taken at 20× magnification showing no structural significance. **(b)** - SEM image of an EIROF surface taken at 20× magnification showing a rough structured surface containing 100-200 nm clusters.

An EDX analysis map of the surface confirmed that these large clusters were in fact composed primarily of IrO_x, as indicated by the higher intensity of both Ir and O in these regions (Figure 4.19).

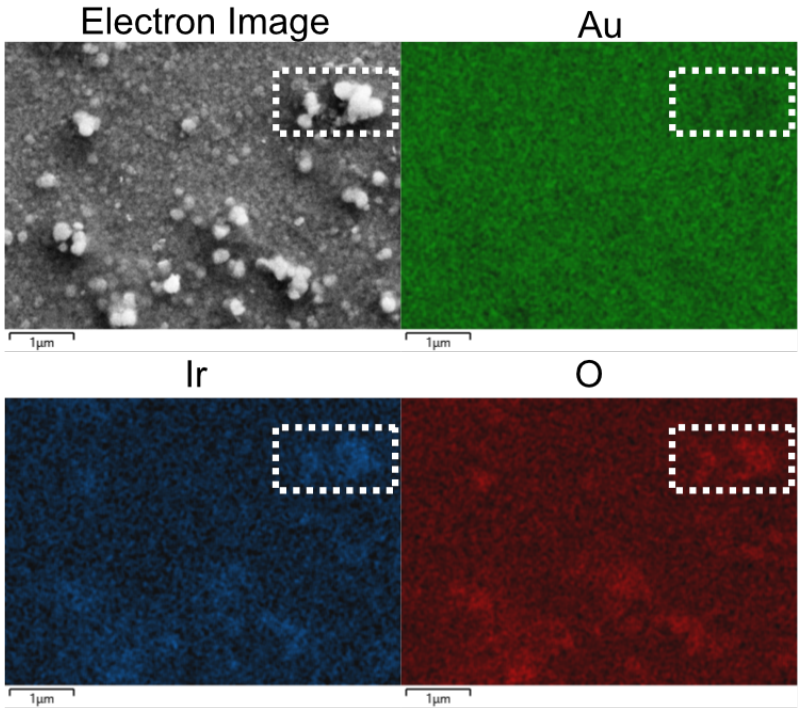

Figure 4.19: SEM image alongside EDX analysis maps of the EIROF surface showing the Au (Green), Ir (Blue), and O (Red) intensity profiles. An example IrO nanoparticle/cluster is highlighted by the white box in each image. Lighter areas indicate higher density of the measured material.

Compositional analysis of the film using EDX showed that, as expected, the EIROF was primarily composed of Ir and O. EDX also showed the presence of Au, Cr, and Si from the underlying electrode and substrate (Figure 4.20). As the probe depth for this analysis was calculated to be >1 μm, it was expected that the substrate and underlying electrode would also be visible in these readings.

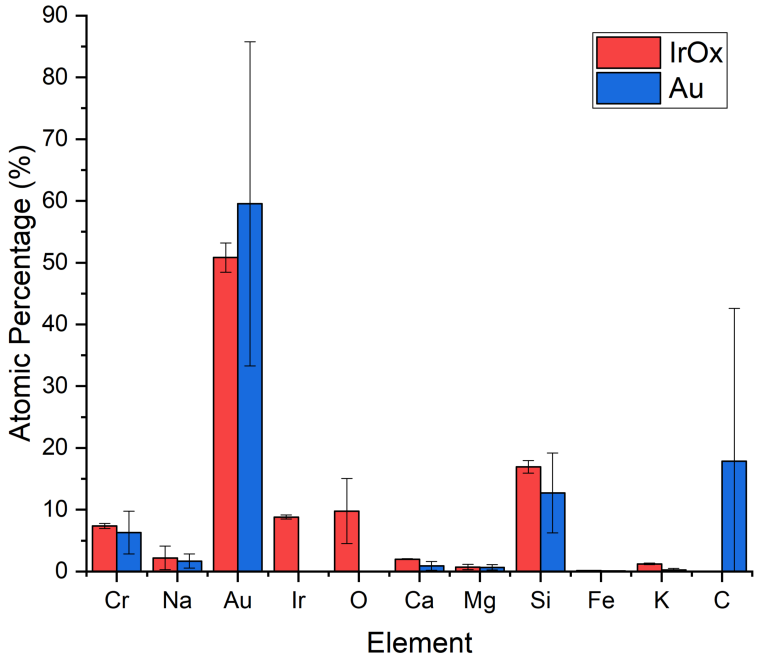

Figure 4.20: Elemental composition of both IrO_x (Red) and Au (Blue) surfaces calculated using AZtec EDX analysis software (Oxford Instruments) across three measurement points. The error reported is the SD of the measured points.

Other trace elements were observed such as K, Ca, and Na, however, these were thought to be due to either adsorbed salt from the buffers used for analysis, or from the elements present in the glass substrate. Analysis of the bare Au electrode showed no signs of Ir or O at the surface, indicating that the O observed on the EIROF electrode was a result of the IrO_x. An atomic percentage analysis of the EIROF (calculated using AZtec EDS analysis, Oxford Instruments) suggests that the Ir and O exists as a ratio of between 1:1.77 and 1:0.49. However, this is subject to significant error, as both the Au and Ir peaks overlap with one another (Figure 4.21), and the lack of a reference standard sample make quantification of oxygen content using EDX difficult [316].

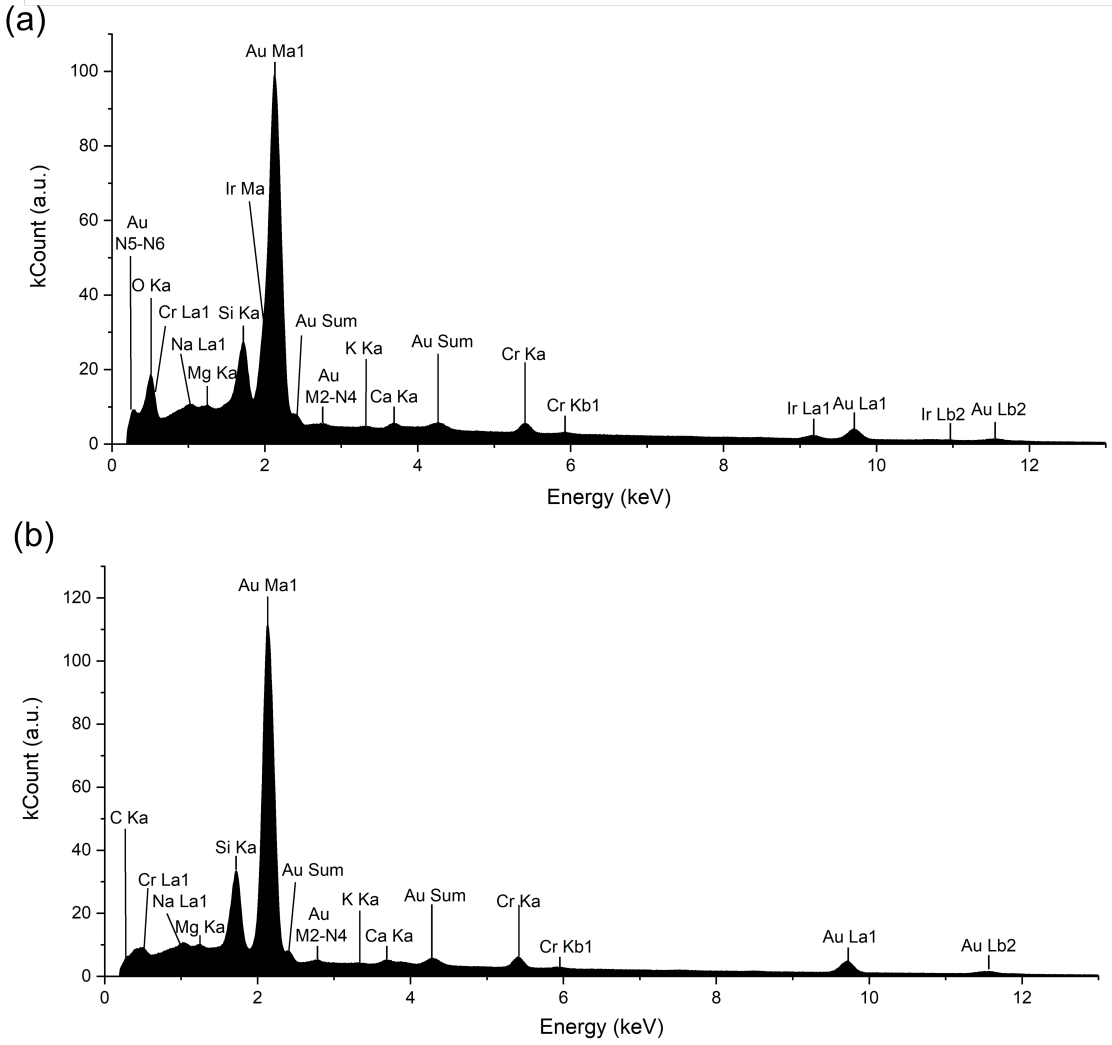

Figure 4.21: EDX analysis of the EIROF surface **(a)** and planar Au surface **(b)**. Significant peaks have been marked.

4.5.3 X-ray Photoelectron Spectroscopy (XPS)

Although EDX analysis of the EIROF gave an indication of the surface composition, overlapping peaks and lack of a reference did not allow for accurate quantification [316]. Furthermore, the resolution of EDX does not allow for the determination of oxidation states. A technique which has been shown to allow for both quantification of elemental composition and Ir oxidation states, is XPS [317, 318]. XPS measurements and peak fittings were carried out by Ben Coulson using a bespoke XPS system maintained by the Andy Pratt lab at the University of York. An initial survey of the EIROF surface showed only the presence of Ir, O, and C (Figure 4.22).

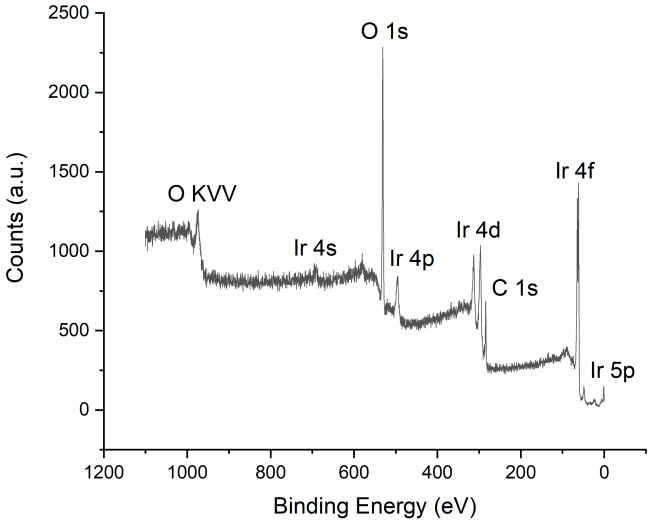

Figure 4.22: Initial XPS survey of the EIROF surface with significant peaks labelled.

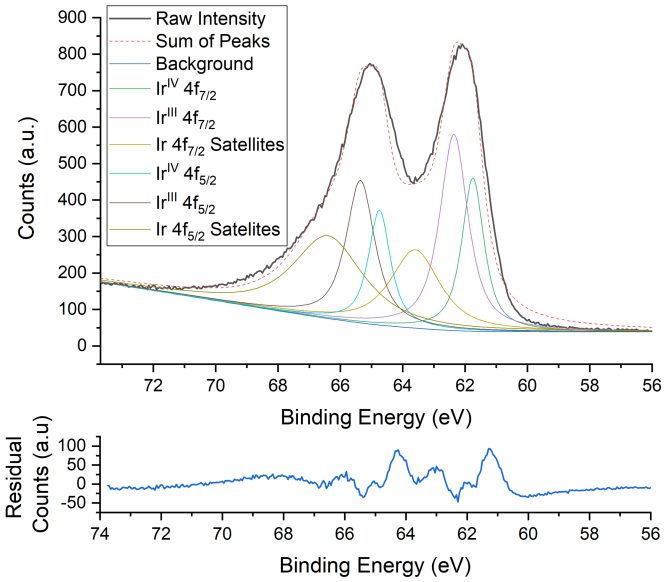

Figure 4.23: XPS survey of the Ir4f region (Black) of the EIROF surface. The dashed red line shows the sum of the fitted Ir4f peaks. The lower graph shows the residual counts after the peak fitting. Peak fitting was performed using XPSPEAK 4.1.

Deconvolution of the individual regions was then carried out, in an attempt to investigate the composition of the material in detail. Broad peaks were observed in the Ir4f region, indicating the presence of both Ir(III) and Ir(IV) [317, 318]. Figure 4.23. shows the deconvolution of the Ir4f region where peaks from both Ir(III)- and Ir (IV) 4f spin polarisations can be seen, alongside corresponding satellite peaks resulting from interactions of the emitted photoelectrons with the remaining bound electrons [319]. Integration of these peaks suggests a Ir(III):Ir(IV) ratio of 1.6:1. This mixed oxide corresponds well with the work done by Olthius et al., who suggest that the variation in the sensitivity observed in EIROF devices is a result in the mixed oxidation states present in the IrO_x layer [229].

Deconvolution of the O1s region suggested the presence of oxides, hydroxides and water throughout the layer (Figure 4.24). The ratio of these forms of oxygen were calculated at a ratio of 1:2.9:1.1, respectively. As discussed in chapter 2, the high water/hydroxide content of the EIROF is reported to be necessary for increased pH sensitivity observed with these films and is only said to be present in IrO_x produced through electrodeposition methods [229][230].

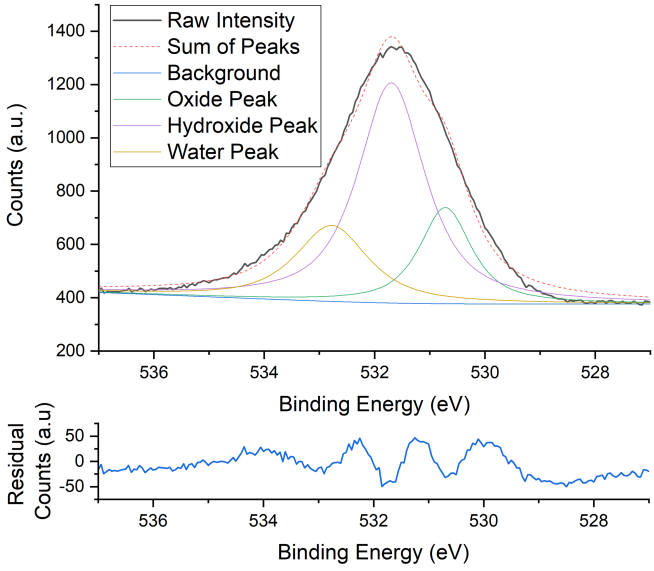

Figure 4.24: XPS survey of the O1s region (Black) of the EIROF surface. The dashed red line shows the sum of the fitted O1s peaks. The lower graph shows the residual counts after the peak fitting. Peak fitting was performed using XPSPEAK 4.1.

Integration of the specific, O1s , Ir4f, and Ir4d regions and accounting for the sensitivity factors of each of the elements allowed for quantification of the elemental ratios present within the EIROF surface [320]. For the measured sample, a Ir:O ratio of 1:7.6 was calculated, consistent with a hydrated, amorphous IrO_x layer with a high water/hydroxide content [318].

To ensure that the observed signal was in fact due to the hydration of the IrO_x, the sample was subject to a high temperature of 160 $^{\circ}C$ over 60 min, using a DC heating plate. Following this heating, the resulting XPS spectra was repeated (Figure 4.25).

Initial inspection of the resulting spectra shows a significant decrease in the O content

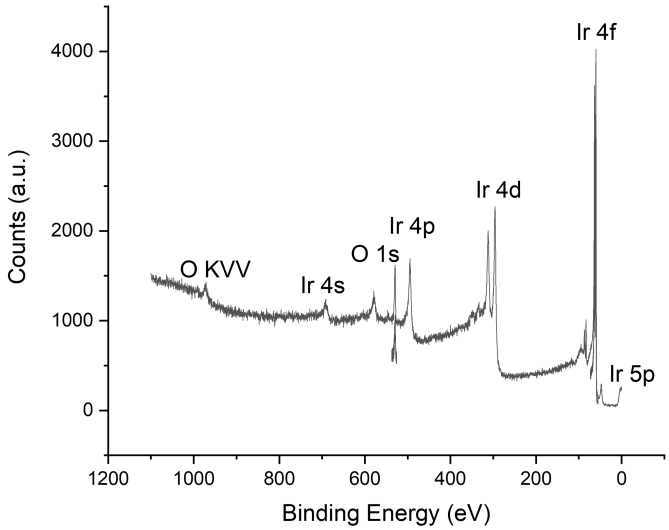

Figure 4.25: XPS survey of the EIROF surface following exposure to high-temperature with significant peaks labelled.

of the sample. Further analysis of the O1s region (Figure 4.26) showed a reduction in the water and hydroxide content observed when compared to the level of oxide present in the film. Following heating, the resulting oxide:hydroxide:water ratio was 1:1.4:0.4.

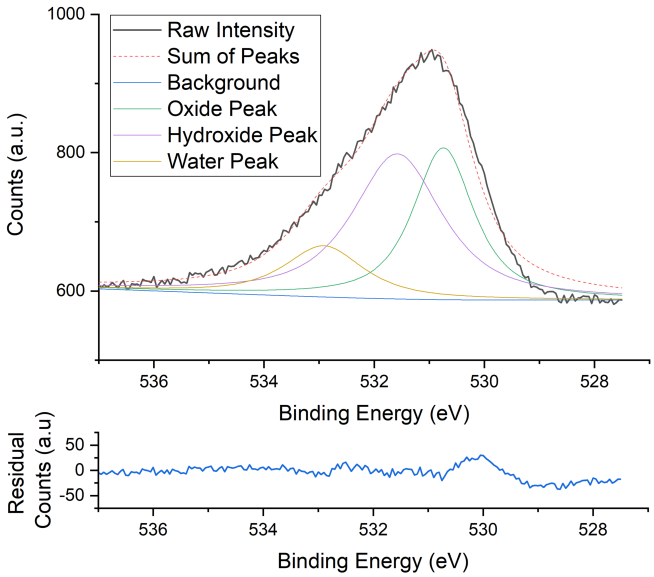

Figure 4.26: XPS survey of the O1s region (Black) of the EIROF surface post heat treatment. The dashed red line shows the sum of the fitted O1s peaks. The lower graph shows the residual counts after the peak fitting. Peak fitting was performed using XPSPEAK 4.1.

Analysis of the Ir4f region (Figure 4.27) indicated that there was a slight reduction in the Ir(III) content of the EIROF with the I(III):Ir(IV) ratio giving a value of approximately 1.23:1. However, this was still comparable to the pre-annealed sample.

Heating the sample also showed the disappearance of any C within the sample (Figure 4.25). Integration of the individual Ir and O regions showed a ratio of 1:1.17, respectively. These observations appear to show the dehydration of an amorphous iridium oxide surface,

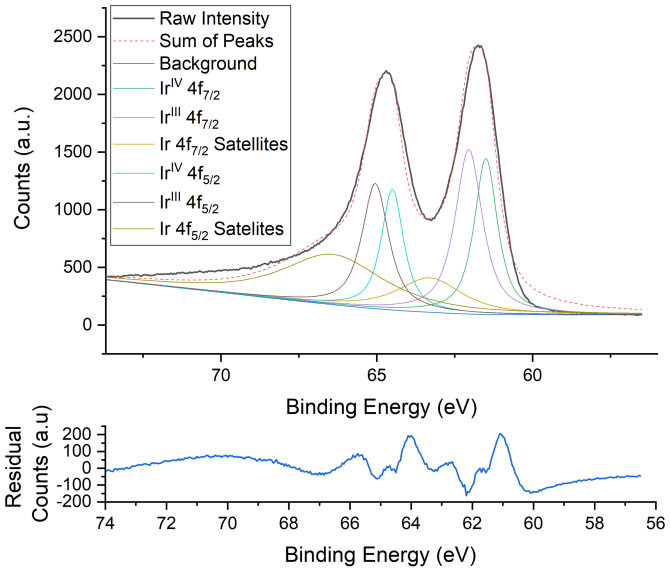

Figure 4.27: XPS survey of the Ir4f region (Black) of the EIROF surface post heat treatment. The dashed red line shows the sum of the fitted Ir4f peaks. The lower graph shows the residual counts after the peak fitting. Peak fitting was performed using XPSPEAK 4.1.

further supporting the evidence of a EIROF film with a high water content.

4.5.4 X-ray Diffraction (XRD)

Although no obvious macro-scale crystallinity was observed when performing SEM analysis of the surface, it was unknown whether any crystallinity was present within the EIROF. To investigate this, X-ray Diffraction was performed on an EIROF sample.

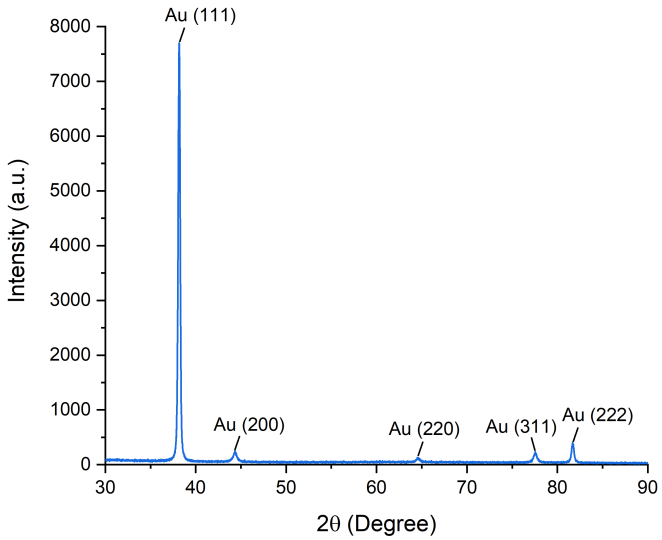

Figure 4.28: X-ray diffraction measurement of the EIROF surface showing no indication of IrO_x crystallinity. The marked peaks indicate a gold surface (COD ref: 9008463).

Peaks were fitted using the Crystallography Open Database [280–286]. The observed patterns showed no traces of Ir crystallinity, showing only peaks relating to the gold

electrode (Figure 4.28) [321, 322], confirming that the EIROF was amorphous. These results also agree with previous work, where it was suggested that EIROF films do not show any measurable crystallinity [323].

4.6 Conclusions

This chapter has described the development and testing of an iridium oxide based EGFET with a high pH sensitivity and a fast response time. Investigation into the physical properties of the EIROF show that the surface is an amorphous, nanoporous film with a high level of hydration, required for the high pH sensitivity observed in the developed devices [230].

Ion-sensitive electrode parameters did not appear to show any correlation with device sensitivity; however, this may be due to the large variation in the observed sensitivity between devices. XPS analysis of the EIROF indicated that a mixture of Ir(III) and Ir(IV) existed at the surface. The ratio of these two oxidation states has been shown to relate to the device sensitivity [229], which may give some indication as to why a large variability was seen. Future work on this could explore the nature of this Ir(III) and Ir(IV) mixture and determine its affect on device sensitivity.

A parameter which was not explored in this work was the potential cycle speed at which the devices were fabricated. Investigation into this parameter may allow for future improvements into both the stability and sensitivity of the EIROF electrodes.

Finally, the developed devices were produced using Au electrodes fabricated using metal-evaporation techniques. These electrodes require specialist techniques to fabricate and use expensive materials. Future work could explore the effect of this electrode material and investigate the use of a printed circuit boards (PCBs) with copper electrodes. Using PCB electrodes would remove the need for the expensive gold structures and improve the scalability of device fabrication.

Chapter 5

EGFET-based detection of β-lactamase Activity

5.1 Introduction

It is well established that the hydrolysis of β-lactam antibiotics can lead to acidification of weakly-buffered systems [17, 18, 135, 139–141]. This has motivated the body of research in the area between β-lactam antibiotics and ISFET biosensors. However, this is typically for the purpose of β-lactam detection [254, 255, 324], rather than detection of β-lactamase-mediated β-lactam resistance. Aside from the common growth-based assays, novel β-lactamase assays often rely on colorimetric compounds such as nitrocefin [120] or pH indicators [17], or they are based on genotypic detection of the β-lactamase [86]. These measurements are excellent for qualitatively describing the presence of β-lactamase, however, they often require expensive and bulky instruments to produce quantifiable information about β-lactamase activity.

This chapter discusses the development of a quantitative β-lactamase assay which utilises the developed EGFET device to detect pH acidification due to β-lactam hydrolysis. The assay is based around a weakly-buffered analyte containing β-lactamase antibiotics. As β-lactamases are added to the analyte, the bulk solution will begin to acidify due to hydrolysis of the β-lactam. The analyte pH should only acidify when active β-lactamase are present in the solution, meaning that a change in pH can be used as a proxy for β-lactamase activity. Furthermore, the fast time-response of the EGFET device allows for measurements of the kinetics of pH change. By quantifying these kinetics, it is possible to quantify the activity of β-lactamase. A diagram of this proposed assay is shown in Figure 5.1.

The chapter begins with a discussion on the theory surrounding β-lactam acidification, investigating the mechanism through which this effect occurs. Following this, the chapter discusses the development of the analyte used for the assay, discussing the effect that the various parameters have on the buffer capacity and thus, the observed pH change. Finally, this chapter explores the use of the developed EGFET device in conjunction with a designed β-lactamase assay to allow for quantification of β-lactamase activity.

5.2 Acidification due to β-lactam Hydrolysis

As discussed in chapter 2, β-lactam antibiotics contain a characteristic 4-membered ring structure, known as a β-lactam ring, which is key to the operation of the antibiotic.

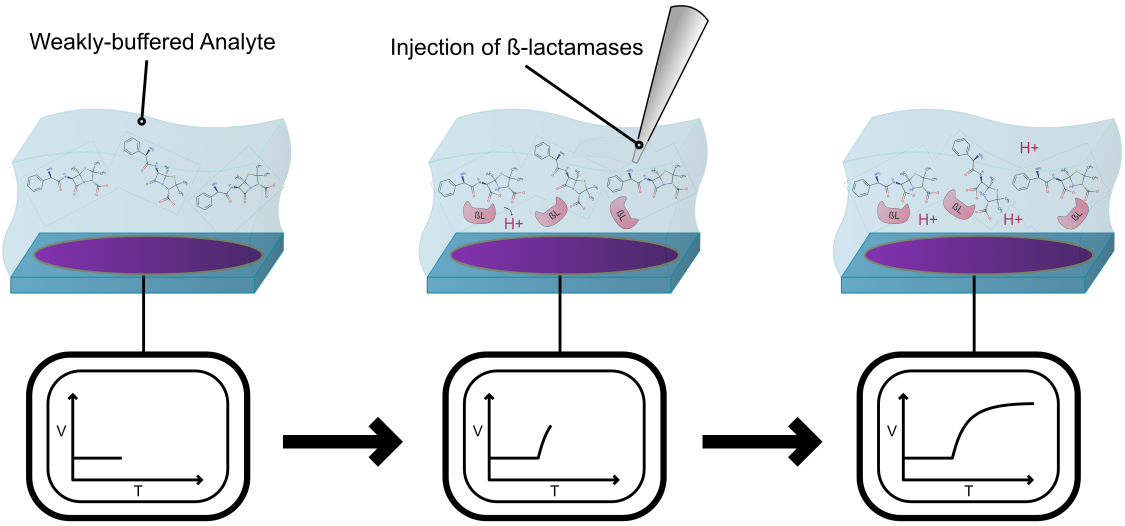

Figure 5.1: Diagram showing the proposed β-lactamase detection assay. A weakly-buffered analyte containing ampicillin is injected with a solution containing β-lactamase enzymes, after which, the pH of the solution begins to acidify, leading to a response in the observed EGFET voltage.

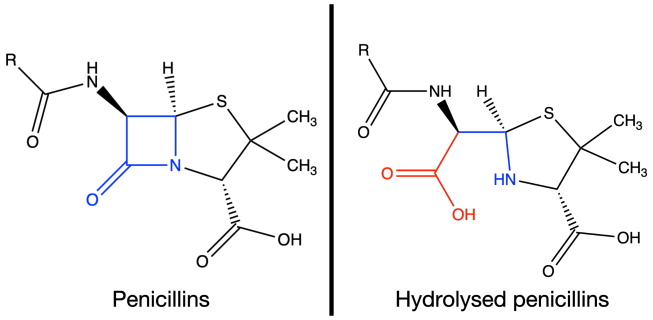

Figure 5.2: Schematic diagram showing both an intact penicillin β-lactam antibiotic (left) and its hydrolysed form (right). The β-lactam ring is highlighted in blue on the intact penicillin. Following hydrolysis, an additional carboxylic acid (highlighted in red) and amine group (highlighted in blue) are present within the drug's structure.

Bacterial resistance to this is usually mediated by an enzyme, known as β-lactamase, which hydrolyses this β-lactam ring (Shown in figure 5.2). It is often reported that [139–141]:

$$\beta\text{-lactam} + H_2O \xrightarrow{\beta-lactamase} \beta\text{-lactam acid} + H^+ \tag{5.1}$$

However, this is not strictly correct, as the release of the additional H^+ ion is caused by a change in the pK_a of the hydrolysed β-lactam and thus is dependent on the solvent pH. This leads to two major discrepancies with equation 5.1. First, H^+ ions will only be produced if the solution is at a pH where the molecule will deprotonate. For example, if the surrounding solution is at a pH below the pK_a of the acidic groups on the β-lactam, the concentration of H^+ ions will make it less likely that the hydrolysed β-lactam will donate H^+ ions to the solution. Second, the production of H^+ ions will not be a 1:1 ratio with the number of hydrolysed β-lactams, regardless of the initial pH. Although there is an additional carboxylic acid group formed on the molecule, which is typically an H^+

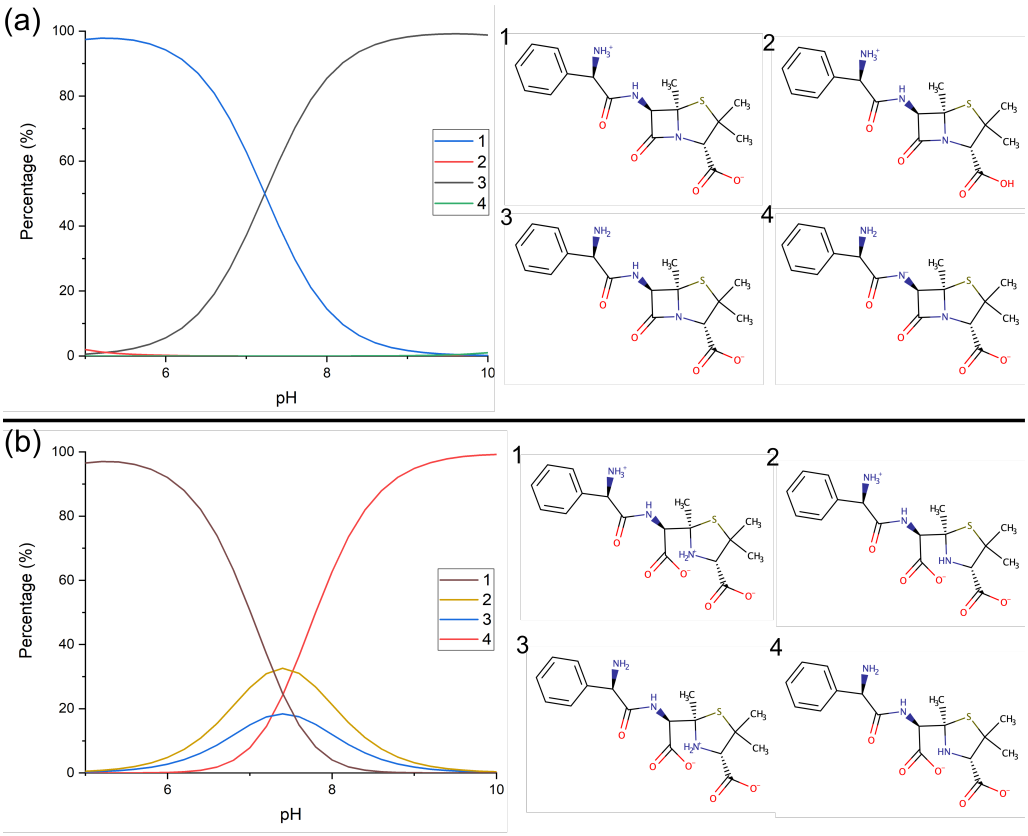

Figure 5.3: **(a)** A simulated fractional composition diagram indicating the percentage of the total species present for ampicillin between pH 5-10. **(b)** A simulated fractional composition diagram indicating the percentage of the total species present for hydrolysed ampicillin between pH 5-10. Both diagrams were simulated using MarvinSketch (ChemAxon)

ion donor at most pH levels, the additional amine group typically behaves as an alkaline group, removing the donated H^+ ions. This means that, for most cases, the hydrolysed β-lactam will behave as a zwitterion, a molecule with an equal number of oppositely charged moieties, meaning no there will be no net change in H^+ ions. Acidification of the solution following hydrolysis relies on an imbalance between protonation and deprotonation of these groups. To estimate the ratio at which H^+ ions are produced, and thus the pH change expected, pK_a simulations were carried out of both ampicillin and its hydrolysed form using MarvinSketch (ChemAxon). These simulations empirically estimate the percentage of sites which are protonated and deprotonated, with respect the pH of the surrounding solution (Figure 5.3). Although the pK_a values calculated for these molecules are only estimates, the software used has been shown to perform well for many pharmaceutical compounds [325]. For clarity, only the simulation data from pH 5 to pH 10 is shown here, as pH levels above and below these values are not suitable for β-lactamase-mediated hydrolysis and are therefore irrelevant.

Using these simulations, the estimated number of dissociated H^+ ions for each molecule was calculated (Figure 5.4). By calculating the number of H^+ ions dissociated for both the intact and hydrolysed antibiotics, it can be shown that, within the applicable pH range for the β-lactamase catalysed reaction, the hydrolysed form of ampicillin will deprotonate to a greater extent. However, as the pH of the surrounding solution tends towards pH 5.22,

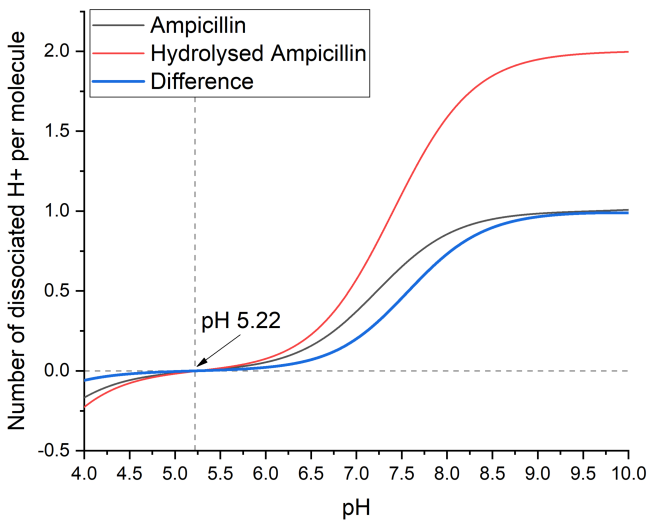

Figure 5.4: The calculated number of dissociated H+ ions per molecule of ampicillin (Black) and hydrolysed ampicillin (Red) between pH 4-10. The blue trace indicates the number of H+ ions that would be added to the solution for each ampicillin molecule that is hydrolysed.

the difference in deprotonation between the intact and hydrolysed ampicillin becomes negligible, meaning β-lactam hydrolysis should only be able to acidify a solution to a minimum pH level of 5.22. Past this point, hydrolysis would, in theory, make the solution more basic, due to the higher level of protonation of the amine groups within its structure. However, this pH level is beyond the viable region of hydrolysis for many β-lactamase.

Although only an estimate, simulation of the pK_a for both an ampicillin molecule and its hydrolysed form suggests that, for a solution at a pH of 7, approximately 54% more H+ ions will be donated for the hydrolysed form than for the intact β-lactam. Unfortunately, analytical calculation of the expected pH change due to hydrolysis is complex for two main reasons. The first is due to the pH-dependence of the β-lactam deprotonation. The initial hydrolysis will lead to a decrease in pH, further altering the number of H^+ ions that will dissociate from the hydrolysed β-lactam, thus changing the pH further, repeating until an equilibrium is reached. The second is due to the buffering effect of the β-lactamase and other components in the solution. Proteins contain many acidic and basic groups within their structure which are capable of donating and accepting H^+ ions, thus contributing to the observed pH change.

This section analytically demonstrates the relationship between hydrolysis of a β-lactam antibiotic and the acidification of the surrounding solution. In previous reports [139–141], this has not been explored in detail and appears to assume a 1:1 ratio of hydrolysed β-lactams to H^+ ions. Here, it has been shown that this is not technically the case. The more acidic the surrounding solution, the smaller this ratio becomes, leading to a smaller change in pH due to hydrolysis. It has also been analytically shown that this decrease in deprotonation trends towards a minimum pH of 5.22 for ampicillin, at which point, little pH change will be seen when the antibiotic is hydrolysed.

5.3 Determining a Suitable Assay Buffer

A buffer solution is one whose pH is stable, even with the addition of small amounts of acid or base. These solutions are commonplace in many biological systems and they are used to ensure a specific pH is maintained [326]. Importantly for this work, a buffer is required to ensure the activity of β-lactamase; however, it must also be weak enough that a pH change occurs after β-lactam hydrolysis. This section will give an introduction to theory behind buffer solutions as well as discuss the conditions required to allow for a pH change to occur.

5.3.1 Buffer solutions

Buffers are able to withstand changes in their pH due to the presence of both a weak acid and its conjugate base, or vice versa. If these are both in high enough concentration, then addition of acid (H^+ ions) or base (OH^- ions) is neutralised by the opposing buffer component. The pH of a buffer is determined by the ratio of these two components and their pKa and can be calculated using the Henderson-Hasselbach equation [138]:

$$pH = pK_a + \log_{10}\left(\frac{[A^-]}{[HA]}\right) \tag{5.2}$$

Where $[A^-]$ is the concentration of the conjugate salt (or weak base); $[HA]$ is the concentration of the weak acid (or conjugate salt for weak base buffers); and pKa is $-\log_{10}(K_a)$, where K_a is the acid dissociation constant. When both components of the buffer are in equal concentration, it can be shown that:

$$pH = pK_a \tag{5.3}$$

This is the point at which the buffer is most effective, as there are equal number of proton acceptors and donors. As shown in figure 5.5, a buffer is very effective at mitigating changes in pH around the pK_a level. However, for pH levels $pK_a \pm 1$, the buffer is considered ineffective and will not maintain a stable pH with the addition of further H^+ or OH^- ions. Generally, this is considered to be the point at which the pH has shifted by one pH level from its starting pH.

The ability of a buffer to maintain a stable pH is determined by the buffer capacity, β. This term is defined as the concentration of acid or base that must be added to a buffer to significantly influence the pH. Typically, this is the amount of acid or base (measured in Moles) that needs to be added to one litre of buffer to shift the pH value by one. Formally, this is given by equation 5.4 [327]:

$$\beta = \frac{dC_b}{dpH} = -\frac{dC_a}{dpH} \tag{5.4}$$

Where C_b is the normalised concentration of OH^- ions added, and C_a is the normalised concentration of H^+ ions added. This equation describes a continuous term for the buffer capacity which gives the pH change that would be seen for the addition of an infinitesimally

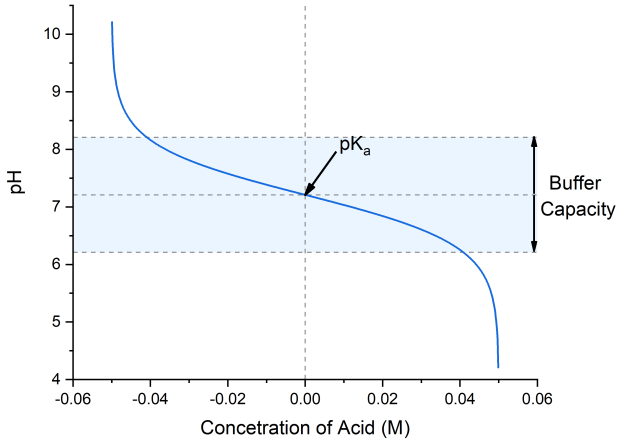

Figure 5.5: Diagram demonstrating the response of a buffer to addition of base or acid. The highlighted region centring on the pK_a of the buffer (7.21) indicates the buffer capacity of the buffer. In this instance, negative concentrations of acid implies the addition of base (OH^-).

small concentration of acid or base. However, numerically, an approximation of the buffer capacity is simpler to work with [327]:

$$\beta_{aprx} \approx -\frac{\Delta C_a}{\Delta pH} \tag{5.5}$$

It should be noted, that for small values of C_a, the error of the approximation reduces significantly.

Buffers are important for many biological systems. If a pH diverges from its ideal point, it can lead to the denaturing of proteins and disruption of cells. Enzymes often show a large dependence on pH. Deviation from an enzyme's optimal pH can significantly reduce its catalytic efficiency [328]; thus, they are heavily dependent on the surrounding solution being buffered, especially when the enzymatic reaction involves, or produces, H^+ ions. Work done by Waley, Bicknell, and Knott-Hunziker [329, 330] showed that, for the two β-lactamase used in this project (A blend of β-lactamase I and β-lactamase II), the optimal pH at which these enzymes are most efficient is approximately pH 7 for β -lactamase I, and either pH 6.6 or 7.25 for β-lactamase II. These values were calculated from the measured pK values for K_{cat}/K_M for each enzyme. The discrepancy of optimal pH for β-lactamase II is due to the use of two different β-lactamase II enzymes; in their work, Bicknell et al. used both a zinc-requiring and a copper-requiring β-lactamase II. As the type of β-lactamase II is not specified for the purchased blend, both values have been reported. It should also be noted that the pK values observed for β-lactamase I appeared to be substrate-dependent, showing a lower pK_1 point, and thus, a lower optimal point for benzylpenicillin (pH 6.73) in comparison to ampicillin [329]. As the work done by Bicknell [330] to calculate the pH dependence of β-lactamase II was carried out using benzylpenicillin as a substrate, the calculated values are only an approximation as to the optimal pH for ampicillin. It should also be noted that pH-dependence calculations for other β-lactamases not used in this project show similar optimal pH levels of approximately

pH 7 [331–334], indicating that the optimal region does not change drastically for other β-lactamase enzymes. Importantly for this work, the chosen buffer must allow for efficient β-lactamase operation, whilst also having a low enough buffer capacity that the β-lactam hydrolysis leads to a measurable pH change.

As discussed, ampicillin behaves as a weak acid, even before hydrolysis. The effect of ampicillin on bulk pH must also be considered in the decision for most appropriate buffer, as ampicillin addition could shift the pH out of the optimal range for β-lactamase hydrolysis. For detection of low concentrations of β-lactamase, achieving an optimal rate of hydrolysis is important; therefore, it was decided that the addition of ampicillin should not reduce the pH by > 0.5 away from the optimal pH of 7, as, from the work done by Waley, Bicknell, and Knott-Hunziker, this is approximately the value where the β-lactamase efficiency begins to decrease significantly. The effect of pH on β-lactamase efficiency was not explored any further although, this could be a potential area for future research as buffer capacity for low molarity buffers shows a gaussian distribution around the pK_a value of the buffer (Figure 5.6), meaning that this could potentially allow for larger pH shifts due to β-lactam hydrolysis. However, the simulations carried out suggest the pH shift will be limited to the equivalence point of pH 5.22 where no additional H^+ ions will be introduced due to hydrolysis. Thus, there will be a trade-off between the reduced buffer capacity and the number of H^+ ions gained through hydrolysis.

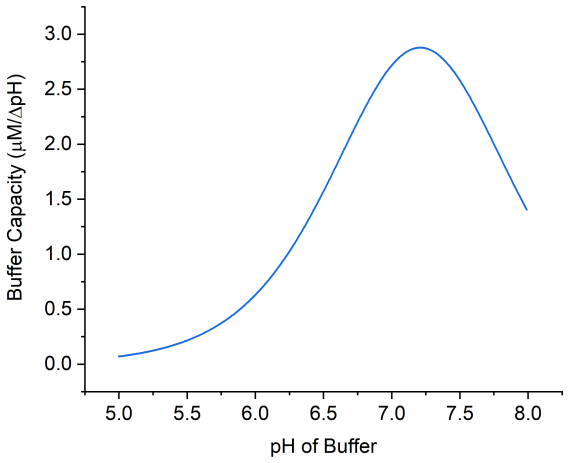

Figure 5.6: The calculated buffer capacity of a 500 μM KPi solution ($pK_a = 7.21$) with respect to the pH of the buffer.

Due to its pKa of 7.21 and ease of preparation, a commonly used buffer for biological applications is potassium phosphate buffer (KPi). For these reasons, this was the chosen buffer for this project. Typically, buffers are used at a concentration (50-100 mM) to ensure their buffer capacity is high enough to mitigate any pH changes, however, for this work, it was necessary to reduce the buffer capacity to allow acidification of the solution due to β-lactam hydrolysis, but prevent a pH change larger than 0.5 after the initial addition of ampicillin. Typically, bacteria are deemed to be resistant to ampicillin if their MIC is within the low $\mu g/mL$ region [335]. Therefore, this was chosen to be the concentration

region for ampicllin in the analyte. As discussed previously, the H^+ dissociation level is complex for multiprotic molecules such as ampicillin. However, accepting that this value would be an overestimate, a maximum estimated depronation of 37% for intact ampicillin at pH 7 (Figure 5.4) was used to determine the pH change from the initial addition of ampicillin. Comparing buffer capacity against buffer concentration showed a linear relationship between the two parameters (Figure 5.7). From this calculation, a 500 μM concentration was chosen, correlating to a buffer capacity of 272×10^{-6} $M/\Delta pH$. This value was selected as it was a round value which gave a low buffer capacity, however, it was large enough to prevent a 0.5 pH change up to, an estimated, 128 $\mu g/mL$ concentration of ampicillin. Due to the low buffer molarity, 100 mM of potassium sulphate (K_2SO_4) was also added to the buffer to ensure a stable ionic connection between the EGFET sensing pad and the Ag/AgCl reference electrode. The effect of K_2SO_4 addition on the 500 μM buffer pH was found to be negligible, changing the pH by < 0.1, which was expected as K_2SO_4 is a neutral salt.

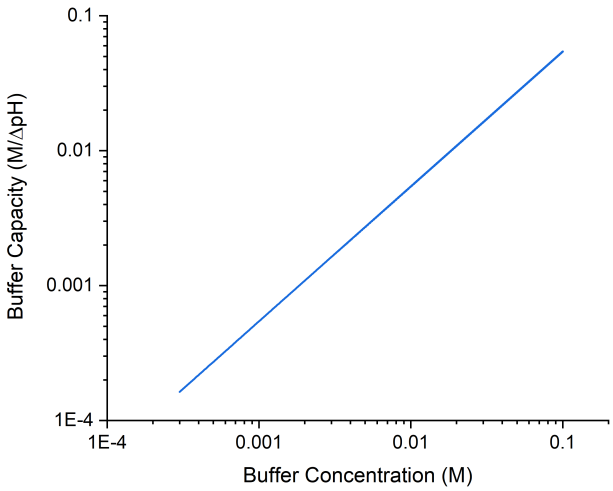

Figure 5.7: The calculated buffer capacity of a pH 7 KPi solution ($pK_a = 7.21$) with respect to the molar concentration of the buffer.

To ensure that the chosen buffer concentration would suitably prevent a pH change of 0.5 after adding low $\mu g/mL$ concentrations of ampicillin, it was explored experimentally. 100 mL of 500 μM pH 7 KPi was prepared by diluting a 50 mM stock. 25 mG of ampicillin was diluted in 3 mL of the prepared KPi. The ampicillin solution was slowly added to the prepared buffer in 50 μL increments whilst continuously stirring. After each addition, the solution was left for 1 min to settle and the pH was measured using a glass pH probe. Measurement of the initial pH with the addition of ampicillin confirmed the suitability of the chosen buffer, showing only a 0.35 shift in pH for 0.25 mg/mL (Figure 5.8a). This shift was lower than the calculated value, which was expected, as the previous estimation assumed a maximum level of deprotonation for the ampicillin.

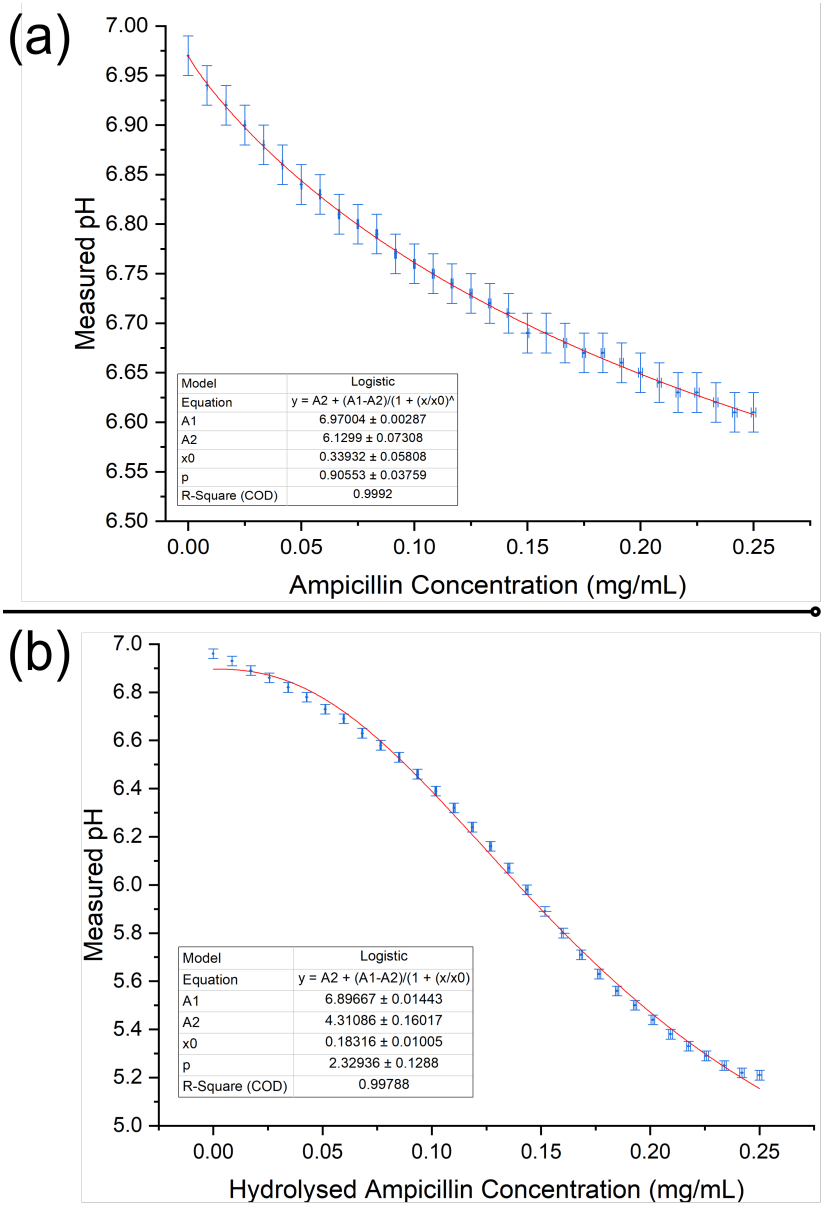

Figure 5.8: **(a)** - The measured pH of a 500 μM pH 7 KPi buffer with respect to ampicillin concentration. Error in the measured pH is reported as ± 0.02 given by the reported error of the pH measurement probe. Error in the ampicillin concentration was calculated from the reported error for the pipettes. **(b)** - The measured pH of a 500 μM pH 7 KPi buffer with respect to hydrolysed ampicillin concentration. Error in the measured pH is reported as ± 0.02 given by the reported error of the pH measurement probe. Error in the ampicillin concentration was calculated from the reported error for the pipettes.

Following the selection of a buffer that would suitably prevent a large pH change from the addition of ampicillin, the chosen buffer was tested to ensure that it allowed a pH change due to hydrolysed β-lactamase. As previously, 100 mL of 500 μM pH 7 KPi was prepared by diluting a 50 mM stock; 25 mG of ampicillin was diluted in 3 mL of the prepared KPi; However, for this experiment, the ampicillin was combined with a blend of recombinant β-lactamase proteins. The β-lactamase blend was purchased from Sigma-Aldrich (L7920) and used without further purification. The stock contained 40-70 IU β-lactamase I and 6-10 IU β-lactamase II. After combining the β-lactamase blend and ampicillin solution, it was then incubated at 37 $°C$ for 30 min to ensure full hydrolysis of the β-lactam. As shown in figure 5.8b, there is a significant reduction in pH when hydrolysed ampicillin was added, in comparison to the addition of intact ampicillin. The sigmoidal shape of the pH response is believed to be due to the combination of two effects. The first being the response of the weak buffer to the addition of small amounts of acid, which follows a similar trend to that shown in figure 5.5. The second is thought to be due to hydrolysed ampicillin behaving as a weak acid as, at approximately pH 5.2, the addition of ampicillin does not appear to shift the pH any further (Figure 5.8b). This was thought to be due to the weak acid properties of ampicillin, as pH 5.22 was calculated to be the point at which no further H^+ ions would dissociate from the hydrolysed ampicillin (Figure 5.4), thus its addition would not further decrease the pH when added to solution. However, this lack of pH change may also be due to a reduction in enzyme activity at this acidic pH. As well as demonstrating the suitability of this buffer for the detection of β-lactam hydrolysis, this experiment supports the previously discussed simulation of the pK_a values for ampicillin, suggesting the limit of the pH change due to the addition of hydrolysed ampicillin is approximately 5.2.

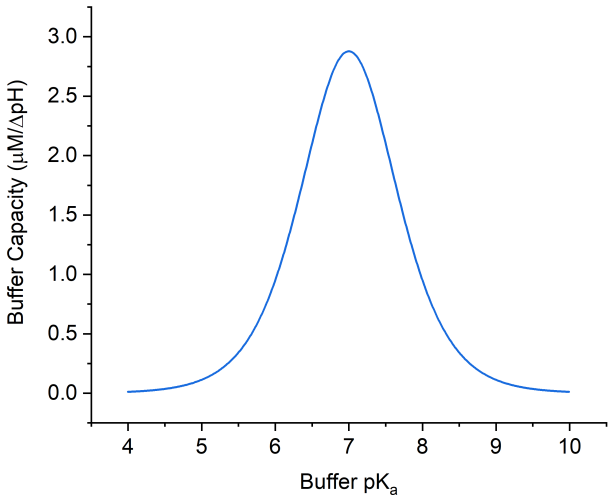

Figure 5.9: The calculated buffer capacity of a 500 μM pH 7 buffer solution with respect to the pK_a of the buffer.

A final parameter space which could have been explored was the pK_a of the buffer. However, due to ease of preparation of KPi and time restrictions, this was not explored further. Calculation of the buffer capacity against pK_a shows a similar trend to that of

the effect of the buffer capacity against buffer pH (Figure 5.9). This was expected as the parameter that affects the buffer capacity is the difference between the two. Comparing the effects of the three buffer parameters: concentration, initial pH, and pK_a (Figures 5.7, 5.6, and 5.9) it can be shown that the dominant variable affecting buffer capacity is the buffer concentration. Furthermore, as shown in figure 5.8, the chosen buffer parameters were suitable for detecting β-lactamase hydrolysis. However, as discussed, it would be possible to optimise the buffer parameters further if the β-lactamase efficiency was explored in further detail.

5.4 Determining the Effect of β-lactam Concentration

The susceptibility assay is based around two components, the pH sensing EGFET and a weakly-buffered analyte containing a β-lactam antibiotic. If the analyte is combined with a β-lactamase-containing solution, its pH should begin to acidify. The analyte pH should only shift in the presence of β-lactamase, thus, if a change occurs, this indicates β-lactamase activity. Furthermore, the EGFET's response-time to changing pH is in the order of seconds, allowing measurements of β-lactamase activity kinetics. By quantifying this pH change over time, it should also be possible to determine the concentration of β-lactamase present.

After determining a suitable buffer for detecting β-lactamase-mediated β-lactam hydrolysis through acidification, an investigation was carried out to both evaluate the capability of the developed EGFET device to detect this reaction and optimise the β-lactam concentration within the analyte. Unfortunately, the previously used fluidic manifold did not allow for the injection of a second solution required for the assay; therefore, these initial measurements were carried out by placing the EGFET sensing pad into a beaker and injecting the β-lactamase solution using a pipette. This method does not allow for precise control of the β-lactamase addition, meaning there may be differences in the diffusion of β-lactamase throughout the solution. A redesign of the fluidic manifold, which would allow for mixing of two solutions at the sensor, would allow for greater control of β-lactamase addition and could be explored in future work.

Measurements were performed using 15 mL solutions of ampicillin in the 500 μM pH 7 KPi buffer described previously. To this, 100 μL of stock concentration of the purchased β-lactamase blend was added and pipetted back and forth several times to encourage mixing. A typical trace for the EGFET response is shown in figure 5.10a. As shown in figure 5.10a a response was seen in the output of the device almost instantly after injecting the β-lactamase solution. As discussed in chapter 4, EGFET sensors often suffer from significant drift, even in stable pH solutions. In an attempt to account for this drift, all data has been linearly corrected to the observed drift across a 100 s period before the injection of β-lactamase (Figure 5.10a). The linear fit shows a seemingly poor R^2 value for the raw output of the device (= 0.511). However, this is believed to be due to the noise of the system, as performing a rolling average filter on the data improved the fit R^2 value significantly (= 0.861), but does not alter the calculated slope. It is accepted that this only partially accounts for sensor drift, due to the non-linear response over longer periods.

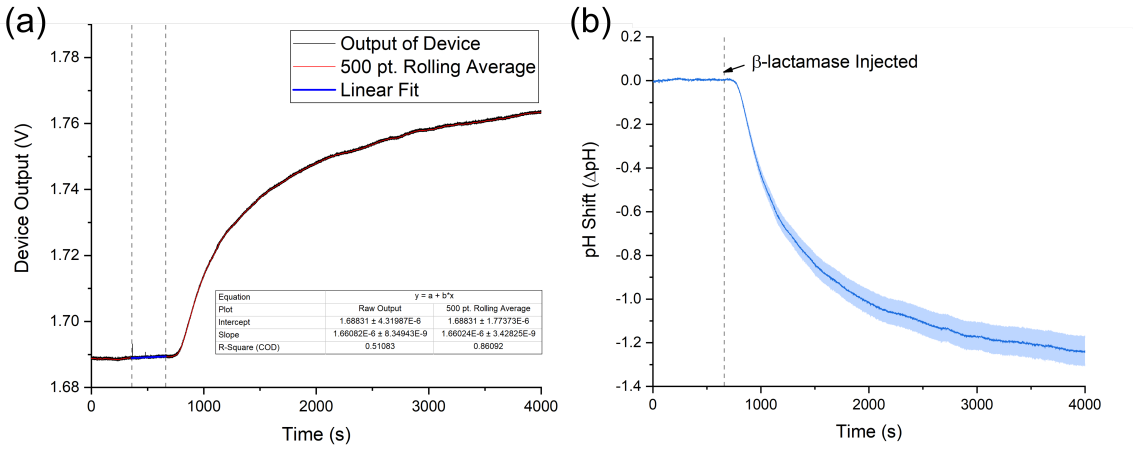

Figure 5.10: **(a)** Example output of an EGFET device measuring β-lactam hydrolysis. Dotted lines indicate the region in which the linear fit for correction was performed. **(b)** The calculated pH response of the EGFET device following linear correction and sensitivity normalisation. The solid line indicates the output of the device, with the error reported as the highlighted region. The error reported was calculated from the standard error (SE) of the device pH sensitivity. The dotted line indicates the point at which β-lactamase were injected.

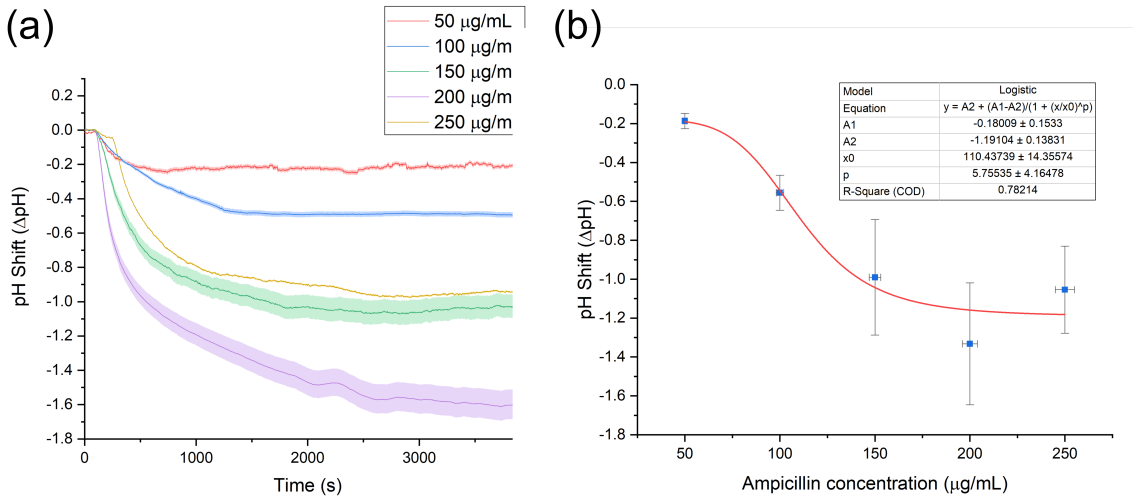

Figure 5.11: **(a)** Example traces of the measured pH change over time for varying concentrations of ampicillin after the injection of β-lactamase. The error reported was calculated using the SE of the device pH sensitivity. **(b)** Mean pH change after 60 min of β-lactamase exposure with respect to the ampicillin concentration. The error reported is the standard deviation (SD) of the data. The fitted line (Red trace) was calculated by fitting a logistic function using a Levenberg-Marquardt algorithm (LMA) (Origin Pro 2018)

Due to the large disparity in the pH response of the sensors, as discussed in chapter 4, each of the sensors were tested for their pH sensitivity prior to measuring the β-lactam reaction. The device pH sensitivity measurements were carried out as described in chapter 4; the EGFET device output was measured while submerging the ion-sensitive electrode in pH meter calibration solutions of pH 4, 7, and 10 (Thermo Scientific). This measurement was repeated twice and a line was fitted through the output with respect to the solution pH. From this point, all results have been normalised to account for the device sensitivity, showing the calculated pH change, rather than the voltage output of the device (Figure 5.10b). The error reported in these results was calculated using the standard error of the line-fit used to determine the pH sensitivity.

The developed assay relies on the pH change due to β-lactam hydrolysis being large enough to observe, thus, the concentration of ampicillin within the analyte should allow for the largest possible pH change. To determine a suitable concentration of ampicillin, and to investigate the assay response to these varying concentrations, measurements were carried out in triplicate using concentrations of ampicillin between $50 - 250\ \mu g/mL$. As expected, results showed a clear correlation between the concentration of ampicillin in the analyte and the pH shift seen after an hour of β-lactamase exposure figure 5.11. As previously discussed, it is assumed that pH change in response to increasing concentrations of hydrolysed ampicillin should have sigmoidal response due to both the buffer capacity and the natural pH of the ampicillin. The obtained results were found to somewhat fit the expected logistic response ($R^2 = 0.782$), appearing to plateau around $150\ \mu g/mL$ (Figure 5.11 (b)). Thus, it was determined that a concentration of $150\ \mu g/mL$ was suitable for the analyte as, beyond this concentration, no significant increase in pH change was observed.

The larger error seen in the response of the device at higher concentrations of ampicillin is thought to be due to the stochastic nature of the β-lactamase. As the concentration of ampicillin increases, the solution acidifies more rapidly. As discussed, the activity of β-lactamases is dependent on a number of factors such as the substrate concentration, the solution pH, and the solution temperature. At lower pH levels, the effect of temperature and substrate concentration on the reaction rate is enhanced [328], meaning that any change in either factor results in a larger error in the observed pH change. As the temperature of the solution was not actively controlled, this would be expected to have a larger effect on the activity of the enzyme at the lower pH levels.

To ensure that the observed change in output voltage was a result of β-lactamase-mediated β-lactam hydrolysis, a number of control experiments were performed. The first was to remove ampicillin from the analyte and the second was to use inhibited β-lactamases. The β-lactamases were inhibited by incubating the stock solution with $10\ mM$ sulbactam (Sigma Aldrich - S9701), a commonly used β-lactamase inhibitor for the treatment of β-lactam-resistant infections [336]. This inhibitor operates by strongly binding to the active site of β-lactamase, thus inhibiting their ability to hydrolyse β-lactams. As shown in figure 5.12, both control measurements showed little change after the injection of β-lactamase, suggesting that the observed pH change was due to β-lactamase-mediated β-lactam hydrolysis.

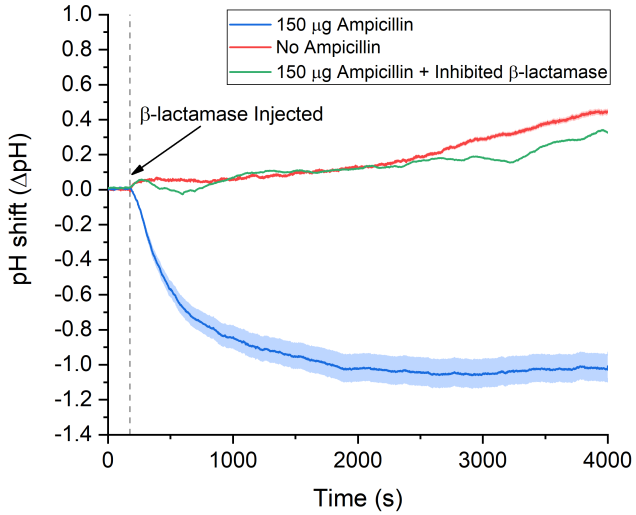

Figure 5.12: pH shift over time after the injection of: β-lactamase into 15 mL of 150 $\mu g/mL$ ampicillin in 500 mM pH KPi (Blue); β-lactamase into 15 mL of 500 mM pH KPi (Red); Sulbactam-inhibited β-lactamase into 150 $\mu g/mL$ ampicillin in 500 mM pH KPi (Green). The error reported was calculated using the SE of the device pH sensitivity.

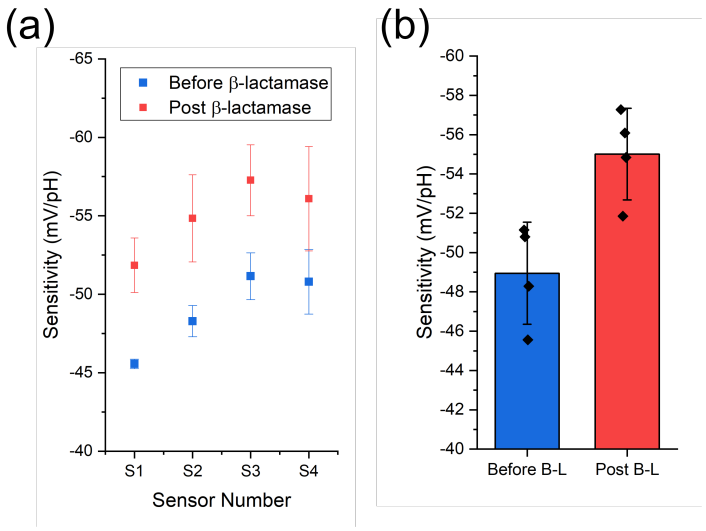

Figure 5.13: **(a)** Calculated sensitivity of four EGFET devices before (Blue) and after (Red) exposure to β-lactamases. Error is reported as the SE of the pH sensitivity. **(b)** Mean value of the calculated sensitivities before (Blue) and after (Red) exposure to β-lactamases. Error reported as the SD of the mean.

It has previously been reported that pH-sensing devices can show signs of sensitivity reduction after immobilisation of β-lactamase [241]. Surface-adhered enzymes could be problematic if they alter the pH sensitivity of the device, as they could inhibit measurement of pH change due to β-lactam hydrolysis. To explore this, the sensitivities of several devices were measured prior to and following exposure to β-lactamase. As shown in figure 5.13, enzyme exposure did not appear to reduce the pH sensitivity of the device, instead, an increase in the sensitivity was observed. It is unknown why an increase in sensitivity was seen after enzyme exposure. This could be due to increased hydration at the surface caused by additional hydrophilic groups from the fouling enzyme since, as previously discussed in chapter 2, the iridium oxide sensing layer relies on hydration for its high sensitivity. However, this was not investigated any further, as new sensors were used for each β-lactam hydrolysis measurement. Contamination of the surface by β-lactamase would affect the observed signal if any surface-adhered enzymes were still active.

5.5 Solution-phase Detection of β-lactamase Concentration

As the EGFET device is capable of quantifying pH changes with a fast time-response, the device should allow for quantification of β-lactamase activity, rather than simple qualitative answer. The ability of the EGFET device to quickly respond to, and quantify, pH over time is of importance to this measurement due to the nature of the assay. Although enzymatic activity may be reduced as the pH decreases, the β-lactamases will continue to hydrolyse the β-lactams until they have all been hydrolysed. For a fixed concentration of β-lactams, this will result in the magnitude of the pH shift reaching the same point, regardless of β-lactamase concentration. However, the rate at which this reaction occurs is dependent on the concentration and activity of β-lactamase present; thus, at earlier time-points, there should be variation in the observed pH change as a function of β-lactamase concentration.

To test this hypothesis, the analyte was prepared at a fixed ampicillin concentration of 150 $\mu g/mL$ in 500 μM pH 7 KPi. As there was no simple way of altering the activity of the β-lactamase, varying concentrations of β-lactamase were prepared from $1 - 100$ $\%v/v$ of the stock concentration. As before, 100 μL of β-lactamase blend was added to 15 mL of the prepared analyte (Figure 5.14).

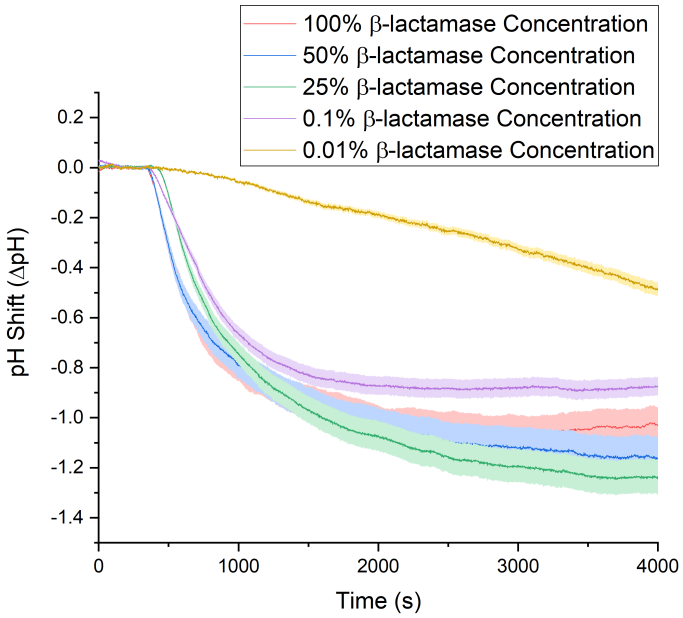

Figure 5.14: Example traces of the measured pH change over time for varying concentrations of β-lactamase injected into 150 $\mu g/mL$ ampicillin in 500 μM pH 7 KPi. The error reported was calculated using the SE of the device pH sensitivity.

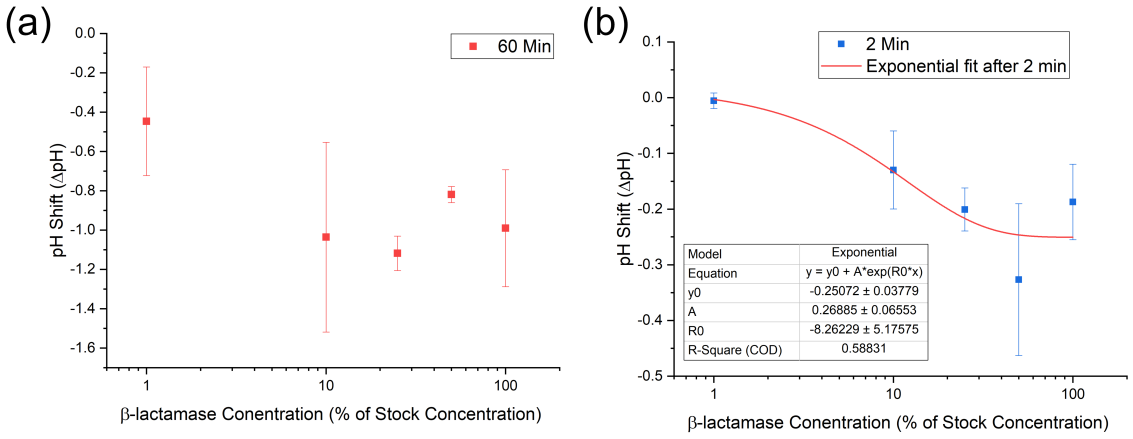

Figure 5.15: Mean pH change after 60 min **(a)** and 60 min **(b)** of β-lactamase exposure with respect to the β-lactamase concentration (% v/v). The error is reported the standard deviation (SD) of the data. The fitted line (Red trace) **(b)** was calculated by fitting an exponential function using a Levenberg-Marquardt algorithm (LMA) (Origin Pro 2018)

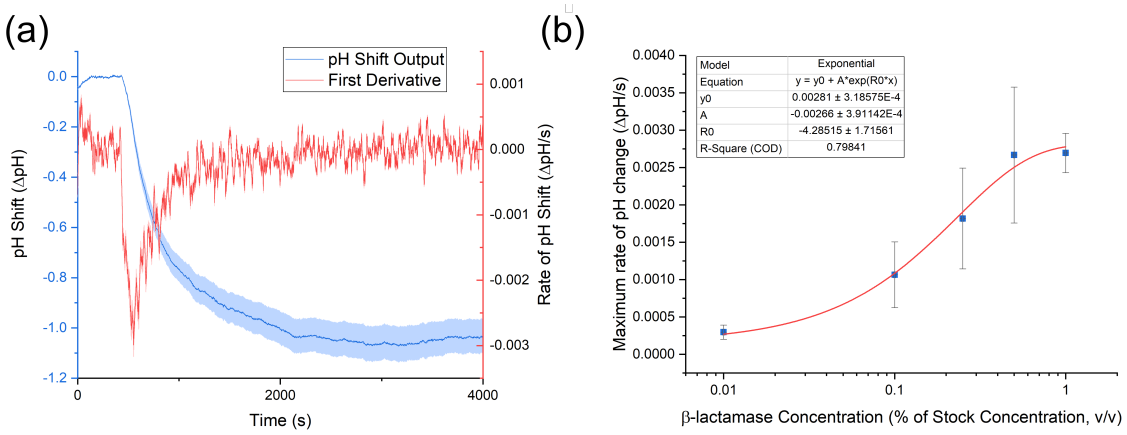

Figure 5.16: **(a)** Example trace of the calculated pH response after injection of β-lactamase (Blue) with its first derivative (Red) used to calculate the maximum rate of pH change. The error reported was calculated using the SE of the device pH sensitivity. **(b)** Mean of the maximum rate of pH change after β-lactamase exposure with respect to the β-lactamase concentration (% v/v). The error is reported the standard deviation (SD) of the data. The fitted line (Red trace) was calculated by fitting an exponential function using a Levenberg-Marquardt algorithm (LMA) (Origin Pro 2018)

As expected, no significant correlation was found between the magnitude of the pH shift after 60 *min* and the concentration of injected β-lactamases (Figure 5.15a). However, by measuring the magnitude after 2 min of β-lactamase exposure, some correlation can be seen, showing a loose fit to the expected exponential response (Figure 5.15b, $R^2 = 0.588$). As the rate of enzyme hydrolysis is dependent on the enzyme-substrate ratio, the response of the pH shift with respect to β-lactam concentration was deemed to be an increasing exponential decay. The lack of sigmoidal response is thought to be due to the observed pH change after 2 *min* not being large enough to exceed the buffer capacity; thus, the pH response of the buffer to addition of acid should be linear within the buffer capacity region.

As seen previously with increasing concentrations of ampicillin, there appears to be a larger error with higher concentrations of β-lactamase. As well as being due to the stochastic nature of the enzyme, it is also thought that this error is due to the method by which the β-lactamase were injected. Unfortunately, by injecting the β-lactamase using a pipette, rather than a more controlled injection, there is a large dependence on both the diffusion time of the enzyme and the distance of the injection from the sensor. To avoid disturbing the sensors, no mixing was carried out after injection. This issue could be solved using a purpose-built fluidic device. Given this diffusion dependence, the best time at which magnitude should be measured is unknown for each sample, thus, in order to remove this unknown, the rate of pH change was explored, rather than the magnitude.

By measuring the rate of pH change over time, the point at which the enzymes are most active can be easily seen as a peak in the signal (Figure 5.16). The magnitude of this peak should also be enzyme-concentration dependent, as the more enzymes that are present, the larger the maximum rate of pH change. To explore this for the developed assay, the first derivative of each measurement was obtained and the maximum rate of pH change was recorded.

The response of the maximum rate of pH change with respect to β-lactamase concentration shows a significantly improved fit to the expected exponential response ($R^2 = 0.798$). There still appears to be some error in the measured response, however, as previously discussed, the enzyme activity is largely dependent on pH and temperature. Despite this, the results still show a strong correlation between the maximum rate of pH change and the concentration of β-lactamase.

5.6 Conclusions

This chapter has discussed the successful detection of β-lactam hydrolysis using an EGFET device which allows for quantification of β-lactamase activity through direct measurement of pH change kinetics. Interestingly, the slow response time of many other pH sensors, such as the glass electrode, would not be suitable for measuring the time-resolved pH change required for these kinetic measurements. Furthermore, the electronic nature of the EGFET device also allows for the simple addition of analogue circuitry to reduce noise or perform the necessary differentiation required for the pH change rate measurements, reducing the need for computational power and making this device more suitable as a point-of-care device.

The assay described in this chapter was capable of detecting concentrations of 1 $\%v/v$ of the purchased stock concentration. In order to test the applicability of this assay for clinical use, future work would have to investigate the response of assay to more specific β-lactamase enzymes, such as AmpC, TEM-1, and NDM-1. By investigating the response of the assay to these enzymes, it would be possible to determine specificity of the assay for detecting different forms of resistance. As the protein concentration for the purchased blend of β-lactamase was not specified, the detection limit of this assay cannot be quantified. By using specific β-lactamase, this measurement could also be carried out.

Although limit of detection measurements were not performed, results indicate that the limit is close to the measured 1 $\%v/v$. Further optimisation of the buffer parameters, such as the pKa or initial pH, could increase this limit. However, as discussed in this chapter, this could increase the error observed due to the pH, temperature and substrate concentration dependence of the β-lactamase. It has been shown that measurements are also affected by diffusion, as the EGFET device is only able to detect the pH of the solution present at the surface. This means that for detection at low concentrations, changes in the bulk solution are often not detected. One method for overcoming this would be to force the reaction to occur directly at the surface. The next chapter will discuss the development and testing of a surface-bindable β-lactam antibiotic which would allow for the *beta*-lactamase hydrolysis reaction to occur directly at the sensor surface, potentially increasing the response for lower concentrations of enzyme.

Chapter 6

Immobilisation of a Tethered β-lactam for β-lactamase Detection

Disclaimer - Much of the work in this chapter has been published as a joint lead-authorship publication in *ACS: Applied Materials and Interfaces* under the title 'A Surface-bound Antibiotic for the Detection of β-lactamases' [337]. For clarity, work done by the other authors, primarily Dr. Lisa M. Miller (LMM) and Mr. Reyme Herman (RH), is included in this chapter, but will be explicitly specified.

6.1 Introduction

As discussed in chapter 5, solution-phase measurements using ISFETs are only able to detect changes in pH at the interface of the device. This means that, for detection at low concentrations, changes occurring in the bulk solution are often not detected. One method for overcoming this is to bring the reaction closer to the surface by binding part of it through surface-functionalisation [19]. By doing this, the surface concentration of H^+ ions should increase as the reaction occurs, increasing the measured signal. As well as potentially increasing the observed pH change at the ISFET surface, a surface-based assay of β-lactam resistance would also be compatible with a range of other high sensitivity, low cost and label-free analytical techniques developed for point-of-care diagnostics [338–342]. This chapter discusses the testing of several surface-bindable β-lactam antibiotics, capable of responding to the presence of β-lactamase enzymes.

The modified surface-bindable β-lactam used for this work was based around the cephalexin β-lactam, which was chosen for its robustness, clinical relevance [343], and free amine group located away from the β-lactam ring [337]. The cephalexin molecule was directly attached to a surface-bindable tether, at the end of which was a maleimide functional group, allowing the antibiotic to be anchored to a variety of prepared surfaces, whilst minimising the effect on the drug activity [344]. Initially, a carbon-chain linker was used as this tether, however, as will be discussed in this chapter, this was later replaced with a Poly Ethylene Glycol (PEG) chain. A structural diagram of this surface-bindable antibiotic can be seen in figure 6.1b. Synthesis of the surface-bindable β-lactams was carried out by LMM.

The chapter discusses the testing of both the carbon-chain-tethered and PEG-tethered surface-bindable cephalexin molecule in order to determine their suitability for β-lactamase detection. Finally, the chapter concludes by demonstrating the functionality of the chosen surface-bindable antibiotic is preserved in undiluted urine, a necessity for rapid testing of urinary tract infections [40].

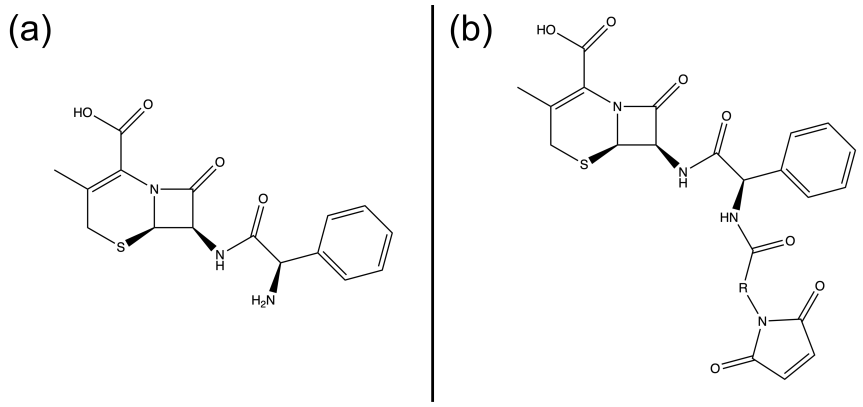

Figure 6.1: (**a**) - Structure of cephalexin **(b)** - Structure of tethered cephalexin, where R is either a carbon-chain or PEG linker.

6.2 Functionalisation and Testing of a Surface-bound Carbon-chain Cephalexin.

To determine whether a surface-bound β-lactam would be suitable for β-lactamase detection, a surface-functionalisation procedure, which maintained the functionality of the molecule, had to be developed. There were three main criteria which had to be met for the procedure to be deemed viable. First, the β-lactam ring had to remain intact, as this is the target of the β-lactamase enzyme. Secondly, the β-lactam ring had to be accessible to an incoming β-lactamase enzyme. If this was not the case, the approach would not be able to detect the presence of β-lactamase via hydrolysis of the immobilised β-lactam. Finally, the surface-bound β-lactam had to allow the β-lactamase to desorb once the reaction had occurred, as surface fouling could interfere with any measurement. To initially test the first two criteria, PM-IRRAS was used due to its capability to determine chemical structures present at the surface [345].

As discussed in chapter 3, PM-IRRAS is typically suited towards highly-reflective, metal surfaces. Therefore, for initial testing, experiments were carried out using planar, 100 nm thick gold films deposited on top of Si wafers using electron-beam evaporation. In order to bind the formulated tethered-β-lactams to the surface, a complimentary functional group, capable of binding to the maleimide group present in the molecule, had to be added to the planar gold surface. Maleimide groups are capable of covalently binding to thiol groups through a thioether bond, without the need for multiple steps or additional reagents [346]. For this reason, 1,3-propane dithiol was chosen to produce the required thiolated layer on the planar gold surface due to its previous usage in the formation of active thiol-terminated SAMs on gold surfaces [347]. Furthermore, SAMs have been shown to give high-density layers of surface-bound molecules, ensuring a good coverage of functional groups [348–350]. As this molecule has two thiol terminal groups, it was capable of binding to both the gold and the maleimide-tagged cephalexin [351]. The first tether which was trialled for the surface-bindable β-lactam was the carbon-chain linker (Figure 6.2). This maleimide-tagged β-lactam with a 6-membered carbon-chain linker will herein be referred to as cephalexin-C6.

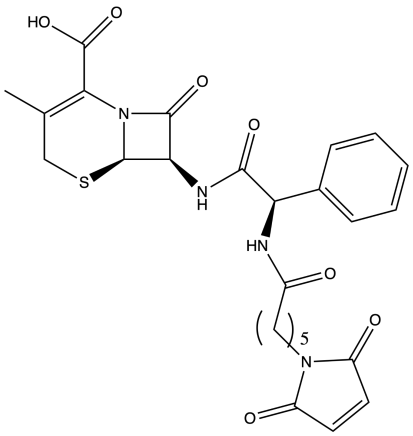

Figure 6.2: Structural diagram of cephalexin-C6

Surface-functionalisation of the cephalexin-C6 was achieved using the following protocol. Cleaned planar gold surfaces were submerged for 24 h in a 10 μM 1,3-propane dithiol MeOH solution, after which they were rinsed in MeOH and dried using N_2 gas. Following this, the surfaces were submerged for 24 h in 2 μM cephalexin-C6 in 25% DMSO/H_2O and then rinsed in 50% DMSO/H_2O and finally dried with N_2 gas. This functionalisation procedure is demonstrated in figure 6.3.

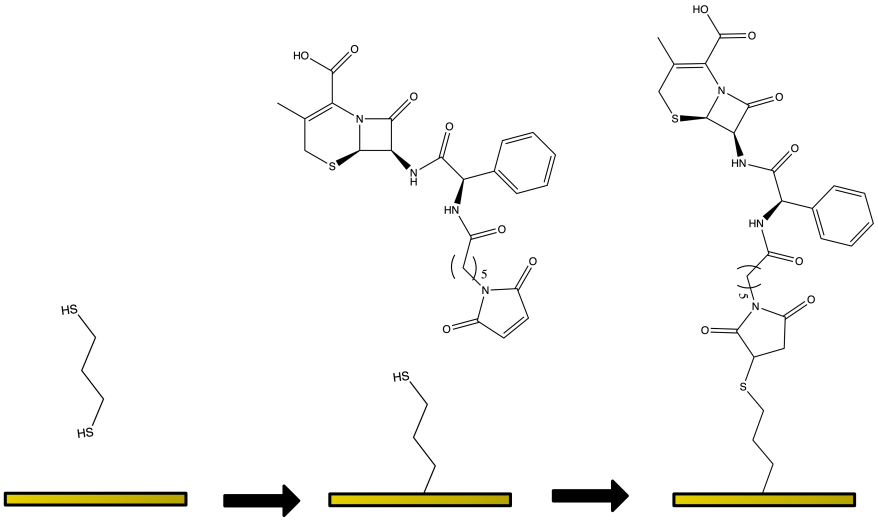

Figure 6.3: Structural diagram demonstrating the formation of the cephalexin-C6 functionalised surface using 1,3-propane dithiol.

PM-IRRAS analysis of the cephalexin-C6 functionalised surface confirmed that the β-lactam ring remained intact once bound to the surface, indicated by the presence of a small IR band at 1776 cm^{-1}, characteristic of the β-lactam ring (Figure 6.4 - Blue) [352]. As expected, analysis of an unfunctionalised planar gold surface showed no similar characteristic peaks (Figure 6.4 - Red). This work demonstrated that this protocol met at least the first of the three criteria discussed above; the immobilisation procedure did not alter the active region of β-lactam antibiotic, the β-lactam ring.

Following successful immobilisation of the cephalexin-C6 molecule onto a gold surface,

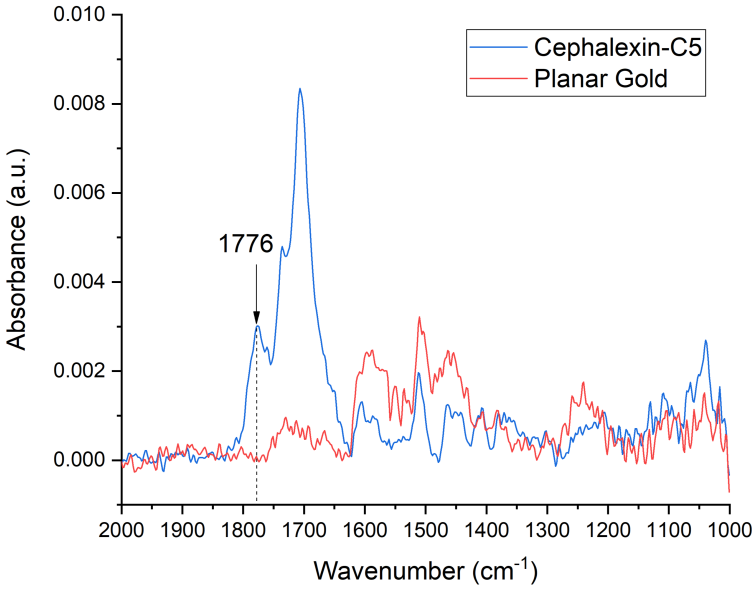

Figure 6.4: PM-IRRAS spectra of cephalexin-C6 bound to 1,3-propane dithiol on a planar Au surface (Blue) and a planar gold surface (Red). The highlighted peak at 1776 cm^{-1} is indicative of the β-lactam ring present within the cephalexin-C6 structure.

the second criterion was tested, confirming the ability of this surface-bound β-lactam to be recognised and hydrolysed by β-lactamases. For this work, a blend of recombinant β-lactamase proteins, expressed in E. coli, was purchased from Sigma-Aldrich (L7920) and used without further purification. This stock contained 40-70 IU β-lactamase I and 6-10 IU β-lactamase II, which was diluted 6-fold. Concentrations were maintained at this dilution throughout all surface-bound cephalexin experiments.

A planar gold surface was functionalised with cephalexin-C6 using the aforementioned protocol. This sample was then immersed in a solution of 50 mM potassium phosphate buffer (KPi), spiked with β-lactamases. To ensure the enzymes were behaving optimally, the surface was incubated at 37 °C for 2 hours to allow the enzymes to hydrolyse the surface-bound drug. Following incubation, PM-IRRAS showed the disappearance of the 1776 cm^{-1} β-lactam carbonyl band, confirming that hydrolysis has occurred, shown in figure 6.5 - Red. This hydrolysis was confirmed to be enzyme-catalysed, as the surface was shown to be stable without the presence of β-lactamases (Figure 6.5 - Green). Although PM-IRRAS is not completely quantifiable, the reduction in absorption is indicative of removal of a bond type.

Unfortunately, it was also noted that after exposure to β-lactamases, PM-IRRAS showed the appearance of a large band centred around the amide I region (1623-1698 cm^{-1}), indicating protein fouling [353]. To prevent any interference with whichever surface-affinity biosensor the surface-bindable β-lactam is used, the immobilised drug layer should allow for the β-lactamase to hydrolyse the β-lactam ring and then detach from the surface. The inability to do this, as shown in figure 6.5, was thought to be a potential issue as any measurement of hydrolysis could be masked by a large enzyme interference. Due to the semi-quantitative nature of PM-IRRAS, it was not possible to quantify the protein

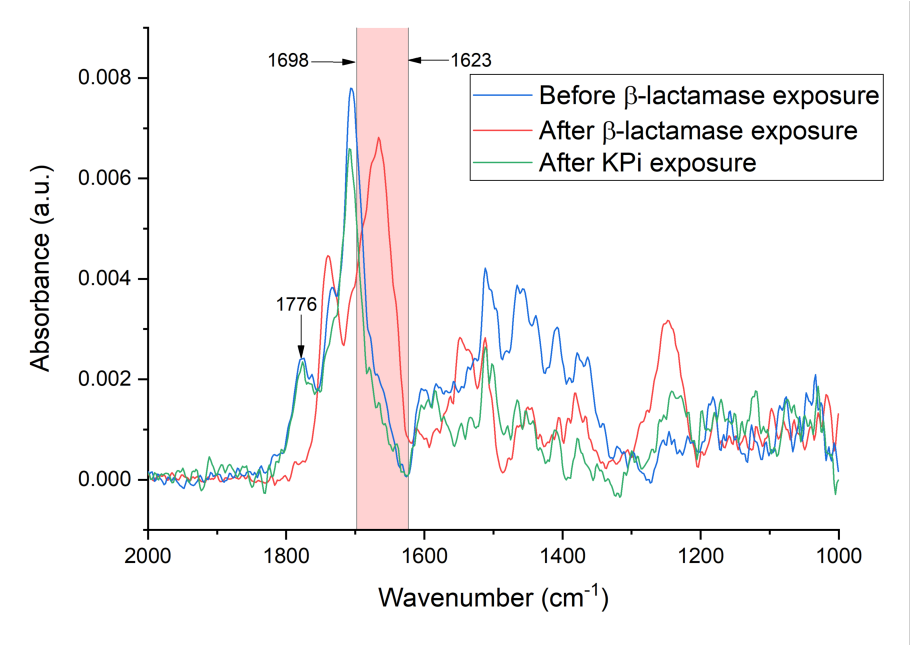

Figure 6.5: PM-IRRAS spectra of a cephalexin-C6 functionalised planar gold surface before (blue) and after (red) a 2 hr exposure to β-lactamases as well as a cephalexin-C6 surface after a 2 hr exposure to KPi (Green). The disappearance of the highlighted peak at 1776 cm^{-1}, after exposure to β-lactamases is indicative of enzyme-mediated β-lactam hydrolysis. The appearance of the amide I band at 1623-1698 cm^{-1} indicates protein fouling.

fouling using this method, as even small amounts of protein fouling can still introduce a large amide I band.

To investigate enzyme fouling, and to further confirm the ability of the surface-bound drug to react to the presence of β-lactamases, Quartz Crystal Microbalance with Dissipation (QCM-D) was used, as this technique allows for quantifiable measurements of surface-adhered layers. Dissipation data was taken for this work (Figure 6.6 - Dashed lines); however, no significant details were obtained. For clarity, only the frequency data is presented and discussed herein. In order to explore the versatility of the surface-bound antibiotics, as well as the differences that the substrate could have on surface fouling, two different materials were investigated. QCM-D sensors coated with either Au or SiO_2 were functionalised with cephalexin-C6. Cephalexin-C6 was immobilised onto the Au sensors using the previously discussed thiol-SAM method. This surface chemistry was adapted for the SiO_2 sensors using 3-mercaptopropyltrimethoxysilane (MPTS), a silane-based chemical, typically used for thiolation of oxide surfaces. As was predicted by the previous PM-IRRAS measurements, a large amount of fouling was seen on Au and SiO_2 sensors after the introduction of β-lactamase (Figure 6.6). For sensors coated with cephalexin-C6, only a small reduction in β-lactamase fouling was seen after washing with 2% sodium dodecyl sulfate (SDS) solution, with both the functionalised Au and SiO_2 sensors adsorbing approximately 230±81 ng and 500±30 ng of irremovable enzymes, respectively. QCM-D assays were performed in duplicate and thus the error in bound enzyme is the standard deviation across the two replicates.

The inability to remove any of the surface-bound enzyme from the cephalexin-C6

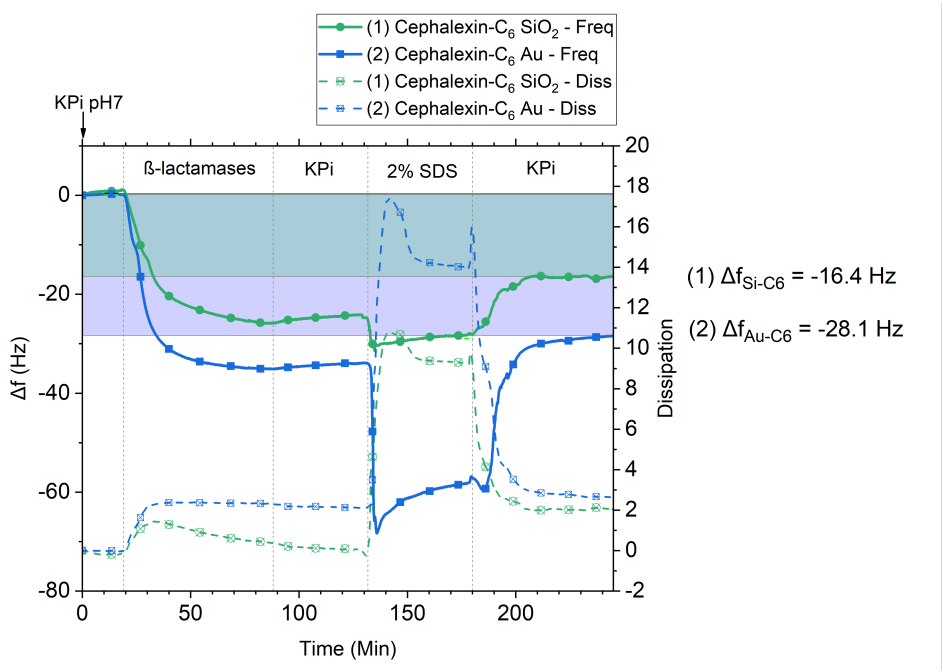

Figure 6.6: QCM-D experiment comparing β-lactamase fouling on: cephalexin-C6 on SiO_2 ((1)-Green) and cephalexin-C6 on Au ((2)-Blue). Frequency data is marked with a solid line and dissipation data is marked with a dashed line. The introduction of each solution is indicated by vertical dashed lines and is labelled in each section. The running order for this experiment was: 1-KPi; 2-β-lactamases; 3-KPi; 4-2% SDS; 5-KPi. The magnitude of the shift in frequency is noted at the end of each trace and is highlighted along the frequency axis.

surface meant that this molecule did not fit the criteria needed to be a suitable β-lactamase probe. Therefore, a second molecule was synthesised and tested which contained a different tether, in the hope that this would reduce the surface-fouling.

6.3 Functionalisation and Testing of a Surface-bound PEG Tethered Cephalexin.

The six-chain carbon linker was replaced with a four-subunit Poly Ethylene Glycol (PEG) linker, shown in figure 6.7b. The chosen PEG tether has two main advantages over the previous alkane chain. First, PEG molecules have been shown to inhibit physisorption of proteins onto surfaces [354, 355]. Secondly, due to the flexibility of PEG, they also allow conformational manoeuvrability of the attached molecule [356], which may improve access to the β-lactam ring. The PEG-tethered β-lactam will be referred to as cephalexin-PEG from this point. As shown in the PM-IRRAS spectra of figure 6.7a - Blue, replacing the tether on the surface-bindable drug did not affect the ability of the β-lactam ring to remain intact once bound, as the band around 1776 cm^{-1} was still present. Hydrolysis of the surface bound cephalexin-PEG by the β-lactamases was also still observed; however, the IR amide I band (1623-1698 cm^{-1}) still remained, indicating that protein fouling of the surface was still occurring.

To quantify this fouling, further QCM-D analysis was performed following the same protocol used for the previous enzyme fouling measurement, replacing the cephalexin-

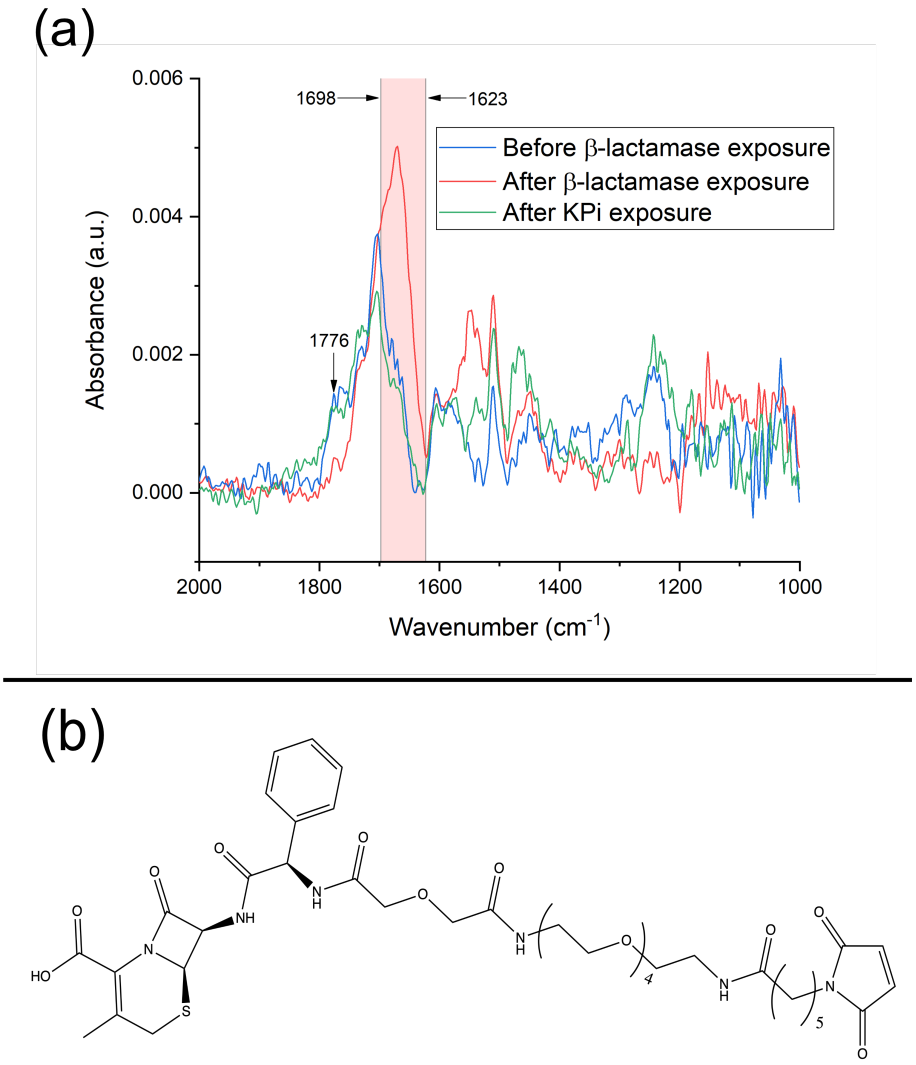

Figure 6.7: **(a)** - PM-IRRAS spectra of a cephalexin-PEG functionalised planar gold surface before (blue) and after (red) a 2 hr exposure to β-lactamases as well as a cephalexin-PEG surface after a 2 hr exposure to KPi (Green). The disappearance of the highlighted peak at 1776 cm^{-1}, after exposure to β-lactamases indicates that enzyme-mediated β-lactam hydrolysis was still possible when the carbon-chain tether was replaced with a PEG linker. The appearance of the amide I band at 1623-1698 cm^{-1} indicates protein fouling is still occurring. **(b)** - Structural diagram of the PEG tethered cephalexin, terminated with a maleimide functional group.

C6 with cephalexin-PEG. As expected, sensors coated with cephalexin-PEG analogue appeared to show a larger resilience to fouling in comparison to the cephalexin-C6 coated sensors. The Au sensor showed almost total removal of the enzyme after washing in SDS, with, approximately, 40±5 ng remaining (Figure 6.8 - Orange). SiO_2 sensors showed some fouling remained (105±76 ng)(Figure 6.8 - Purple), however this was, on average, less than was observed with the cephalexin-C6 coated sensors. Once again tests were carried out in duplicate and error reported is the SD across the two tests. Given the reduction of biofouling, all subsequent QCM-D analyses were performed using Au and SiO_2 sensors functionalised with cephalexin-PEG.

To ensure that the differences in the amount of enzyme fouling between substrate ma-

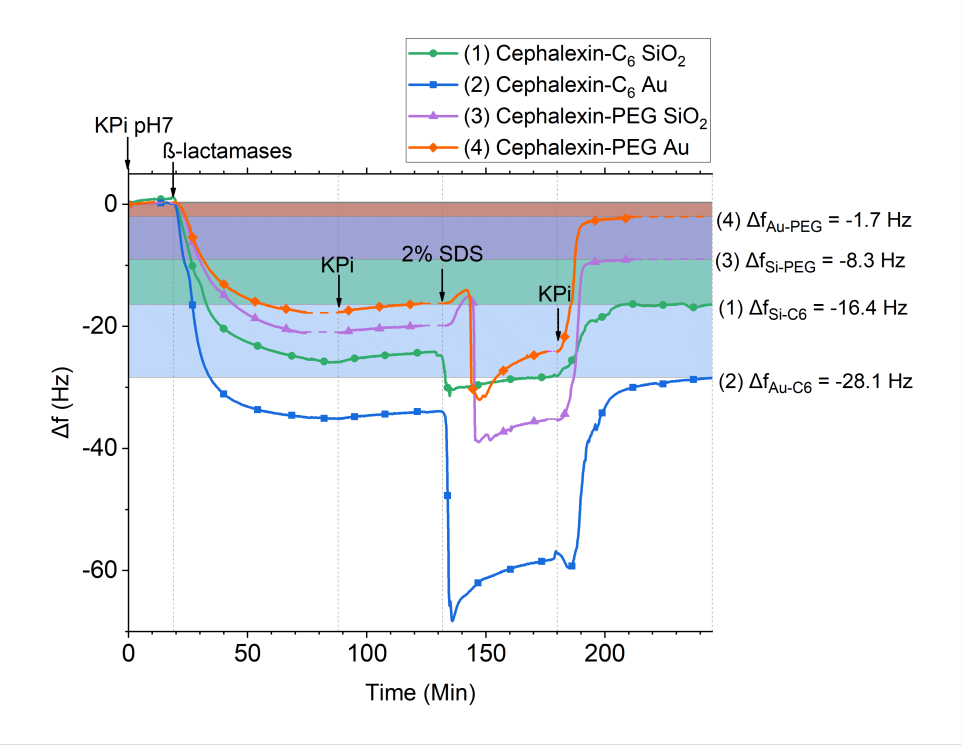

Figure 6.8: QCM-D experiment comparing β-lactamase fouling on: cephalexin-C6 on SiO_2 ((1)-Green); cephalexin-C6 on Au ((2)-Blue); cephalexin-PEG on SiO_2 ((3)-Purple); and cephalexin-PEG on SiO_2 ((4)-Orange). To produce the initial thiolated layer, Au surfaces were functionalised using 1,3-propane dithiol and SiO_2 surfaces were functionalised with MPTS. The introduction of each solution is indicated by dashed lines and is labelled in each section. The running order for this experiment was: 1-KPi; 2-β-lactamases; 3-KPi; 4-2% SDS; 5-KPi. The magnitude of the shift in frequency is noted at the end of each trace and is highlighted along the frequency axis. Dashed data indicates where the trace has been shifted to align the introduction of each solution.

terials were not due to differences in functionalisation procedure, a QCM-D measurement was carried out of the cephalexin-PEG binding *in situ*. Au and SiO_2 sensors were thiolated using the previously discussed protocols, however the cephalexin-PEG functionalisation was now performed in flow during the measurement. Measurements of these surfaces showed that the concentration of cephalexin-PEG was comparable on both the Au and SiO_2 coated sensors (Figure 6.9). Both coatings were calculated to have comparable densities of approximately $1.8\times10^{14}\pm2.4\times10^{12}$ molecules/cm^2 for SiO_2 and $1.4\times10^{14}\pm5\times10^{13}$ molecules/cm^2 for Au, both of which are typical densities for PEG monolayers [349, 357]. This result demonstrates the universality of this surface-bindable β-lactam and its compatibility with variety of biosensor surfaces.

Unlike PM-IRRAS, QCM-D measurements are not able to detect whether the β-lactam surface has been hydrolysed. Even without surface-fouling, the drug-enzyme complex is short-lived and there is no significant change in mass of the surface-bound drug after β-lactam hydrolysis. In this case, a secondary probe is required to confirm hydrolysis. Penicillin-binding protein (PBP) was chosen in this instance, as it is the pharmaceutical target of β-lactam antibiotics. This protein covalently binds to active β-lactams, allowing confirmation of both the orientation and state of the surface-bound β-lactams (Figure 6.10). Expression and purification of the PBPs was carried out by LMM and RH. Details

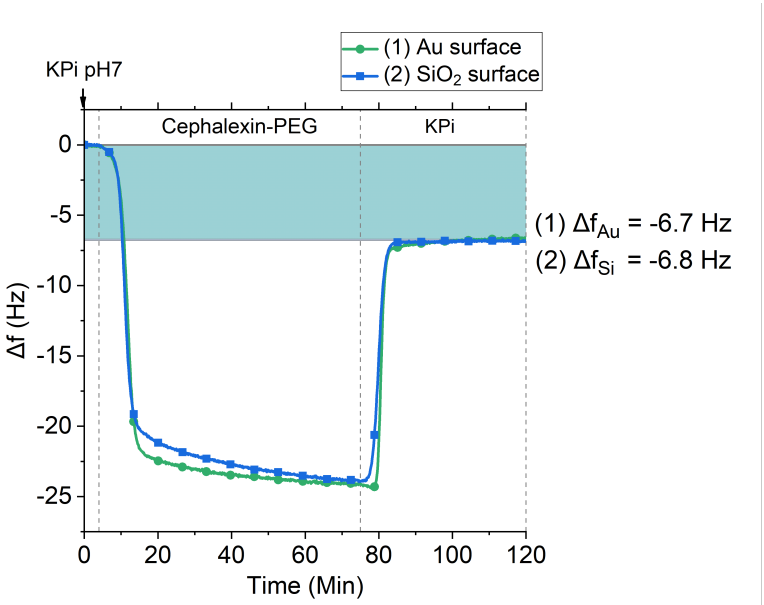

Figure 6.9: QCM-D experiment monitoring cephalexin-PEG binding to surfaces of: Au coated with 1,3-propane dithiol ((1)-Green), and SiO_2 coated with MPTS ((2)-Blue). The introduction of each solution is indicated by dashed lines and is labelled in each section. The running order for this experiment was: 1-KPi; 2-cephalexin-PEG; 3-KPi. The highlighted bars on the frequency axis show the shift for both Au and SiO_2.

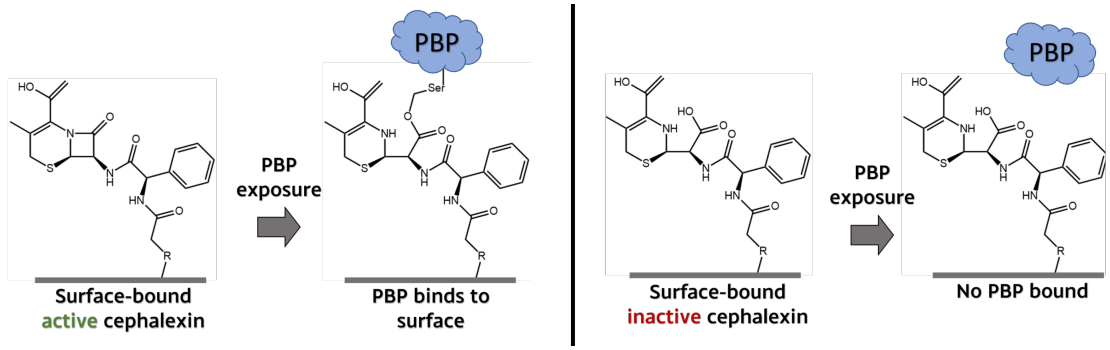

Figure 6.10: Diagram showing the use of PBP as a functional probe for QCM-D studies. As shown, only surfaces with intact β-lactam rings should covalently bind to PBP.

of this work are described in the published manuscript [337]. Protein concentration was determined using the Beer-Lambert law from the absorbance at 280 nm with an extinction coefficient of 58790 M^{-1} cm^{-1}. For surface experiments using PBP, solutions were prepared to 1 μM protein in 50 mM KPi (pH 7).

PBP was confirmed as a suitable probe for hydrolysis using QCM-D measurements. Three sensors were functionalised with cephalexin-PEG. The first sensor was exposed to PBPs; the second was challenged with PBPs which had been pre-incubated with cephalexin to block the binding site, thus deactivating it; while the third was pre-exposed to 1 M NaOH for 30 min to chemically hydrolyse the β-lactam ring. Following this, the sensors were washed with 2% SDS to remove any non-specifically bound protein. As shown in figure 6.11, a significant shift in resonant frequency was observed when both the β-lactam ring and PBPs were active, suggesting that the density of PBPs bound to the surface was

circa 10^{12} PBPs/cm^2. This surface density is typical of a well-packed protein monolayer [358] and also suggests that PBPs are unable to bind to every surface-bound cephalexin molecules, as the approximate PBP density is nearly two orders of magnitude lower than the surface-bound cephalexin. However, this was expected due to the much larger size of PBP in comparison to the surface-bound β-lactam, thus, it would not be able to pack as densely. Conversely, it was shown that, when either component was deactivated, the number of PBPs bound to the surface was almost a magnitude lower, confirming the suitability of PBPs as a probe for active β-lactam rings.

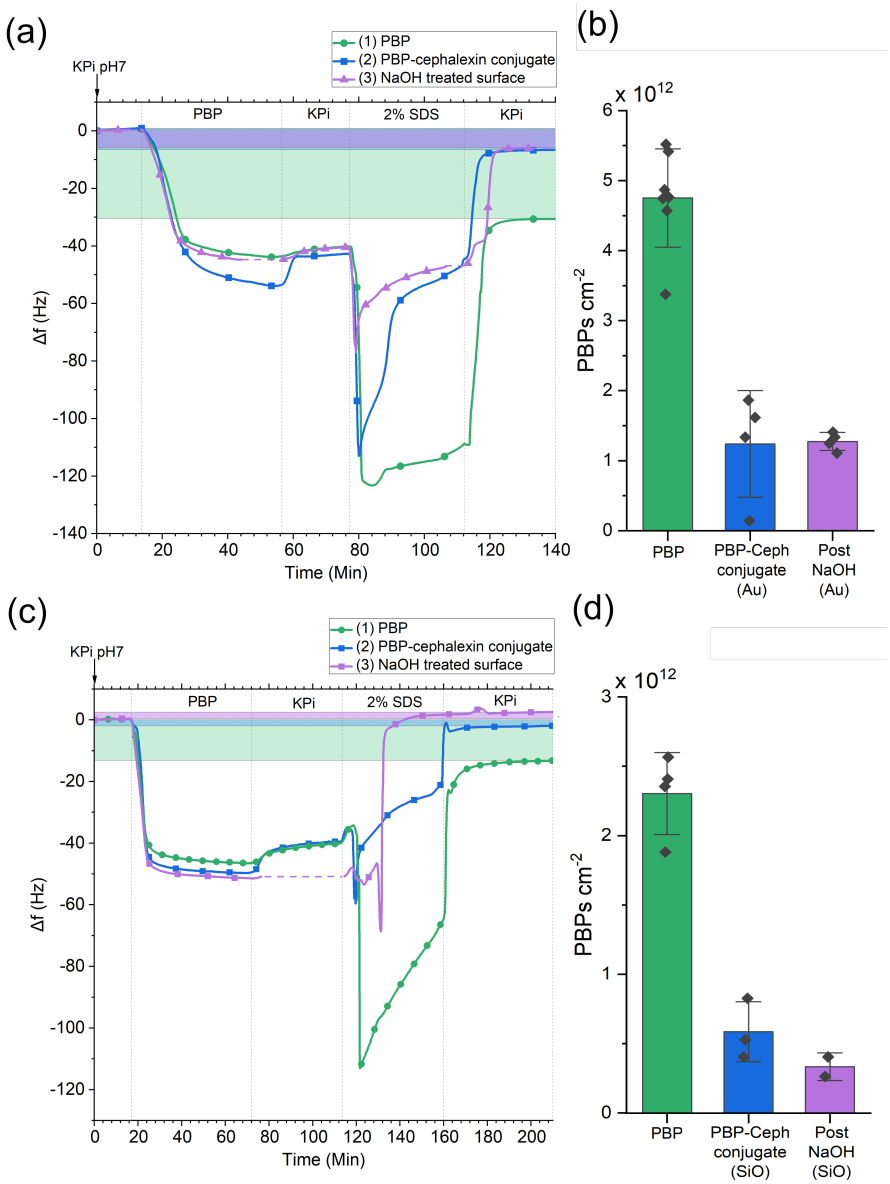

Figure 6.11: QCM-D experiment of cephalexin-PEG bound to Au **(a)** and SiO_2 **(c)** under three conditions: PBPs only ((1)-Green); PBP pre-incubated with cephalexin ((2)-Blue); PBP after the surface-bound cephalexin-PEG was pre-treated with NaOH to chemically hydrolyse it ((3)-Purple). The introduction of each solution is indicated by dashed lines and is labelled in each section. The running order for this experiment was: 1-KPi; 2-PBP; 3-KPi; 4-2% SDS; 5-KPi. Dashed data indicates where the trace has been shifted to align the introduction of each solution. The highlighted bars on the frequency axis show the shift due to the bound PBP. **(b)** and **(d)** show the density of PBP bound to Au and SiO_2 surfaces for each condition, respectively. Data reported as mean value across at least three repeats ± standard deviation.

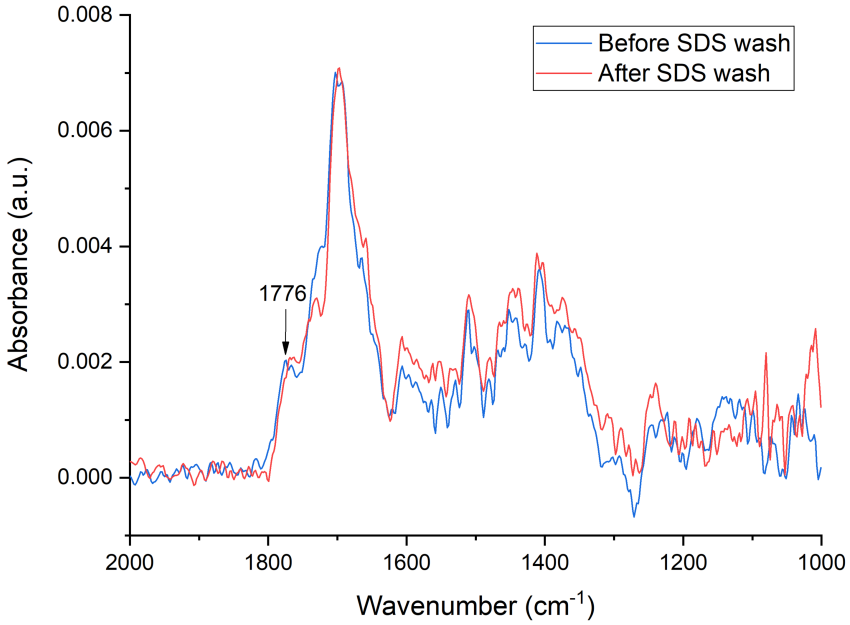

Figure 6.12: PM-IRRAS spectra of a cephalexin-PEG functionalised planar gold surface before (blue) and after (red) rinsing in 2% SDS solution. The highlighted peak at 1776 cm^{-1}, indicative of the β-lactam ring, remained after exposure to SDS.

As shown in figure 6.11, after washing with SDS, a large shift in resonant frequency was observed. This was initially thought to be due to viscosity differences between KPi and SDS, as this is known to affect QCM-D resonance. However, the shape and magnitude of the SDS step appeared to be larger when the PBP was thought to be covalently bound to the sensor (as is the case with PBP to intact cephalexin) (Figure 6.11 - Green). This difference in observed frequency was theorised to be due to the covalent nature of protein-drug bond. In cases where the protein is more strongly bound to the surface, it was thought that the surfactant would interact with the bound PBPs, but would be unable to remove them from the surface, causing a greater interaction between the surfactant and proteins leading to a larger decrease in the observed frequency. In cases where the proteins were not strongly bound to the surface, the SDS should simply assemble round the proteins and remove them from the surface, leading to a smaller decrease in frequency. Unfortunately, there was no simple way to confirm whether this was the case, thus, this was simply an observation. There was also a concern that SDS would disrupt the intact β-lactam or remove the surface-bound cephalexin-PEG. However, PM-IRRAS measurements of a cephalexin-PEG surface before and after washing with 2% SDS showed no significant change in the observed β-lactam ring signal, indicating no interaction between the SDS and β-lactam ring, as well as strong adhesion to the surface (Figure 6.12).

After confirming the suitability of PBP as a probe for β-lactam hydrolysis, additional QCM-D measurements were performed to further confirm the suitability of the cephalexin-PEG surface for the detection of β-lactamases. After challenging the cephalexin-PEG surface with β-lactamases, significantly less binding of PBPs ($2.68\times10^{12}\pm2.6\times10^{11}$ PBPs/cm^2 (Au) and $5.85\times10^{11}\pm4.38\times10^{11}$ PBPs/cm^2 (SiO_2)) was seen in comparison to the unex-

posed surfaces ($4.75\times10^{12}\pm7\times10^{11}$ PBPs/cm^2 (Au) and $2.3\times10^{12}\pm2.95\times10^{11}$ PBPs/cm^2 (SiO_2)), further confirming the surface hydrolysis (Figure 6.13). In contrast, after exposing the surface to sulbactam-inhibited β-lactamase, using the same method described in chapter 5, a slight reduction in PBP binding was seen, however, it appeared that PBPs were still capable of binding to the surface. It should be noted that the binding seen after exposure to inhibited enzyme was $3.8\times10^{12}\pm1.2\times10^{11}$ PBPs/cm^2 (Au) and $1.29\times10^{12}\pm6.7\times10^{11}$ PBPs/cm^2 (SiO_2), a slightly reduced amount in comparison to the un-exposed surface, implying that the inhibition was at least somewhat effective. The discrepancy was thought to be caused by either β-lactamase fouling of the surface, and thus blocking some of the binding sites, or incomplete inhibition of the enzyme, as the blend of β-lactamase used for this project contained some metallo-enzymes, known not to be inhibited by this compound, leading to partial hydrolysis of the surface. It was also noted that the aforementioned increase in frequency after the introduction of SDS was lower for β-lactamase exposed surfaces. It is believed that these results, combined with the PM-IRRAS data (Figure 6.7), confirm that β-lactamases are still capable of hydrolysing the surface-bound antibiotics, thus proving their capability for β-lactamase activity detection.

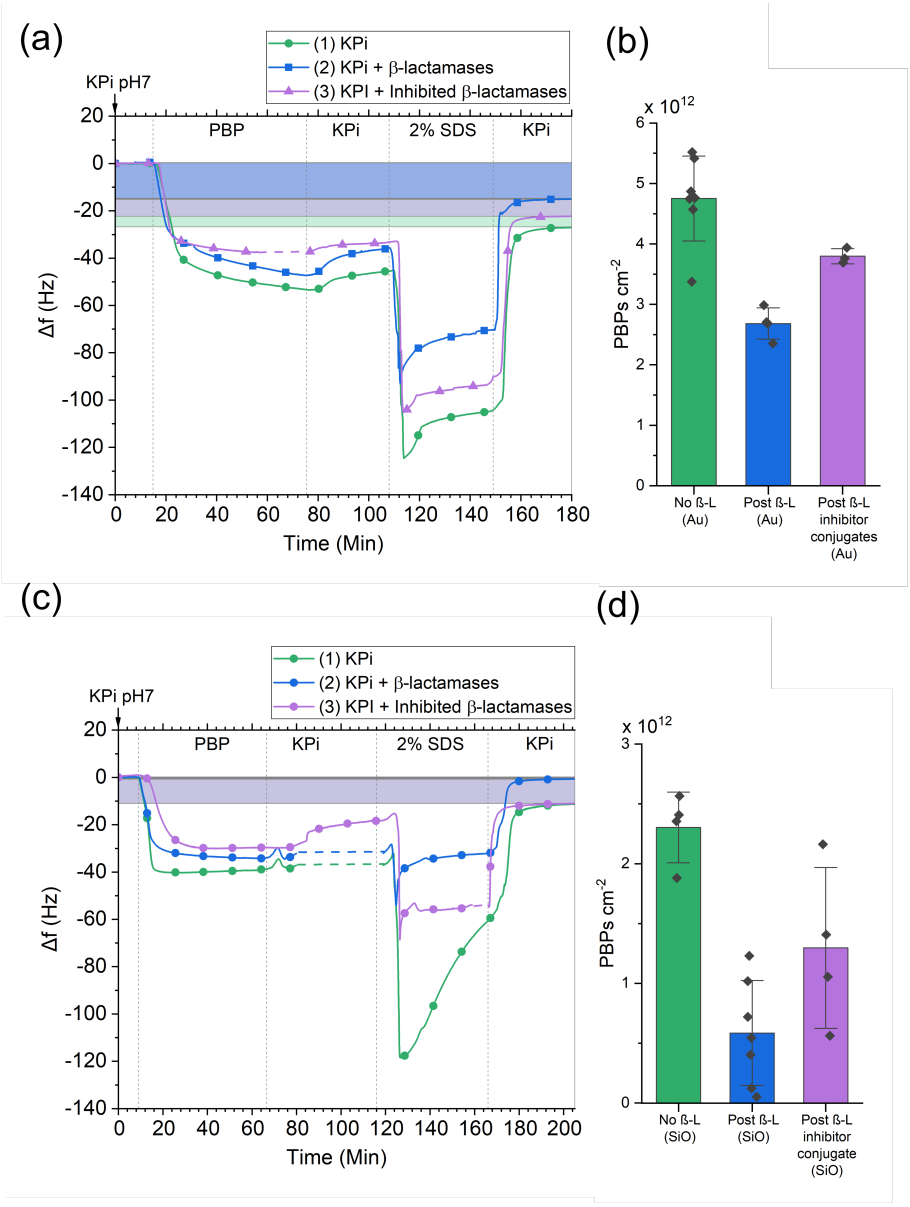

Figure 6.13: QCM-D experiment showing PBP binding to a planar Au **(a)** and SiO_2 **(c)** cephalexin-PEG surface under three conditions: No treatment ((1)-Green); after exposure to β-lactamases ((2)-Blue); after exposure to β-lactamases inhibited with sulbactam ((3)-Purple). The introduction of each solution is indicated by dashed lines and is labelled in each section. The running order for this experiment was: 1-KPi; 2-KPi (1), β-lactamases(2), or inhibited β-lactamases(3); 3-KPi; 4-2% SDS (2); 5-KPi; 6- PBP; 7-KPi; 8- 2% SDS; 9-KPi. For clarity, only the PBP binding steps have been shown in this figure. Dashed data indicates where the trace has been shifted to align the introduction of each solution. The highlighted bars on the frequency axis show the shift due to the bound PBP. **(b)** and **(d)** show the density of PBP bound to Au and SiO_2 surfaces for each condition, respectively. Data reported as mean value across at least three repeats ± standard deviation.

6.4 Testing the Cephalexin Surface for β-lactamase Detection in Complex Media

A stage often overlooked in novel susceptibility test development is the need for pathogenic cells to be isolated from clinical samples. As discussed in chapter 2, current techniques for bacterial isolation can take several days to complete, introducing a large delay in the time taken from sample collection to diagnosis and treatment. For rapid susceptibility testing to become viable, tests must be able to be performed directly on clinical samples [40]. To this end, this section demonstrates the amenability and selectivity of the surface-bindable β-lactam for the detection of β-lactamases in physiological samples of urine. Urinary-tract infections (UTIs) are one of the most common forms of bacterial infections, affecting millions of patients every year [359]. An alarming number of these infections show signs of resistance to β-lactam antibiotics [360, 361]. Therefore, being able to rapidly and reliably test for resistance to these drugs is necessary to provide effective treatment. Urine provides a non-invasive method of sampling a patient but, as a complex biological media, it contains a raft of cells, proteins, and other small molecules creating a challenge for in-matrix detection.

To test the cephalexin-PEGs capability in complex media, previous experiments were repeated using urine, rather than KPi. Urine samples were collected anonymously from thirteen healthy adults who had shown no symptoms of infection, nor taken antibiotics within one month prior to sample collection. Samples were filter-sterilised using 0.22 μm syringe filters to remove large particulates. To ensure the urine stock would not interfere with the β-lactam, LMM carried out HPLC measurements comparing cephalexin after 24 h in urine. As shown in figure 6.14, these tests showed no significant difference in the peak area between cephalexin in buffer (peak area = 2295023) and in urine (peak area = 2153543), indicating there were no β-lactamase present within the urine stock.

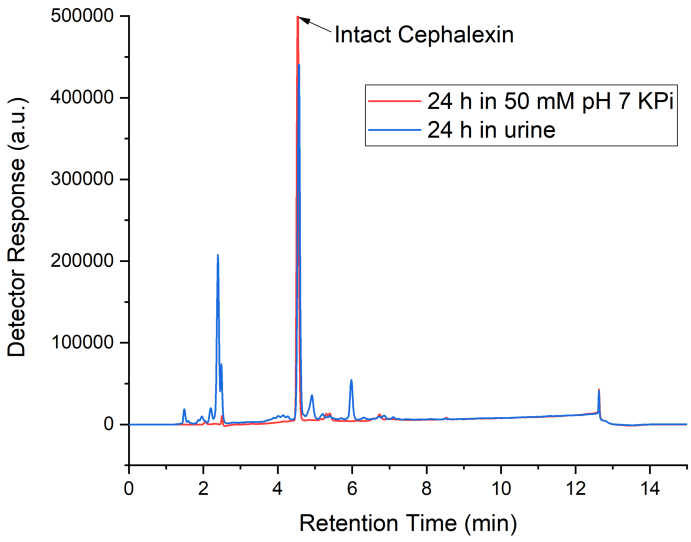

Figure 6.14: HPLC data showing the retention time of components within solutions of 4.6mM cephalexin in 50 mM KPi (Red) and urine (Blue).

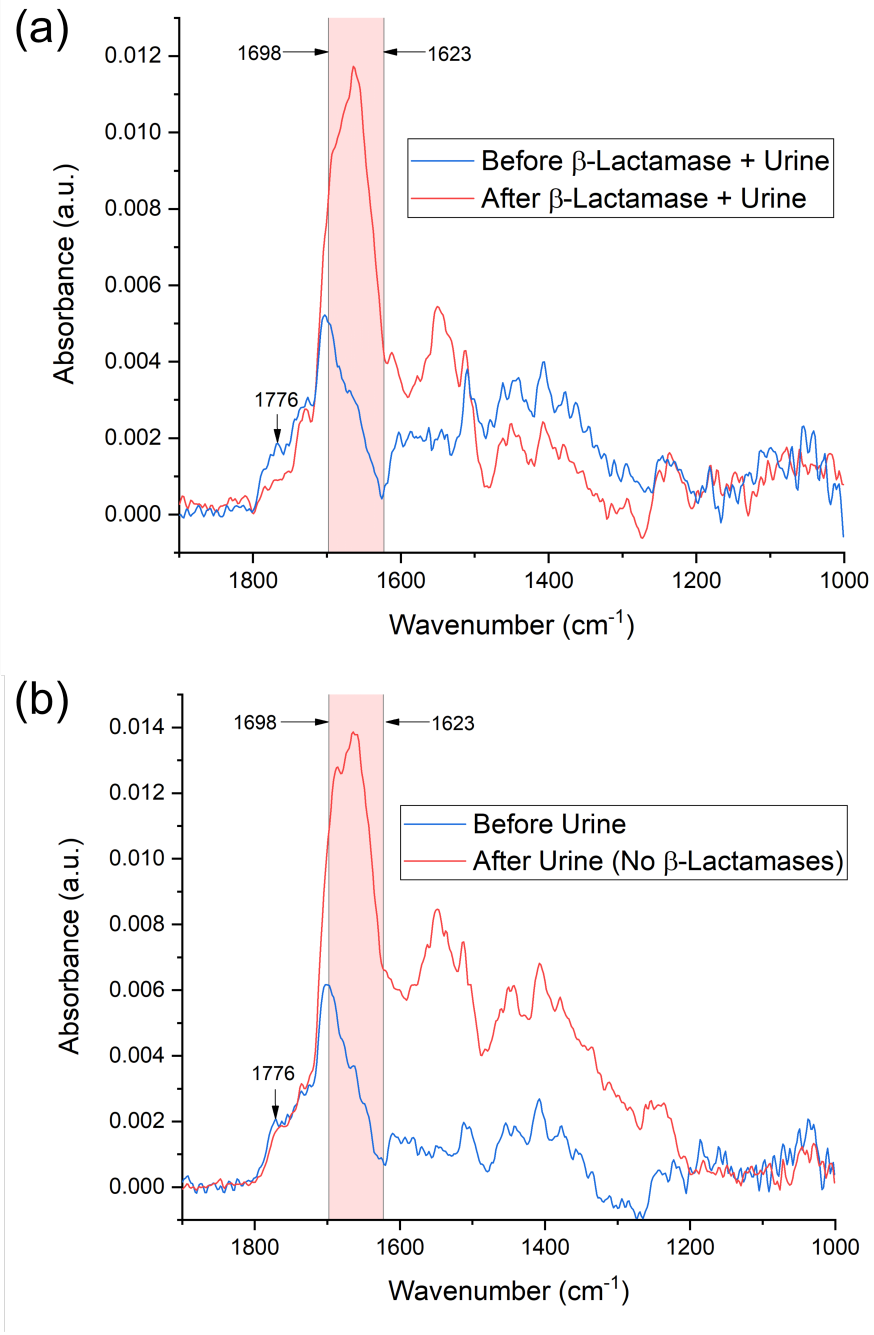

Figure 6.15: **(a)** - PM-IRRAS spectra of a cephalexin-PEG functionalised planar gold surface before (blue) and after (red) a 24-hour exposure to urine spiked with β-lactamases. The reduction of the highlighted peak at 1776 cm^{-1}, after exposure to β-lactamases indicates that enzyme-mediated β-lactam hydrolysis was still possible in urine. The large amide I band at 1623-1698 cm^{-1} indicates protein fouling. **(b)** - PM-IRRAS spectra of a cephalexin-PEG functionalised planar gold surface before (blue) and after (red) a two hour exposure to urine without β-lactamases. The highlighted peak at 1776 cm^{-1} remained after exposure to urine, indicating that no hydrolysis occurred. The large amide I band at 1623-1698 cm^{-1} indicates protein fouling.

PM-IRRAS experiments were carried out using the same functionalisation protocol on planar gold substrates used for previous KPi experiments. Following functionalisation with cephalexin-PEG, all samples were exposed to either urine spiked with β-lactamases or urine only. Initially, samples were exposed for 2 hours; however, when compared to the peak reduction seen in KPi tests, only a small change was seen after this short time. It is believed that this reduction in hydrolysis is due to an increase in biofouling, introduced by competing proteins in the urine. This increase in fouling was further indicated by a much larger increase in the amide I band (1623-1698 cm^{-1}). After an overnight incubation, the surfaces demonstrated β-lactam hydrolysis in response to β-lactamase exposure, with reduction in the β-lactam carbonyl band only being observed in the samples exposed to urine spiked with β-lactamases (Figure 6.15(a)). Exposure to urine without β-lactamases showed no obvious change, demonstrating the stability of the antibiotic surface in urine (Figure 6.15(b)). It should be noted that complete hydrolysis was not observed, even after overnight incubation. However, other than the introduction of the PEG linker, no further effort was made to reduce surface fouling, therefore the reduction in hydrolysis was not surprising.

QCM-D experiments further confirmed the capability of the drug surface for measurements in urine. Cephalexin-PEG-coated sensors were exposed to samples of urine, using the same conditions as the previously described PM-IRRAS experiments (overnight in urine spiked with β-lactamases or urine only). All sensors were washed after exposure to the urine to remove any non-specifically bound proteins. To ensure all sensors were cleaned to the same extent, washing was done once the sensors were loaded into the QCM-D. A steady flow of 2% SDS was washed over each sensor for 1 hour, allowing a consistent baseline to be achieved. As shown in Figure 6.16, considerably more PBP bound to the surfaces that has not been exposed to β-lactamases, confirming the cephalexin-PEG's ability to work in urine. Studies in urine were comparative to results obtained in KPi buffer (Figure 6.13); however, it can be concluded that fouling has a large effect on PBP binding to the cephalexin-PEG surface, as the results from tests using urine show a large decrease in the amount of bound PBP.

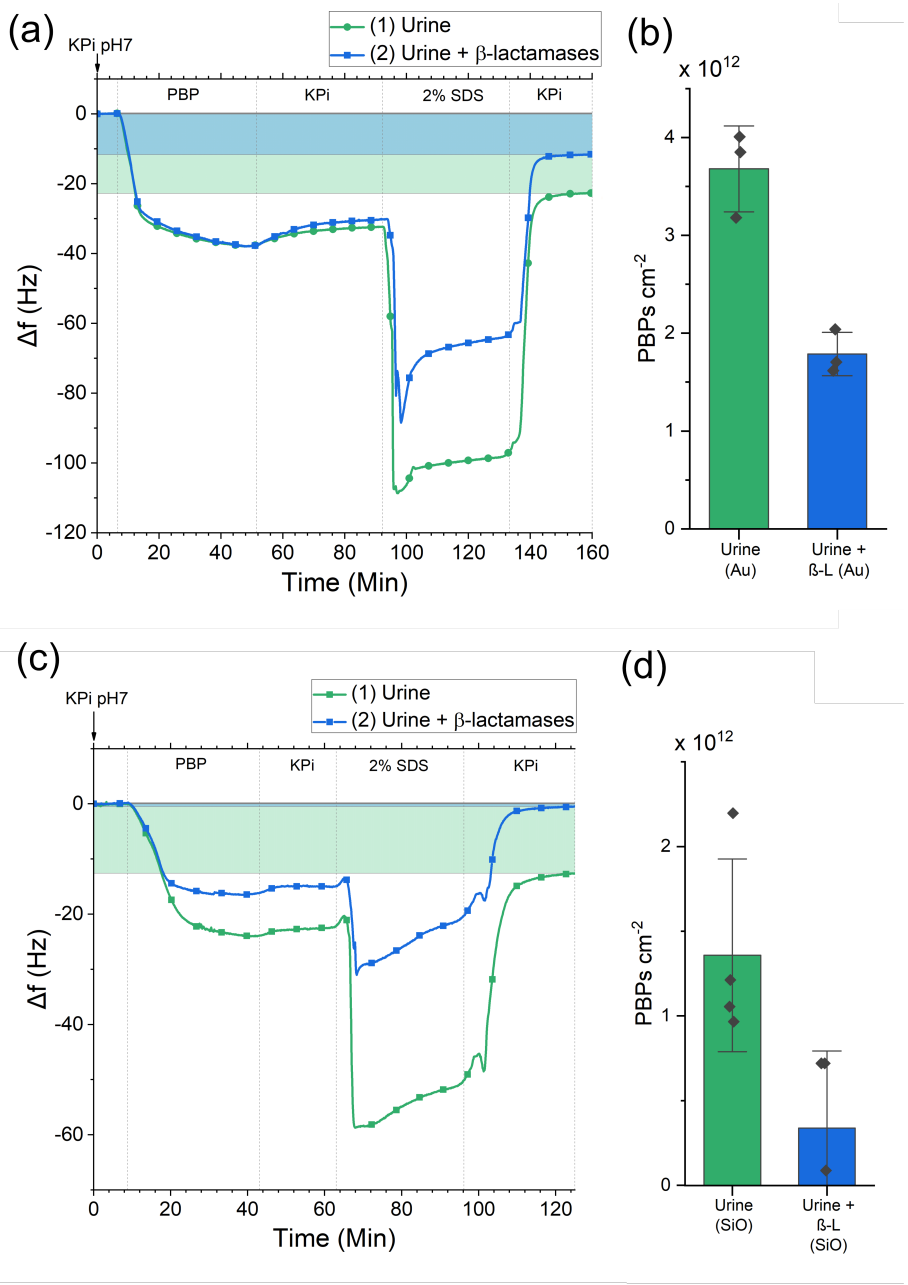

Figure 6.16: QCM-D experiment showing PBP binding to a planar Au **(a)** and SiO_2 **(b)** cephalexin-PEG surface under two conditions: after exposure to urine for 24 h ((1)-Green); after 24 h exposure to urine spiked with β-lactamases ((2)-Blue). The introduction of each solution is indicated by dashed lines and is labelled in each section. All sensors were exposed to urine before the experiment. The running order for this experiment was: 1-KPi; 2-2% SDS; 3-KPi; 4- PBP; 5-KPi; 6- 2% SDS; 7-KPi. For clarity, only the PBP binding steps have been shown in this figure. The highlighted bars on the frequency axis show the shift due to the bound PBP for each condition. **(b)** and **(d)** show the density of PBP bound to Au and SiO_2 surfaces for each condition, respectively. Data reported as mean value $\pm$ standard deviation.

6.5 Conclusions

In conclusion, this chapter discussed the development and testing of a surface-bindable β-lactam antibiotic, capable of reacting in the presence of β-lactamases within 2 hours. Studies using PM-IRRAS and QCM-D have shown the ability of the surface-bound β-lactam to hydrolyse in the presence of β-lactamase enzymes. The surface-bindable antibiotic has also been shown to work in complex media, such as urine. The ability to work in these media is a necessity for rapid diagnostic testing, as it would remove the need for bacterial isolation, allowing for direct testing on a clinical sample. It should be noted that testing in urine did increase the time-to-result; however, no further work was done to improve upon the surface fouling caused by the additional proteins.

Although only a single β-lactam compound has been tested in this work, it is believed that by using various surface-bound β-lactam antibiotics, it will be possible to determine resistance levels to specific β-lactam compounds. This technique of surface-bound antibiotics could be used for detection of other classes of resistance, as many of these are expressed by a lack of binding affinity towards a target protein. Therefore, surface-bound antibiotics could be used as probes for detecting the presence of target proteins using surface-affinity biosensors, indicating susceptibility towards the surface-bound antibiotic.

The surface-bindable β-lactam has also been shown to be compatible with multiple surface chemistries, making it compatible with a number of surface-sensitive biosensing technologies. Previous work has demonstrated the potential of surface-bound β-lactam probes on gold [362], however, none have demonstrated their use against β-lactamase enzymes on multiple substrates, using a fouling-reducing tether, or in complex media. It is hoped that by integrating this surface-bindable antibiotic with the EGFET device used in this project, the detected β-lactam-β-lactamase reaction will occur closer to the ion-sensitive surface, increasing the surface-concentration of H^+ ions. The outlook section in chapter 7 will discuss the integration of this surface-bindable β-lactam with the iridium oxide based EGFETs.

Chapter 7

Conclusions and Outlook

7.1 Summary and Conclusions

This thesis has described the development and testing of an IrO_x discrete EGFET device for use in a diagnostic assay for the detection of the most common form of antibiotic resistance, β-lactam resistance. The assay relies on the acidification of a weakly-buffered solution due to the β-lactam-β-lactamase reaction. Additionally, this thesis demonstrates the use of a surface-bindable β-lactam probe which responds to the presence of β-lactamase enzymes which could localise the acidification to the sensor surface, potentially increasing the limit of detection of the EGFET assay, or could be incorporated into a number of alternative surface-sensitive biosensor technologies.

As discussed in chapter 1, there is a need for technology which would enable accurate and effective prescribing behaviours of antibiotics at point-of-care. Many techniques exist for the detection of β-lactamases (Chapter 2, however, the currently used technologies suffer from a number of drawbacks. The phenotypic assays most commonly used rely on several overnight growth steps in order to obtain a result, at which point, an antibiotic has often been prescribed without any diagnostic knowledge of the infection, meaning it may not suitable [363]. Genotypic tests offer a faster time-to-result than the growth-based assays, however, their operation assumes a known gene is responsible for encoding the production of β-lactamase. In the case of new β-lactamase variants, performing these measurements as the only method for detection could lead to an ineffective prescription. Furthermore, their operation often requires bulky, expensive, and specialist equipment, making them impractical in many point-of-care settings. Colorimetric tests exist which allow the detection of specific β-lactamase enzymes using pH sensitive dyes in a point-of-care setting [17, 18]. The nature of these tests allows them to produce qualitative results, however, in cases of low-level expression of β-lactamase, these results have been shown to be ambiguous due to incomplete shifts in colour [134]. The work described in this thesis is the first example of acidimetric β-lactamase detection with a quantifiable readout which could be miniaturised to work in a point-of-care setting. Although quantitative detection may not be required for some applications, the voltage-based output of the developed device would also reduce the ambiguity of low-level detection, as its output is less subjective than the output produced by colorimetric assays.

In chapter 4, the development and testing of the bespoke IrO_x-based pH sensor was discussed. The device is based on the discrete extended-gate ion-sensitive field-effect transistor (EGFET) design discussed in a number of works [186, 191, 192]. The sensor uses a commercial, discrete MOSFET as the transducing element for an ion-sensitive extended electrode whose surface potential is dependent on the concentration of ions in the con-

nected solution. By connecting this electrode to the gate of the MOSFET, changes in the extended electrode surface potential can be read as changes in the source-drain current of the MOSFET, which can thus be turned into a simply-measured voltage. The devices demonstrate a high pH-sensitivity of up to $\approx$ 75 mV/pH, higher than the typical Nernstian limit seen by other pH sensing instruments, as well as a good time-response of $<$ 2 s between pH changes. It was noted that these devices did show a large variability in sensitivity, however, although a majority of the devices showed sensitivities between 47-63 mV/pH. XPS analysis of the IrO_x film indicated that a mixture of Ir(III) and Ir(IV) existed at the surface. The ratio of these two oxidation states has been shown to relate to the device sensitivity [229], which may give some indication as to why a large variability was seen and could be explored further in future work. Even considering the variability of the devices, the sensitivity and noise level allowed for limits of detection of a $<$ 0.09 change in pH. Further investigation into the physical properties of the EIROF also showed that the surface is an amorphous, nanoporous film with a high level of hydration, typical of those which demonstrate high pH sensitivity [230]. Analysis of the ion-sensitive electrode parameters, such as film thickness and electrode size, did not appear to show any correlation with device sensitivity; however, any association may have been masked by the large variation in the observed sensitivity between devices.

Following the development of a pH sensitive EGFET device, chapter 5 discussed the development and measurement of a β-lactamase acidimetric assay. In this work, the mechanism through which the β-lactam acidification occurs was explored in detail, as this has not been discussed previously. Specifically, pK_a and isoelectric simulations were carried out of ampicillin in both its intact and hydrolysed forms, giving an indication of the overall differences in protonation and deprotonation between each molecule, which lead to a change in overall solution pH. By combining this β-lactam hydrolysis with a low-molarity buffer, a measurable pH change of $\approx$ 1 pH level was obtained in under an hour, significantly greater than the limit of detection (0.09 pH units). Exploiting this low LOD, devices were shown to be able to measure the expected correlation between β-lactam concentration and observed pH change. Interestingly, the slow response time of many other pH sensors, such as the glass electrode, would not be suitable for measuring the time-resolved pH change required for these kinetic measurements. With a time-response found to be greater than 2 pH levels per second for the developed devices, the rate of pH change due to β-lactam hydrolysis over time could be measured. This quantity was found to be correlated to the β-lactamase concentration and the acidimetric assay demonstrated measurements of β-lactamase activity down to 1 $\%v/v$ of the purchased β-lactamase stock concentration, equating to approximately 0.4-0.7 IU β-lactamase I and 0.06-0.1 IU β-lactamase II. However, the clinical relevance of these concentrations is unknown and testing of this assay in the future should investigate the response of assay to specific, clinically relevant, β-lactamase enzymes.

Finally, the development of a surface-bindable β-lactam molecule which is capable of reacting in the presence of β-lactamases was presented in chapter 6. Previous work had demonstrated the potential of surface-bound β-lactam probes on gold [362]. However,

their work only showed the use of a short-tether against a penicillin recognition protein and did not consider its use for β-lactamase detection. In this work, a cephalexin β-lactam molecule was synthesised to include a maleimide-tagged tether. Studies using PM-IRRAS and QCM-D demonstrated the ability of the surface-bound β-lactam to hydrolyse in the presence of β-lactamase enzymes. Initially, the employed tether was a carbon-chain linker, however, investigation of the surface using QCM-D showed that surfaces coated in this molecule were liable to surface-fouling of the β-lactamase enzymes, which could interfere with surface-sensitive biosensor measurements of this probe. In an attempt to reduce fouling, the carbon-chain tether was replaced with a PEG tether, which have been shown to reduce the physisorption of proteins [354, 355]. This tether was shown to reduce the surface adhesion of the β-lactamase enzymes somewhat, however, further work is required to inhibit surface-fouling entirely. The surface-bound cephalexin-PEG was shown to react to the presence of β-lactamase in under two hours, showing complete hydrolysis of the probe in this time. Furthermore, the surface-bindable cephalexin-PEG was shown to be compatible with multiple surface chemistries, enabling its use with a number of surface-sensitive biosensing technologies utilising different surface materials. Finally, the surface-bindable antibiotic was also shown to work in urine, a complex media containing a number of other components. The ability to work in these media is a necessity for rapid diagnostic testing, as it removes the need for overnight processes such as bacterial isolation, allowing for direct testing on a clinical sample at the point-of-care. It is hoped that by combining this surface-bindable antibiotic with the EGFET device used in this project, the detected β-lactam-β-lactamase reaction will occur closer to the ion-sensitive surface, increasing the surface-concentration of H^+ ions.

7.2 Outlook and Future Work

This thesis has introduced the use of an IrO_x EGFET pH sensor for the detection of β-lactamase using a developed assay as well as the development and testing of a surface-bindable β-lactam which can be incorporated into a number of surface-sensitive biosensors. However, a number of elements have to be addressed before this technology can be implemented at point-of-care. Furthermore, several areas could be explored in order to improve the reliability and viability of the device. Some work has been done to explore these areas, however, there is more to do. This section will discuss some of the work done on these potential avenues as well as the further work which needs to take to place to achieve these goals.

7.2.1 Integration of the Surface-bindable Cephalexin onto the EGFET Sensor

An application which was hoped to be explored in this work was the combination of the surface-bindable cephalexin-PEG and the IrO EGFET pH sensor. It was thought that bringing the β-lactamase reaction closer to the sensor surface may improve the signal-to-noise ratio, as has been demonstrated in other work [19]. Some work was done towards this

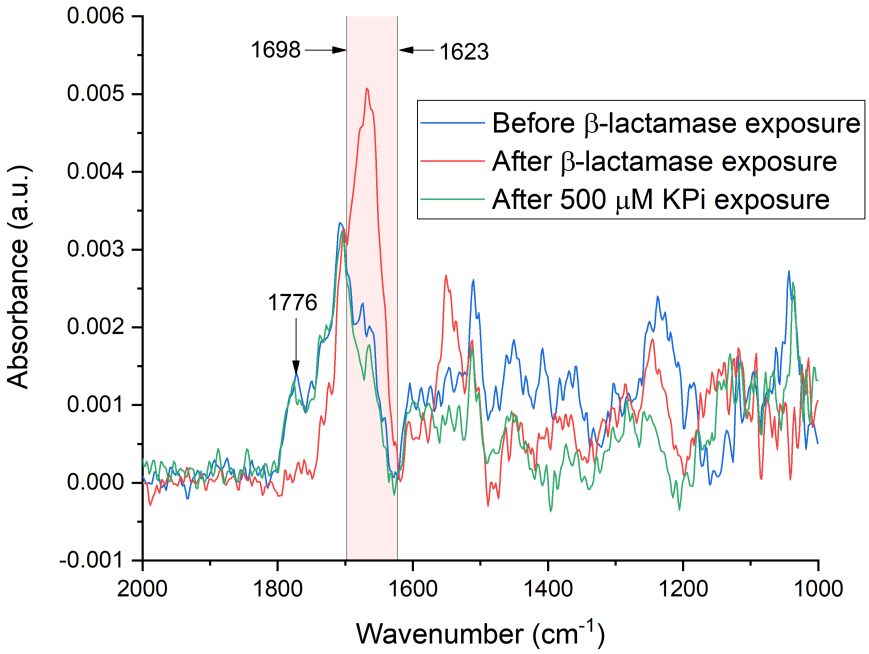

Figure 7.1: PM-IRRAS spectra of a cephalexin-PEG functionalised planar gold surface before (blue) and after (red) a 2 hr exposure to β-lactamases in 500 μM pH 7 KPi buffer as well as a cephalexin-PEG surface after a 2 hr exposure to KPi (Green). The highlighted peak at 1776 cm^{-1} is indicative of the β-lactam ring in the cephalexin-PEG. The appearance of the amide I band at 1623-1698 cm^{-1} indicates protein fouling is occurring.

integration of the two technologies, however, more needs to be done to confirm whether this will improve the output of the β-lactamase assay.

If the assay is to be used to detect pH changes due to the hydrolysis of the surface-bound cephalexin-PEG, then the cephalexin-PEG must be able to be hydrolysed in the presence of β-lactamases in low-molarity buffer, as was used in chapter 5 for the solution-phase β-lactamase assay. In order to determine whether this was the case, the PM-IRRAS experiments carried out in chapter 6 were repeated using the optimised pH 7, 500 μM buffer. Experiments were carried out using planar 100 nm thick Au surfaces, fabricated on top of Si wafers using electron-beam evaporation. These substrates were functionalised with cephalexin-PEG using the 1,3-propane dithiol protocol discussed in chapter 6. Following functionalisation, the surfaces were exposed to β-lactamases in 500 μM pH7 KPi at the same 6-times dilution used in chapter 6 for 2 hours in a 37 °C incubator. PMIRRAS results showed clear enzymatic hydrolysis of surface-bound β-lactam in the low molarity buffer, comparable to the hydrolysis observed using 50 mM KPi buffer, as demonstrated in chapter 6 (Figure 7.1 - Red). Furthermore, no degradation was seen after exposure to the low-molarity buffer without β-lactamases, suggesting the cephalexin-PEG is still stable (Figure 7.1 - Green).

In order to combine the cephalexin-PEG and the IrO_x, a compatible surface functionalisation protocol has to be developed. There is evidence to suggest that a silane-based functionalisation, such as MPTS, will work on the IrO_x film, as these layers have been shown to work on other metal-oxides [364–367]. However, confirmation of this surface-

functionalisation is not possible using the previously used techniques, as PM-IRRAS requires an IR-reflective substrate. An attempt was made to fabricate an EIROF-coated QCM-D sensor, however, the films appeared to lower the mass sensitivity of the QCM-D sensor significantly, making measurements of the cephalexin-PEG impractical using this method. If the cephalexin-PEG and EGFETs are to be reliably combined in the future, then a technique must be used to confirm the presence of a functionalised surface. One method to do this would be to use a secondary maleimide-tagged probe with a fluorescent or redox active tag to ensure the formation of the thiolated layer. Although this method is not ideal, as it only confirms the presence of a thiolated layer, this would determine a suitable thiolation protocol for the EIROF which would in-turn allow for surface modification with the maleimide-tagged cephalexin-PEG. Confirmation of the cephalexin-PEG layer was not carried out in this work, however, to determine whether MPTS-cephalexin-PEG would have any detrimental effect on the device sensitivity, three devices were measure before and after functionalisation. As shown in figure 7.2, some difference were seen across the sensors after functionalisation and the pH sensitivity was maintained within the variability observed between EIROF EGFET devices. There also appears to be a narrower distribution in the spread of sensitivities after functionalisation which may be due to the formation of identical surfaces across the devices, however, this was not explored any further and could be the subject of future work.

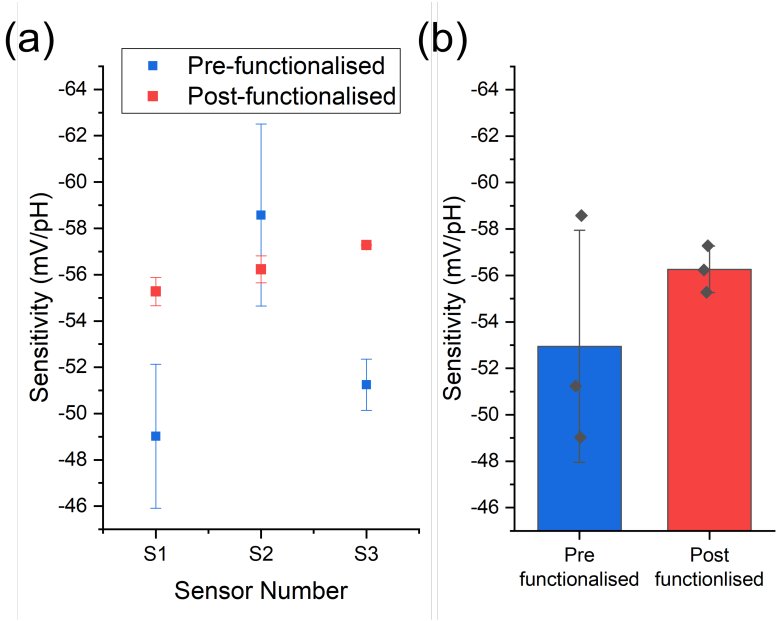

Figure 7.2: **(a)** Calculated sensitivity of four EGFET devices before (Blue) and after (Red) functionalisation with MPTS and cephalexin-PEG. Error is reported as the SE of the pH sensitivity. **(b)** Mean value of the calculated sensitivities before (Blue) and after (Red) functionalisation with MPTS and cephalexin-PEG. Error is reported as the SE of the pH sensitivity. Error reported as the SD of the mean across the three sensors.

Once the functionalisation of the EIROF surface has been confirmed, work could begin on testing whether the surface-functionalisation improves the observed change in signal due to the presence of β-lactamases. It is unknown whether the level of surface functionalisation will be enough to observe a large signal, however, techniques such as the

nanoparticle functionalisation technique used in J. Rothberg's work [19] or functionalisable hydrogels [368, 369] could be used to increase the number of molecules at the surface and thus increase the signal-to-noise ratio.

7.2.2 Further Investigation into Variability

As discussed in chapter 4, a large variability in pH sensitivity was seen across the EIROF EGFET sensors. The cause of this was investigated using several of the material analysis techniques discussed in chapter 4 (SEM, EDX, XRD), however, no discernible difference in terms of their physical properties or chemical composition was observed. For the IrO_x EGFET to be a viable device for point-of-care use, this variability would have to be investigated further. It is thought that the device variability may be due to differences in oxidation state, as this has been shown to affect the pH sensitivity of IrO_x [229]. To confirm this, further XPS could be carried out, as this technique was shown to be able to determine the oxidation state ratio present in the EIROF. However, this technique is only able to probe a few nanometers into the surface, thus, it may not give a full picture of the oxidation states present throughout the film. P. Steegstra and E. Ahlberg, demonstrated an approach to reduce the variability of EIROF pH sensors by optimising the oxidation state through potential conditioning [231]. This technique could be tested to determine whether this improves the reliability of the IrO_x EGFETs. Furthermore, a parameter which was not explored in this work was the cycle speed at which the EIROF was deposited. It was found that introducing potential cycling instead of applying a static voltage improved adhesion of the IrO_x to the gold electrode, thus, altering the speed of the potential cycle may have other effects which were not explored in this work.

As well as the variability of pH sensitivity between sensors, as discussed in chapter 5, some variability was observed between measurements of β-lactamases, particularly in samples where larger shifts in pH was observed. This was thought to be due to combination of external parameters such as temperature having a larger impact on the β-lactamase activity at low pH levels. For the assay to be able to reliably quantify β-lactamase activity in a point-of-care setting, this variability would have to be addressed. One investigation would be to fix the temperature of the device under measurement to determine whether this reduces the observed variability. Furthermore, the assay was performed by injecting β-lactamase using a pipette. This method does not allow for accurate control of the introduction of β-lactamases, which may be introducing additional error. A redesign of the fluidic manifold used in chapter 4 would allow for this injection to be controlled microfluidically and would remove this source of error.

7.2.3 Application of the Developed β-lactamase Assay with Clinically Relevant Samples

Chapter 5 described the use of the IrO_x EGFET to measure β-lactamase hydrolysis. However, the β-lactamases used for this work were a blend of recombinant enzymes. Although it is possible for a single bacteria to produce multiple different β-lactamases [370], the enzymes used in this work are not particularly clinically relevant. Furthermore, the enzyme

concentration for these blends was not specified, thus, a detection limit for the assay could not be determined. In order to test the applicability of this assay for clinical use, future work could investigate the response of assay to specific β-lactamase enzymes at known concentrations. As well as being able to determine a limit of detection, the investigation of specific β-lactamases would allow for an assay which could potentially discriminate between different levels of β-lactam resistance. Additionally, by altering the β-lactam antibiotic used in the assay, resistance profiles to different antibiotics could be determined. Finally, the β-lactamase enzymes that were measured in this work were measured in isolation. In a real setting these enzymes would be alongside a number of other proteins and biological matter. For this assay to be able to work in a point-of-care setting, it must also be able to detect these β-lactamase enzymes in the presence of this additional matter. To enable this form of detection, further work using this assay should look at the detection of β-lactamase enzymes from bacterial cell lysate, as this would determine the clinical relevance of this assay.

7.2.4 Reducing the Cost of the IrO EGFET

The IrO_x EGFET was chosen as the pH sensing device for a number of reasons. First, its high sensitivity due to the EIROF allowed for a greater signal-to-noise ratio for detecting small changes in pH. Secondly, its fast response allowed the detection of pH changes in the order of seconds, required for quantifying the kinetics of β-lactam hydrolysis. Finally, discrete EGFET devices which use commercial MOSFETs are able to be produced without the need for a cleanroom environment and specialist instrumentation, allowing the full pH sensing device to be produced at a low cost. However, the fabrication methods and materials used for producing the Au extended gate electrode were expensive and required cleanroom instruments such as an E-beam or thermal evaporator. One approach for removing the reliance on cleanroom processing would be to use copper PCB technology, which is well established for producing electronic devices and could easily be scaled to mass-manufacturing [247]. Furthermore, for the device to be able to operate in a point-of-care setting, it would have to be integrated with fluidics which allows for sample handling and processing. By using PCB as the device substrate, low-cost microfluidics could also be integrated directly into the device PCB [247].

Work is currently being carried out by a colleague, Rhys Ashton, to develop a copper-PCB based IrO_x ISFET device which would be able to be mass manufactured at a low-cost. These devices show similar levels of sensitivity to those described in this thesis. Furthermore, the electrodeposition technique used for the deposition of the IrO_x film could easily be scaled as the iridium oxalate solution has been shown to be stable over several uses. By combining a low-cost, mass-manufacturing technology such as PCB with discrete EGFET devices, a low-cost and point-of-care technology could be realised.

References

1. World Health Organization. *Antimicrobial Resistance: Key Facts* https://www.who.int/news-room/fact-sheets/detail/antimicrobial-resistance (Feb. 10, 2021).
2. Albrich, W. C., Monnet, D. L. & Harbarth, S. Antibiotic selection pressure and resistance in Streptococcus pneumoniae and Streptococcus pyogenes. *Emerging infectious diseases* **10,** 514–7 (Mar. 2004).
3. Davies, J. & Davies, D. Origins and evolution of antibiotic resistance. *Microbiology and molecular biology reviews : MMBR* **74,** 417–33 (Sept. 2010).
4. Klein, E. Y. *et al.* Global increase and geographic convergence in antibiotic consumption between 2000 and 2015. *Proceedings of the National Academy of Sciences of the United States of America* **115,** E3463–E3470 (Apr. 2018).
5. O'Neil, J. Antimicrobial Resistance: Tackling a crisis for the health and wealth of nations. The Review on Antimicrobial Resistance Chaired by Jim O'Neill (2014).
6. European Centre for Disease Prevention and Control. The bacterial challenge: time to react (2009).
7. Centers for Disease Control and Prevention. Antibiotic/Antimicrobial Resistance (2018).
8. De Kraker, M. E. A., Stewardson, A. J. & Harbarth, S. Will 10 Million People Die a Year due to Antimicrobial Resistance by 2050? *PLOS Medicine* **13** (Nov. 2016).
9. Word Health Organization. *Creative campaigns spread awareness on antibiotic resistance* http://www.who.int/news-room/feature-stories/detail/creative-campaigns-spread-awareness-on-antibiotic-resistance (May 29, 2021).
10. Public Health England. Keep Antibiotics Working : Overview. https://campaignresources.phe.gov.uk/resources/campaigns/58-keep-antibiotics-working/Overview (May 29, 2021) (2017).
11. Department of Health. UK Five Year Antimicrobial Resistance Strategy 2013 to 2018. https://assets.publishing.service.gov.uk/government/uploads/system/uploads/attachment_data/file/244058/20130902_UK_5_year_AMR_strategy.pdf (May 17, 2021) (2013).
12. Chaintarli, K. *et al.* Impact of a United Kingdom-wide campaign to tackle antimicrobial resistance on self-reported knowledge and behaviour change. *BMC public health* **16,** 393 (2016).
13. Shapiro, D. J., Hicks, L. A., Pavia, A. T. & Hersh, A. L. Antibiotic prescribing for adults in ambulatory care in the USA, 2007–09. *Journal of Antimicrobial Chemotherapy* **69,** 234–240 (Jan. 2014).
14. Armitage, R. & Nellums, L. B. Antibiotic prescribing in general practice during COVID-19. *The Lancet Infectious Diseases* **21,** e144 (June 2021).
15. Syal, K. *et al.* Current and emerging techniques for antibiotic susceptibility tests. *Theranostics* **7,** 1795–1805 (2017).
16. Bauer, A. W., Kirby, W. M. M., Sherris, J. C. & Turck, M. Antibiotic Susceptibility Testing by a Standardized Single Disk Method. *American Journal of Clinical Pathology* **45,** 493–496 (Apr. 1966).
17. Nordmann, P., Dortet, L. & Poirel, L. Rapid detection of extended-spectrum-β-lactamase-producing Enterobacteriaceae. *Journal of Clinical Microbiology* **50,** 3016–3022 (Sept. 2012).
18. Nordmann, P., Poirel, L. & Dortet, L. Rapid detection of carbapenemase-producing enterobacteriaceae. *Emerging Infectious Diseases* **18,** 1503–1507 (Aug. 2012).
19. Rothberg, J. M. *et al.* An integrated semiconductor device enabling non-optical genome sequencing. *Nature* **475,** 348–352 (July 2011).
20. Madigan, M., Martinko, J., Dunlap, P. & Clark, D. *Brock, Biology of Microorganims* 12th ed. (Pearson Education, Inc., 2009).
21. Razonable, R. R. Antiviral Drugs for Viruses Other Than Human Immunodeficiency Virus. *Symposium on Antimicrobial Therapy* **86,** 1009–1026 (2011).
22. Alexander Fleming. Penicillin. Alexander Fleming: Nobel Lecture (1945).
23. NHS. *Antibiotics: Overview* https://www.nhs.uk/conditions/antibiotics/ (Feb. 10, 2021).
24. Moore, D. *Antibiotic Classification and Mechanism* https://www.orthobullets.com/basic-science/9059/antibiotic-classification-and-mechanism (June 29, 2018).
25. Silver, C. Biosensors for Antimicrobial Resistance: Literature Review (Unpublished) (2018).
26. Kohanski, M. A., DePristo, M. A. & Collins, J. J. Sublethal Antibiotic Treatment Leads to Multidrug Resistance via Radical-Induced Mutagenesis. *Molecular Cell* **37,** 311–320 (Feb. 2010).

27. Andersson, D. I. & Hughes, D. Microbiological effects of sublethal levels of antibiotics. *Nature Reviews Microbiology* **12,** 465–478 (May 2014).

28. Andrews, J. M. Determination of minimum inhibitory concentrations. *Journal of Antimicrobial Chemotherapy* **48,** 5–16 (July 2001).

29. England, P. H. *Health matters: antimicrobial resistance* `https://www.gov.uk/government/publications/health-matters-antimicrobial-resistance/health-matters-antimicrobial-resistance` (Feb. 10, 2021).

30. Munita, J. M. & Arias, C. A. Mechanisms of Antibiotic Resistance. *Microbiology spectrum* **4** (2016).

31. Zeng, X. & Lin, J. Beta-lactamase induction and cell wall metabolism in Gram-negative bacteria. *Frontiers in Microbiology* **4,** 128 (May 2013).

32. Shaikh, S., Fatima, J., Shakil, S., Rizvi, S. M. D. & Kamal, M. A. Antibiotic resistance and extended spectrum beta-lactamases: Types, epidemiology and treatment. *Saudi Journal of Biological Sciences* **22,** 90–101 (Jan. 2015).

33. Bush, K. Past and present perspectives on β-lactamases. *Antimicrobial Agents and Chemotherapy* **62** (Oct. 2018).

34. Hammes, W. P. & Neuhaus, F. C. On the mechanism of action of vancomycin: inhibition of peptidoglycan synthesis in Gaffkya homari. *Antimicrobial agents and chemotherapy* **6,** 722–8 (Dec. 1974).

35. Cox, G. & Wright, G. D. Intrinsic antibiotic resistance: Mechanisms, origins, challenges and solutions. *International Journal of Medical Microbiology* **303,** 287–292 (Aug. 2013).

36. Lewis, K. Platforms for antibiotic discovery. *Nature Reviews Drug Discovery* **12,** 371–387 (May 2013).

37. Niranjan, V. & Malini, A. Antimicrobial resistance pattern in Escherichia coli causing urinary tract infection among inpatients. *Indian Journal of Medical Research* **139,** 945–948 (2014).

38. Wellcome. *Why is it so hard to develop new antibiotics?* `https://wellcome.org/news/why-is-it-so-hard-develop-new-antibiotics` (Feb. 10, 2021).

39. Silver, L. L. Challenges of antibacterial discovery. *Clinical microbiology reviews* **24,** 71–109 (Jan. 2011).

40. Davenport, M. *et al.* New and developing diagnostic technologies for urinary tract infections. *Nature Reviews Urology* (2017).

41. Huang, M. B., Baker, C. N., Banerjee, S. & Tenover, F. C. Accuracy of the E test for determining antimicrobial susceptibilities of staphylococci, enterococci, Campylobacter jejuni, and gram-negative bacteria resistant to antimicrobial agents. *Journal of clinical microbiology* **30,** 3243–8 (Dec. 1992).

42. Balouiri, M., Sadiki, M. & Ibnsouda, S. K. Methods for in vitro evaluating antimicrobial activity: A review. *Journal of Pharmaceutical Analysis* **6,** 71–79 (Apr. 2016).

43. McGregor, A. *et al.* The microscan walkaway diagnostic microbiology system — an evaluation. *Pathology* **27,** 172–176 (Jan. 1995).

44. Sanders, C. C. *et al.* Potential impact of the VITEK 2 system and the advanced expert system on the clinical laboratory of a university-based hospital. *Journal of Clinical Microbiology* **39,** 2379–2385 (2001).

45. Ligozzi, M. *et al.* Evaluation of the VITEK 2 system for identification and antimicrobial susceptibility testing of medically relevant gram-positive cocci. *Journal of Clinical Microbiology* **40,** 1681–1686 (2002).

46. Leverstein-van Hall, M. A. *et al.* Evaluation of the Etest ESBL and the BD Phoenix, VITEK 1, and VITEK 2 automated instruments for detection of extended-spectrum beta-lactamases in multiresistant Escherichia coli and Klebsiella spp. *Journal of Clinical Microbiology* **40,** 3703–3711 (Oct. 2002).

47. Carroll, K. C. *et al.* Evaluation of the BD Phoenix automated microbiology system for identification and antimicrobial susceptibility testing of Enterobacteriaceae. *Journal of Clinical Microbiology* **44,** 3506–3509 (Oct. 2006).

48. NHS. *Treatment and recovery: Sepsis* `https://www.nhs.uk/conditions/sepsis/treatment-and-recovery/` (Feb. 10, 2021).

49. Khan, Z. A., Siddiqui, M. F. & Park, S. Current and emerging methods of antibiotic susceptibility testing. *Diagnostics* **9** (2019).

50. Cobo, F. Application of maldi-tof mass spectrometry in clinical virology: a review. *The open virology journal* **7,** 84–90 (2013).

51. Zhang, Z., Kermekchiev, M. B. & Barnes, W. M. Direct DNA amplification from crude clinical samples using a PCR enhancer cocktail and novel mutants of Taq. *The Journal of molecular diagnostics : JMD* **12,** 152–61 (Mar. 2010).

52. Satake, S., Clark, N., Rimland, D., Nolte, F. S. & Tenover, F. C. Detection of vancomycin-resistant enterococci in fecal samples by PCR. *Journal of clinical microbiology* **35,** 2325–30 (Sept. 1997).

53. Pournajaf, A. *et al.* PCR-based identification of methicillin-resistant Staphylococcus aureus strains and their antibiotic resistance profiles. *Asian Pacific Journal of Tropical Biomedicine* **4,** S293–S297 (2014).

54. Cunningham, R. *et al.* Effect on MRSA transmission of rapid PCR testing of patients admitted to critical care. *Journal of Hospital Infection* **65,** 24–28 (Jan. 2007).

55. Fluit, A. C., Visser, M. R. & Schmitz, F. J. Molecular detection of antimicrobial resistance. *Clinical microbiology reviews* **14,** 836–71, table of contents (Oct. 2001).

56. European Society of Clinical Microbiology and Infectious Diseases. Antimicrobial susceptibility testing EUCAST disk diffusion method. *Version 9.0* (Jan. 2021).

57. Prais, D. *et al.* Bacterial susceptibility to oral antibiotics in community acquired urinary tract infection. *Archives of Disease in Childhood* **88,** 215–218 (Mar. 2003).

58. Public Health England. *English Surveillance Programme for Antimicrobial Utilisation and Resistance (ESPAUR)* (Feb. 19, 2021).

59. National Institure for Healthcare and Excellence. *Antibiotic resistance is now "common" in urinary tract infections* `https://www.nice.org.uk/news/article/antibiotic-resistance-is-now-common-in-urinary-tract-infections` (Feb. 10, 2021).

60. Kresse, H., Belsey, M. J. & Rovini, H. The antibacterial drugs market. *Nature Reviews Drug Discovery* **6,** 19–20 (Jan. 2007).

61. Thakuria, B. & Lahon, K. The beta lactam antibiotics as an empirical therapy in a developing country: An update on their current status and recommendations to counter the resistance against them. *Journal of Clinical and Diagnostic Research* **7,** 1207–1214 (June 2013).

62. Gaynes, R. The discovery of penicillin—new insights after more than 75 years of clinical use. *Emerging Infectious Diseases* **23,** 849–853 (May 2017).

63. Houbraken, J., Frisvad, J. C. & Samson, R. A. Fleming's penicillin producing strain is not Penicillium chrysogenum but P. rubens. *IMA Fungus* **2,** 87–95 (June 2011).

64. Nobel Media AB. *Gerhard Domagk – Facts* `https://www.nobelprize.org/prizes/medicine/1939/domagk/facts/` (Feb. 10, 2021).

65. Abraham, E. P. *et al.* Further Observations On Penicillin. *The Lancet* **238,** 177–189 (Aug. 1941).

66. Nobel Media AB. *The Nobel Prize in Physiology or Medicine 1945* `https://www.nobelprize.org/prizes/medicine/1945/summary/` (Feb. 10, 2021).

67. Neelanjana, P. & Cascella, M. in *Antibiotic Discovery and Development* 79–117 (Springer US, Apr. 2012).

68. Mcstrother. *Penicillin inhibition* `https://commons.wikimedia.org/wiki/File:Penicillin_inhibition.svg` (Feb. 10, 2021).

69. Sauvage, E., Kerff, F., Terrak, M., Ayala, J. A. & Charlier, P. *The penicillin-binding proteins: Structure and role in peptidoglycan biosynthesis* Mar. 2008.

70. Tipper, D. J. & Strominger, J. L. Mechanism of action of penicillins: a proposal based on their structural similarity to acyl-D-alanyl-D-alanine. *Proceedings of the National Academy of Sciences of the United States of America* **54,** 1133–1141 (1965).

71. Fernández, L. & Hancock, R. E. Adaptive and mutational resistance: Role of porins and efflux pumps in drug resistance. *Clinical Microbiology Reviews* **25,** 661–681 (Oct. 2012).

72. Efflux pump, the masked side of ß-lactam resistance in Klebsiella pneumoniae clinical isolates. *PLoS ONE* **4** (Mar. 2009).

73. Cushnie, T. P., O'Driscoll, N. H. & Lamb, A. J. Morphological and ultrastructural changes in bacterial cells as an indicator of antibacterial mechanism of action. *Cellular and Molecular Life Sciences* **73,** 4471–4492 (July 2016).

74. Naas, T. *et al.* Beta-lactamase database (BLDB)–structure and function. *Journal of Enzyme Inhibition and Medicinal Chemistry* **32,** 917–919 (Jan. 2017).

75. Bush, K. The ABCD's of β-lactamase nomenclature. *Journal of Infection and Chemotherapy* **19,** 549–559 (Jan. 2013).

76. Ambler, R. P. The structure of beta-lactamases. *Philosophical transactions of the Royal Society of London. Series B, Biological sciences* **289,** 321–331 (May 1980).

77. Bush, K. & Jacoby, G. A. Updated functional classification of β-lactamases. *Antimicrobial Agents and Chemotherapy* **54,** 969–976 (Mar. 2010).

78. Tooke, C. L. *et al.* β-Lactamases and β-Lactamase Inhibitors in the 21st Century. *Journal of Molecular Biology* **431,** 3472–3500 (Aug. 2019).

79. He, Y., Lei, J., Pan, X., Huang, X. & Zhao, Y. The hydrolytic water molecule of Class A β-lactamase relies on the acyl-enzyme intermediate ES* for proper coordination and catalysis. *Scientific Reports* **10,** 10205 (Dec. 2020).

80. Page, M. I. & Badarau, A. The mechanisms of catalysis by metallo β-lactamases. *Bioinorganic Chemistry and Applications* **2008** (June 2008).

81. Meini, M. R., Llarrull, L. I. & Vila, A. J. *Overcoming differences: The catalytic mechanism of metallo-β-lactamases* July 2015.

82. Palacios, A. R. *et al.* The reaction mechanism of metallo-lactamases is tuned by the conformation of an active-site mobile loop. *Antimicrobial Agents and Chemotherapy* **63** (Jan. 2019).

83. Walsh, T. R., Toleman, M. A., Poirel, L. & Nordmann, P. Metallo-β-lactamases: The quiet before the storm? *Clinical Microbiology Reviews* **18,** 306–325 (Apr. 2005).

84. Worthington, R. J. & Melander, C. Overcoming resistance to β-Lactam antibiotics. *Journal of Organic Chemistry* **78,** 4207–4213 (May 2013).

85. Martinez-Martinez, L. *et al. EUCAST guidelines for detection of resistance mechanisms and specific resistances of clinical and/or epidemiological importance*

86. Woodford, N. & Sundsfjord, A. Molecular detection of antibiotic resistance: When and where? *Journal of Antimicrobial Chemotherapy* **56,** 259–261 (Aug. 2005).

87. Lo, Y. D., Chiu, R. W. & Chan, K. A. *Clinical applications of PCR* 2nd ed. (Humana Press, 2006).

88. Enzoklop. *Polymerase chain reaction* `https://en.wikipedia.org/wiki/File:Polymerase_chain_reaction.svg` (Apr. 19, 2021).

89. Senda, K. *et al.* PCR detection of metallo-beta-lactamase gene (blaIMP) in gram-negative rods resistant to broad-spectrum beta-lactams. *Journal of Clinical Microbiology* **34** (1996).

90. Markoulatos, P., Siafakas, N. & Moncany, M. Multiplex polymerase chain reaction: A practical approach. *Journal of Clinical Laboratory Analysis* **16,** 47–51 (2002).

91. Polz, M. F. & Cavanaugh, C. M. Bias in template-to-product ratios in multitemplate PCR. *Applied and Environmental Microbiology* **64,** 3724–3730 (1998).

92. Elnifro, E. M., Ashshi, A. M., Cooper, R. J. & Klapper, P. E. Multiplex PCR: Optimization and application in diagnostic virology. *Clinical Microbiology Reviews* **13,** 559–570 (2000).

93. Pérez-Pérez, F. J. & Hanson, N. D. Detection of plasmid-mediated AmpC β-lactamase genes in clinical isolates by using multiplex PCR. *Journal of Clinical Microbiology* **40,** 2153–2162. ISSN: 00951137 (2002).

94. Ellington, M. J., Kistler, J., Livermore, D. M. & Woodford, N. Multiplex PCR for rapid detection of genes encoding acquired metallo-β-lactamases [1]. *Journal of Antimicrobial Chemotherapy* **59,** 321–322 (Feb. 2007).

95. Dallenne, C., da Costa, A., Decré, D., Favier, C. & Arlet, G. Development of a set of multiplex PCR assays for the detection of genes encoding important β-lactamases in Enterobacteriaceae. *Journal of Antimicrobial Chemotherapy* **65,** 490–495 (Jan. 2010).

96. Voets, G. M., Fluit, A. C., Scharringa, J., Cohen Stuart, J. & Leverstein-Van Hall, M. A. A set of multiplex PCRs for genotypic detection of extended-spectrum β-lactamases, carbapenemases, plasmid-mediated AmpC β-lactamases and OXA β-lactamases. *International Journal of Antimicrobial Agents* **37,** 356–359 (Apr. 2011).

97. Chavda, K. D. *et al.* Evaluation of a multiplex PCR assay to rapidly detect Enterobacteriaceae with a broad range of β-lactamases directly from perianal swabs. *Antimicrobial Agents and Chemotherapy* **60,** 6957–6961 (Nov. 2016).

98. Ogutu, J. O. *et al.* Development of a multiplex PCR system and its application in detection of blaSHV, blaTEM, blaCTX-M-1, blaCTX-M-9 and blaOXA-1 group genes in clinical Klebsiella pneumoniae and Escherichia coli strains. *Journal of Antibiotics* **68,** 725–733 (Dec. 2015).

99. Espy, M. J. *et al.* Real-time PCR in clinical microbiology: Applications for routine laboratory testing. *Clinical Microbiology Reviews* **19,** 165–256 (Jan. 2006).

100. Frickmann, H., Masanta, W. O. & Zautner, A. E. Emerging rapid resistance testing methods for clinical microbiology laboratories and their potential impact on patient management. *BioMed Research International* **2014.** ISSN: 23146141 (2014).

101. Kralik, P. & Ricchi, M. A basic guide to real time PCR in microbial diagnostics: Definitions, parameters, and everything. *Frontiers in Microbiology* **8,** 108 (Feb. 2017).

102. Yang, S. & Rothman, R. E. PCR-based diagnostics for infectious diseases: Uses, limitations, and future applications in acute-care settings. *Lancet Infectious Diseases* **4,** 337–348 (June 2004).

103. Diene, S. M., Bruder, N., Raoult, D. & Rolain, J. M. Real-time PCR assay allows detection of the New Delhi metallo-β- lactamase (NDM-1)-encoding gene in France. *International Journal of Antimicrobial Agents* **37,** 544–546 (June 2011).

104. Birkett, C. I. *et al.* Real-time TaqMan PCR for rapid detection and typing of genes encoding CTX-M extended-spectrum β-lactamases. **56,** 52–55 (Jan. 2007).

105. Mendes, R. E. *et al.* Rapid Detection and Identification of Metallo-Lactamase-Encoding Genes by Multiplex Real-Time PCR Assay and Melt Curve Analysis. *JOURNAL OF CLINICAL MICROBIOLOGY* **45,** 20 (2007).

106. Alfaresi, M. S. & Elkoush, A. A. Real-time polymerase chain reaction for rapid detection of genes encoding SHV extended-spectrum β-lactamases. *Indian Journal of Medical Microbiology* **28,** 332–336 (Oct. 2010).

107. Ellem, J., Partridge, S. R. & Iredell, J. R. Efficient direct extended-spectrum β-lactamase detection by multiplex real-time PCR: Accurate assignment of phenotype by use of a limited set of genetic markers. *Journal of Clinical Microbiology* **49,** 3074–3077 (Aug. 2011).

108. Monteiro, J., Widen, R. H., Pignatari, A. C., Kubasek, C. & Silbert, S. Rapid detection of carbapenemase genes by multiplex real-time PCR. *Journal of Antimicrobial Chemotherapy* **67,** 906–909 (Apr. 2012).

109. Zheng, F., Sun, J., Cheng, C. & Rui, Y. The establishment of a duplex real-time PCR assay for rapid and simultaneous detection of blaNDM and blaKPC genes in bacteria. **12,** 1–5 (Oct. 2013).

110. Roschanski, N., Fischer, J., Guerra, B. & Roesler, U. Development of a multiplex real-time PCR for the rapid detection of the predominant beta-lactamase genes CTX-M, SHV, TEM and CIT-type ampcs in enterobacteriaceae. *PLoS ONE* **9,** 100956 (July 2014).

111. Singh, P., Pfeifer, Y. & Mustapha, A. Multiplex real-time PCR assay for the detection of extended-spectrum β-lactamase and carbapenemase genes using melting curve analysis. *Journal of Microbiological Methods* **124,** 72–78 (May 2016).

112. Notomi, T. *et al.* Loop-mediated isothermal amplification of DNA. *Nucleic acids research* **28,** e63 (2000).

113. Liu, W. *et al.* Sensitive and rapid detection of the new delhi metallo-beta- lactamase gene by loop-mediated isothermal amplification. *Journal of Clinical Microbiology* **50,** 1580–1585 (May 2012).

114. Cheng, C., Zheng, F. & Rui, Y. Rapid detection of blaNDM, blaKPC, blaIMP, and blaVIM carbapenemase genes in bacteria by loop-mediated isothermal amplification. *Microbial Drug Resistance* **20,** 533–538 (Dec. 2014).

115. Thirapanmethee, K., Pothisamutyothin, K., Nathisuwan, S., Chomnawang, M. T. & Wiwat, C. Loop-mediated isothermal amplification assay targeting the blaCTX-M9 gene for detection of extended spectrum β-lactamase-producing Escherichia coli and Klebsiella pneumoniae. *Microbiology and Immunology* **58,** 655–665 (Dec. 2014).

116. Takano, C. *et al.* Development of a novel loop-mediated isothermal amplification method to detect guiana extended-spectrum (GES) β-lactamase genes in Pseudomonas aeruginosa. *Frontiers in Microbiology* **10,** 25 (Feb. 2019).

117. García-Fernández, S. *et al.* Evaluation of the eazyplex® SuperBug CRE system for rapid detection of carbapenemases and ESBLs in clinical Enterobacteriaceae isolates recovered at two Spanish hospitals. *Journal of Antimicrobial Chemotherapy* **70,** 1047–1050 (Sept. 2014).

118. GmbH, A. *eazyplex, AmplexDiagnostics GmbH* `https://www.eazyplex.com/eazyplex-e/` (Feb. 19, 2021).

119. Martineau, F. *et al.* Correlation between the resistance genotype determined by multiplex PCR assays and the antibiotic susceptibility patterns of Staphylococcus aureus and Staphylococcus epidermidis. *Antimicrobial Agents and Chemotherapy* **44,** 231–238 (Feb. 2000).

120. O'Callaghan, C. H., Morris, A., Kirby, S. M. & Shingler, A. H. Novel method for detection of beta-lactamases by using a chromogenic cephalosporin substrate. *Antimicrobial agents and chemotherapy* **1,** 283–288 (1972).

121. Pitkälä, A., Salmikivi, L., Bredbacka, P., Myllyniemi, A. L. & Koskinen, M. T. Comparison of tests for detection of β-lactamase-producing staphylococci. *Journal of Clinical Microbiology* **45,** 2031–2033 (June 2007).

122. BioVision. *EZScreen™ Beta-Lactamase Activity Colorimetric Assay Kit (384-well) — K954 — BioVision, Inc.* `https://www.biovision.com/ezscreentm-beta-lactamase-activity-colorimetric-assay-kit-384-well` (May 24, 2021).

123. Amplite. *Amplite™ Colorimetric Beta-Lactamase Activity Assay Kit — AAT Bioquest* `https://www.aatbio.com/products/amplite-colorimetric-beta-lactamase-activity-assay-kit` (May 24, 2021).

124. LSBio. *Beta-Lactamase Activity Kit (Colorimetric) - LS-K700* `https://www.lsbio.com/assaykits/beta-lactamase-activity-kit-colorimetric-ls-k700/700#publications-section` (May 24, 2021).

125. ApexBio. *APExBIO - Beta-Lactamase Activity Colorimetric Assay Kit* `https://www.apexbt.com/beta-lactamase-activity-colorimetric-assay-kit` (May 24, 2021).

126. Voladri, R. K. R. & Kernodle, D. S. Characterization of a chromosomal gene encoding type B β-lactamase in phage group II isolates of Staphylococcus aureus. *Antimicrobial Agents and Chemotherapy* **42,** 3163–3168 (Dec. 1998).

127. Renvoise, A. *et al.* Evaluation of the βlacta test, a rapid test detecting resistance to third-generation cephalosporins in clinical strains of enterobacteriaceae. *Journal of Clinical Microbiology* **51,** 4012–4017 (Dec. 2013).

128. Gallah, S., Decré, D., Genel, N. & Arlet, G. The β-Lacta test for direct detection of extended-Spectrum-β-Lactamase-producing Enterobacteriaceae in Urine. *Journal of Clinical Microbiology* **52,** 3792–3794 (Oct. 2014).

129. Hasso, M., Porter, V. & Simor, A. E. Evaluation of the β-lacta test for detection of extended-spectrum-β-lactamase (ESBL)-producing organisms directly from positive blood cultures by use of smudge plates. *Journal of Clinical Microbiology* **55,** 3560–3562 (Dec. 2017).

130. Poirel, L., Fernández, J. & Nordmann, P. Comparison of three biochemical tests for rapid detection of extended-spectrum-β-lactamase-producing enterobacteriaceae. *Journal of Clinical Microbiology* **54,** 423–427 (Feb. 2016).

131. Dortet, L., Poirel, L. & Nordmann, P. Rapid detection of extended-spectrum-β-lactamase-producing Enterobacteriaceae from urine samples by use of the ESBL NDP test. *Journal of Clinical Microbiology* **52,** 3701–3706 (Oct. 2014).

132. Deepa, R., Ravichandran, M., Banu, S. T. & Sharmila, R. Evaluation of Nordmann, Dortet, and Poirel test for the identification of extended spectrum betalactamase production among urinary isolates of Escherichia coli. *Journal of Laboratory Physicians* **9,** 269–272 (Oct. 2017).

133. Affolabi, D. *et al.* Rapid detection of extended-spectrum-β-lactamase-producing Enterobacteriaceae in blood cultures using the ESBL NDP test in Cotonou, Benin. *Journal of Medical Microbiology* **66,** 884–887 (July 2017).

134. Tijet, N., Boyd, D., Patel, S. N., Mulvey, M. R. & Melano, R. G. Evaluation of the carba NP test for rapid detection of carbapenemase- producing enterobacteriaceae and Pseudomonas aeruginosa. *Antimicrobial Agents and Chemotherapy* **57,** 4578–4580 (Sept. 2013).

135. Lucas, T. J. An evaluation of 12 methods for the demonstration of penicillinase. *Journal of Clinical Pathology* **32,** 1061–1065 (1979).

136. DeBoer, T. R. *et al.* An Enzyme-Mediated Amplification Strategy Enables Detection of β-Lactamase Activity Directly in Unprocessed Clinical Samples for Phenotypic Detection of β-Lactam Resistance. *ChemBioChem* **19,** 2173–2177 (Oct. 2018).

137. Meletis, G. Carbapenem resistance: overview of the problem and future perspectives. *Therapeutic Advances in Infectious Disease* **3,** 15–21 (Feb. 2016).

138. Berg, J. M., Tymoczko, J. L., Stryer, L. & Gumport, R. I. *Biochemistry* (W.H. Freeman amp; Co Ltd, 2006).

139. Lee, S. R., Rahman, M. M., Sawada, K. & Ishida, M. Fabrication of a highly sensitive penicillin sensor based on charge transfer techniques. *Biosensors and Bioelectronics* **24,** 1877–1882 (Mar. 2009).

140. Penicillin detection by tobacco mosaic virus-assisted colorimetric biosensors. *Nanotheranostics* **2,** 184–196 (2018).

141. Kharewal, T., Verma, N., Gahlaut, A. & Hooda, V. Biosensors for penicillin quantification: a comprehensive review. *Biotechnology Letters* **42,** 1829–1846 (Oct. 2020).

142. Kan, V. *et al. Organic Primitives: Synthesis and Design of pH-Reactive Materials using Molecular I/O for Sensing, Actuation, and Interaction* in *Proceedings of the 2017 CHI Conference on Human Factors in Computing Systems* (ACM, New York, NY, USA, 2017), 989–1000.

143. Hamann, C. H., Hamnett, A. & Vielstich, W. *Electrochemistry* 2nd (Wiley-VCH, 1998).

144. Vivaldi, F. *et al.* Recent advances in optical, electrochemical and field effect pH sensors. *Chemosensors* **9,** 1–17 (Feb. 2021).

145. Van Zeghbroeck, B. *Principles of Semiconductor Devices. Chapter 6: MOS Capacitors* `https://ecee.colorado.edu/~bart/book/book/chapter6/ch6_2` (Apr. 19, 2021).

146. Senturia, S. D. & Wedlock, B. D. *Electronic circuits and applications* (Wiley, 1975).

147. Storey, N. *Electronics: a systems approach* 2nd (Pearson, 1998).

148. Berveld, P. *ISFET, Theory and Pracice* in (IEEE Sensor Conference Toronto proceedings, Oct. 2003).

149. Damaskin, B. B. & Petrii, O. A. Historical development of theories of the electrochemical double layer. *Journal of Solid State Electrochemistry* **15,** 1317–1334 (Feb. 2011).

150. Gouy, M. Sur la constitution de la charge électrique à la surface d'un électrolyte. *Journal de Physique Théorique et Appliquée* **9,** 457–468 (Jan. 1910).

151. Chapman, D. L. LI. A contribution to the theory of electrocapillarity. *The London, Edinburgh, and Dublin Philosophical Magazine and Journal of Science* **25,** 475–481 (Apr. 1913).

152. Stern, O. ZUR THEORIE DER ELEKTROLYTISCHEN DOPPELSCHICHT. *Zeitschrift für Elektrochemie und angewandte physikalische Chemie* **30,** 508–516 (Nov. 1924).

153. Tosaka. *Electric double-layer* `https://commons.wikimedia.org/wiki/File:Electric_double-layer_(BMD_model)_NT.PNG` (Feb. 10, 2021).

154. Zheng, Z., Zhang, H., Zhai, T. & Xia, F. Overcome Debye Length Limitations for Biomolecule Sensing Based on Field Effective Transistors. *Chinese Journal of Chemistry* **39,** 999–1008. ISSN: 1614-7065 (Apr. 2021).

155. Kaisti, M. Detection principles of biological and chemical FET sensors. *Biosensors and Bioelectronics* **98,** 437–448 (Dec. 2017).

156. Van Hal, R. E., Eijkel, J. C. & Bergveld, P. A general model to describe the electrostatic potential at electrolyte oxide interfaces. *Advances in Colloid and Interface Science* **69,** 31–62 (Dec. 1996).

157. Bard, A. J. & Faulkner, L. R. *Electrochemical Methods: Fundamentals and Applications* 2nd (John Wiley and Sons Inc., 2001).

158. Yates, D. E., Levine, S. & Healy, T. W. Site-binding model of the electrical double layer at the oxide/water interface. *Journal of the Chemical Society, Faraday Transactions 1: Physical Chemistry in Condensed Phases* **70,** 1807–1818 (Jan. 1974).

159. Martinoia, S. & Massobrio, G. Behavioral macromodel of the ISFET in SPICE. *Sensors and Actuators, B: Chemical* **62,** 182–189 (Mar. 2000).

160. Bergveld, P. Short Communications: Development of an Ion-Sensitive Solid-State Device for Neurophysiological Measurements. *IEEE Transactions on Biomedical Engineering* **BME-17,** 70–71 (1970).

161. Bergveld, P. Development, Operation, and Application of the Ion-Sensitive Field-Effect Transistor as a Tool for Electrophysiology. *IEEE Transactions on Biomedical Engineering* **BME-19,** 342–351 (1972).

162. Bergveld, P. Thirty years of ISFETOLOGY: What happened in the past 30 years and what may happen in the next 30 years. *Sensors and Actuators, B: Chemical* **88,** 1–20 (Jan. 2003).

163. Pachauri, V. & Ingebrandt, S. Biologically sensitive field-effect transistors: From ISFETs to NanoFETs. *Essays in Biochemistry* **60,** 81–90 (June 2016).

164. Hierlemann, A. & Baltes, H. CMOS-based chemical microsensors. *Analyst* **128,** 15–28 (Jan. 2003).

165. Milgrew, M. J., Riehle, M. O. & Cumming, D. R. A large transistor-based sensor array chip for direct extracellular imaging. *Sensors and Actuators, B: Chemical* **111-112,** 347–353 (Nov. 2005).

166. Hizawa, T., Sawada, K., Takao, H. & Ishida, M. Fabrication of a two-dimensional pH image sensor using a charge transfer technique. *Sensors and Actuators, B: Chemical* **117,** 509–515 (Oct. 2006).

167. Yeow, T. C., Haskard, M. R., Mulcahy, D. E., Seo, H. I. & Kwon, D. H. A very large integrated pH-ISFET sensor array chip compatible with standard CMOS processes. **44,** 434–440. ISSN: 09254005 (Oct. 1997).

168. Bausells, J., Carrabina, J., Errachid, A. & Merlos, A. Ion-sensitive field-effect transistors fabricated in a commercial CMOS technology. *Sensors and Actuators, B: Chemical* **57,** 56–62 (Sept. 1999).

169. Errachid, A., Zine, N., Samitier, J. & Bausells, J. FET-based chemical sensor systems fabricated with standard technologies. *Electroanalysis* **16,** 1843–1851 (Nov. 2004).

170. Kalofonou, M. & Toumazou, C. A Low Power Sub-μW chemical gilbert cell for isfet differential reaction monitoring. *IEEE Transactions on Biomedical Circuits and Systems* **8,** 565–574 (2014).

171. Sohbati, M. & Toumazou, C. Dimension and shape effects on the ISFET performance. *IEEE Sensors Journal* **15,** 1670–1679 (Mar. 2015).

172. Milgrew, M. J. & Cumming, D. R. Matching the transconductance characteristics of CMOS ISFET arrays by removing trapped charge. *IEEE Transactions on Electron Devices* **55,** 1074–1079 (Apr. 2008).

173. Hu, Y., Moser, N. & Georgiou, P. A 32 × 32 ISFET Chemical Sensing Array with Integrated Trapped Charge and Gain Compensation. *IEEE Sensors Journal* **17,** 5276–5284 (Aug. 2017).

174. Nakazato, K. An Integrated ISFET Sensor Array. *Sensors* **9,** 8831–8851 (Nov. 2009).

175. Chin, Y. L., Chou, J. C., Sun, T. P., Chung, W. Y. & Hsiung, S. K. A novel pH sensitive ISFET with on chip temperature sensing using CMOS standard process. *Sensors and Actuators, B: Chemical* **76,** 582–593 (June 2001).

176. Moser, N., Keeble, L., Rodriguez-Manzano, J. & Georgiou, P. ISFET arrays for lab-on-chip technology: A review. *2019 26th IEEE International Conference on Electronics, Circuits and Systems, ICECS 2019,* 57–60 (Nov. 2019).

177. Moser, N., Lande, T. S., Toumazou, C. & Georgiou, P. ISFETs in CMOS and Emergent Trends in Instrumentation: A Review. *IEEE Sensors Journal* **16,** 6496–6514 (Sept. 2016).

178. Oelßner, W. *et al.* Encapsulation of ISFET sensor chips. *Sensors and Actuators, B: Chemical* **105,** 104–117 (Feb. 2005).

179. Pullano, S. A. *et al.* EGFET-based sensors for bioanalytical applications: A review. *Sensors (Switzerland)* **18** (Nov. 2018).

180. Van der spiegel, J., Lauks, I., Chan, P. & Babic, D. The extended gate chemically sensitive field effect transistor as multi-species microprobe. *Sensors and Actuators* **4,** 291–298 (Jan. 1983).

181. Rajan, N. K., Brower, K., Duan, X. & Reed, M. A. Limit of detection of field effect transistor biosensors: Effects of surface modification and size dependence. *Applied Physics Letters* **104,** 084106 (Feb. 2014).

182. Pullano, S. A. *et al.* Deep submicron EGFET based on transistor association technique for chemical sensing. *Sensors (Switzerland)* **19** (Mar. 2019).

183. Ayele, G. T. *et al. Development of ultrasensitive extended-gate Ion-sensitive-field-effect-transistor based on industrial UTBB FDSOI transistor* in *European Solid-State Device Research Conference* (Editions Frontieres, Oct. 2017), 264–267.

184. Jeon, J. H. & Cho, W. J. High-performance extended-gate ion-sensitive field-effect transistors with multi-gate structure for transparent, flexible, and wearable biosensors. *Science and Technology of Advanced Materials* **21,** 371–378 (Jan. 2020).

185. Chi, L. L., Chou, J. C., Chung, W. Y., Sun, T. P. & Hsiung, S. K. *New structure of ion sensitivite field effect transistor* in *Proceeding of the Biomedical Engineering Society 1998 Annual Symposium, Taiwan* (1998), 332–334.

186. Chi, L. L., Chou, J. C., Chung, W. Y., Sun, T. P. & Hsiung, S. K. Study on extended gate field effect transistor with tin oxide sensing membrane. *Materials Chemistry and Physics* **63,** 19–23 (Feb. 2000).

187. Voorthuyzen, J. A. & Bergveld, P. Photoelectric effects in Ta2O5SiO2Si structures. *Sensors and Actuators: B. Chemical* **1,** 350–353 (1990).

188. Neužil, P. ISFET integrated sensor technology. *Sensors and Actuators: B. Chemical* **24,** 232–235 (Mar. 1995).

189. Yin, L. T., Chou, J. C., Chung, W. Y., Sun, T. P. & Hsiung, S. K. Separate structure extended gate H+-ion sensitive field effect transistor on a glass substrate. *Sensors and Actuators, B: Chemical* **71,** 106–111 (Nov. 2000).

190. Prodromakis, T., Liu, Y. & Toumazou, C. A low-cost disposable chemical sensing platform based on discrete components. *IEEE Electron Device Letters* **32,** 417–419 (Mar. 2011).

191. Prodromakis, T., Liu, Y., Yang, J., Hollinghurst, D. & Toumazou, C. *A novel design approach for developing chemical sensing platforms using inexpensive technologies* in *2011 IEEE Biomedical Circuits and Systems Conference, BioCAS 2011* (2011), 369–372.

192. Kaisti, M. *et al.* Hand-Held Transistor Based Electrical and Multiplexed Chemical Sensing System. *ACS Sensors* **1,** 1423–1431 (Dec. 2016).

193. Lue, C. E. *et al.* PH sensing reliability of flexible ITO/PET electrodes on EGFETs prepared by a roll-to-roll process. *Microelectronics Reliability* **52,** 1651–1654 (Aug. 2012).

194. Odijk, M. *et al.* Microfabricated solid-state ion-selective electrode probe for measuring potassium in the living rodent brain: Compatibility with DC-EEG recordings to study spreading depression. *Sensors and Actuators, B: Chemical* **207,** 945–953 (Feb. 2015).

195. Baldacchini, C. *et al.* A reliable biofet immunosensor for detection of p53 tumour suppressor in physiological-like environment. *Sensors (Switzerland)* **20,** 1–14. `www.mdpi.com/journal/sensors` (Nov. 2020).

196. Schöning, M. J. & Poghossian, A. Recent advances in biologically sensitive field-effect transistors (BioFETs). *Analyst* **127,** 1137–1151 (Sept. 2002).

197. Tarasov, A. *et al.* A potentiometric biosensor for rapid on-site disease diagnostics. *Biosensors and Bioelectronics* **79,** 669–678 (May 2016).

198. Matsumoto, A. & Miyahara, Y. Current and emerging challenges of field effect transistor based bio-sensing. *Nanoscale* **5,** 10702–10718 (Nov. 2013).

199. Vieira, N. C. *et al.* Label-free electrical recognition of a dengue virus protein using the SEGFET simplified measurement system. *Analytical Methods* **6,** 8882–8885 (Nov. 2014).

200. Lin, Y. H. *et al.* Extended-gate field-effect transistor packed in micro channel for glucose, urea and protein biomarker detection. *Biomedical Microdevices* **17,** 1–9 (Dec. 2015).

201. Yin, L. T., Wang, H. Y., Lin, Y. C. & Huang, W. C. A novel instrumentation circuit for electrochemical measurements. *Sensors (Switzerland)* **12,** 9687–9696 (July 2012).

202. Yang, C. M. *et al.* Low cost and flexible electrodes with NH3 plasma treatments in extended gate field effect transistors for urea detection. *Sensors and Actuators, B: Chemical* **187,** 274–279 (Oct. 2013).

203. Silva, G. O. & Mulato, M. Urea Detection Using Commercial Field Effect Transistors. *ECS Journal of Solid State Science and Technology* **7,** Q3014–Q3019 (Mar. 2018).

204. Pijanowska, D. G. & Torbicz, W. pH-ISFET based urea biosensor. *Sensors and Actuators, B: Chemical* **44,** 370–376 (Oct. 1997).

205. Chen, J. C., Chou, J. C., Sun, T. P. & Hsiung, S. K. Portable urea biosensor based on the extended-gate field effect transistor. *Sensors and Actuators, B: Chemical* **91,** 180–186 (June 2003).

206. Pandya, D., Nagrajappa, A. K. & Ravi, K. S. Assessment and correlation of urea and creatinine levels in saliva and serum of patients with chronic kidney disease, diabetes and hypertension– A research study. *Journal of Clinical and Diagnostic Research* **10,** ZC58–ZC62 (Oct. 2016).

207. Sung, D. & Koo, J. A review of BioFET's basic principles and materials for biomedical applications. *Biomedical Engineering Letters 2021 11:2* **11,** 85–96. `https://link.springer.com/article/10.1007/s13534-021-00187-8` (Apr. 2021).

208. Vu, C. A. & Chen, W. Y. Predicting future prospects of aptamers in field-effect transistor biosensors. *Molecules* **25** (Feb. 2020).

209. Cho, W. J. & Lim, C. M. Sensing properties of separative paper-based extended-gate ion-sensitive field-effect transistor for cost effective pH sensor applications. *Solid-State Electronics* **140,** 96–99 (Feb. 2018).

210. Matsuo, T. & Esashi, M. Methods of isfet fabrication. *Sensors and Actuators* **1,** 77–96 (Jan. 1981).

211. Weng, C. S., Hashim, U. & Liu, W. W. *Fabrication of silicon nitride ion sensitive field-effect transistor (ISFET)* in *Proceedings - RSM 2013: 2013 IEEE Regional Symposium on Micro and Nano Electronics* (2013), 204–207.

212. Chaudhary, R. *et al.* Fabrication and characterisation of Al gate n-metal-oxide-semiconductor field-effect transistor, on-chip fabricated with silicon nitride ion-sensitive field-effect transistor. *IET Computers and Digital Techniques* **10,** 268–272 (Sept. 2016).

213. Saengdee, P. *et al.* A silicon nitride ISFET based immunosensor for Ag85B detection of tuberculosis. *Analyst* **141,** 5767–5775 (Oct. 2016).

214. Jiang, Y. *et al.* A high-sensitivity potentiometric 65-nm CMOS ISFET sensor for rapid E. coli Screening. *IEEE Transactions on Biomedical Circuits and Systems* **12,** 402–415. ISSN: 19324545 (Apr. 2018).

215. Jamasb, S., Collins, S. D. & Smith, R. L. A physical model for threshold voltage instability in Si3N4-Gate H+-sensitive FET's (pH ISFET's). *IEEE Transactions on Electron Devices* **45,** 1239–1245 (1998).

216. Kurzweil, P. Metal oxides and ion-exchanging surfaces as pH sensors in liquids: State-of-the-art and outlook. *Sensors (Switzerland)* **9,** 4955–4985 (June 2009).

217. Manjakkal, L., Szwagierczak, D. & Dahiya, R. Metal oxides based electrochemical pH sensors: Current progress and future perspectives. *Progress in Materials Science* **109,** 100635 (Apr. 2020).

218. Chou, J. C. & Wang, Y. F. Preparation and study on the drift and hysteresis properties of the tin oxide gate ISFET by the sol-gel method. *Sensors and Actuators, B: Chemical* **86,** 58–62 (Aug. 2002).

219. Jhan, S. S., Chiang, J. L., Chen, Y. C., Chou, J. C. & Su, J. F. Design and fabrication of pH detecting system using lead titanate series gate ion-sensitive field effect transistors. *Ferroelectrics* **383,** 111–118 (2009).

220. Yao, P. C., Chiang, J. L. & Lee, M. C. Application of sol-gel TiO2 film for an extended-gate H + ion-sensitive field-effect transistor. *Solid State Sciences* **28,** 47–54 (Feb. 2014).

221. Singh, K., Lou, B. S., Her, J. L., Pang, S. T. & Pan, T. M. Super Nernstian pH response and enzyme-free detection of glucose using sol-gel derived RuOx on PET flexible-based extended-gate field-effect transistor. *Sensors and Actuators, B: Chemical* **298,** 126837 (Nov. 2019).

222. Guerra, E. M., Silva, G. R. & Mulato, M. Extended gate field effect transistor using V2O5 xerogel sensing membrane by sol-gel method. *Solid State Sciences* **11,** 456–460 (Feb. 2009).

223. Vieira, N. C., Fernandes, E. G., Faceto, A. D., Zucolotto, V. & Guimarães, F. E. Nanostructured polyaniline thin films as pH sensing membranes in FET-based devices. *Sensors and Actuators, B: Chemical* **160,** 312–317 (Dec. 2011).

224. Bergveld, P. *et al.* How electrical and chemical requirements for refets may coincide. *Sensors and Actuators* **18,** 309–327 (July 1989).

225. Fujihira, M., Fukui, M. & Osa, T. Chemically modified parylene gate field effect transistors. Preparation of pH insensitive parylene gate for chemical modification. *Journal of Electroanalytical Chemistry* **106,** 413–418 (Jan. 1980).

226. Trantidou, T. *et al.* The dual role of Parylene C in chemical sensing: Acting as an encapsulant and as a sensing membrane for pH monitoring applications. *Sensors and Actuators, B: Chemical* **186,** 1–8 (Sept. 2013).

227. Trantidou, T., Tariq, M., Terracciano, C. M., Toumazou, C. & Prodromakis, T. Parylene C-based flexible electronics for pH monitoring applications. *Sensors (Switzerland)* **14,** 11629–11639 (July 2014).

228. Das, A. *et al.* Highly sensitive palladium oxide thin film extended gate FETs as pH sensor. *Sensors and Actuators, B: Chemical* **205,** 199–205 (Dec. 2014).

229. Olthuis, W., Robben, M. A. M., Bergveld, P., Bos, M. & Van Der Linden, W. E. pH Sensor Properties of Electrochemically Grown Iridium Oxide. *Sensors and Actuators B* **2,** 247–256 (May 1990).

230. Burke, L. D. & Whelan, D. P. A voltammetric investigation of the charge storage reactions of hydrous iridium oxide layers. *Journal of Electroanalytical Chemistry* **162,** 121–141 (Mar. 1984).

231. Steegstra, P. & Ahlberg, E. Influence of oxidation state on the pH dependence of hydrous iridium oxide films. *Electrochimica Acta* **76,** 26–33 (Aug. 2012).

232. Sardarinejad, A., Maurya, D. K. & Alameh, K. The pH sensing properties of RF sputtered RuO2 thin-film prepared using different Ar/O2 flow ratio. *Materials* **8,** 3352–3363 (2015).

233. Yamanaka, K. Anodically electrodeposited iridium oxide films (AEIROF) from alkaline solutions for electrochromic display devices. *Japanese Journal of Applied Physics* **28,** 632–637 (Apr. 1989).

234. Petit, M. A. & Plichon, V. Anodic electrodeposition of iridium oxide films. *Journal of Electroanalytical Chemistry* **444,** 247–252 (Mar. 1998).

235. Baur, J. E. & Spaine, T. W. Electrochemical deposition of iridium(IV) oxide from alkaline solutions of iridium(III) oxide. *Journal of Electroanalytical Chemistry* **443,** 208–216 (Feb. 1998).

236. Marzouk, S. A. Improved electrodeposited iridium oxide pH sensor fabricated on etched titanium substrates. *Analytical Chemistry* **75,** 1258–1266 (Mar. 2003).

237. Elsen, H. A., Monson, C. F. & Majda, M. Effects of Electrodeposition Conditions and Protocol on the Properties of Iridium Oxide pH Sensor Electrodes. *Journal of The Electrochemical Society* **156,** F1 (Nov. 2009).

238. Marzouk, S. A. *et al.* Electrodeposited iridium oxide pH electrode for measurement of extracellular myocardial acidosis during acute ischemia. *Analytical Chemistry* **70,** 5054–5061. ISSN: 00032700 (Dec. 1998).

239. Huang, W. D., Cao, H., Deb, S., Chiao, M. & Chiao, J. C. A flexible pH sensor based on the iridium oxide sensing film. *Sensors and Actuators, A: Physical* **169,** 1–11 (Sept. 2011).

240. Rawson, T. M. *et al.* Towards a minimally invasive device for beta-lactam monitoring in humans. *Electrochemistry Communications* **82,** 1–5 (Sept. 2017).

241. Gowers, S. A. *et al.* Development of a Minimally Invasive Microneedle-Based Sensor for Continuous Monitoring of β-Lactam Antibiotic Concentrations in Vivo. *ACS Sensors* **4,** 1072–1080 (Apr. 2019).

242. Hendrikse, J., Olthuis, W. & Bergveld, P. A method of reducing oxygen induced drift in iridium oxide pH sensors. *Sensors and Actuators, B: Chemical* **53,** 97–103 (Nov. 1998).

243. Kim, Y. J., Lee, Y. C., Sohn, B. K., Lee, J. H. & Kim, C. S. A Novel pH Microsensor with a Built-in Reference Electrode. *Journal of the Korean Physical Society* **43,** 769–772 (Nov. 2003).

244. Lee, C. S., Kyu Kim, S. & Kim, M. Ion-sensitive field-effect transistor for biological sensing. *Sensors* **9,** 7111–7131 (Sept. 2009).

245. Sakurai, T. & Husimi, Y. Real-Time Monitoring of DNA Polymerase Reactions by a Micro ISFET pH Sensor. *Analytical Chemistry* **64,** 1996–1997 (1992).

246. Toumazou, C. *et al.* Simultaneous DNA amplification and detection using a pH-sensing semiconductor system. *Nature Methods* **10,** 641–646 (July 2013).

247. Moschou, D. & Tserepi, A. The lab-on-PCB approach: tackling the μTAS commercial upscaling bottleneck. *Lab on a Chip* **17,** 1388–1405 (Apr. 2017).

248. Moschou, D. *et al.* Surface and electrical characterization of Ag/AgCL pseudo-reference electrodes manufactured with commercially available PCB technologies. *Sensors (Switzerland)* **15,** 18102–18113 (July 2015).

249. Papamatthaiou, S., Estrela, P. & Moschou, D. Printable graphene BioFETs for DNA quantification in Lab-on-PCB microsystems. *Scientific Reports* **11,** 1–9 (Dec. 2021).

250. Caras, S. & Janata, J. Field effect transistor sensitive to penicillin. *Analytical Chemistry* **52,** 1935–1937 (1980).

251. Anzai, J. I., Hashimoto, J. Y., Osa, T. & Matsuo, T. Penicillin Sensors Based on an Ion-Sensitive Field Effect Transistor Coated with Stearic Acid Langmuir-Blodgett Membrane. *Analytical Sciences* **4,** 247–250 (Jan. 1988).

252. Soldatkin, A. P., Gorchkov, D. V., Martelet, C. & Jaffrezic-Renault, N. Application of charged polymeric materials as additional permselective membranes for modulation of the working characteristics of penicillin sensitive ENFETs. *Materials Science and Engineering C* **5,** 35–40 (Sept. 1997).

253. Liu, J., Liang, L., Li, G., Han, R. & Chen, K. H+ISFET-based biosensor for determination of penicillin G. *Biosensors and Bioelectronics* **13,** 1023–1028 (Oct. 1998).

254. Poghossian, A., Schöning, M. J., Schroth, P., Simonis, A. & Lüth, H. An ISFET-based penicillin sensor with high sensitivity, low detection limit and long lifetime. *Sensors and Actuators, B: Chemical* **76,** 519–526 (June 2001).

255. Poghossian, A. *et al.* Penicillin detection by means of field-effect based sensors: EnFET, capacitive EIS sensor or LAPS? *Sensors and Actuators, B: Chemical* **78,** 237–242 (Aug. 2001).

256. Minteer, S. D., Zaouk, R., Park, B. Y. & Madou, M. J. in *Microfluidic techniques: reviews and protocols* 5–15 (Humana Press, 2006).

257. Kohli, R. & Mittal, K. L. *Developments in surface contamination and cleaning* (William Andrew, 2016).

258. Vig, J. R. & Bus, J. W. UV Ozone Cleaning of Surfaces. *IEEE Transactions on Parts, Hybrids, and Packaging* **12,** 365–370 (1976).

259. Awan, T. I., Bashir, A. & Tehseen, A. *Chemistry of nanomaterials: fundamentals and applications* (Elsevier, 2020).

260. Ito, T. & Okazaki, S. Pushing the limits of lithography. *Nature* **406,** 1027–1031 (Aug. 2000).

261. Eckermann, A. L., Feld, D. J., Shaw, J. A. & Meade, T. J. *Electrochemistry of redox-active self-assembled monolayers* Aug. 2010.

262. Yamanaka, K. The electrochemical behavior of anodically electrodeposited iridium oxide films and the reliability of transmittance variable cells. *Japanese Journal of Applied Physics* **30,** 1285–1289 (June 1991).

263. Steegstra, P. & Ahlberg, E. Involvement of nanoparticles in the electrodeposition of hydrous iridium oxide films. *Electrochimica Acta* **68,** 206–213 (Apr. 2012).

264. Bezbaruah, A. N. & Zhang, T. C. Fabrication of anodically electrodeposited iridium oxide film pH microelectrodes for microenvironmental studies. *Analytical Chemistry* **74,** 5726–5733 (Nov. 2002).

265. Bergveld, P. The operation of an ISFET as an electronic device. *Sensors and Actuators* **1,** 17–29 (Jan. 1981).

266. Palán, B., Santos, F. V., Karam, J. M., Courtois, B. & Husák, M. New ISFET sensor interface circuit for biomedical applications. *Sensors and Actuators, B: Chemical* **57,** 63–68 (Sept. 1999).

267. Sakata, T., Kamahori, M. & Miyahara, Y. DNA analysis chip based on field-effect transistors. *Japanese Journal of Applied Physics, Part 1: Regular Papers and Short Notes and Review Papers* **44,** 2854–2859 (Apr. 2005).

268. Kaisti, M. *et al.* Real-Time wash-free detection of unlabeled PNA-DNA hybridization using discrete FET sensor. *Scientific Reports* **7,** 1–8 (Dec. 2017).

269. Vij, D. R. *Handbook of applied solid state spectroscopy* (Springer, 2006).

270. Biesinger, M. *X-ray Photoelectron Spectroscopy (XPS) Reference Pages: Spin Orbit Splitting* `http://www.xpsfitting.com/2012/08/spin-orbit-splitting.html` (Apr. 19, 2021).

271. Barron, A. R. & Raja, P. M. V. *Physical Methods in Chemistry and Nano Science* (MiDAS Green Innovation, 2019).

272. Muso. *EDX-scheme* `https://commons.wikimedia.org/wiki/File:EDX-scheme.svg` (Feb. 10, 2021).

273. Jenkins, R., Manne, R., Robin, R. & Senemaud, C. Nomenclature System for X-Ray Spectroscopy. *Pure and Applied Chemistry* **63,** 735–746 (Jan. 1991).

274. Kanaya, K. & Okayama, S. Penetration and energy-loss theory of electrons in solid targets. *Journal of Physics D: Applied Physics* **5,** 43–58 (Jan. 1972).

275. Luke, K. L. Choice of a range-energy relationship for the analysis of electron-beam-induced-current line scans. *Journal of Applied Physics* **76,** 1081–1091 (June 1994).

276. Liao, Y. Practical electron microscopy and database. *An Online Book* (2006).

277. Hammond, C. *The basics of crystallography and diffraction* 3rd ed. (Oxford University Press, 2009).

278. D. N. Chan, C. *Braggs Law* `https://commons.wikimedia.org/wiki/File:Loi_de_bragg.png` (Feb. 10, 2021).

279. Hydrargyrum. *Bragg diffraction* `https://commons.wikimedia.org/wiki/File:Bragg_diffraction_2.svg` (Feb. 10, 2021).

280. Downs, R. T. & Hall-Wallace, M. The American Mineralogist Crystal Structure Database. *American Mineralogist* **88,** 247–250 (2003).

281. Gražulis, S. *et al.* Crystallography Open Database – an open-access collection of crystal structures. *Journal of Applied Crystallography* **42,** 726–729 (Aug. 2009).

282. Grazulis, S. *et al.* Crystallography Open Database (COD): an open-access collection of crystal structures and platform for world-wide collaboration. *Nucleic Acids Research* **40,** D420–D427 (2012).

283. Grazulis, S., Merkys, A., Vaitkus, A. & Okulic-Kazarinas, M. Computing stoichiometric molecular composition from crystal structures. *Journal of Applied Crystallography* **48,** 85–91 (Feb. 2015).

284. Merkys, A. *et al. COD::CIF::Parser*: an error-correcting CIF parser for the Perl language. *Journal of Applied Crystallography* **49** (Feb. 2016).

285. Quirós, M., Gražulis, S., Girdzijauskaitė, S., Merkys, A. & Vaitkus, A. Using SMILES strings for the description of chemical connectivity in the Crystallography Open Database. *Journal of Cheminformatics* **10** (May 2018).

286. Vaitkus, A., Merkys, A. & Gražulis, S. Validation of the Crystallography Open Database using the Crystallographic Information Framework. *Journal of Applied Crystallography* **54,** 661–672 (Apr. 2021).

287. Larkin, P. *IR and raman spectroscopy: principles and spectral interpretation* (Elsevier, 2011).

288. Becerra P., T. *Molecular Vibration* `https://en.wikipedia.org/wiki/Molecular_vibration` (Feb. 10, 2021).

289. Griffiths, P. R. & A., D. H. J. *Fourier transform infrared spectrometry* (Wiley-Interscience, 2007).

290. Settle, F. A. & Hsu, C.-P. S. in *Handbook of instrumental techniques for analytical chemistry* (Prentice-Hall, 1997).

291. Saptari, V. *Fourier transform spectroscopy instrumentation engineering* (SPIE, 2003).

292. Sanchonx. *Interferometer for FTIR* `https://commons.wikimedia.org/wiki/File:FTIR_Interferometer.png` (Feb. 10, 2021).

293. Thermo-Nicolet. *FT-IR vs Dispersive Infrared* `http://www.thermo.com.cn/Resources/200802/productPDF_21615.pdf` (Feb. 19, 2021).

294. Abbott-Lyon, H. *Research Methods: Surface Science Methods* `http://facultyweb.kennesaw.edu/habbott/research/instruments.php` (Feb. 19, 2021).

295. Gericke, A. & Hühnerfuss, H. In situ investigation of saturated long-chain fatty acids at the air/water interface by external infrared reflection-absorption spectrometry. *Journal of Physical Chemistry* **97,** 12899–12908 (1993).

296. Blaudez, D. *et al.* Investigations at the air/water interface using polarization modulation IR spectroscopy. *Journal of the Chemical Society - Faraday Transactions* **92,** 525–530 (Jan. 1996).

297. Mendelsohn, R., Mao, G. & Flach, C. R. Infrared Reflection-Absorption Spectroscopy: Principles and Applications to Lipid-Protein Interaction in Langmuir Films (2009).

298. Liu, S. X. & Kim, J.-T. Application of Kevin—Voigt Model in Quantifying Whey Protein Adsorption on Polyethersulfone Using QCM-D. *JALA: Journal of the Association for Laboratory Automation* **14,** 213–220 (Aug. 2009).

299. Ohlsson, G. *Why it is useful to use multiple overtones in QCM measurements* `https://www.biolinscientific.com/blog/why-it-is-useful-to-use-multiple-overtones-in-qcm-measurements`.

300. Sauerbrey, G. Verwendung von Schwingquarzen zur Wägung dünner Schichten und zur Mikrowägung. *Zeitschrift für Physik* **155,** 206–222 (1959).

301. Johannsmann, D. Viscoelastic, mechanical, and dielectric measurements on complex samples with the quartz crystal microbalance. *Physical Chemistry Chemical Physics* **10,** 4516–4534. `https://pubs.rsc.org/en/content/articlehtml/2008/cp/b803960g%20https://pubs.rsc.org/en/content/articlelanding/2008/cp/b803960g` (July 2008).

302. Voinova, M. V., Rodahl, M., Jonson, M. & Kasemo, B. Viscoelastic Acoustic Response of Layered Polymer Films at Fluid-Solid Interfaces: Continuum Mechanics Approach. *Physica Scripta* **59,** 391–396 (May 1999).

303. Rani, R. A. & Sidek, O. *ISFET pH sensor characterization: Towards biosensor microchip application* in *IEEE Region 10 Annual International Conference, Proceedings/TENCON* **D** (2004).

304. Mo, Y. *et al.* In situ iridium LIII-edge X-ray absorption and surface enhanced Raman spectroscopy of electrodeposited iridium oxide films in aqueous electrolytes. *Journal of Physical Chemistry B* **106,** 3681–3686. ISSN: 10895647 (Apr. 2002).

305. Armbruster, D. A. & Pry, T. Limit of blank, limit of detection and limit of quantitation. *The Clinical biochemist. Reviews* **29 Suppl 1,** S49–52 (Aug. 2008).

306. Milotti, E. *1/f noise: a pedagogical review* `http://arxiv.org/abs/physics/0204033` (Feb. 10, 2021).

307. Wolfinger, R. D. *et al.* Two approaches for estimating the lower limit of quantitation (LLOQ) of microRNA levels assayed as exploratory biomarkers by RT-qPCR. *BMC Biotechnology* **18,** 1–9 (Feb. 2018).

308. Gui-Hua, W., Dun, Y. & Yao-Lin, W. ISFET temperature characteristics. **11,** 221–237 (Apr. 1987).

309. Chung, W. Y. *et al.* New ISFET interface circuit design with temperature compensation. *Microelectronics Journal* **37,** 1105–1114 (Oct. 2006).

310. Hazarika, C., Neroula, S. & Sharma, S. *Long Term Drift Observed in ISFET Due to the Penetration of H+ Ions into the Oxide Layer* in *Lecture Notes in Computer Science (including subseries Lecture Notes in Artificial Intelligence and Lecture Notes in Bioinformatics)* **11942 LNCS** (Springer, Dec. 2019), 543–553.

311. Khanna, V. K. in *Extreme-Temperature and Harsh-Environment Electronics Physics, technology and applications* (IOP Publishing, 2017).

312. Yin, L. T., Chou, J. C., Chung, W. Y., Sun, T. P. & Hsiung, S. K. Study of indium tin oxide thin film for separative extended gate ISFET. *Materials Chemistry and Physics* **70,** 12–16 (Apr. 2001).

313. Cogan, S. F., Plante, T. D. & Ehrlich, J. *Sputtered indium oxide films (SIROFs) for low-impedance neural stimulation and recording electrodes* in *Annual International Conference of the IEEE Engineering in Medicine and Biology - Proceedings* **26 VI** (NIH Public Access, 2004), 4153–4156.

314. Hasenkamp, W., Musa, S., Alexandru, A., Eberle, W. & Bartic, C. *Electrodeposition and characterization of iridium oxide as electrode material for neural recording and stimulation* in *IFMBE Proceedings* **25** (Springer Verlag, 2009), 472–475.

315. McIntyre, J. D. E., Peck, W. F. & Nakahara, S. Oxidation State Changes and Structure of Electrochromic Iridium Oxide Films. *Journal of The Electrochemical Society* **127,** 1264–1268 (June 1980).

316. Newbury, D. E. & Ritchie, N. W. Is scanning electron microscopy/energy dispersive X-ray spectrometry (SEM/EDS) quantitative? *Scanning* **35,** 141–168 (May 2013).

317. Pfeifer, V. *et al.* The electronic structure of iridium and its oxides. *Surface and Interface Analysis* **48,** 261–273 (May 2016).

318. Freakley, S. J., Ruiz-Esquius, J. & Morgan, D. J. The X-ray photoelectron spectra of Ir, IrO2 and IrCl3 revisited. *Surface and Interface Analysis* **49,** 794–799 (Aug. 2017).

319. Carlson, T. A. The nature of secondary electrons created as the result of electron shake off and vacancy cascades. *Radiation Research* **64,** 53–69 (1975).

320. Wagner, C. D. Sensitivity factors for XPS analysis of surface atoms. *Journal of Electron Spectroscopy and Related Phenomena* **32,** 99–102 (Jan. 1983).

321. Wyckoff, R. W. G. *Crystal structures* (Interscience Publishers, 1963).

322. Yan, W., Petkov, V., Mahurin, S. M., Overbury, S. H. & Dai, S. Powder XRD analysis and catalysis characterization of ultra-small gold nanoparticles deposited on titania-modified SBA-15. *Catalysis Communications* **6,** 404–408 (June 2005).

323. Lu, Y. *et al.* Anodically electrodeposited iridium oxide films microelectrodes for neural microstimulation and recording. *Sensors and Actuators, B: Chemical* **137,** 334–339 (Mar. 2009).

324. Van der Schoot, B. H. & Bergveld, P. ISFET based enzyme sensors. *Biosensors* **3,** 161–186 (Jan. 1987).

325. Liao, C. & Nicklaus, M. C. Comparison of nine programs predicting pKa values of pharmaceutical substances. *Journal of Chemical Information and Modeling* **49,** 2801–2812 (Dec. 2009).

326. Kurtzman, N. A. in *Urolithiasis* 19–22 (Springer US, Sept. 1989).

327. Urbansky, E. T. & Schock, M. R. Understanding, Deriving, and Computing Buffer Capacity. *Journal of Chemical Education* **77,** 1640–1644 (Dec. 2000).

328. Price, N. C. & Stevens, L. *Fundamentals of enzymology* (Oxford University Press, 1999).

329. Waley, S. G. The pH dependence and group modification of β lactamase I. *Biochemical Journal* **149,** 547–551 (1975).

330. Bicknell, R., Knott-Hunziker, V. & Waley, S. G. The pH-dependence of class B and class C beta-lactamases. *The Biochemical journal* **213,** 61–66 (1983).

331. Guillaume, G. *et al.* Site-directed mutagenesis of glutamate 166 in two β-lactamases. Kinetic and molecular modeling studies. *Journal of Biological Chemistry* **272,** 5438–5444 (Feb. 1997).

332. Page, M. I. & Laws, A. P. The mechanism of catalysis and the inhibition of β-lactamases. *Chemical Communications,* 1609–1617 (Aug. 1998).

333. Li, T. *et al.* Biochemical Characteristics of New Delhi Metallo-β-Lactamase-1 Show Unexpected Difference to Other MBLs. *PLoS ONE* **8** (ed Khan, R. H.) e61914 (Apr. 2013).

334. Stojanoski, V. *et al.* A triple mutant in the Ω-loop of TEM-1 β-lactamase changes the substrate profile via a large conformational change and an altered general base for catalysis. *Journal of Biological Chemistry* **290,** 10382–10394 (Apr. 2015).

335. ESCMID - European Society of Clinical Microbiology and Infectious Diseases. *EUCAST - Clinical breakpoints - breakpoints and guidance* `https://www.eucast.org/clinical_breakpoints/` (Apr. 10, 2021).

336. Akova, M. Sulbactam-containing β-lactamase inhibitor combinations. *Clinical Microbiology and Infection* **14,** 185–188 (Jan. 2008).

337. Miller, L. M. *et al.* Surface-Bound Antibiotic for the Detection of β-Lactamases. *ACS Applied Materials and Interfaces* **11,** 32599–32604 (Sept. 2019).

338. Wongkaew, N., Simsek, M., Griesche, C. & Baeumner, A. J. Functional Nanomaterials and Nanostructures Enhancing Electrochemical Biosensors and Lab-on-a-Chip Performances: Recent Progress, Applications, and Future Perspective. *Chemical Reviews* **119,** 120–194 (Jan. 2019).

339. Nguyen, H. *et al.* Surface Plasmon Resonance: A Versatile Technique for Biosensor Applications. *Sensors* **15,** 10481–10510 (May 2015).

340. Reimhult, E. & Höök, F. Design of Surface Modifications for Nanoscale Sensor Applications. *Sensors (Basel, Switzerland)* **15,** 1635 (2015).

341. Waggoner, P. S. & Craighead, H. G. Micro- and nanomechanical sensors for environmental, chemical, and biological detection. *Lab on a Chip* **7,** 1238 (Oct. 2007).

342. Pitruzzello, G. & Krauss, T. F. Photonic crystal resonances for sensing and imaging. *Journal of Optics* **20,** 073004 (June 2018).

343. Greenwood, D., Finch, R. G., . Norrby, S. R., Whitely, R. J. & B., S. W. *Antibiotic and chemotherapy, 9th Edition* 170–199 (2010).

344. Qi, X., Gunawan, P., Xu, R. & Chang, M. W. Cefalexin-immobilized multi-walled carbon nanotubes show strong antimicrobial and anti-adhesion properties. *Chemical Engineering Science* **84,** 552–556 (Dec. 2012).

345. Mehne, J. *et al.* Characterisation of morphology of self-assembled PEG monolayers: a comparison of mixed and pure coatings optimised for biosensor applications. *Analytical and Bioanalytical Chemistry* **391,** 1783–1791 (2008).

346. Fontaine, S. D., Reid, R., Robinson, L., Ashley, G. W. & Santi, D. V. Long-term stabilization of maleimide-thiol conjugates. *Bioconjugate Chemistry* **26,** 145–152 (Jan. 2015).

347. Fan, M. & Brolo, A. G. Self-Assembled Au Nanoparticles as Substrates for Surface-Enhanced Vibrational Spectroscopy: Optimization and Electrochemical Stability. *ChemPhysChem* **9,** 1899–1907 (Sept. 2008).

348. Schwartz, D. K. Mechanisms and kinetics of self-assembled monolayer formation. *Annual Review of Physical Chemistry* **52,** 107–137 (Nov. 2001).

349. Hinterwirth, H. *et al.* Quantifying Thiol Ligand Density of Self-Assembled Monolayers on Gold Nanoparticles by Inductively Coupled Plasma–Mass Spectrometry. *ACS Nano* **7,** 1129–1136 (2013).

350. Casalini, S., Bortolotti, C. A., Leonardi, F. & Biscarini, F. Self-assembled monolayers in organic electronics. *Chemical Society Reviews* **46,** 40–71 (Jan. 2017).

351. Xue, Y., Li, X., Li, H. & Zhang, W. Quantifying thiol-gold interactions towards the efficient strength control. *Nature Communications* **5,** 1–9 (June 2014).

352. Gil, M., Núñez, J. L., Palafox, M. A. & Iza, N. FTIR study of five complex β-lactam molecules. *Biopolymers* **62,** 278–294 (Jan. 2001).

353. KONG, J. & YU, S. Fourier Transform Infrared Spectroscopic Analysis of Protein Secondary Structures. *Acta Biochimica et Biophysica Sinica* **39,** 549–559 (Aug. 2007).

354. Prime, K. L. & Whitesides, G. M. Adsorption of proteins onto surfaces containing end-attached oligo(ethylene oxide): a model system using self-assembled monolayers. *Journal of the American Chemical Society* **115,** 10714–10721 (1993).

355. Banerjee, I., Pangule, R. C. & Kane, R. S. Antifouling Coatings: Recent Developments in the Design of Surfaces That Prevent Fouling by Proteins, Bacteria, and Marine Organisms. *Advanced Materials* **23,** 690–718 (2010).

356. Weimer, B. C., Walsh, M. K. & Wang, X. Influence of a poly-ethylene glycol spacer on antigen capture by immobilized antibodies. *Journal of Biochemical and Biophysical Methods* **45,** 211–219 (Sept. 2000).

357. Unsworth, L. D., Sheardown, H. & Brash, J. L. Polyethylene oxide surfaces of variable chain density by chemisorption of PEO-thiol on gold: Adsorption of proteins from plasma studied by radiolabelling and immunoblotting. *Biomaterials* **26,** 5927–5933 (2005).

358. Chang, E. P. *et al.* Synergistic Biomineralization Phenomena Created by a Combinatorial Nacre Protein Model System. *Biochemistry* **55,** 2401–2410 (2016).

359. Flores-Mireles, A. L., Walker, J. N., Caparon, M. & Hultgren, S. J. Urinary tract infections: epidemiology, mechanisms of infection and treatment options. *Nature Reviews Microbiology* **13,** 269–284 (May 2015).

360. Rizvi, M., Khan, F., Shukla, I., Malik, A. & Shaheen. Rising prevalence of antimicrobial resistance in urinary tract infections during pregnancy: necessity for exploring newer treatment options. **3,** 98–103 (2 2011).

361. Takaba, K. *et al.* Emergence of extended-spectrum beta-lactamase-producing Escherichia coli in catheter-associated urinary tract infection in neurogenic bladder patients. *American journal of infection control* **42,** 29–31 (3 2014).

362. Dreesen, L. *et al.* Adsorption Properties of the Penicillin Derivative DTPA on Gold Substrates. *ChemPhysChem* **8,** 1071–1076 (May 2007).

363. Fournier, P. E. *et al.* Modern clinical microbiology: New challenges and solutions. *Nature Reviews Microbiology* **11,** 574–585 (Aug. 2013).

364. Liu, Y., Li, Y., Li, X. M. & He, T. Kinetics of (3-aminopropyl)triethoxylsilane (aptes) silanization of superparamagnetic iron oxide nanoparticles. *Langmuir* **29,** 15275–15282 (Dec. 2013).

365. Kim, H. & Kwon, J. Y. Enzyme immobilization on metal oxide semiconductors exploiting amine functionalized layer. *RSC Advances* **7,** 19656–19661 (Mar. 2017).

366. Serodre, T. *et al.* Surface silanization of graphene oxide under mild reaction conditions. *Journal of the Brazilian Chemical Society* **30,** 2488–2499 (Oct. 2019).

367. Wolf, N. R. *et al.* Surface Functionalization of Platinum Electrodes with APTES for Bioelectronic Applications. *ACS Applied Bio Materials* **3,** 7113–7121 (Oct. 2020).

368. Cengiz, N., Rao, J., Sanyal, A. & Khan, A. Designing functionalizable hydrogels through thiol-epoxy coupling chemistry. *Chemical Communications* **49,** 11191–11193 (Nov. 2013).

369. Adatia, K. K., Keller, S., Götz, T., Tovar, G. E. & Southan, A. Hydrogels with multiple clickable anchor points: Synthesis and characterization of poly(furfuryl glycidyl ether)-: Block-poly(ethylene glycol) macromonomers. *Polymer Chemistry* **10,** 4485–4494 (Aug. 2019).

370. Rawat, D. & Nair, D. Extended-spectrum ß-lactamases in gram negative bacteria. *Journal of Global Infectious Diseases* **2,** 263 (2010).